

Characterization of Structural Adhesives Using Lap Shear and Pin and Collar Tests

by

Yogesh Nandwani

A thesis
presented to the University of Waterloo
in fulfillment of the
thesis requirement for the degree of
Master of Applied Science
in
Mechanical Engineering

Waterloo, Ontario, Canada, 2015

© Yogesh Nandwani 2015

AUTHOR'S DECLARATION

I hereby declare that I am the sole author of this thesis. This is a true copy of the thesis, including any required final revisions, as accepted by my examiners.

I understand that my thesis may be made electronically available to the public.

ABSTRACT

Increasingly stringent government regulations on vehicle fuel economy and emission standards have challenged auto manufacturers to improve the fuel economy of cars built for sale in North America. Lightweighting vehicles is an efficient method of achieving this goal, as lighter vehicles have better fuel economy compared to heavier ones. Vehicle weight can be reduced by optimized design and by using alternative lightweight materials, such as aluminum and magnesium. Combining both approaches results in a vehicle which is comprised of strategically-placed materials to fulfill performance requirements.

Constructing a vehicle frame with dissimilar materials using traditional joining methods can be challenging. Adhesive bonding is one alternative to traditional methods with advantages in areas such as mitigation of galvanic corrosion, reducing stress concentrations, and enhanced fatigue strength.

The strength of an adhesive bond is highly dependent on the conditions of the surfaces of the bonded materials. Two different toughened epoxy structural adhesives were investigated in this study, a two part epoxy (DP460NS) and a one-part epoxy (SA9850). Experimental lap shear tests were undertaken to identify optimum strength combinations between adhesives and adherend surface preparation. Each adherend was prepared using a variety of pretreatment methods including conversion coatings, anodization, mechanical abrasion and intentional contamination by forming lubricant. The samples were assembled at different time periods to observe the effect of time on the surface pretreatment methods. One limitation of this test is that the joint is subjected to mixed-mode loading. The experimental tests were simulated using a commercially available FEA software package and measured material properties to provide insight into the measured strength values.

Pin and collar tests were performed to measure adhesive strength in pure shear loading at varying strain rates. Several displacement measurement methods were investigated, with an optical displacement providing the highest resolution in measurement.

When bonding aluminum, it was found that adhesive joints made with DP460NS exhibited higher dependence on surface preparation methods, compared to the joints produced with SA9850. Gritblasted surface produced the best adhesion to DP460NS. Bonds created with SA9850 produced relatively high joint strength numbers on all tested combinations, with contamination of adherends with a metal forming lubricant (drylube E1) producing the strongest bonds.

When bonding magnesium, the highest joint strength numbers were acquired by a gritblasted surface with DP460NS, and contaminated surface with SA9850. However, the joint strength numbers were consistently lower than those acquired with aluminum adherends, suggesting the need for research into other types of pretreatment methods.

For the pin and collar tests, the adhesives exhibited an increase in strength at higher shear deformation rates. The very small deformations, on the order of microns and similar to the deformation of the adherends during the test, did not allow for full stress-strain curves to be developed. However, the strength characteristics were measured, where the two-part epoxy (DP460NS) demonstrated a larger increase in strength with strain rate compared to the one-part epoxy (SA9850).

Recommendations for future work include testing dissimilar adherend materials to investigate the effect of imbalanced joints on adhesive strength. Additional tests should be investigated to measure shear properties such as the edge notch flexural beam.

Ultimately, the contributions of this research include the evaluation of surface preparations for adhesive joining of important lightweighting materials, and the measurement of strength in shear loading, which is necessary for implementation of these properties with computer aided engineering approaches.

ACKNOWLEDGEMENTS

The author wishes to acknowledge the important collaboration of various people involved in this work:

Mary M. Caruso-Dailey and Kent Nielson at 3M corp.

University of Waterloo laboratory and machine shop personnel, especially Tom Gawel and Jeff Wemp.

Professor Duane Cronin, for his extensive knowledge and continuous guidance.

DEDICATION

This work is dedicated to my parents, to whom I owe all of my successes.

TABLE OF CONTENTS

Author's Declaration	ii
Abstract.....	iii
Acknowledgements	v
Dedication	vi
Table of Contents	vii
List of Tables	x
List of Figures.....	xi
List of Equations	xvi
1 Introduction.....	1
1.1. Research Motivation	1
1.2. Thesis Outline	5
2 Background.....	6
2.1. Joining methods	6
2.2. Adhesives	7
2.3. Adhesive Testing.....	10
2.3.1. Adhesive Joint Testing	10
2.3.2. Bulk Adhesive Testing	14
2.4. Lightweighting materials.....	16
2.4.1. High Strength Steel	16
2.4.2. Aluminum.....	18
2.4.3. Magnesium	19
2.5. Surface Preparation for adhesive joining	22
2.5.1. Gritblasting (mechanical pretreatment).....	22
2.5.2. Aluminum Anodization (Chemical Pretreatment).....	24
2.5.3. Alodine Conversion Coatings	25

2.5.4.	Contamination	25
2.6.	Accelerated testing for Environmental Effects	26
2.7.	Numerical Representation of Adhesive Joints	27
2.7.1.	Tiebreak Contact Definition	28
2.7.2.	Solid Continuum Mechanics Approach.....	29
2.7.3.	Fracture Mechanics Approach.....	30
2.7.4.	Cohesive Zone Model	31
3	Lap Shear Test.....	34
3.1.	Background	34
3.2.	Methods.....	38
3.2.1.	Preliminary Tests and Results	41
3.3.	Test Apparatus Compliance Measurement.....	44
3.4.	Test Results and Discussion	47
3.4.1.	Summary of Results	48
3.5.	Effect of Environmental Exposure on joint strength.....	54
3.6.	Numerical Simulation	58
3.6.1.	Geometry and Boundary Conditions	58
3.6.2.	Material Model.....	58
3.6.3.	Results	61
3.6.4.	Discussion and recommendations	66
4	Pin and Collar Test	68
4.1.	Background	68
4.2.	Methods.....	70
4.2.1.	Test Matrix	71
4.2.2.	Equipment	72
4.2.3.	Displacement Measurement	72
4.2.4.	Development of Average Curves	77

4.2.5. Sectioned Sample Analysis	80
4.3. Results	82
4.3.1. Sectioned Sample Results	87
4.4. Discussion and Limitations	90
4.5. Numerical Simulation	91
4.5.1. Geometry and Boundary Conditions	92
4.5.2. Material Model.....	94
4.5.3. Results	95
4.5.4. discussions and Limitations.....	100
5 Summary and Recommendations	101
Appendix A: Technical Data Sheets	105
Appendix B: Lap Shear Data Charts	119
Appendix C: Pin and Collar Data Charts.....	127
Appendix D: LS-DYNA Cards.....	135
Appendix E: Lap Shear Test MathCAD Solution.....	141
Appendix F: Pin and Collar MathCAD Solution.....	145
Appendix G: Open sandwich samples.....	153
Appendix H: SAMP-1 Material Model Information	159
Bibliography	162

LIST OF TABLES

Table 1-1: Base curb weight of Ford F150 pickup truck, model year 2014 and 2015, 3.7L V6 engine. Sources: Ford F-150 Specifications [9, 10]	2
Table 2-1: Mechanical properties of two structural adhesives (DP460NS, SA9850) tests conducted at quasi-static strain rate of 1.2×10^{-3} (mm/mm) (adapted from Trimiño and Cronin [43])	8
Table 2-2: Aluminum applications in the automotive industry (1993 North American car percentages in parentheses) (adapted from Cole and Sherman [8]).....	19
Table 2-3: Mechanical properties of three aluminum alloys (source: Matweb [84]).....	19
Table 2-4: Producers of magnesium alloys and applications on car models (adapted from Kulekci M. [85])	20
Table 2-5: Mechanical properties of magnesium alloys (adapted from Miles [92], Boba [93]).....	21
Table 3-1: Material thicknesses for lap shear testing.....	38
Table 3-2: Finalized matrix for lap shear tests.....	44
Table 3-3: Environmental exposure test matrix.....	54
Table 3-4: Loading slopes of lap shear tests	64
Table 4-1: Pin and collar test variables.....	71
Table 4-2: Accuracy comparison table between the actuator, LVDT and the clip gauge, and video image analysis.....	76
Table 4-3: Calculated values of shear moduli of the adhesives	80
Table 4-4: Constants of the equation fit for all data.....	82
Table 4-5: Increase of shear strength per decade of shear rate for DP460NS and SA9850.....	83
Table 4-6: Calculated shear modulus value using various tracked points	90
Table 4-7: Properties of steel adherends used for pin and collar numerical simulation	94
Table 4-8: Shear stress values at different timestamps from FEA.....	99

LIST OF FIGURES

Figure 1-1: Relation between vehicle weight and fuel economy, data compiled from EPA certified vehicles in 1977. (adapted from Yamane K. and Furuhashi S. [5]).....	1
Figure 1-2: Super Light Car Body in White (taken from Goede M. [17]).....	3
Figure 1-3: Front end structure of 2012 Audi A7 (taken from Audi Collision Frame Technology Guide [25])	4
Figure 2-1: Examples of joining methods: adhesive bonding (A), mechanical fastener (B), welding (C), rivet (D).....	6
Figure 2-2: uniaxial tension results at various strain rates (DP460NS [L], SA9850 [R]).....	9
Figure 2-3: Thick adherend lap shear results at various deformation rates (DP460NS [L], SA9850 [R]) ...	9
Figure 2-4: Shear stress vs shear rate of DP460NS and SA9850, data acquired from thick adherend lap shear tests.....	10
Figure 2-5: Adhesive joint modes of loading (adapted from Adderley C.S.[45])	11
Figure 2-6: SEM observation of adhesive layer under pure tension load. Craze are identified as ‘particle’; ‘cavitation’ refers to bare spots formed during heat curing process (taken from Hao C. [47])	11
Figure 2-7: SEM observation of adhesive layer under pure shear load. Craze are identified as ‘particle’; ‘cavitation’ refers to bare spots formed during heat curing process (taken from Hao C.[47])	12
Figure 2-8: Joint failure types (cohesive [L], interfacial [M], structural [R]).....	12
Figure 2-9: Relationship between lap shear strength with bond thickness of an epoxy adhesive (Left: taken from Teutenberg and Hahn [50], Right: taken from Arenas et al. [49]).....	13
Figure 2-10: Lap shear test [L], rotated lap shear joint during loading [R] (taken from Kafkalidis and Thouless [59])	13
Figure 2-11: Bulk adhesive test geometries (tension [Top], compression [Middle], shear [Bottom] (adapted from Dolev and Ishai [68]).....	15
Figure 2-12: Bulk tensile sample geometry, micro-sized	15
Figure 2-13: material distribution for an average North American 3360lb 2005 vehicle manufactured by U.S. automakers – Daimler, Ford and GM (adapted from Cole, G.S. [70])	16
Figure 2-14: Elongation to failure (%) versus ultimate tensile strength <i>banana curve</i> of automotive steels (taken from Billur M.S. [72]).....	17
Figure 2-15: True stress versus plastic strain curves of magnesium AZ31b (taken from Boba [93])	21
Figure 2-16: True stress versus plastic strain curves of magnesium ZEK100 (taken from Boba [93]).....	22
Figure 2-17: Surface morphology of aluminum 5251 alloy after grit blasting (taken from Brewis D.M. et al. [96]).....	23

Figure 2-18 Visualization of Ra value with respect to a surface profile (taken from The Home of Surface Measurement [98]).....	24
Figure 2-19: Schematic diagram of porous alumina template (adapted from Jagminas A.[105])	25
Figure 2-20: Dependence of joint strength upon water uptake for variously prepared joints (taken from Brewis et al. [111])	27
Figure 2-21: Double lap shear joint, modelled with tiebreak contact (taken from Xiao X. et al.[120])	28
Figure 2-22: Validation tests for SAMP-1 material model under various loading conditions: Tensile (TL), tensile with unloading (TR), compression (BL), three-point bending (BR) (taken from Kolling et al [124])	30
Figure 2-23: Validation shear test simulated with SAMP-1 material model (taken from Kolling et al [124])	30
Figure 2-24: Fracture mechanics modes of crack propagation (taken from Roylance [115])	31
Figure 2-25: Distinction of the two different zones in the crack (taken from Christensen [118])	32
Figure 2-26: Numerical simulation of a lap shear joint with cohesive elements (taken from Da Silva et al. [113])	32
Figure 2-27: Schematics of the parameters used in cohesive zone calculations (taken from Yang and Thouless [126])	33
Figure 2-28: Cohesive element mixed-mode traction-separation law (taken from LS-DYNA Keyword User's Manual Volume II: Material Models [127]).....	33
Figure 3-1: Schematic of lap shear loading. Lap shear specimen as prepared, unloaded [L]. Lap shear specimen demonstrating bending deformation in the vicinity of the adhesive joint [R].	34
Figure 3-2: Single lap shear (ASTM D1002) [128] [L]. Double lap shear (ASTM D3528) [129] [R]	34
Figure 3-3: ASTM D1002 test specimen profile [128]	35
Figure 3-4: ASTM D3165 test specimen profile [53]	35
Figure 3-5: ASTM D5656 test specimen profile [61]	35
Figure 3-6: Idealized lap shear joint deformations, with rigid adherends (image taken from Da Silva et al. [57])	36
Figure 3-7: Distribution of adhesive shear stress in a single lap joint (adapted from Da Silva et al. [57])	37
Figure 3-8: Effect of length of bond overlap length onto bond strength (Left: taken from Da Silva et al.[58], Right: taken from Kafkalidis and Thouless [59])	37
Figure 3-9: Thick adherend lap shear tests from [44].	38
Figure 3-10: Dimensions of lap shear specimens (not to scale) (Side view [T]; top view [B]).....	38
Figure 3-11: Construction of lap shear samples (Exploded [T], assembled [B]).....	39
Figure 3-12: Assembled samples between the glass panels.....	40

Figure 3-13: Lap shear sample located in the test jaws	41
Figure 3-14: Result of preliminary lap shear test, DP460NS, aluminum 6061-T6, Alodine (failure shear strength [L], fracture surface [R])	42
Figure 3-15: Result of preliminary lap shear test, DP460NS, aluminum 6061-T6, gritblasting (failure shear strength [L], fracture surface[R]).....	42
Figure 3-16: Result of preliminary lap shear test, DP460NS, aluminum 6061-T6, anodization (failure shear strength [L], fracture surface [R]).....	42
Figure 3-17: Result of preliminary lap shear test, DP460NS, aluminum 6061-T6, Alodine HC (failure shear strength [L], fracture surface [R]).....	43
Figure 3-18: Result of preliminary lap shear test, DP460NS, aluminum 6061-T6, contamination (failure shear strength [L], fracture surface [R]).....	43
Figure 3-19: Figure of lap shear sample versus compliance bar (lap shear sample [T], compliance bar sample [B]).....	45
Figure 3-20: Tracked points in the compliance tester bar	46
Figure 3-21: Displacement of actuator and sample.....	46
Figure 3-22: Examples of force versus actuator displacement data charts	47
Figure 3-23: Plot of lap shear test results.....	48
Figure 3-24: Summary of lap shear results (Adhesive: DP460NS, Adherends: Aluminum, Day 0)	49
Figure 3-25: Summary of lap shear results (Adhesive: DP460NS, Adherends: Magnesium, Day 0)	49
Figure 3-26: Summary of lap shear results (Adhesive: SA9850, Adherends: Aluminum, Day 0)	50
Figure 3-27: Summary of lap shear results (Adhesive: SA9850, Adherends: Magnesium, Day 0)	50
Figure 3-28: Comparison of results between different Alodine treatment batches. Adherend material used was aluminum 6061-T6, bonded with DP460NS	51
Figure 3-29: Open sandwich samples. (Contaminated aluminum [TL], gritblasted aluminum [TR], gritblasted magnesium [BR], contaminated magnesium [BL])	52
Figure 3-30: Open sandwich sample. DP460NS, Magnesium AZ31b, Gritblasting. (Before exposure [T], after exposure of 24 hours [B])	55
Figure 3-31: Open sandwich sample. SA9850, Aluminum 6061-T6, Contamination. (Before exposure [T], after exposure of 330 hours [B])	55
Figure 3-32: Aluminum 6061-T6 exposure test results. Statistically significant reduction of joint strength marked with an asterisk.	56
Figure 3-33: Magnesium AZ31b exposure test results. Statistically significant reduction of joint strength marked with an asterisk.	57
Figure 3-34: Lap shear mesh density (full view [L], zoomed in on the overlap joint [R]).....	58

Figure 3-35: Mechanical properties of aluminum 6061-T6 adherends as imported into numerical simulation.....	59
Figure 3-36 – DP460NS cohesive traction-separation properties.....	59
Figure 3-37 – SA9850 cohesive traction-separation properties.....	60
Figure 3-38: Stress distribution across the adhesive joint. Simulation depicted is DP460NS.....	61
Figure 3-39: Shear stress distribution across the length of adhesive joint at various times.....	62
Figure 3-40: Shear stress distribution across the length of the adhesive joint, at outer edge of joint, in comparison with analytical results. Crosshead displacement is 0.09mm.	62
Figure 3-41: Regions of strain along a single lap shear adhesive joint (taken from Da Silva et al. [58]) ..	63
Figure 3-42: Test progression, experiment [T] versus simulation [B]. Simulation depicted is DP460NS with aluminum 6061-T6 adherends.	63
Figure 3-43: Force versus crosshead displacement, simulation versus experimental results (DP460NS [T], SA9850 [B]).....	64
Figure 3-44: Results of SA9850 lap shear test numerical simulation with varying values of $G_{II}C$	65
Figure 3-45: Variation of mode II energy release rate obtained by napkin ring tests with ductile adhesive (adapted from Chai [146])	66
Figure 3-46: Variation of mode II energy release rate obtained by ENF tests (adapted from Da Silva et al. [149])	66
Figure 4-1: Short beam shear tests (3-point bending [T], 4-point bending [B]) (adapted from Abali et al. [151])	68
Figure 4-2: Single edge notched beam (schematics [L], actual [R]) (taken from Yang et al. [155]).....	69
Figure 4-3: Dimensions of the collar substrate	70
Figure 4-4: Dimensions of the pin substrate	70
Figure 4-5: Pin and collar sample specimen (before cleaning [L], after machining with lathe [R])	71
Figure 4-6: Pin and collar test rig [L], Schematic [R].....	72
Figure 4-7: Actuator voltage reading during idle period of one second	73
Figure 4-8: LVDT voltage reading during idle period of one second.....	74
Figure 4-9: Clip-on gauge voltage reading during idle period of one second.....	74
Figure 4-10: Comparison of results between <i>Tracker</i> and <i>VIC-2D</i>	75
Figure 4-11: Sample of analyzed video image.....	76
Figure 4-12: Position of tracked idle point in x and y coordinates	76
Figure 4-13: Comparison between original data and curve fit.....	78
Figure 4-14: Plastic responses of DP460NS at 0.1/s (Original [T], Discretized [B])	79

Figure 4-15: Shear stress – shear strain result of DP460NS with shear modulus line overlaid (adapted from Tomblin et al.[160])	80
Figure 4-16: Sectioned sample (Schematic [T], Tested sample [B])	81
Figure 4-17: Figures of a failed specimen (pin [L], collar [R])	83
Figure 4-18: Shear rate dependency of DP460NS and SA9850 as obtained from pin and collar tests. Data acquired from thick adherend lap shear tests shown for comparison as dashed lines (green: DP460NS, purple: SA9850).....	83
Figure 4-19: Average curves of DP460NS at various shear rates.....	85
Figure 4-20: Average curves of SA9850 at various shear rates.....	85
Figure 4-21: Variation of shear moduli at various nominal shear rates (DP460NS [L], SA9850 [R]).....	86
Figure 4-22: Plot of force versus crosshead displacement for the sectioned sample	87
Figure 4-23: Section sample analysis window position.....	88
Figure 4-24: Sectioned sample analysis tracked points positions.....	88
Figure 4-25: Tracked displacements of collar [L] and pin [R] points at various progressions.....	88
Figure 4-26: Predicted axial deformations of pin and collar adherends in y-direction during loading of 2711N.....	89
Figure 4-27: Plot of force and tracked adherend displacements against time.....	90
Figure 4-28: axisymmetric geometry elements (full [L]; five different densities, zoomed in view [R])....	93
Figure 4-29: SAMP-1 input curves information (Tension [T], Shear [B])	95
Figure 4-30: Shear stress on the top adhesive element across the bond at different mesh densities (Elapsed time to normal termination [T], shear stress at top adhesive bond element versus mesh element size [B] 96	96
Figure 4-31: Adhesive bond shear strain prior to failure	97
Figure 4-32: Shear stress versus shear strain FEA results at different nominal shear rates.....	97
Figure 4-33: Shear stress versus collar displacement of pin and collar numerical simulation	98
Figure 4-34: Stress distribution along the length of the adhesive joint at various collar displacement values	99
Figure 4-35: Stress distribution along the length of the adhesive joint, according to analytical method developed by Martinez et al.[64]	99
Figure 13-1: Yield surface utilized when only tension curves are defined (taken from LS-DYNA manual [127])	159
Figure 14-2: Yield surface with two curves defined (taken from LS-DYNA manual [127]).....	159
Figure 14-3: Yield surface with three curves defined (taken from LS-DYNA manual [127]).....	160

LIST OF EQUATIONS

Equation 2.1: Surface roughness.....	23
Equation 3.1: Shear strength of a single lap shear joint.....	36
Equation 3.2: Compliance Correction Factor	47
Equation 3.3: Confidence interval limits equation.....	48
Equation 4.1: General form of Ramberg-Osgood equation	78
Equation 4.2: Shear equivalent form of Ramberg-Osgood equation	78
Equation 4.3: Shear modulus equation	80
Equation 4.4: Distribution of shear stress across the length of a pin and collar joint, as developed by Martinez et al.[64].....	91
Equation 4.5: Von Mises yield criterion equation	98
Equation 4.6: Von Mises yield criterion equation, simplified for pure shear condition	98
Equation 14.1: Yield stress interpolations	160

CHAPTER 1

INTRODUCTION

1.1. RESEARCH MOTIVATION

The ever increasing demand for improved fuel efficiency has been a dominant driving force for innovation in the transportation industry [1]. In 1975, the U.S government enacted legislation due to rising concerns regarding dependence on foreign oil [2], in the form of Corporate Average Fuel Economy (CAFE) standards. The standard states that manufacturers of automobiles in the U.S need to achieve certain average fuel efficiency, and failure to comply could result in a monetary penalty. Since enactment of the CAFE standard, the average fuel efficiency of light-duty vehicles in the United States has increased from 15 miles per gallon (mpg) to 25 mpg within 10 years [3]. The National Highway Traffic Safety Administration (NHSTA) estimated that the CAFE standards for passenger cars could continue to increase, with the most conservative estimate (2% annual increase) predicting CAFE standard of 46 mpg for passenger cars by 2025 [4].

Designing a lighter vehicle chassis is one of approach to increasing vehicle fuel efficiency (Figure 1-1) [5]. Other methods include disciplined driving style, optimized vehicle shape (e.g. to reduce drag), and drivetrain optimization. Lightweighting is an effective approach since it allows for the downsizing of other parts of the vehicle such as the engine and suspension system, leading to further reductions in total vehicle weight [6]. With this ripple effect, it is estimated that a decrease of 10% in total vehicle weight will improve vehicle fuel efficiency by 7% [1]. This approach has stimulated research into using advanced materials to form the vehicle body and structure; such as aluminum, magnesium, and polymers [6].

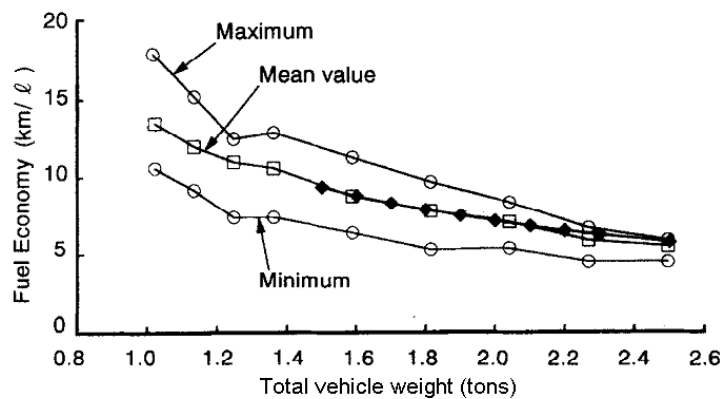


Figure 1-1: Relation between vehicle weight and fuel economy, data compiled from EPA certified vehicles in 1977. (adapted from Yamane K. and Furuhashi S. [5])

Aluminum is roughly one-third as dense as steel and is relatively easy to form. Usage of aluminum in automotive applications has grown significantly during the last decade, particularly in various power train parts, engine blocks, and transmission parts [7, 8]. By heavily incorporating aluminum in the body construction of the F150 pickup truck, Ford was able to significantly decrease the curb weight of the 2015 model (Table 1-1).

Type	Base curb weight		Weight reduction
	2014 model	2015 model	
Regular cab, 4 x 2	4685 lbs	4050 lbs	13.6%
Regular cab, 4 x 4	4925 lbs	4309 lbs	12.5%
Super cab, 4 x 2	5043 lbs	4371 lbs	13.3%
Super cab, 4 x 4	5333 lbs	4587 lbs	14.0%

Table 1-1: Base curb weight of Ford F150 pickup truck, model year 2014 and 2015, 3.7L V6 engine. Sources: Ford F-150 Specifications [9, 10]

Magnesium alloys demonstrate a good strength to weight ratio [11] and very low density ($\rho_{Mg} = 1.7 \text{ g/cm}^3$ [12]), making these alloys attractive for lightweighting applications. One of the earliest uses of magnesium on vehicles dates back to 1936, when Volkswagen used approximately 20kg of magnesium castings for the transmission housing and engine block in the Beetle [13]. While aluminum is widely used in vehicle design, magnesium use is still quite limited [14]. Issues impeding widespread magnesium use include high manufacturing cost, a limited supply base, and inferior mechanical properties compared to other lightweight materials; such as low fatigue and creep resistance [15]. Yet during the last two decades, magnesium has received widespread attention due to the large potential for weight savings leading to improved fuel economy.

In terms of lightweighting, strategic placement of application-specific materials to reduce vehicle weight (Figure 1-2) has been proposed. However, conventional joining methods such as welding and mechanical fasteners are often unsuitable for use with dissimilar materials. Novel joining methods have been identified to address this challenge, such as friction stir welding [16] and structural adhesives.

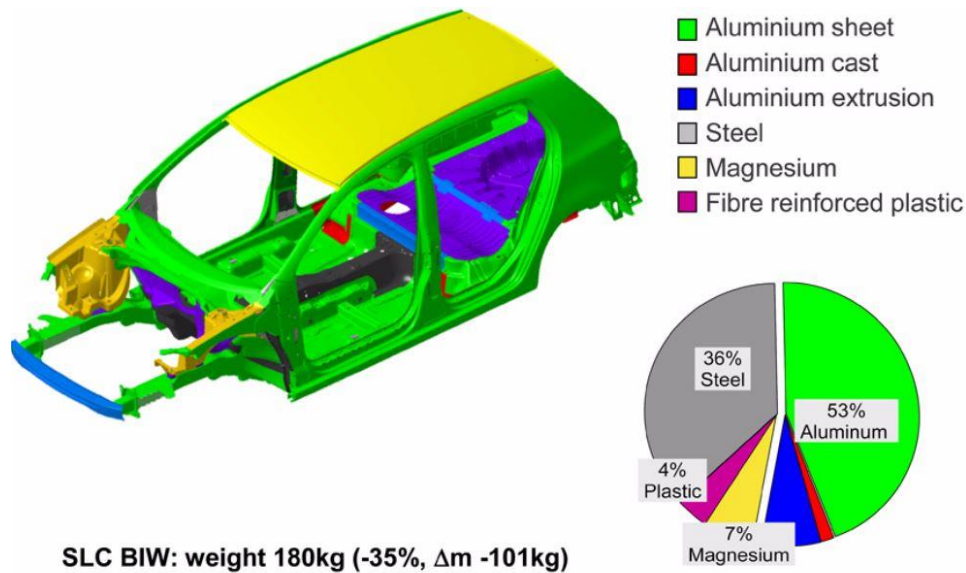


Figure 1-2: Super Light Car Body in White (taken from Goede M. [17])

High-strength synthetic adhesives were first commercially available in the 1940s, which led to the use of adhesives for joining metals [18]. Proper application of adhesives requires pretreatment of bonding surfaces, curing procedure, and a specific joint design [19]. Attractive surface finish that is demanded in the automotive industry is in contrast with rougher surfaces which are more advantageous for adhesive bonding [18, 20, 21]. These issues have impeded widespread adoption in large scale production, where consistency and cost effectiveness are of foremost importance.

The advantages of using adhesives include increased joint stiffness, sealed joints and the ability to join dissimilar materials [22]. Dissimilar materials can produce galvanic corrosion upon contact (e.g. steel and aluminum), a problem which can be addressed by an adhesive bond which electrically isolates the materials [23]. Traditional joining methods such as spot welding and mechanical fasteners can only operate on materials above certain minimum thickness values, to prevent damage (e.g tearing, bending, burning) in the material during joining. Adhesives are advantageous as they can be applied to materials of any thickness, with minimal modification to the adherends. Mechanical fastening commonly introduces a hole into the material joined, which results in stress concentrations. Spot welding does not join aluminum effectively due to the high electrical resistance on the surface owing to an oxide layer [24], and is incapable of joining non-metal matrix composites (e.g ceramics, plastics). Although spot welding works well on steels; it will damage coatings on the steel surface. Surface preparation is an essential element of a robust and consistent adhesive joint and requires investigation for different materials. An example of a vehicle structure assembled out of a combination of steel and aluminum is the Audi A7 [25]. This vehicle

incorporates various joining methods including a combination of punch riveting, clinching, self-tapping screws, and adhesive bonding. As an example, the front end strut mount for the Audi A7 is joined to the side members by combining adhesives with a punch rivet (Figure 1-3).

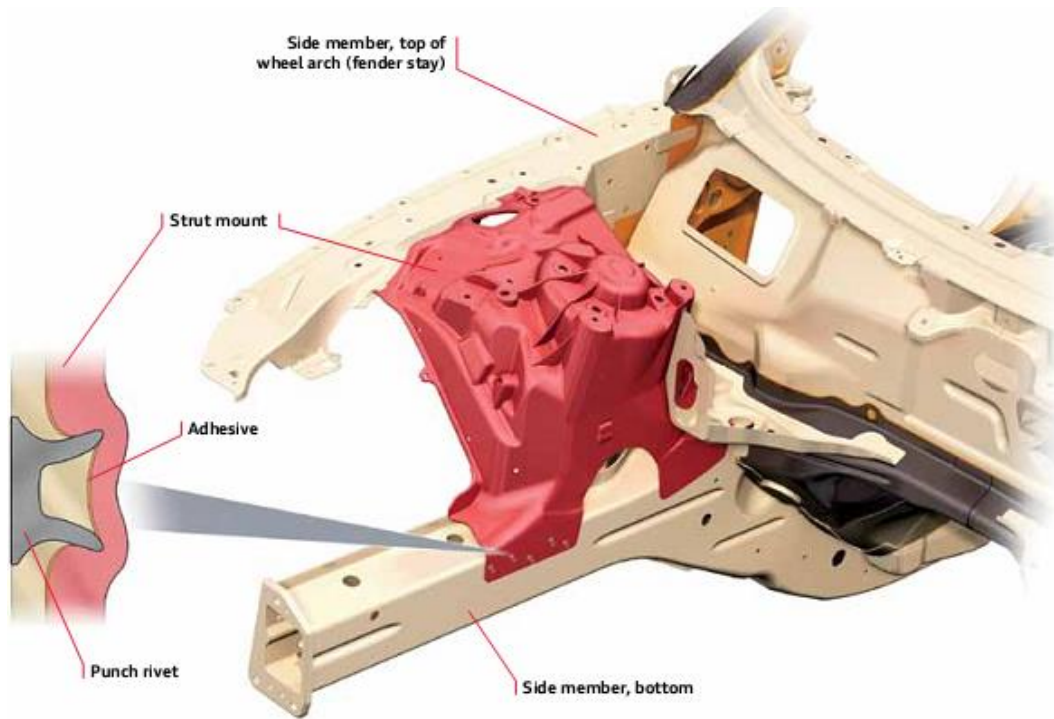


Figure 1-3: Front end structure of 2012 Audi A7 (taken from Audi Collision Frame Technology Guide [25])

Modern vehicles are expected to provide protection for occupants in the event of crash [26]. Specifically, full vehicles must meet compliance standards in various impact crash tests scenarios [27] to be sold to consumers. Prototyping a vehicle is costly and time-consuming, making it an inefficient method to observe the effects of design changes or to ensure a new vehicle design meets the compliance standards. A well-developed computer model is invaluable in this effort, as it can be used to evaluate design modifications prior to manufacturing prototypes. However, a computer model is only reliable if it can replicate the physical responses of the materials and structures of the vehicle. To develop a functional model of an adhesively-bonded vehicle, a detailed study into the response of adhesive bonds under crash loading conditions is essential.

The mechanical response of structural adhesives is complex, demonstrating a dependence on deformation rate, with different properties in tension and compression leading to an asymmetric yield surface [20]. This entails extensive material characterization efforts subjected to high strain rates under various loading conditions.

The aim of this research is to evaluate the performance of different adhesive-adherend combinations, the effect of time delay between surface preparation and assembly on the performance of the bond, and the measurement of material properties under shear mode of loading for use in numerical models of adhesive joints. These studies will ultimately aid the adoption of adhesive technology into the automotive industry.

1.2. THESIS OUTLINE

The second chapter of this thesis provides background information related to the present study including general information on adhesives, lightweighting materials, adhesive testing methods, finite element modeling of adhesives, and various surface preparation methods.

The research into the performance of surface preparation methods is discussed in chapter three, evaluated using lap shear tests. This data allowed for the determination of the best performing surface treatment, material and adhesive combinations. The investigation into effect of environmental exposure in an adhesive joint is also discussed.

Chapter four discusses shear testing using pin and collar test samples. This study was undertaken to characterize adhesive bonds in shear loading under various deformation rates, from quasi-static to high deformation rates. Numerical simulations were undertaken to analyze the stress distribution inside the adhesive bond.

The fifth and final chapter contains a summary of the research and conclusions drawn from the findings. Recommendations for future research are also offered.

CHAPTER 2 BACKGROUND

2.1. JOINING METHODS

A joining method is defined as “the process of bringing two or more surfaces into intimate contact in order to establish continuity of a field across the resulting interface” [28], typically done to form a more functional structure. Common joining methods include welding, adhesive bonding, mechanical fastening (Figure 2-1), and riveting.

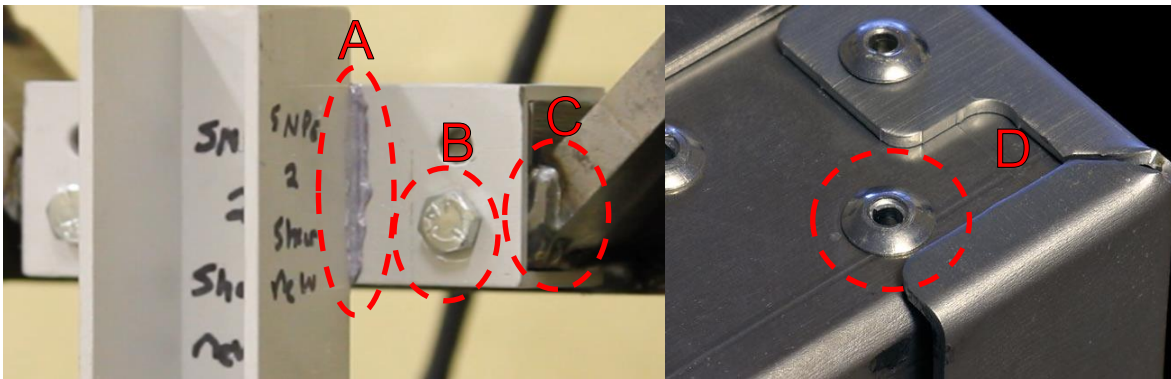


Figure 2-1: Examples of joining methods: adhesive bonding (A), mechanical fastener (B), welding (C), rivet (D)

Traditional mechanical fastening frequently requires the fastener to pierce through the substrate to execute an assembly, usually in the shape of a round hole. The resulting stress concentration reduces the strength of the adherend as well as the mechanical joint; while also amplifying the potential for fatigue failure [29]. The geometry of the substrate itself has to be designed to accommodate the tools required to complete a mechanical fastening assembly and the strength of the fastener must be sufficient to ensure joint integrity. Vibrations, such as those experienced during vehicle motion, can be transmitted through mechanically fastened joints, which can loosen thread-locked assemblies [30]. However, mechanical fasteners make it possible for joints to be assembled and disassembled easily, something that cannot be done with most other joining methods.

Welding is a joining method available only for metals and certain plastics. It introduces highly localized heat to raise the temperature of the materials being joined above their melting points. With the addition of a filler material, the substrates then coalesce when they return to their solid forms [28].

Traditional welding techniques cannot join dissimilar materials, and are incapable of joining certain alloys such as sulfurized, phosphatized and leaded steels [31]. However, new developments in welding

techniques (e.g. electron beam welding [32], friction stir welding [16, 33]) have allowed the welding of dissimilar materials. The introduction of heat often distorts the material on cooling, especially during a manual welding procedure where the process is prolonged. This effect is exaggerated on thin materials commonly used in automotive structures.

Automotive structures are also subject to stringent recyclability standards. Targets set by End of Life Vehicles Directive (2000/53/EC) of the European Union stated that all vehicles must be 95% recyclable by January 2015 [34]. Common methods to address recyclability issues of bonded structures are to mechanically destroy the adhesive joint by thermal degradation or cutting of the adhesive [35-37] before sending the remaining structures through regular recycling procedure. However, recent developments [38, 39] have successfully introduced the possibility of imbedding thermally expandable particles in the adhesive layer to enable debonding of the joint on command.

Adhesive joint strength is highly dependent on the nature of the adherend surfaces. An adherend with improper surface preparation can lead to joint strengths that are much lower than the expected strength from the mechanical properties of the bulk adhesive. Chemical reactions occur in epoxy based adhesives, giving raise to environmental concerns and potentially hazardous work environment. Adhesive joints are inherently weak in mode I of loading [19] and as such, require some consideration when it comes to joint design. Imperfect application of adhesives leading to incomplete surface to adhesive contact or the presence of voids is difficult to detect. Several investigations have been carried out to inspect bond quality via non-destructive methods to good success, such as thermal inspection, infrared photographs and vibrational analysis [40, 41].

Adhesive bonding requires no modification to the structure of the adherend, although some adhesives might require special surface preparations. Adhesives are able to join dissimilar materials, and conveniently act as a barrier between materials that are problematic when in contact, such as dissimilar materials like steel and aluminum which may form a galvanic couple [23]. Adhesives also require no minimum material thickness to function. While some adhesives require heat for curing, the temperatures involved are commonly lower than those associated with a phase change in metals [42, 43].

2.2. ADHESIVES

Traditional adhesives were made from organic ingredients, such as animal protein extracted from bones and tissues, or starch and natural polymers extracted from plants. In contrast, modern structural adhesives are known as toughened structural epoxies. This term is used to describe bonds that are formed by complex chemical reactions and are strong enough for use in engineering applications. Epoxies are

attractive for engineering applications because they can bond a variety of substrates and exhibit a relatively high strength [44].

Epoxy properties can be easily modified to suit the requirements by the addition of flexibilizers, diluents, and reinforcements [44]. One of the most successful methods of increasing the toughness of epoxies is through the introduction of rubber particles to the uncured resin. Rubber toughened epoxies are increasingly used as the basis for structural adhesive compositions [45, 46].

In this study, two commercially available toughened structural epoxies were used, DP460NS and SA9850 [47, 48] (manufactured by 3M Corporation, Minnesota). The technical data sheets for these adhesives can be found in Appendix A: Technical Data Sheets.

DP460NS is a 2-part epoxy comprising resin and hardener. When these two components are mixed, the epoxy undergoes an exothermic reaction and hardens to form a joint. SA9850 is a 1-part epoxy, which relies on high temperature to accelerate the curing process.

The measured mechanical properties of the adhesives are summarized in Table 2-1 .

	DP460NS	SA9850
Elastic modulus (MPa)	2,180	1,055
Yield stress (MPa)	35.63	26.50
Fracture stress (MPa)	36.92	21.25
Fracture strain	0.104	0.086
Poisson's ratio	0.41	0.41
Density (kg/m ³)	1,200	1,250

Table 2-1: Mechanical properties of two structural adhesives (DP460NS, SA9850) tests conducted at quasi-static strain rate of 1.2×10^{-3} (mm/mm) (adapted from Trimiño and Cronin [49])

The results tabulated were acquired from tensile stress done on bulk adhesive samples on quasi-static conditions at the University of Waterloo [49]. Other tests were also done to obtain better characterization of the material, such as uniaxial tension at different strain rates (Figure 2-2), and lap shear tests using thick steel adherends (Figure 2-3) [50].

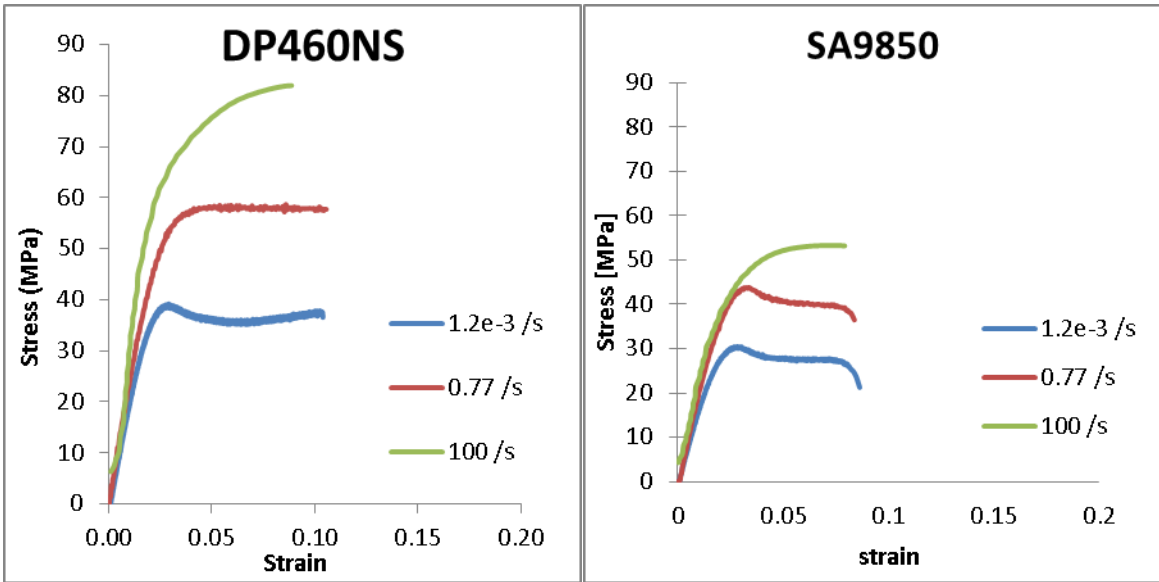


Figure 2-2: uniaxial tension results at various strain rates (DP460NS [L], SA9850 [R])

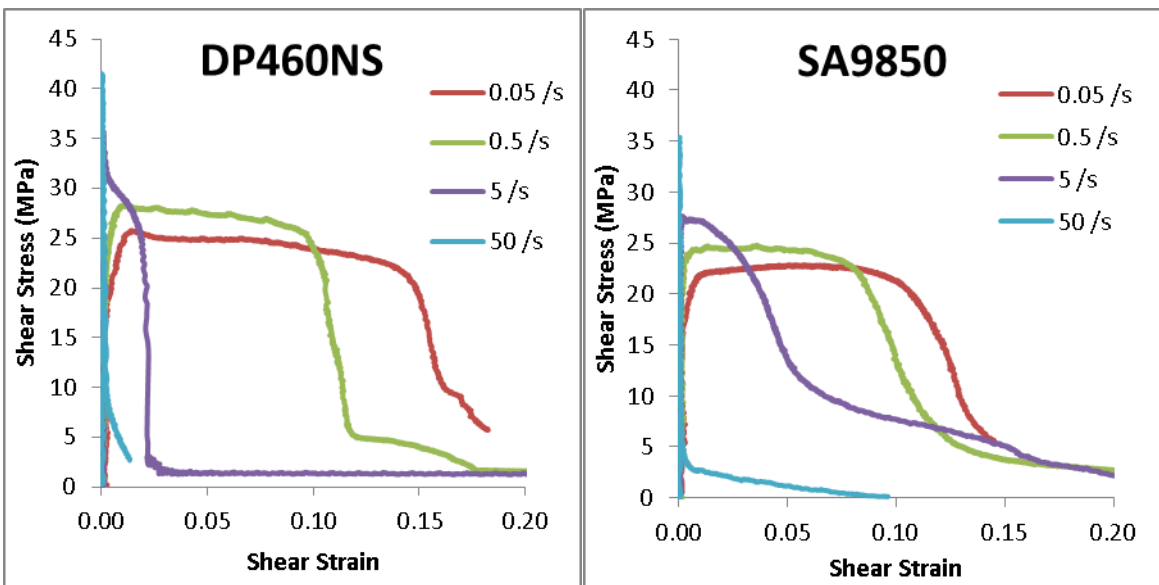


Figure 2-3: Thick adherend lap shear results at various deformation rates (DP460NS [L], SA9850 [R])

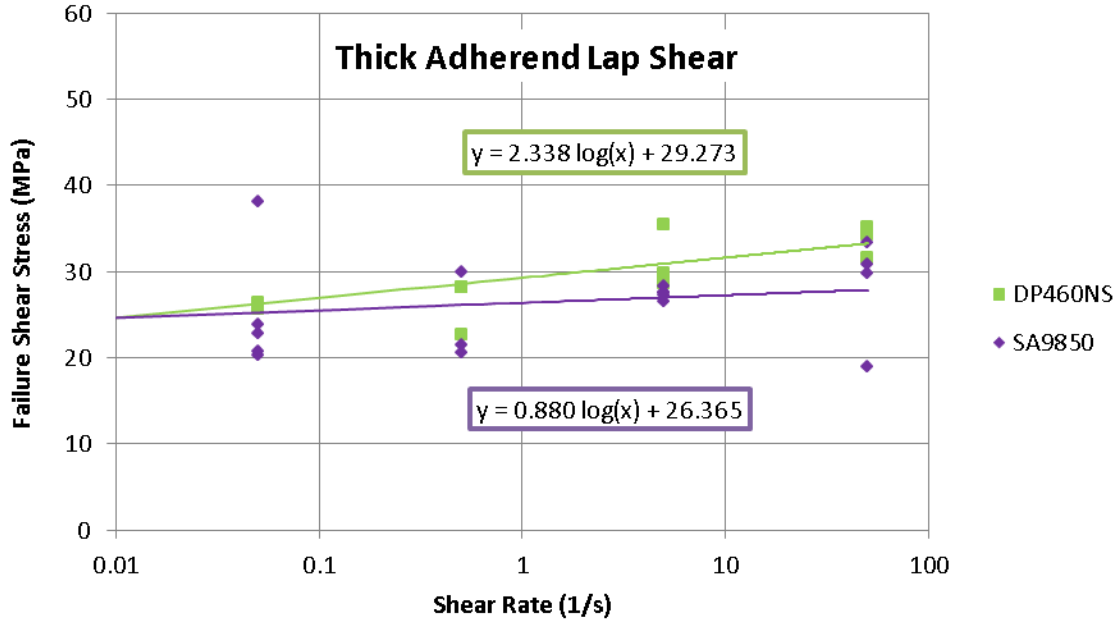


Figure 2-4: Shear stress vs shear rate of DP460NS and SA9850, data acquired from thick adherend lap shear tests

2.3. ADHESIVE TESTING

Adhesive testing can be divided into two main categories: tests on neat resin or bulk specimens, and tests on an adhesive joint (i.e. *in situ*). Tests conducted on actual joints depend on multiple factors including joint geometry, mode of loading, and adherend preparation method. Testing bulk material eliminates many of these extra parameters and produces less variability in the test data, thus providing a good baseline to compare adhesive strength.

2.3.1. ADHESIVE JOINT TESTING

Different modes of loading can be experienced by adhesive joints, depending on the joint geometry and the direction of structure loading. They are often classified as tension, shear, compression, cleavage, and peel (Figure 2-5). Ideally, with sufficient knowledge of these four characteristics, predictions can be made regarding the response of the adhesive under mixed load types.

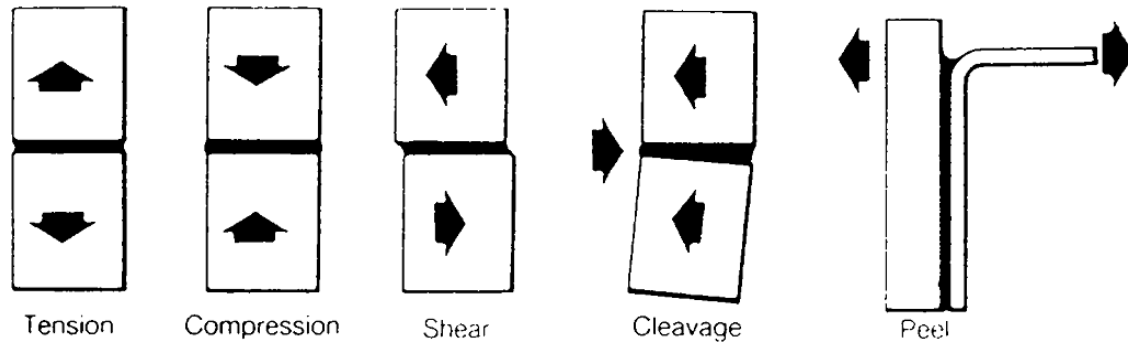


Figure 2-5: Adhesive joint modes of loading (adapted from Adderley C.S.[51])

Unlike most metals, adhesives failure may occur by different mechanisms under different modes of loading. In metals, yielding and plastic deformation may be described by various yield criteria, such as Von Mises or Tresca. This is not the case for adhesives due to material anisotropy. Gali, Dolev and Ishai [52] conducted a series of tests for different loading directions using bulk material and different joint configurations, and confirmed that adhesives do not follow traditional yield criteria.

As noted previously, the mechanisms of deformation and damage accumulation in adhesives depend on the mode of loading. Under tensile stress, voids are generated in the material (Figure 2-6 identifies these voids as ‘particle’). This phenomenon is more commonly called ‘crazing’ and is visibly apparent with discoloration known as stress whitening during a bulk tensile test [53]. The voids or crazes generated in the material provide increased ductility (e.g. a toughened epoxy) until they reach a critical size leading to failure of the material or joint.

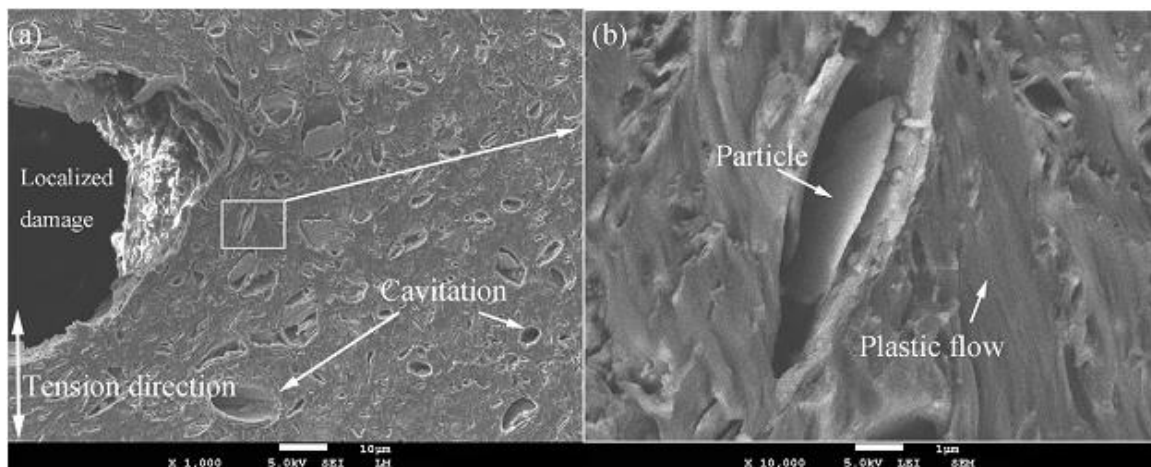


Figure 2-6: SEM observation of adhesive layer under pure tension load. Crazes are identified as ‘particle’; ‘cavitation’ refers to bare spots formed during heat curing process (taken from Hao C. [53])

Under pure shear stress, adhesives deform by a mechanism known as shear banding. This occurs as the molecular chains in the epoxy matrix form micro cracks which undergo significant reorientation towards the direction of the shear [53]. The shear bands postpone the initiation of localized damage, and result in large plastic shear strain before failure (Figure 2-7).

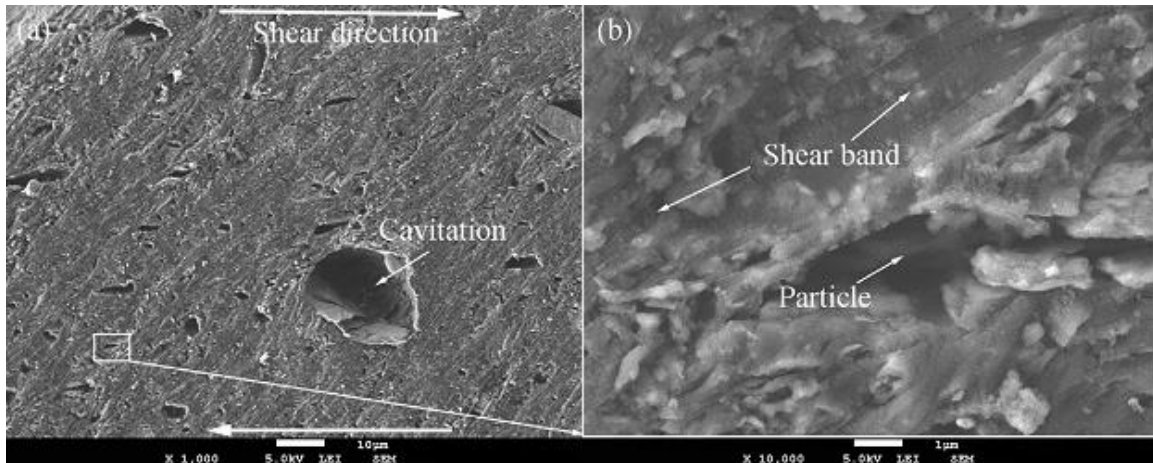


Figure 2-7: SEM observation of adhesive layer under pure shear load. Crazes are identified as ‘particle’; ‘cavitation’ refers to bare spots formed during heat curing process (taken from Hao C.[53])

Adhesive joint failure is typically characterized by one of three modes:

1. Cohesive failure (Figure 2-8 left), or failure of the adhesive itself. This is the most preferable mode of failure for an adhesive joint since it is the where the strength of the adhesive is highest.
2. Interfacial failure (Figure 2-8 middle), or failure at the interface between the adhesive and the adherend, typically resulting from inadequate surface preparation. This type of failure can occur when the peel is the dominant mode of loading and is the least preferable mode of failure, as the full strength of the adhesive is not realized.
3. Structural failure (Figure 2-8 right), or failure of the adherend, occurs when the bond strength exceed the adherend strength.



Figure 2-8: Joint failure types (cohesive [L], interfacial [M], structural [R])

Experiments by multiple researchers [54-56] have shown that, in a lap shear joint configuration, thinner bond lines produce stronger bonds compared to thicker ones. However, Arenas et al. [55] also concluded that thin bond lines increased variability in the data significantly (Figure 2-9 right). A possible explanation for this was offered by Adams and Peppiatt [57] who stated that thicker adhesive bonds are more susceptible to voids and imperfections that might form during curing process; while the excessively thin ones are more susceptible to bare spots due to imperfections during application. Davies et al. [58] studied the effects of bondline thickness using physico-chemical analyses, nano-indentation and mechanical testing. Their research challenged the notions about the presence of defects in relation to bondline thickness, and put more emphasis on the changes of stress state during loading instead.

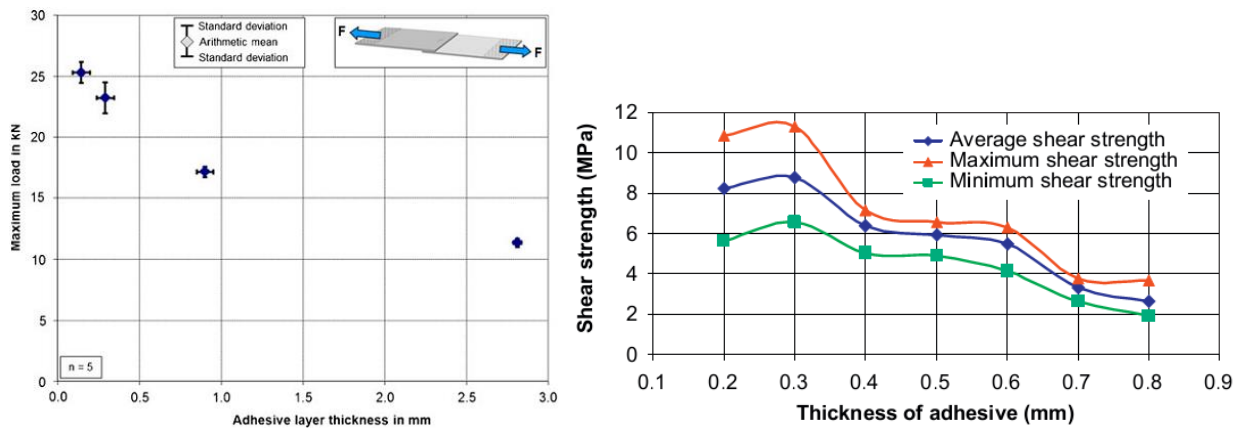


Figure 2-9: Relationship between lap shear strength with bond thickness of an epoxy adhesive (Left: taken from Teutenberg and Hahn [56], Right: taken from Arenas et al. [55])

The single lap shear test (ASTM D3165 [59]) (Figure 2-10) is one of the most widely used tests and is considered the baseline test type for specifying an adhesive strength. It is a simple test to perform, with respect to construction of samples and loading to failure. Volkersen [60], Goland and Reissner [61], and Hart-Smith [62] have been the key researchers on the early study of the lap shear joint. Their work focused on predicting the joint strength of a lap shear joint using simple linear elastic analysis. More solutions have been developed since then [63, 64], with an increasing degree of complexity involving plasticity of the adhesive layer and adherends.

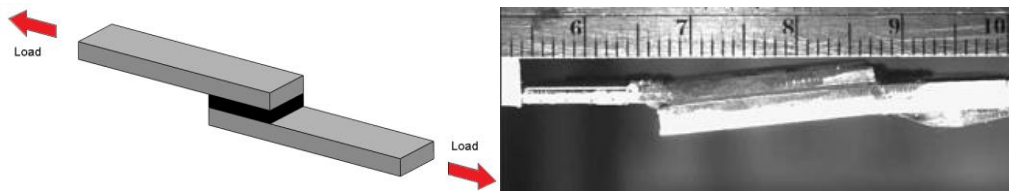


Figure 2-10: Lap shear test [L], rotated lap shear joint during loading [R] (taken from Kafkalidis and Thouless [65])

One challenge with single lap shear tests is the large amount of joint rotation and resulting mixed-mode loading occurring at the joint (Figure 2-10 Right). To address this, some authors [66] have used thicker adherends to minimize joint rotation (ASTM D5656 [67]). Another approach is to use the geometry known as pin and collar testing (ASTM D4562 [68]). A pin and collar sample is created by bonding a hollow circular cylinder (collar) concentric to a solid circular cylinder (pin) resulting in pure shear loading. However, this is not a widely used test due to challenges in sample preparation and displacement measurement. Efforts have been undertaken to analyze this test analytically [69-71] and numerically [72]. Experimental test efforts, such as those conducted by Yokoyama and Shimizu [73], did not address the challenge with displacement measurement and presented nominal displacement values instead. Another benefit of this test is the ability to evaluate mechanical properties at high deformation rates [73].

2.3.2. BULK ADHESIVE TESTING

Bulk adhesive testing is the practice of testing adhesive as a bulk material, as opposed to a joint configuration. This type of test provides insight into the strength of the adhesive material without the complications of adherend effects. The strength values acquired from bulk material tests represent the highest potential strength of the adhesive bond, should it ever be tested in a joint situation.

Dolev and Ishai [74] conducted tests on bulk adhesive specimens under three modes of loading: tension, shear and compression (Figure 2-11). They successfully drew a relationship between the three modes of loading which is distinctly different from traditional yield criteria.

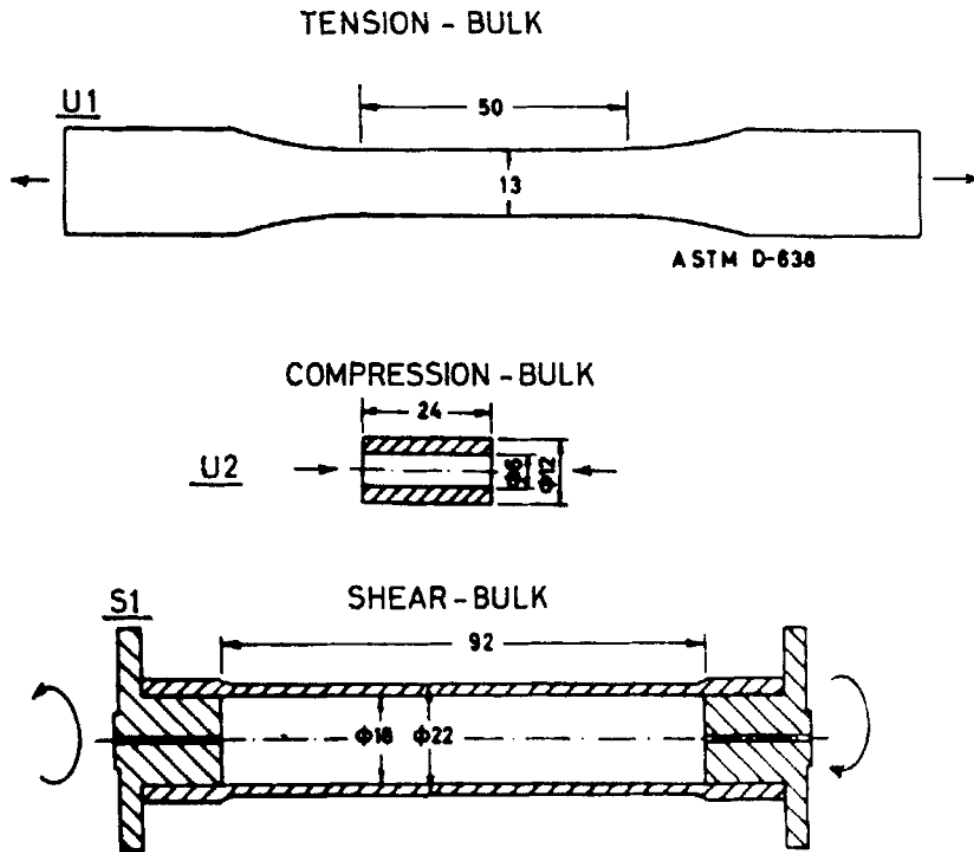


Figure 2-11: Bulk adhesive test geometries (tension [Top], compression [Middle], shear [Bottom]) (adapted from Dolev and Ishai [74])

The geometry shown in Figure 2-11 (Top) is in accordance with ASTM D638 [75]. Trimiño and Cronin [49] characterized the adhesives used in this research using a modified version (Figure 2-12) of the geometry specified in this test standard, due to limitations with the test apparatus. Its accuracy was confirmed to be comparable with the standard size via experimental and numerical methods. The results of this test were shown in Figure 2-2.



Figure 2-12: Bulk tensile sample geometry, micro-sized

2.4. LIGHTWEIGHTING MATERIALS

Modern vehicles are composed of various materials with purposes ranging from structural to cosmetic. Figure 2-13 shows the breakdown of material distribution of an average 3360lb North American 2005 midsize vehicle by weight, where 63.8% of the vehicle comprises steel and cast iron. There is a potential to replace these traditional materials by other materials and achieve the same level or an improved level of crashworthiness while reducing weight.

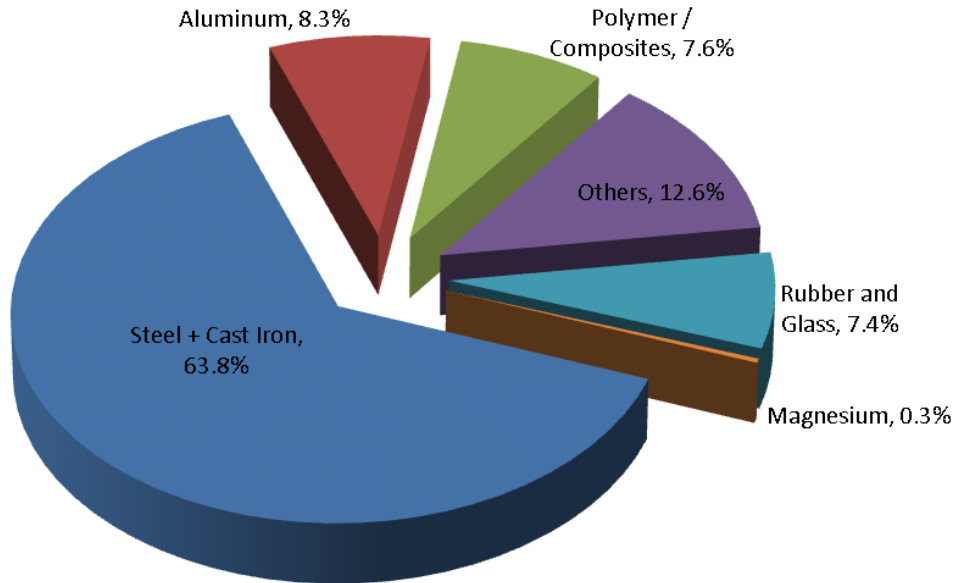


Figure 2-13: material distribution for an average North American 3360lb 2005 vehicle manufactured by U.S. automakers – Daimler, Ford and GM (adapted from Cole, G.S. [76])

Potential weight savings can be obtained in the vehicle structure by using lightweight materials or geometry optimization [77]. A well designed frame must satisfy several criteria, such as low production cost, durability, crash safety, recyclability, reparability, satisfactory NVH levels, strong and stiff where required [6]. Some of these requirements might be more easily met with different materials than others; therefore it is advantageous to compose a multi-material lightweight vehicle, with strategically-located materials.

2.4.1. HIGH STRENGTH STEEL

Steel is the most popular material in production vehicles today (e.g. Figure 2-13) and as such, is subjected to extensive R&D efforts by automakers and the steel industry leading to new alloys of high-strength steels, and many new design, fabrication and assembly techniques [1].

Steel materials are broadly defined as mild steel (strengths up to 270 MPa), high-strength steel (strengths up to 700 MPa, incorporating alloying elements) and advanced or ultra-high strength steels (strengths greater than 700 MPa, incorporating alloying elements and thermal processing) [78].

Totten [79] further defined high-strength steel as an alloy of steel that has:

1. Low amount of carbon (0.03%-0.25%)
2. One or more of the strong carbide-forming microalloying elements (e.g. V, Nb, or Ti)
3. A group of solid solution strengthening elements (e.g. Mn and Si)
4. One or more of the additional microalloying elements (Ca, Zr) and the rare earth elements (particularly Ce and La) for sulfide inclusion shape control and increased toughness

As a result of rapid development in the high strength steels, the industry developed steel alloys that have higher strength compared to conventional HSS, named Advanced High Strength Steels (AHSS). The category of AHSS covers the following generic types: dual phase (DP), transformation induced plasticity (TRIP), complex phase (CP), and martensitic steels (MART) [80]. A depiction of tensile strength and elongation to failure percentage of these alloys are shown in Figure 2-14.

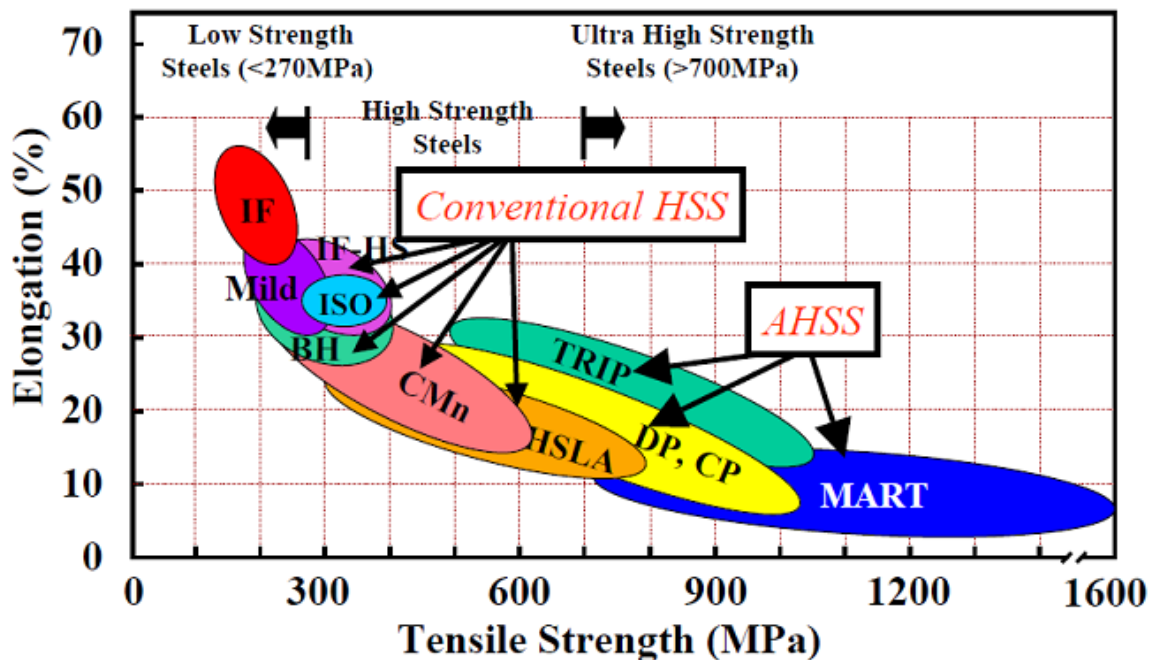


Figure 2-14: Elongation to failure (%) versus ultimate tensile strength *banana curve* of automotive steels (taken from Billur M.S. [78])

Stronger steel with good ductility enables the use of thinner gauge materials, which reduces weight while maintaining the ability to absorb energy and resistance to plastic deformation [81]. The higher strengths

that are exhibited by these alloys are typically accompanied with lower elongation to failure (Figure 2-14). HSS are the most commonly used lightweighting material to replace traditional mild steel [6].

Joining different alloys of steel, while feasible with adhesives, could also be efficiently done with other technologically mature methods such as tailored blanks and specialized welding techniques.

2.4.2. ALUMINUM

Aluminum usage in automotive applications has grown substantially in recent years [7]; the average amount of aluminum used in European passenger cars has doubled between 2004 and 2014 [82].

Development in aerospace industry lends itself to various useful aluminum alloys and production techniques [83], of which the automotive industry can also benefit from. The ease of forming aluminum results in a broad range of opportunities for employing aluminum in automotive parts. There are already several vehicles that employ full aluminum-body components, such as the Acura NSX [84], Audi A8 [85], and the Lincoln Mark VIII [86]. More recently, Ford heavily incorporated aluminum into the chassis of the F-150 line of pickup trucks [9, 10]. Table 2-2 lists some of the applications of aluminum in the automotive industry.

System	Components
Powertrain (castings)	Pistons (100%) Engine blocks (19%), oil pans, engine cover, water pumps Cylinder heads (75%) Intake manifolds (85%) Transmission: cases(100%), valve bodies and channel plates (90%), rear axle and differential housings, driveshafts
Chassis (castings)	Wheels (40%) Brackets Brake: master cylinders Suspension: control arms, supports Steering: airbag supports, steering shafts, knuckles, housings, wheels (Ford, Lincoln, Chrysler Viper) Instrument panels (Corvette) Electric motor, alternator, pump housings
Chassis (wrought)	Wheels Heat shields Bumper reinforcements (Ford Crown Victoria, Porsche 928/968, Saturn)
Body (wrought)	Hoods (9%) Hoods, front fenders and doors (Porsche 928/968) Body structure (Acura NSX and Audi A8)

Air conditioning (wrought)	Condensers, evaporators/compressors (90%) Heater cores, radiators (72%)
----------------------------	--

Table 2-2: Aluminum applications in the automotive industry (1993 North American car percentages in parentheses) (adapted from Cole and Sherman [8])

When aluminum is exposed to the atmosphere, surface oxidation occurs forming a thin layer of aluminum oxide (Al_2O_3 or Alumina). The speed of formation of this layer relative to time follows an inverse logarithmic function where the layer thickness forms very rapidly at first and slows down to zero growth eventually, a condition called the ‘stable layer’ [87]. At standard temperature and pressure, aluminum forms an oxide layer between 20 Å to 100 Å in thickness [88]. This hard and brittle layer acts as a protective barrier between the aluminum and its surroundings. The relative weakness of this layer in comparison to the bare aluminum can result in reduced failure strengths for adhesive bonds. This issue can be addressed through a surface treatment prior to bonding, either by removing the layer or improving its quality.

Aluminum alloy 6000 series aluminum alloys are precipitation hardening alloys and one of the most commonly used structural aluminum alloys, although both 5000 and 7000 series aluminum alloys are also seeing some use in the automotive industry [89]. Table 2-3 list the mechanical properties for some common aluminum alloys, which were used in this study.

	5182	6061-T6
Density (g/cm^3)	2.65	2.70
Yield strength (MPa)	395	276
Ultimate Tensile Strength (MPa)	420	310
Elongation at fracture	4.0%	12%-17%
Elastic modulus (GPa)	69.6	68.9

Table 2-3: Mechanical properties of three aluminum alloys (source: Matweb [90])

2.4.3. MAGNESIUM

Magnesium alloys are desirable for vehicle lightweighting since they have a relatively low density ($1.74 g/cm^3$) and a high specific strength relative to other structural materials [91].

Magnesium production increased during World War I and World War II [92]. Later, one notable large scale use of magnesium was in the 1970s Volkswagen beetle, which used approximately 20kg of magnesium in the Beetle [13]. Interest in magnesium faded when higher structural performance was required; however, a renewed interest in vehicle lightweighting resulting from stricter fuel efficiency targets has now focused attention on vehicle structure application for magnesium [91].

Magnesium also has several challenges in terms of processing and application including high reactivity in the molten state, inferior mechanical properties compared to aluminum and steel, concerns about galvanic corrosion, high cost and low ductility [91]. It is also accepted that common magnesium alloys have poor formability at room temperature, owing to the hexagonal close-packed crystal structure. [93]

As of 2007, there were several automotive manufacturers producing magnesium parts (Table 2-4). On average, there are 10-12 lbs of magnesium used for an average US 3,360lbs vehicle (Daimler Corp., Ford Motor Company, and General Motors) on 2005 [76]. This number is expected to rise to 350lbs by 2020 [76].

Component	Producers and car models
Engine block	BMW: lighter, more powerful and durable six-cylinder inline combustion engine. The world's first engine block made of Noranda's patented alloy AJ62 (Mg-Al-Sr).
Steering wheel frame	Ford(Ford Thunderbird, Cougar, Taurus, Sable), Chrysler(Chrysler Plymouth), Toyota, BMW(MINI), Lexus(Lexus LS430).
Seat frame	GM(Impact),Mercedes-Benz(Mercedes Roadster 300/400/500 SL),Lexus(Lexus LS430)
Instrument panel	GM, Chrysler (jeep), Ford, Audi(A8), Toyota(Toyota Century)
Wheel rims	Toyota(Toyota 2000GT, Toyota Supra), Alfa Romeo(GTV), Porsche AG(911 Serie)
Cylinder head	Dodge(Dodge Raw), Honda Motor(City Turbo), Alfa Romeo(GTV), AutoZAZ-Daewoo (Tavria, Slavuta, Daewoo-Sens), Honda, BMW, Ford, Isuzu, Volvo Motors(LCP), Chrysler
Clutch case	AutoZAZ-Daewoo(Tavria, Slavuta, Daewoo-Sens), Volvo Motors(LCP), Alfa Romeo(GTV)
Transmission case	AutoZAZ-Daewoo(Tavria, Slavuta, Daewoo-Sens), Volvo Motors(LCP), Porsche AG (911 Serie), Volkswagen(Volkswagen Passat), Audi(A4,A6), Mercedes-Benz
Lower crankcase	Chrysler(jeep), Alfa Romeo(GTV), GM(Oldsmobile), McLaren Motors(F1-V12)
Cylinder block	GM(Pontiac Gran AM, Corvette)
Intake manifold	GM (V8 North Star motor), Chrysler
Air intake system	BMW(V8 motor)
Steering link bracing	GM(LH Midsize)
Oil pump body	McLaren Motors(F1-V12)
Camshaft drive chain case	Porsche AG(911 Serie)
Gear controls housing	AutoZAZ-Daewoo(Tavria, Slavuta, Daewoo-Sens)
Brackets for various systems	Chrysler, Volkswagen (Volkswagen Lupo)

Table 2-4: Producers of magnesium alloys and applications on car models (adapted from Kulekci M. [91])

Severe loading conditions, such as a crash or impact, are a great cause of concern for automotive manufacturers. This underlies the importance of material strain rate sensitivity study, as was done by Kurukuri et al [94, 95] with the AZ31b and ZEK100 alloys. Adhesive was used in their experiments to join sheets of magnesium together into a cube for use with the Split Hopkinson Pressure Bar.

Adhesion on bare magnesium alloy is poor because of its high electrochemical activity. An oxide layer forms on the exposed magnesium surface [96], presenting similar adhesion problems encountered with aluminum. Numerous conversion coatings have been developed for magnesium for various purposes, such as better corrosion protection and to improve the adhesion of paint to magnesium [97].

AZ31b is one of the most widely available grades of magnesium alloys (Table 2-5). The material exhibits anisotropy (Figure 2-15). Magnesium alloy ZEK100 is a relatively new alloy designed for increased formability at low temperatures, which is desirable for automotive stamping applications. Its mechanical properties are presented in Table 2-5 and Figure 2-16 (RD: Rolling Direction, TD: Transverse Direction).

	AZ31b	ZEK100
Density (g/cm^3)	1.78	1.78
Coefficient of linear expansion ($\mu\text{m/m}^\circ\text{C}$)	26.8	26.8
Yield strength (MPa)	150 - 180	140 - 220
Ultimate Tensile Strength (MPa)	280	260
Elongation at fracture	13% - 18%	14% - 22%
Elastic modulus (GPa)	45	90

Table 2-5: Mechanical properties of magnesium alloys (adapted from Miles [98], Boba [99])

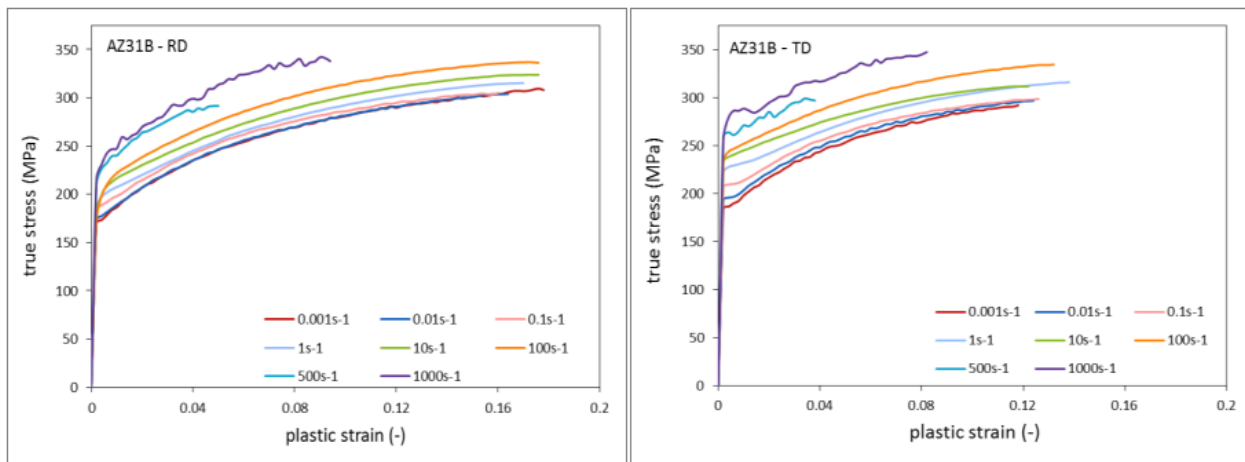


Figure 2-15: True stress versus plastic strain curves of magnesium AZ31b (taken from Boba [99])

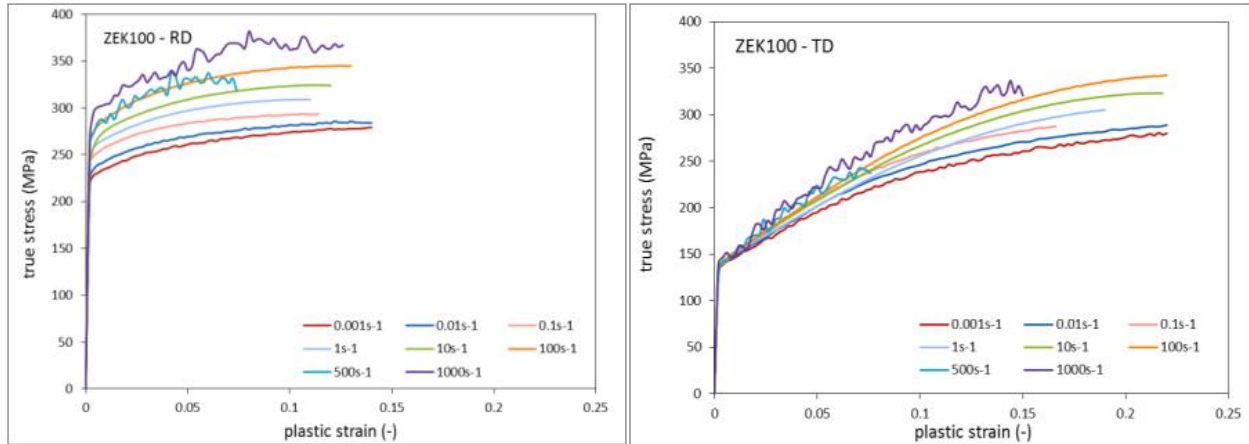


Figure 2-16: True stress versus plastic strain curves of magnesium ZEK100 (taken from Boba [99])

2.5. SURFACE PREPARATION FOR ADHESIVE JOINING

There are numerous reasons for tailoring the surface properties of metals. For automotive applications, these include improved corrosion resistance, improved surface hardness to prevent damage and wear, paint adhesion, and aesthetic/decorative enhancements.

The material surface properties can be altered metallurgically (e.g. via microstructure modification), mechanically, chemically (e.g. to remove layers), or by adding new coating layers to the surface [100]. Many pretreatments have been developed to increase the strength and durability of adhesive bonds to metals, since the adherend surface quality is essential to producing a strong interface with the adhesive [24].

This research selected a few of these pretreatments for further investigation. Background information for these pretreatments is presented in chapters 2.5.1 to 2.5.4.

2.5.1. GRITBLASTING (MECHANICAL PRETREATMENT)

Increasing the effective surface area of the adherend to enhance bonding can be achieved by mechanical roughening methods. One example of such methods is grit blasting, where dry abrasive particles are propelled towards the surface at relatively high speeds. The grit removes loose contaminated layers and chisels away the surface of the material, resulting in non-uniform rough surface with cracks, peaks and valleys (Figure 2-17). The resulting roughness has been theorized to provide more area for the adhesive to adhere and mechanically interlock. More detailed analyses suggest that the roughening process may affect surface energy and wettability [101].

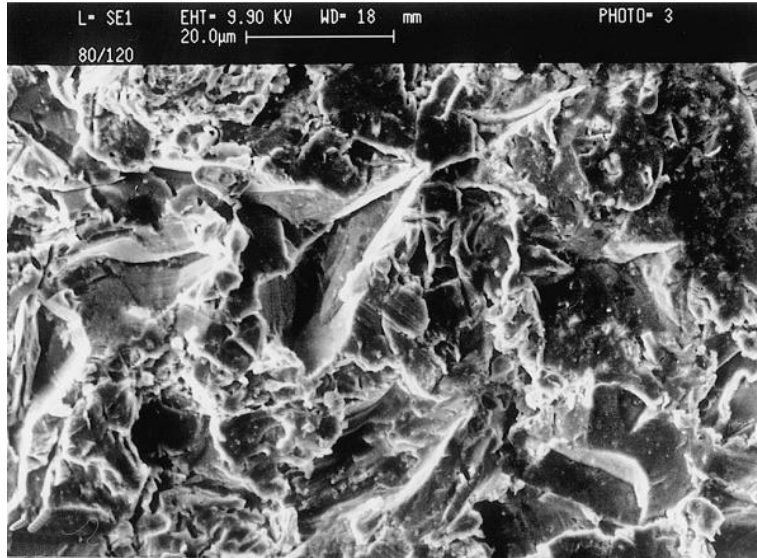


Figure 2-17: Surface morphology of aluminum 5251 alloy after grit blasting (taken from Brewis D.M. et al. [102])

Research carried out by Harris A.F. [101] focused on determining the effect of different kinds of grit blasting mediums on resulting surface roughness, and attempted to establish a correlation between surface roughness and surface energy. It was discovered that a larger grit size produced rougher surface, lower surface energy and higher lap shear strength. This correlation between roughness and lap shear strength was confirmed and expanded upon by Rudawska [103] by including other mechanical abrasion methods such as grinding, lapping, and superfinishing.

Gritblasting is often used to prepared surfaces due to simplicity and reliability [101]. In literature, the term is used interchangeably with ‘airborne particle abrasion’, ‘sand-blasting’, and ‘roughening’.

However, grit blasting a surface damages any other coatings previously applied to the material.

Automotive parts commonly have surface finishes that are useful for other purposes, such as aesthetics and corrosion protection. For such cases, grit blasting is an unfavorable method of preparing a metal surface for adhesion.

Surface roughness is measured with a tool called a profilometer. It works by dragging the tool tip across the sample surface, recording variations in surface height. Surface roughness is frequently expressed as R_a , which is the average departure of the profile from the mean plane (Figure 2-18).

$$R_a = \frac{1}{l} \int_0^l |Z(x)| dx$$

Equation 2.1: Surface roughness

Where

$Z(x)$ = profile ordinates of roughness

l = length of the measured surface

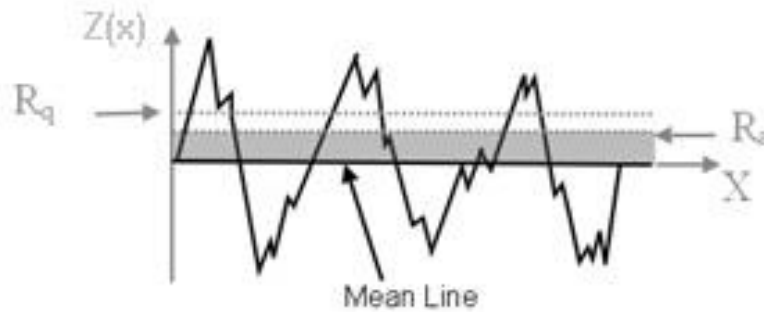


Figure 2-18 Visualization of R_a value with respect to a surface profile (taken from *The Home of Surface Measurement* [104])

2.5.2. ALUMINUM ANODIZATION (CHEMICAL PRETREATMENT)

The high affinity of aluminum surfaces for oxygen ensures the metal will always be covered with an oxide film [105]. Anodization is a process that improves the quality of this natural oxide film and produces an attractive finish, has excellent corrosion resistance, and other commercially desirable qualities. It also increases the porosity and the thickness of the oxide layer, subsequently making it more ideal for adhesive bonding [106].

It is now possible to anodize aluminum to obtain a broad range of pore diameters, cell diameters and barrier-layer thickness by modifying the forming parameters [107, 108]. Cohesive failure of the adhesive is more likely with a thicker oxide layer, since thicker oxide layer is less likely to fail before the adhesive joint. Additionally, the porous surface of aluminum oxide (Figure 2-19) increases the effective amount of surface area for the adhesive to adhere. Anodization is an attractive option for increasing adhesion because essentially it is an improvement to a naturally occurring effect on an aluminum surface.

Therefore, any chip or defect on the anodized aluminum surface will be naturally ‘repaired’ with time.

Anodization as a surface pretreatment for improved adhesion has been studied by multiple researchers [106, 109, 110]. It is generally accepted that, apart from some initial transient behaviour, the aluminum oxide layer formed during anodization process stays relatively inert. This explains why efforts were not usually undertaken into investigating the effect of time into an anodized surface pertaining to strength of the adhesive bond.

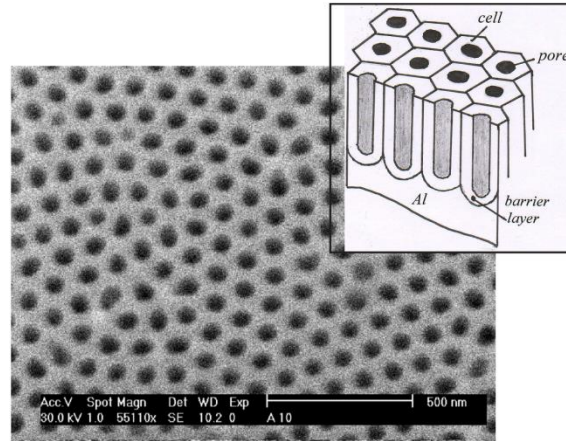


Figure 2-19: Schematic diagram of porous alumina template (adapted from Jagminas A.[111])

2.5.3. ALODINE CONVERSION COATINGS

Alodine 5200 is a conversion coating treatment product specially formulated for aluminum and its alloys. However, the product is also applied to the magnesium samples in this experiment, as research by Gao and Ricketts [112] showed that it can also be applied to magnesium parts to prevent corrosion. Its prior generation, Alodine 1200, contains Hexavalent Chromium, which has been shown to be hazardous to health [113].

Alodine 5200 is designed to prepare the surface of the material for bonding of adhesive/paint, and improve its aesthetic appearance. It is the most commonly used system of protection against corrosion in military/civilian aircrafts [114].

In this document, Alodine 1200 with Hexavalent Chromium would be called Alodine HC, and Alodine 5200 would be shortened to Alodine.

2.5.4. CONTAMINATION

The pretreatments discussed in previous chapters involve cleaning of the surface of the adherends, as clean parts are typically much more conducive for adhesive bonding. However, manufacturing of automotive parts focuses on a different set of priorities, such as using a lubricating agent to aid in the process of forming an automotive part. With respect to bonding, this lubricant is considered a contaminant.

In this experiment, the adhesives were tested with intentionally contaminated surfaces to address this issue. The substrates were contaminated with Multidraw Drylube E1 (manufactured by Zeller+Gmelin), which is a dry film forming lubricant specially formulated to work with steel, high strength steel and

aluminum in the automotive industry. At room temperature, its appearance and texture is similar to wax. The technical data sheet can be found in Appendix A: Technical Data Sheets.

2.6. ACCELERATED TESTING FOR ENVIRONMENTAL EFFECTS

Automotive vehicles are regularly exposed to harsh conditions of the environment such as rain and snow. Severe climate exposes a vehicle body to extreme temperatures. Moisture and salt could catastrophically fail important parts of a vehicle by introducing rust onto exposed parts such as the underbody. Paints and other coatings are standard practice to combat such problems, as well as using materials that stand up to environmental degradation.

If adhesives were to be introduced to the industry, these same concerns would also have to be addressed. Water, in forms as liquid or vapour can potentially degrade adhesive joints by damaging the adhesive bond itself, or weakening the bond between the adhesive-adherend interfaces [115]. An epoxy adhesive contains hydrophilic groups which can attract water molecules and cause swelling [116]. This trapped moisture inside the adhesive bond contributes to the degradation of the adhesive mechanical properties; a process that can happen before, during, or after the curing process.

Multiple researchers have demonstrated that moisture lowers the strength of an adhesive joint [115, 117, 118]. These experiments have a common feature in the shape of the curve of joint strength against time. Joint strength falls rapidly on the early stages of exposure and slows down after a certain period of time. This curve shape is observed in butt and lap type of joints, and is predicted to occur in other type of joints as well. Surface pretreatments on the adherends have a greater influence onto the strength of the joint. Brewis et al. [117] demonstrated that, with specific types of surface preparation methods, low concentrations of water might even have the net effect of strengthening some adhesive joints (Figure 2-20).

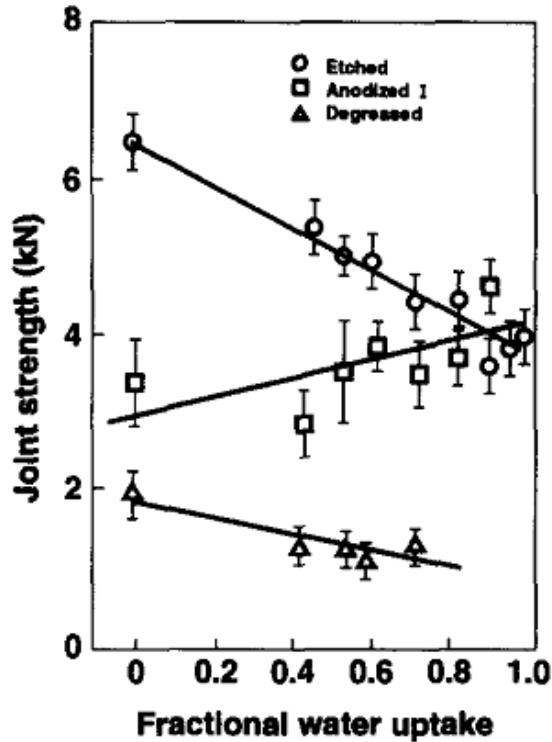


Figure 2-20: Dependence of joint strength upon water uptake for variously prepared joints (taken from Brewis et al. [117])

2.7. NUMERICAL REPRESENTATION OF ADHESIVE JOINTS

It is important for the automotive sector to be able to investigate into the behaviour of bonded joints subjected to crash-type deformations since crashworthiness is a critical aspect of vehicle design [26]. Prototyping a crash-test vehicle is a very straightforward way to accomplish this, but the cost associated is typically very high. Computer models using explicit finite element analysis are invaluable to this effort; models are able to provide a reasonable prediction to how a vehicle would perform in crash scenarios. However, the reliability of a computer model is dependent on its ability to cover most of the mechanical behaviour of the materials involved. A characterization study was undertaken to develop an accurate adhesive model.

Traditionally, adhesive bonds were represented by a series of solid elements assigned with material properties [119]. The maximum values of stress, strain or strain energy predicted by the finite element analysis was compared with the corresponding material allowable values; this is called the solid continuum mechanics approach. This approach provides accurate predictions to the strength of the adhesive bond, provided the mesh is sufficiently fine to capture the stress singularities [119]. Since the adhesive thickness is almost always thinner than the substrate it is bonding to by a significant order, the

mesh density of the model can quickly lead to computational inefficiencies. This problem is demonstrated by Adams et al. [120], who showed that stress values, especially at the re-entrant corners of joints, are highly sensitive to mesh size.

Another approach is based on fracture mechanics. This approach foregoes the assumption that the material is continuous and free of defects, and relies on the definition of an initial flaw/crack, which propagates by a certain displacement under a certain amount of load [121]. However, in many applications this damage initiation is not obvious and hard to characterize.

The cohesive zone method, as proposed by Barenblatt [122] is another approach to modelling adhesive bonds. It offers an improvement to the fracture mechanics approach, and its use has become frequent in recent years [123]. It divides a crack into two parts – physical crack and cohesive zone. The cohesive zone is idealized as two surfaces which are held together by tractions. A relationship is drawn between tractions and the separation distance between the surfaces in this cohesive zone. The depth of the physical crack extends when the traction variables reach critical values, and ultimately fail the entire element [124].

2.7.1. TIEBREAK CONTACT DEFINITION

The tie-break model connects two nodes and inhibits them from sliding apart. Stiffness values which were determined from the adhesives are assigned between the nodes, similar to that of a spring. Once this tied contact definition exceeds certain thresholds of normal or shear stress, it breaks and the nodes are free to slide apart [125]. For an adhesive joint, this tie-break contact would be defined between the two adherends that are meant to be joined together. Defining a joint this way omits the step of creating mesh elements of the adhesive joint.

Xiao X. et al. [126] utilized a tie-break contact method to simulate a double lap shear joint (Figure 2-21) failure with reasonable accuracy, upon comparison with results acquired from analytical calculations.

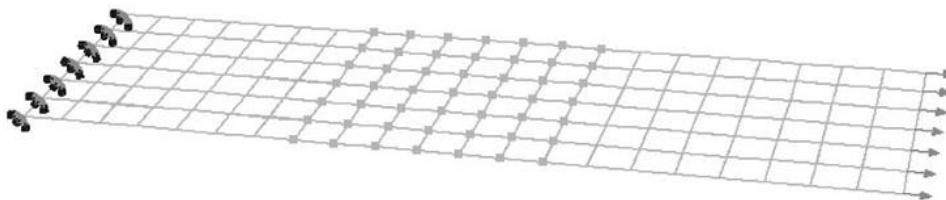


Figure 2-21: Double lap shear joint, modelled with tiebreak contact (taken from Xiao X. et al.[126])

The main appeal of using tie-break elements is its ease of implementation and low computational demands. Its main drawback is that it is incapable of predicting any complex stress distribution inside of

an adhesive joint. During crack propagation, an adhesive joint is expected to grow in length from its initial crack tip under a certain applied stress. With some tie-break models, a newly failed element would pass its load immediately to the next element, which would in turn overload that element. This process is called ‘numerical unzipping’ and is not a realistic behaviour of crack opening in an adhesive joint. Some tie-break models implement crack extension mechanics to address this issue. Another drawback is that this type of contact also does not support strain-rate effects.

2.7.2. SOLID CONTINUUM MECHANICS APPROACH

The solid continuum approach is the traditional approach of modelling any materials. The parts are discretized into elements, each containing information about its stress-strain state in three dimensions. The stress and strain values at each element are evaluated by solving a series of linear equations with displacements at each node as unknowns.

The software used to solve models in this work is the finite element code LS-DYNA LSTC. Work by multiple researchers [127-129] revealed that modern adhesives sustain relatively large strains before failure and hence are well suited to hyperelastic constitutive models. The solid continuum material model used is the SAMP-1 (Semi-Analytical Model for Polymers) model, developed by Kolling et al [130] to provide a material model that is able to recover important phenomena like necking, crazing, strain rate dependency, unloading behaviour and damage.

The input for this material model are given directly as load curves, with the tension load curve being the only compulsory input for SAMP-1 to start working. Each additional input modifies its yield criteria in a unique manner. Traditional yield criteria such as Von Mises or Drucker-Prager are usually inadequate for polymers, due to anisotropy of its reinforcement fibers. The SAMP-1 model aims to formulate a custom quadratic yield surface from the load curves it is supplied with, as opposed to using traditional yield surfaces. The shape of the yield surface is dependent on the amount of information provided to it. Details about the effect of multiple inputs on SAMP-1 yield criterion algorithm are presented in Appendix H: SAMP-1 Material Model Information.

As specified in the literature [130], SAMP-1 has been tested to predict yield surfaces for different polymers such as thermoplastics, polyvinyl chloride (PVC), polystyrene (PS) and acrylonitrile butadiene styrene (ABS) with good success. It has also been validated with dynamic tensile, unload, compression, shear and bending tests (Figure 2-22). However, it is important to note that the predicted shear response was only reasonable up to the yielding point. (Figure 2-23)

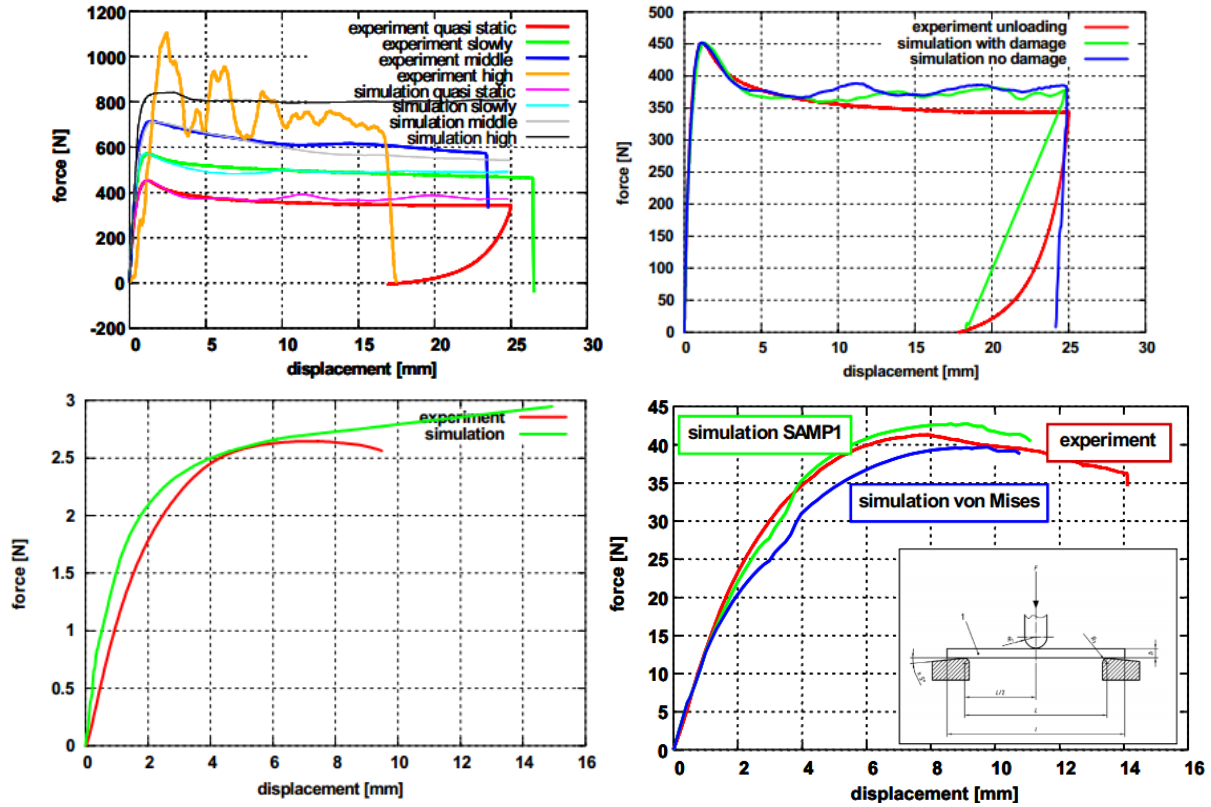


Figure 2-22: Validation tests for SAMP-1 material model under various loading conditions: Tensile (TL), tensile with unloading (TR), compression (BL), three-point bending (BR) (taken from Kolling et al [130])

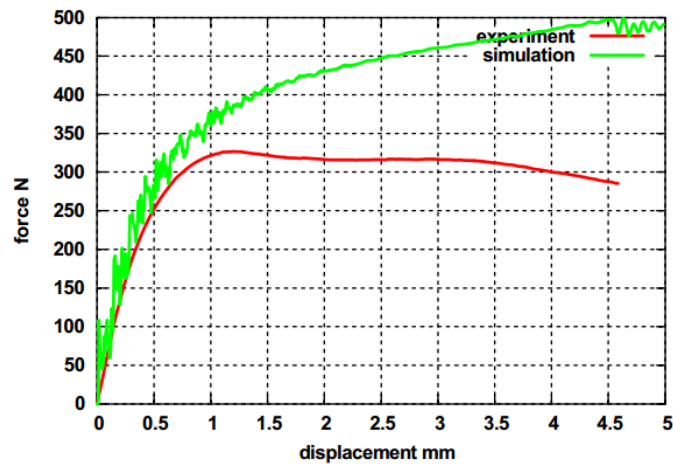


Figure 2-23: Validation shear test simulated with SAMP-1 material model (taken from Kolling et al [130])

2.7.3. FRACTURE MECHANICS APPROACH

Continuum mechanics assumes that the material being modeled is continuous. It assumes that no defects and cracks are present to start a fracture process. As such, continuum mechanics gives no solution for the

case of singular points resulting in sharp increases in stress and strain. Fracture mechanics was developed to handle this situation, since cracks and defects are very common and is the primary cause for fracture in many materials, adhesives included [131]. The presence of crack is assumed, and a study was done to develop quantitative relations between the crack size, material inherent resistance to crack growth, and the critical stress required for the crack to propagate and cause failure.

The conventional method of quantifying these parameters is by introducing a controlled-size crack inside the material, and measuring its propagation under certain amount of force on certain directions (Figure 2-24).

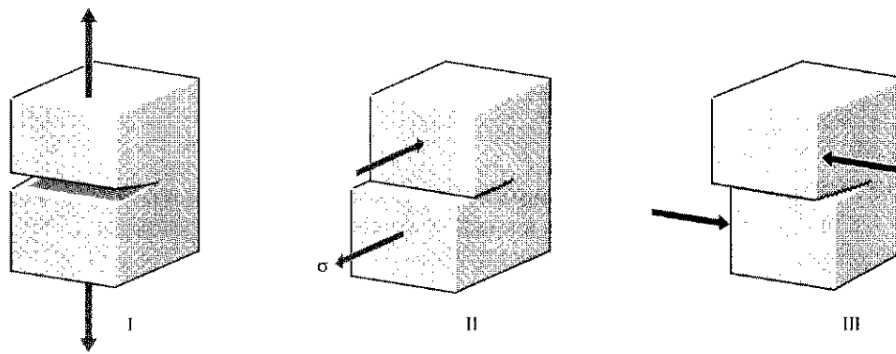


Figure 2-24: Fracture mechanics modes of crack propagation (taken from Roylance [121])

An adhesive joint typically has a thickness value of less than 1mm, and magnitudes smaller in thickness than the adherend materials. Introducing a controlled-size crack into the adhesive is challenging, requiring specialized tools and equipment to create and observe its propagation. Furthermore, to properly study the joint characteristic using FEA approach, the computer model would have to support a very high mesh density near the crack tip, and progressively less dense further away from it. For an adhesive joint, this would lead to unreasonable amount of elements and computational expense. For these reasons, the fracture mechanics approach is not commonly pursued for adhesive joint failures.

2.7.4. COHESIVE ZONE MODEL

The cohesive zone model was proposed by Barenblatt [122] with the intention of describing fracture process via crack propagation. The cohesive zone model divides a crack into two parts: the physical crack and cohesive zone (Figure 2-25). This approach conveniently solves the problem of stress singularities found with linear elastic fracture mechanics approach.

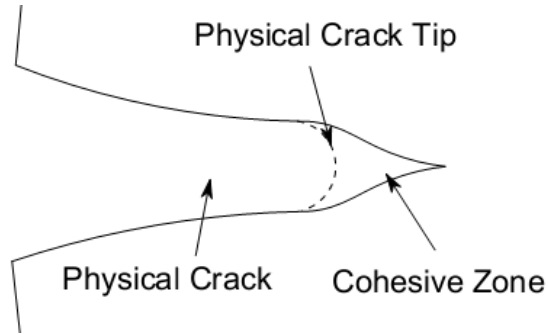


Figure 2-25: Distinction of the two different zones in the crack (taken from Christensen [124])

Cohesive elements are implemented by defining an element between the adherend surfaces (Figure 2-26), and giving the cohesive elements properties that are dependent on the fracture behavior of the adhesive. The technique consists of the establishment of traction-separation laws to model interfaces/regions inside the adhesive layer.

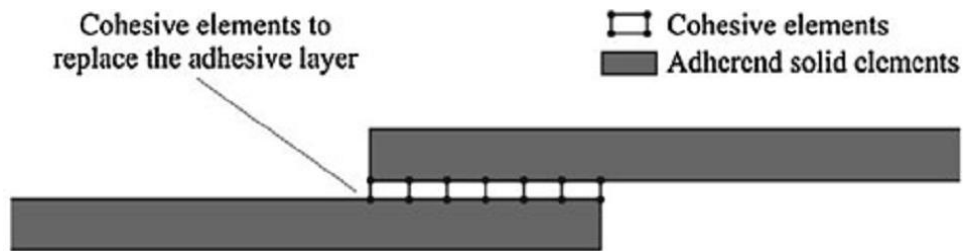


Figure 2-26: Numerical simulation of a lap shear joint with cohesive elements (taken from Da Silva et al. [119])

The properties that it requires are the peak traction stresses ($\hat{\sigma}$ and $\hat{\tau}$) and energy release rate values for both mode I ($G_I C$) and mode II ($G_{II} C$) kinds of loading, in addition to damage curves that relates their tractions to displacements (Figure 2-27). Yang and Thouless [132] concluded that different cohesive laws are required for the two modes of deformation and that they require separate parameters to describe their respective cohesive tractions. Interpolations are done in the case of mixed mode loading (Figure 2-28).

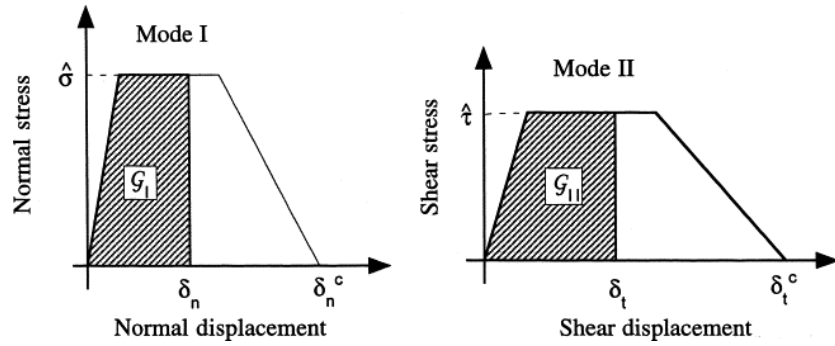


Figure 2-27: Schematics of the parameters used in cohesive zone calculations (taken from Yang and Thouless [132])

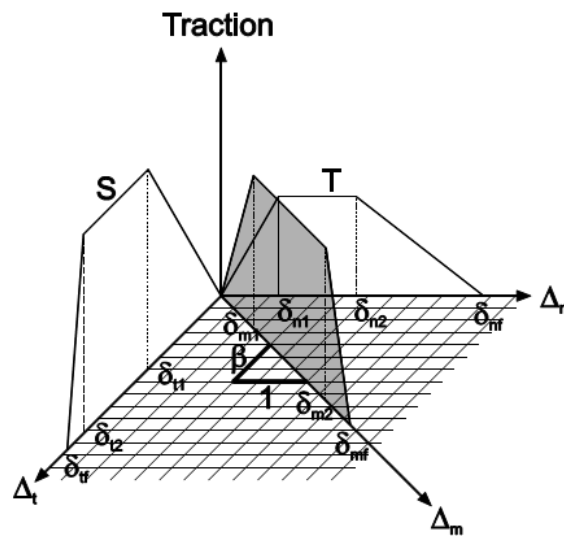


Figure 2-28: Cohesive element mixed-mode traction-separation law (taken from LS-DYNA Keyword User's Manual Volume II: Material Models [133])

The use of cohesive models to predict mechanical behaviour of adhesive bonded joints under mixed-mode loading was studied by De Moura et al. [123] by using double cantilever beam (mode I) and end-notched flexural tests (mode II) to acquire its properties. Trimiño and Cronin [49] acquired the fracture properties of DP460NS and SA9850 by using the double cantilever beam test (mode I) and thick adherend lap shear tests (mode II).

CHAPTER 3

LAP SHEAR TEST

3.1. BACKGROUND

The lap shear test is a standard (ASTM D3165 [59]) test method for determining comparative shear strengths of an adhesive joint [22]. It is the most commonly used test method carried out to observe the effect of different surface pretreatments due to its ease of assembly and simple testing method. Single lap shear test consists of two rectangular pieces joined by the adhesive and subjected to tension forces from the opposite ends.

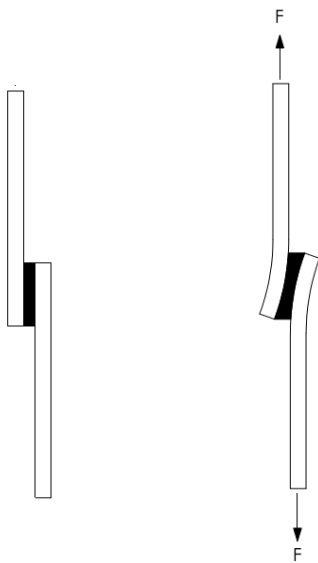


Figure 3-1: Schematic of lap shear loading. Lap shear specimen as prepared, unloaded [L]. Lap shear specimen demonstrating bending deformation in the vicinity of the adhesive joint [R].

There are two common configurations for lap shear samples: single lap shear and double lap shear (Figure 3-2). The double lap shear geometry results in less bending moment in the adherends, but is more complicated to assemble and maintain uniformity. Due to the doubling of strength of the adhesive bond during double lap shear tests, it is recommended to use thicker material on the single adherend side. One challenge with this test is that one-sided fractures can easily occur due to small asymmetries during assembly process and variability in the adhesive strength between the two joints.

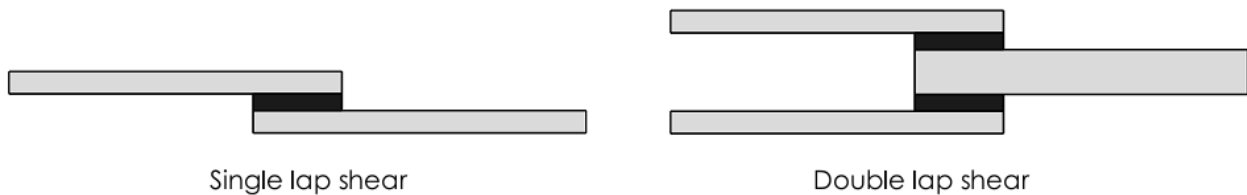


Figure 3-2: Single lap shear (ASTM D1002) [134] [L]. Double lap shear (ASTM D3528) [135] [R]

Although classified as a shear test it is important to note that the type of loading the adhesive joint experiences during a lap shear test is not pure shear. DeVries and Borgmeier [136] claimed that, due to deformation of the adherends, peel stresses rather than shear stresses dominate lap joint fracture. Common improvements to the geometry of the lap shear test are presented on ASTM D3165 [59] (Figure 3-4) and ASTM D5656 [67] (Figure 3-5). The modification of geometry as specified in these two standards reduces the amount of bending experienced by the adherends and reduces the amount of mixed-mode loading on the joint.

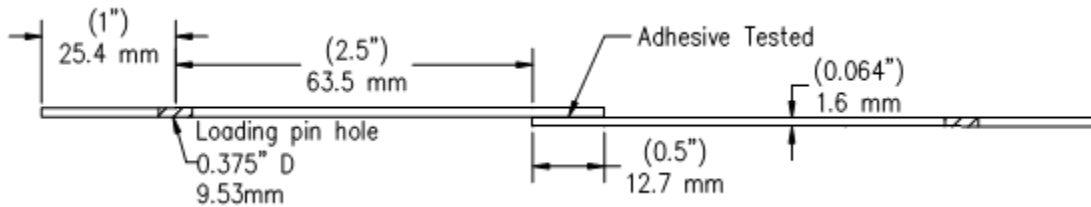


Figure 3-3: ASTM D1002 test specimen profile [134]

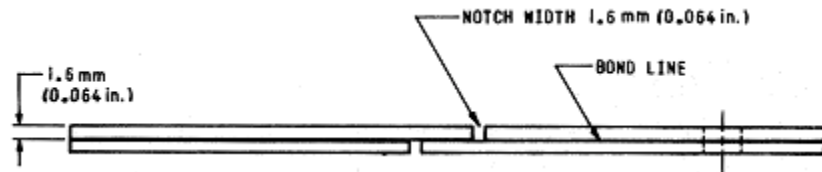


Figure 3-4: ASTM D3165 test specimen profile [59]

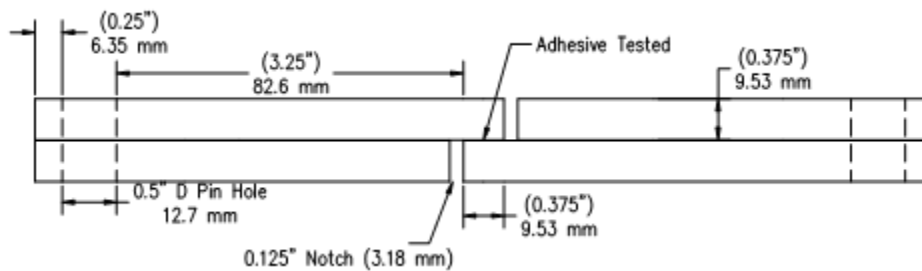


Figure 3-5: ASTM D5656 test specimen profile [67]

The geometry and material properties of the adherends in this test has a sizeable effect on failure of the adhesive joint. The most influential parameters for the bond strength are the surface preparation, adhesive thickness, lap size, and spew fillet geometry [65, 137-139].

The single lap joint is the most studied adhesive joint type in literature. However, the strength prediction of such joints is still widely debated. An overview of these approaches were compiled and reviewed by

Da Silva et al. [63, 64]. In general, many conditions and assumptions have to be made to analyze strength of lap shear joints, with the plasticity of the adhesives and adherends being important considerations.

The measured strength of a lap shear joint is frequently specified by Equation 3.1.

$$\tau = \frac{P}{bl}$$

Equation 3.1: Shear strength of a single lap shear joint

Where

P : applied load

b : joint width

l : overlap length

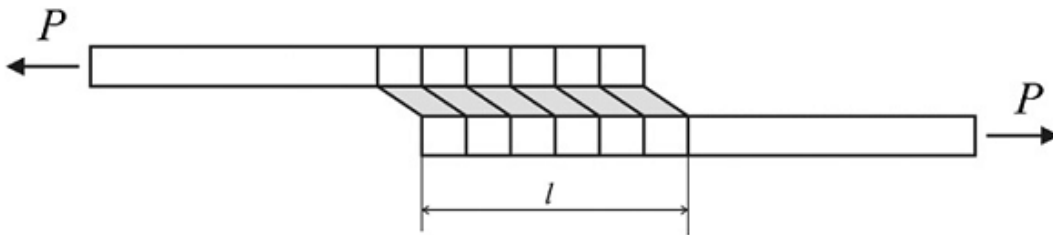


Figure 3-6: Idealized lap shear joint deformations, with rigid adherends (image taken from Da Silva et al. [63])

For this value to be accurate, several assumptions are required: the first being that the adherends are rigid; second, the adhesive layer shears uniformly across the entire bond in a pure shear loading condition; third, the entire adhesive bond fails uniformly at specified applied load value (Figure 3-6). These assumptions are clearly unrealistic for a single lap shear configuration, but this is still the most common manner for quoting adhesive shear strength in many test situations such as ASTM and ISO standards.

The toughened structural adhesives used in this study exhibit relatively large amounts of plasticity prior to failure; they are also relatively high in strength. This has proven to affect deformation of the adherends, as shown by visible bending in some of the adherends and permanent deformation after testing. Adams et al. [140] proposed a simple design methodology which incorporates these effects. Da Silva et al. [64] confirmed its effectiveness on situations where the adhesive is ductile (>10% shear strain to failure) and the adherends are non-elastic.

This analysis shows that maximum adhesive shear stress occurs near the ends of the joint (Figure 3-7). Failure of the joint is therefore predicted to occur at the edges first, when the effective stress exceeds the strength of the adhesive. Adams et al.[140] also showed that the strength of the adhesive joint linearly

increases with longer overlap length, up to a certain point where any increase in overlap length would no longer result in a stronger bond (Figure 3-8). The explanation is that, after a certain point, plastic deformation of the adherends becomes the dominant cause for bond failure instead of intrinsic adhesion strength. Therefore, the reported values of lap shear strength in this study are adherend specific. Different results are expected when testing with different alloys and/or different thickness.

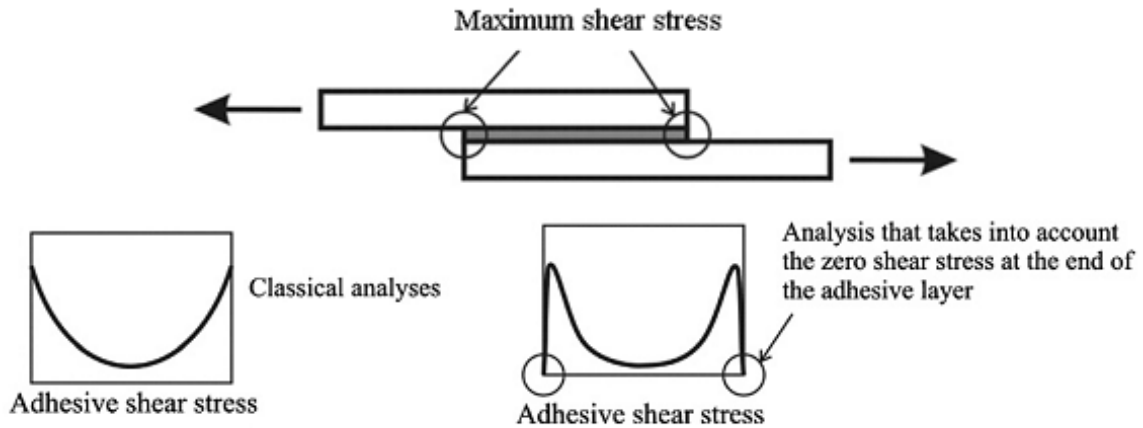


Figure 3-7: Distribution of adhesive shear stress in a single lap joint (adapted from Da Silva et al. [63])

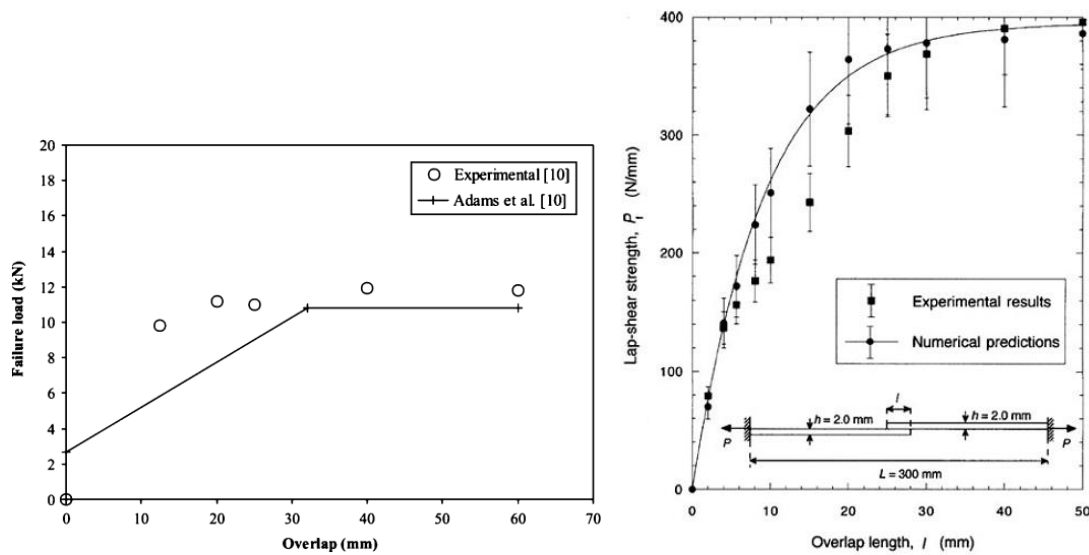


Figure 3-8: Effect of length of bond overlap length onto bond strength (Left: taken from Da Silva et al.[64], Right: taken from Kafkalidis and Thouless [65])

Prior lap shear tests [50] on two adhesives (DP460NS, and a prior formulation of SA9850), using 3 mm thick adherends and a bondline thickness of 1 mm. (Figure 3-9). The samples were tested at five different shear strain rates, ranging from 0.005/s to 50/s (Figure 2-3).

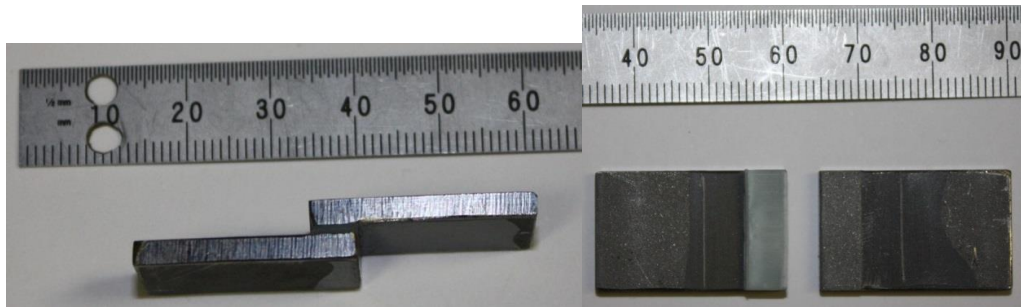


Figure 3-9: Thick adherend lap shear tests from [50].

3.2. METHODS

The lap shear samples were manufactured in accordance to the ASTM Standard D3165 [59]. The shorter piece of the adherend was bonded on the surface of the testing adherend to minimize offset bending moments and stresses.

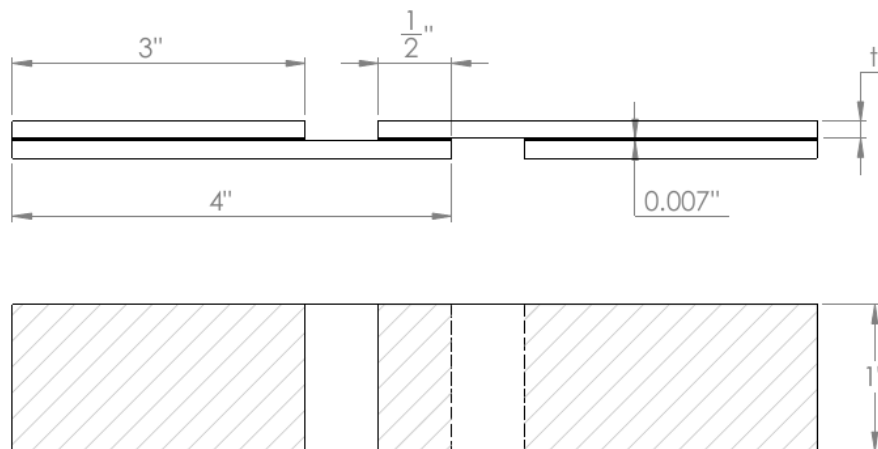


Figure 3-10: Dimensions of lap shear specimens (not to scale) (Side view [T]; top view [B])

Material	t (adherend thickness)
Aluminum 6061-T6	0.0625" [1.588 mm]
Magnesium AZ31b	0.079" [2 mm]

Table 3-1: Material thicknesses for lap shear testing

To make the samples, the adherend pieces were cut from a large sheet of material (4"x1" and 3"x1" [101.6 mm x 25.4 mm] and [76.2 mm x 25.4 mm]). Two of each piece was required to assemble one sample (Figure 3-11). Consistent width values were prioritized (tolerance of ± 0.1 mm) during the

manufacturing process, as the assembly fixture and test rig relied on the consistency of this dimension to maintain proper alignment.

Brass spacer shims were cut from a sheet (0.007" x 0.78" x 0.1" [0.178 mm x 20 mm x 2.5 mm]). The spacer shims were used to control the thickness of the adhesives by placing them between the adherend pieces. Four brass shims were required to assemble one sample. This experiment was done with a relatively thin bond line of 0.007" [0.178 mm] to reflect its application in a more realistic manner. The adhesive thickness was reasonable for an epoxy adhesive [54] and was also in agreement with the recommended thickness value from the manufacturer [141].

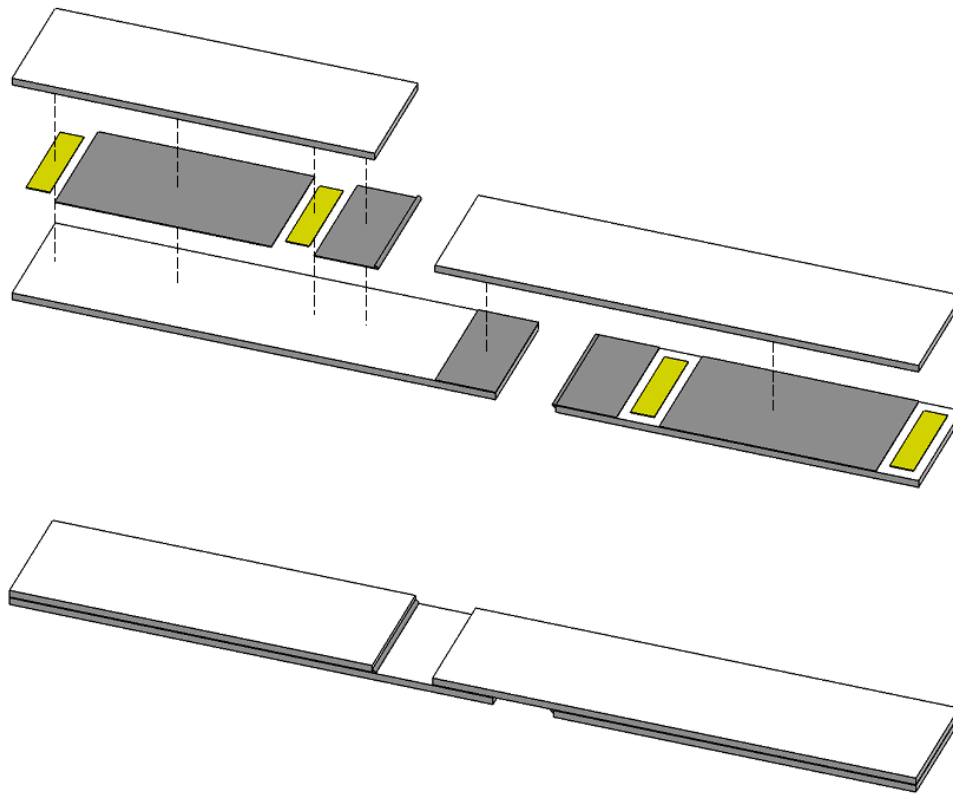


Figure 3-11: Construction of lap shear samples (Exploded [T], assembled [B])

The fixture spacers were cut from aluminum flat bar pieces and polished with sandpaper (8"x0.75" [200 mm x 19 mm]). The thickness of the spacer pieces were double the adherend thicknesses. Brass shims were cut from the stock (0.007"x8"x0.5" [0.178 mm x 200 mm x 12.7 mm]). These spacer pieces were reused in every session.

The spacer pieces were polished, and a thin coating of a mold release solution (FreeKote®, manufactured by Henkel Corp., Germany) was applied. This was done to reduce the chance of the adhesives bonding onto them.

Various pretreatments were applied to the adherend pieces. Details are as follows:

- The process of gritblasting for this experiment was done in the University of Waterloo with grit size of 70 (avg of 203 μm diameter) and a blasting pressure of 60 psi. The application was manual with careful application technique. Ra values of 1.5 μm to 2.5 μm (discussed in chapter 2.5.1) were acquired from the gritblasting procedure. The time spent on gritblasting the samples were estimated to be 5 minutes per lap shear sample.
- Alodine treatments and anodization were carried out at a local metal finishing plant (Waterloo Electroplating and Metal Finishing Inc.). Magnesium anodization was not investigated as the plant did not have the capability of perform the pretreatment. The costs of the pretreatments at the local plant were estimated to be \$6 per lap shear sample.
- Metal forming lubricant (Multidraw Drylube E1, manufactured by Zeller+Gmelin) was lightly applied as a layer of coating to the samples that were selected to represent contaminated adherends. Metalforming lubricants are expected to be present in automotive metalforming applications, and therefore subject to no extra cost.

Samples were cleaned with a Methyl-Ethyl-Ketone (MEK) solution. This was done in a fume hood to quickly evaporate traces of the solution. The only exception was the intentionally contaminated samples, which were left uncleaned after the coating was applied.

Adhesives were applied to the appropriate surfaces of the adherend and spread evenly with a putty knife.

The assembled samples and the fixture pieces were arranged between the two pieces of tempered glass. Binder clips were used to hold the pieces of glass together during curing process. (Figure 3-12)

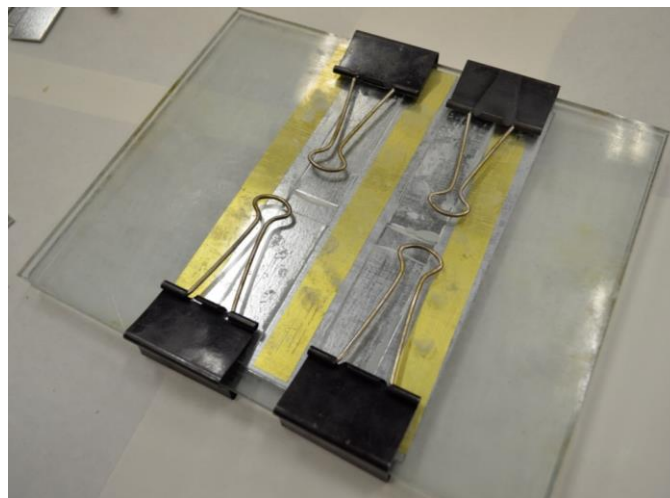


Figure 3-12: Assembled samples between the glass panels

The entire fixture was placed in a convection oven for oven curing cycle. Samples made using DP460NS were oven-cured for 90 minutes at 75°C, and samples made with SA9850 were oven-cured for 90 minutes at 170°C [142].

After the curing cycle, the samples were removed and the excess adhesive were removed from the edges of the samples in a consistent fashion with manual tools. Prior experiments have shown that an excess adhesive (spew fillet) could increase the strength of a joint by reducing the stress concentration on the corners. Since maintaining a consistent fillet size is unmanageable with the aforementioned routine, a decision was made to remove all the fillets to maintain consistency.

A custom built quasi-static testing frame was used to measure force-displacement curves at low rates of displacement, 0.178 mm/s [10.7 mm/min]. The frame included a load cell (capacity of $\pm 20,000$ lb [± 88.96 kN]) and a displacement measurement sensor system with resolution of $4.71 \mu\text{m}$ (manufactured by Schaevitz Sensors). The frame was installed with jaws (Figure 3-13) that accommodate varying lap shear thicknesses from zero up to $\frac{1}{4}$ " [6.35 mm]. The test jaws were installed using the concentrically-aligned threaded attachments at both ends of the hydraulic frame, minimizing the chance of misalignment of the test jaws. The edges of the samples were laid flat on the front wall of both jaws to further minimize risk of misalignment.

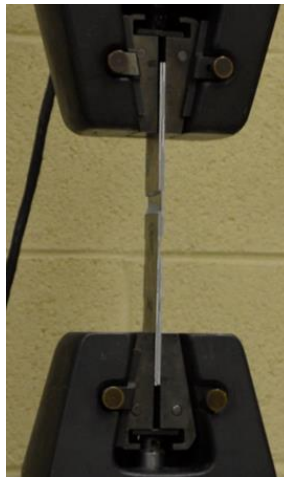


Figure 3-13: Lap shear sample located in the test jaws

3.2.1. PRELIMINARY TESTS AND RESULTS

A preliminary test run was done to confirm the feasibility of the different pretreatments. The selected adherend was aluminum 6061-T6 due to material availability. DP460NS was used for its ease of application and greater reliance on surface preparation for adhesion. Results are shown on Figure 3-14 to Figure 3-18, in the form of average shear strength and 95% confidence interval of the results.

Pretreatments that showed statistically significant reduction of strength with delays between pretreatments and bonding time are denoted with an asterisk (*) next to its respective title.

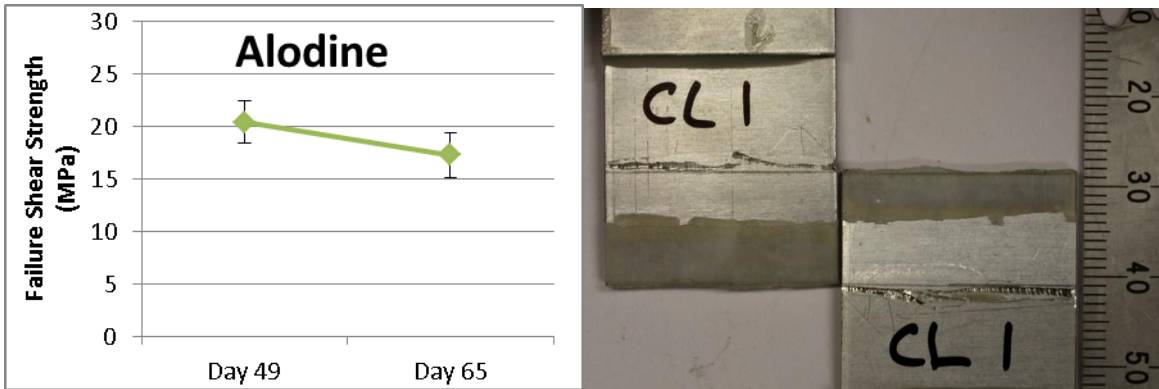


Figure 3-14: Result of preliminary lap shear test, DP460NS, aluminum 6061-T6, Alodine (failure shear strength [L], fracture surface [R])

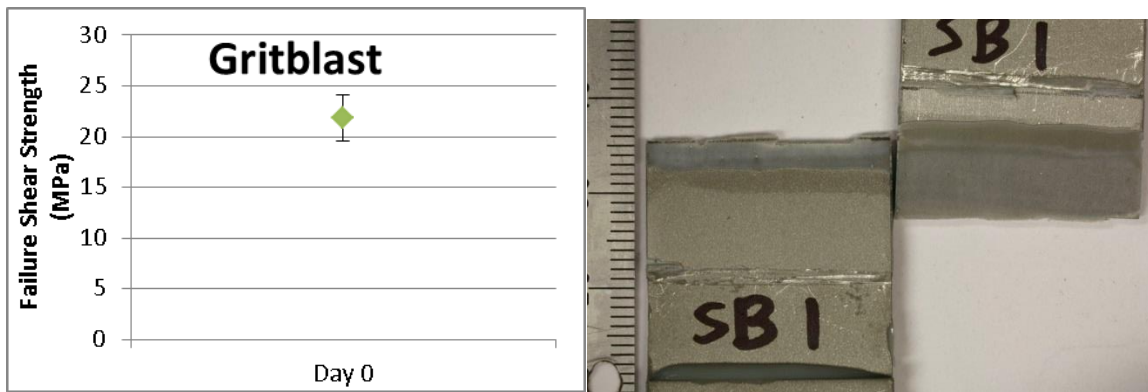


Figure 3-15: Result of preliminary lap shear test, DP460NS, aluminum 6061-T6, gritblasting (failure shear strength [L], fracture surface[R])

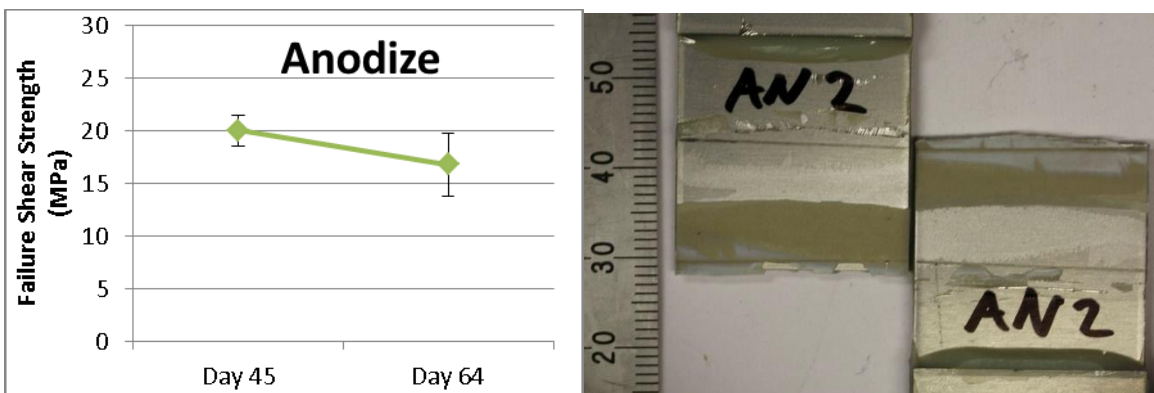


Figure 3-16: Result of preliminary lap shear test, DP460NS, aluminum 6061-T6, anodization (failure shear strength [L], fracture surface [R])

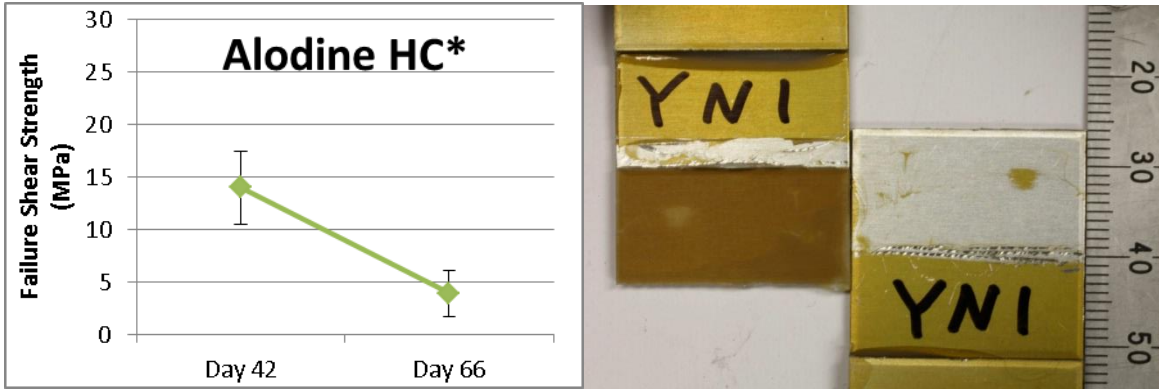


Figure 3-17: Result of preliminary lap shear test, DP460NS, aluminum 6061-T6, Alodine HC (failure shear strength [L], fracture surface [R])

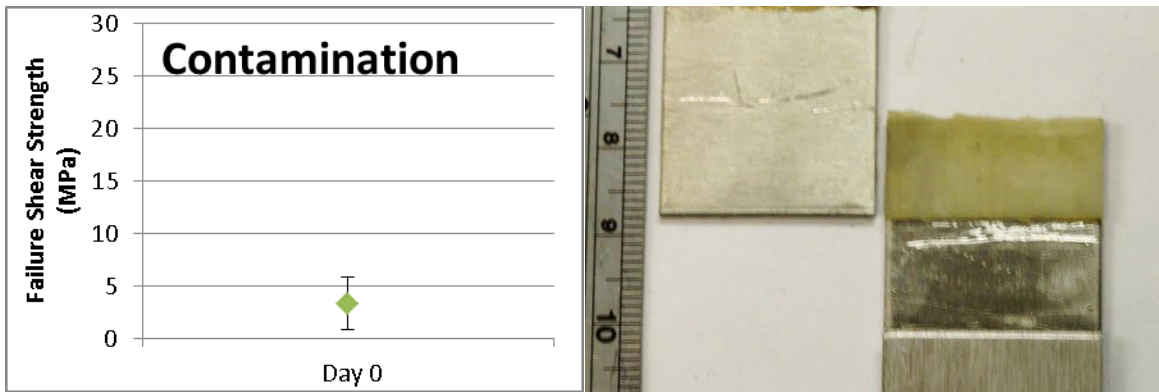


Figure 3-18: Result of preliminary lap shear test, DP460NS, aluminum 6061-T6, contamination (failure shear strength [L], fracture surface [R])

Interfacial failures were identified on all of the tested preliminary samples. In comparison with other configurations, samples treated with Alodine (Figure 3-14), gritblasting (Figure 3-15), and anodization (Figure 3-16) demonstrated the highest bond strength numbers. The time effects on bond strength values for these combinations were not statistically significant in this preliminary test series, although this variable was not tightly controlled.

The joint strengths measured for samples pretreated with Alodine HC (Figure 3-17) were significantly lower than the other pretreatments. A statistically significant decline in joint strength after several days was detected, confirming the existence of a decay effect. The difference of colour on the bonded area after the fracture suggests that the failure occurred in the coating instead of in the adhesive.

Contaminated samples demonstrated low joint strength (Figure 3-18), and the adhesive layer peeled off easily from the adherends following the test. It was found that the DP460NS adhesive did not work in a contaminated environment and was not considered further. Based on the preliminary test results a final

test matrix was developed (Table 3-2) comprising 48 test configurations. The test samples were repeated with focus on controlled assembly time after pretreatment. A minimum of three samples were tested for each configuration.

In addition to the parameters outlined above, some other materials were received and tested late in the program. Specifically, they include aluminum alloy 5182 pretreated with Henkel Bonderite EC² and magnesium ZEK100 pretreated with Henkel Bonderite MgC. These tests contained parameters that were not straightforwardly comparable with the previous ones (Table 3-2).

Adhesive	Material	Pretreatment	Age of pretreatment	Material thickness
DP460NS	Aluminum 6061-T6	Alodine	Day 0,1,7	0.0625" [1.59 mm]
		Alodine HC	Day 0,1,7	
		Anodization	Day 0,1,7	
		Gritblasting	Day 0,1,7	
	Magnesium AZ31b	Alodine	Day 0,1,7	0.079" [2 mm]
		Alodine HC	Day 0,1,7	
Gritblasting		Day 0,1,7		
SA9850	Aluminum 6061-T6	Alodine	Day 0,1,7	0.0625" [1.59 mm]
		Alodine HC	Day 0,1,7	
		Anodization	Day 0,1,7	
		Gritblasting	Day 0,1,7	
		Contamination	Day 0,1,7	
	Magnesium AZ31b	Alodine	Day 0,1,7	0.079" [2 mm]
		Alodine HC	Day 0,1,7	
		Gritblasting	Day 0,1,7	
Contamination		Day 0,1,7		
DP460NS and SA9850	Aluminum 5182	Henkel Bonderite EC ²	Unknown	0.065" [1.59 mm]
DP460NS and SA9850	Magnesium ZEK100	Henkel Bonderite MgC	Unknown	0.054" [1.37 mm]

Table 3-2: Finalized matrix for lap shear tests

3.3. TEST APPARATUS COMPLIANCE MEASUREMENT

In this research, displacement numbers were acquired from the LVDT installed with the test rig. This number represents the amount of movement experienced by the moving test jaw, and should ideally be equal to the amount of displacement experienced by the test sample. However, comparison with

numerical simulation results showed that the actuator crosshead displacement numbers were not equal with displacement experienced by the tested sample.

One of the possible reasons to explain this discrepancy is test apparatus compliance. A study was performed to better understand the relationship between recorded actuator displacement and sample displacement. It was assumed that the test machine behaved as a linear spring with the resulting stiffness termed the compliance correction factor (CCF) value.

An aluminum 6061-T6 flat plate was machined with width, length and thickness the same as the lap shear samples (Figure 3-19). The sample was positioned and loaded in the same manner as the lap shear samples, and a crosshead velocity of 0.178 mm/s was applied.

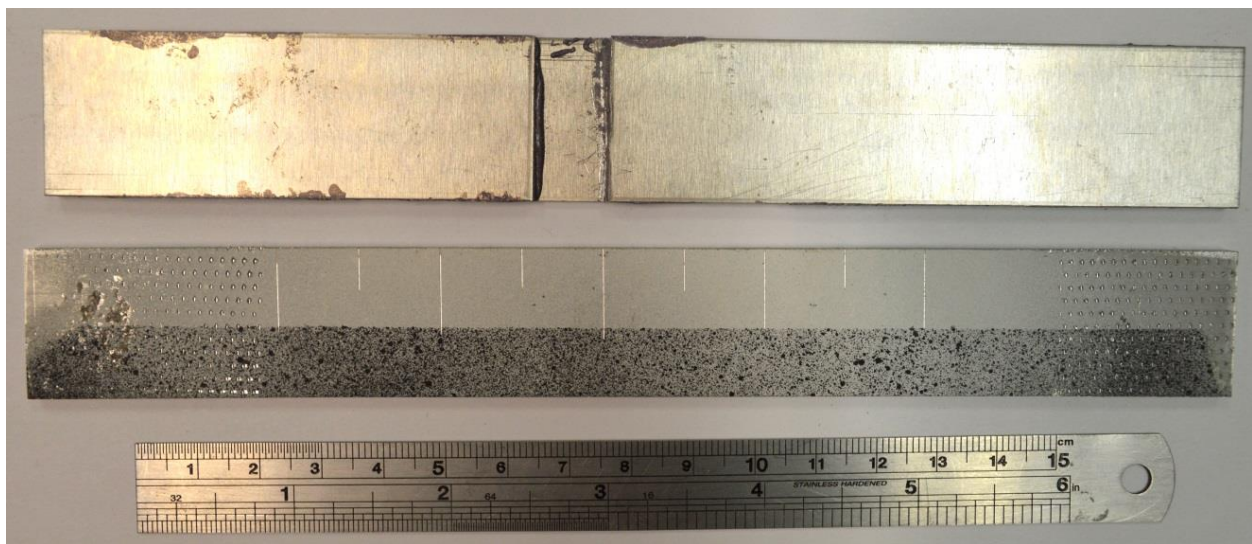


Figure 3-19: Figure of lap shear sample versus compliance bar (lap shear sample [T], compliance bar sample [B])

An optical video image tracking software (Tracker, developed by Douglas Brown, California [143]) was used to track the sample deformation. A speckled pattern was spray painted to the sample for the purpose of increasing *tracker* precision. Details about the resolution and accuracy of *tracker* are discussed in chapter 4.2.3. Deformation of the sample was measured on the aluminum test sample located between the grips (Figure 3-20). The displacement of the jaws was also tracked, and was confirmed to be consistent with the recorded actuator data.

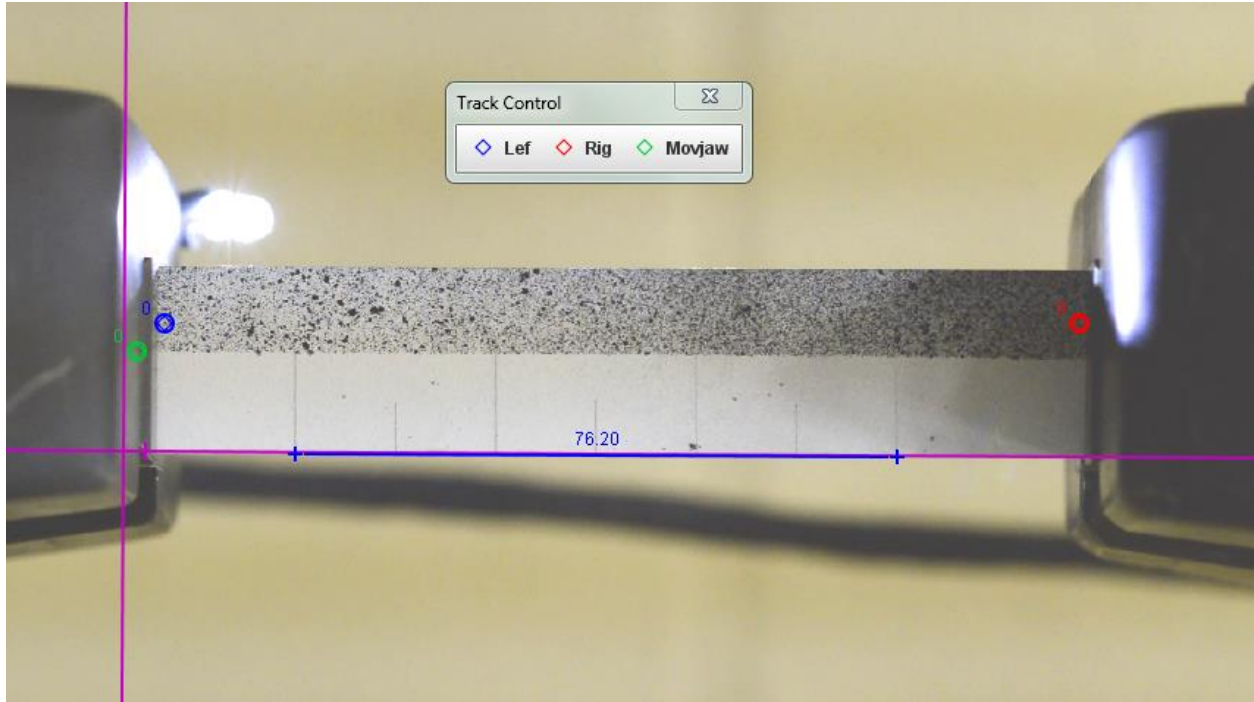


Figure 3-20: Tracked points in the compliance tester bar

The recorded actuator displacement was compared to the tracked results of the points in the sample, shown in Figure 3-21. The initial sudden acceleration that was recorded early on this compliance test ($t < 0.5$ s) wasn't present during the actual lap shear tests. From the graph it is visible that the actuator velocity was stable beyond approximately $t = 6$ s for this test case. Slopes were acquired for both data sets from this timestamp onwards (Figure 3-21). Sample displacement is the result of subtraction between points 'lef' and 'rig'. The physical positions of these points were shown in Figure 3-20.

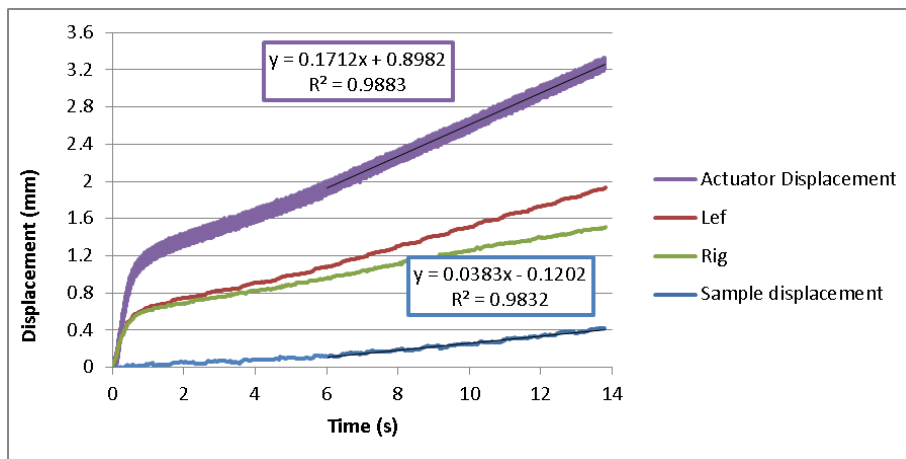


Figure 3-21: Displacement of actuator and sample

The acquired slope of sample displacement was 0.0383 (Figure 3-21). This represents the slope of displacement experienced by the sample and the CCF was determined as:

$$CCF = \frac{0.1712}{0.0383} = 4.47$$

Equation 3.2: Compliance Correction Factor

For subsequent tests, the crosshead displacement was corrected to achieve the sample displacement.

3.4. TEST RESULTS AND DISCUSSION

Data acquired from the lap shear tests follow the shape shown in Figure 3-22. The peak of these data curves represent the failure load of the adhesive, which were converted into failure shear strength via Equation 3.1.

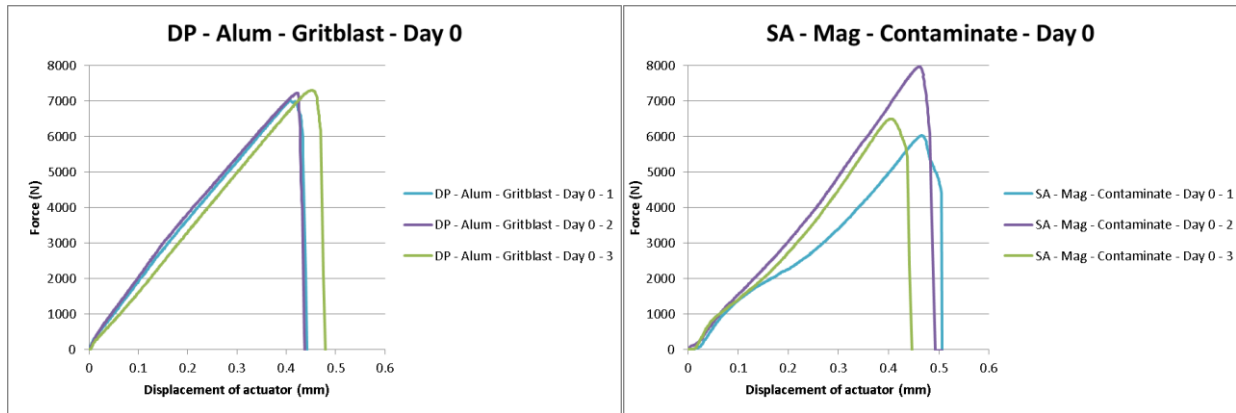


Figure 3-22: Examples of force versus actuator displacement data charts

Individual charts for comparing failure shear strength for all tested combinations can be found in Appendix B: Lap Shear Data Charts. Figure 3-23 shows the appearance of these charts and descriptions of the information contained. The ‘lap shear configuration’ title contains information about the adhesive used (e.g. DP is DP460NS, SA is SA9850), adherend material (e.g. Alum is aluminum, Mag is magnesium), and surface preparation method, respectively. Since the sample size is small and the population standard deviation is unknown, the 95% confidence interval was calculated by applying student t-distribution equation (Equation 3.3) to the failure shear strength numbers.

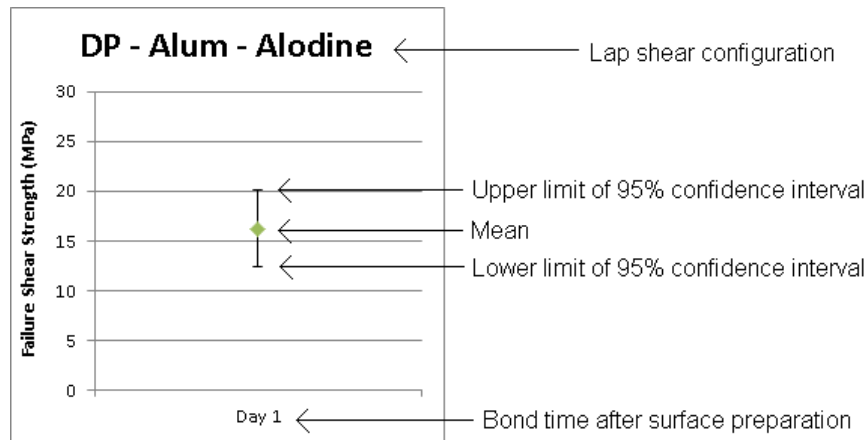


Figure 3-23: Plot of lap shear test results

$$\bar{X} \pm t_{95\%} \frac{S}{\sqrt{n}}$$

Equation 3.3: Confidence interval limits equation

Where \bar{X} is the mean of failure shear strength, $t_{95\%}$ is the t-distribution coefficient, S is the standard deviation of the failure shear strength, and n is the number of samples.

3.4.1. SUMMARY OF RESULTS

The figures presented in this section are summaries of the test results, where ‘day 0’ indicates no significant time elapsed between the surface preparation and bonding of the samples. The charts for each individual test are presented in Appendix B: Lap Shear Data Charts.

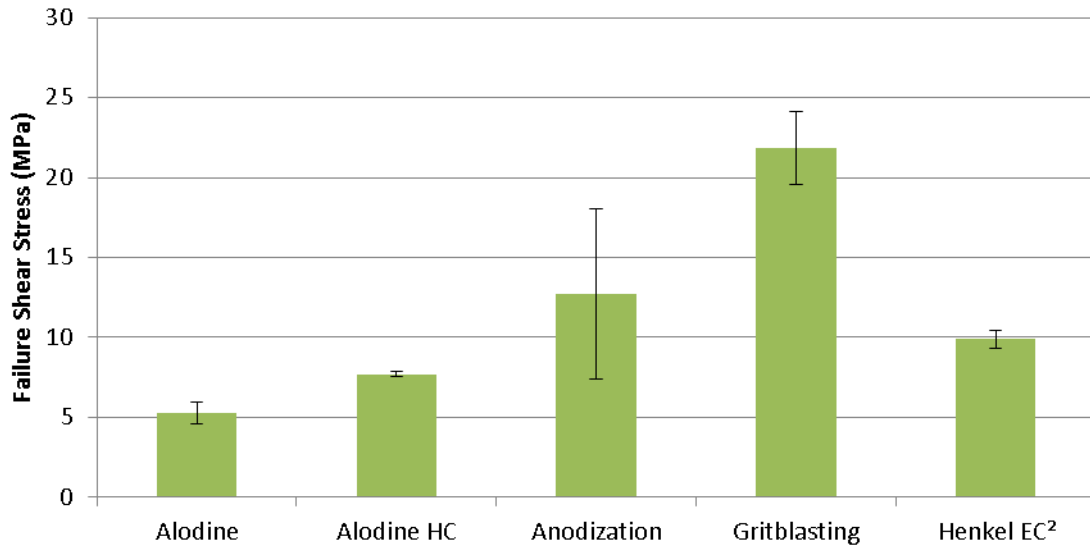


Figure 3-24: Summary of lap shear results (Adhesive: DP460NS, Adherends: Aluminum, Day 0)

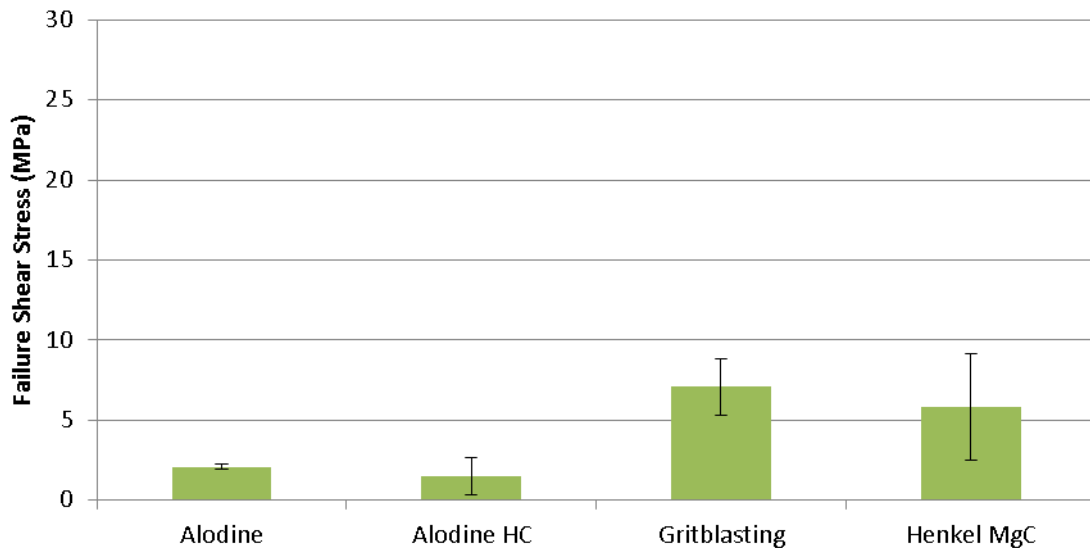


Figure 3-25: Summary of lap shear results (Adhesive: DP460NS, Adherends: Magnesium, Day 0)

In comparison with other pretreatments, gritblasting the surfaces produced samples with the highest bond strength and least amount of variability for DP460NS, for both aluminum and magnesium adherends. Gritblasting was therefore identified to be the preferable method of preparing adherends before bonding with DP460NS. Results acquired for magnesium samples were consistently lower than those acquired for aluminum. Research into other methods of magnesium pretreatments and augmentation of magnesium joints with secondary joining methods (e.g. fasteners) are recommended.

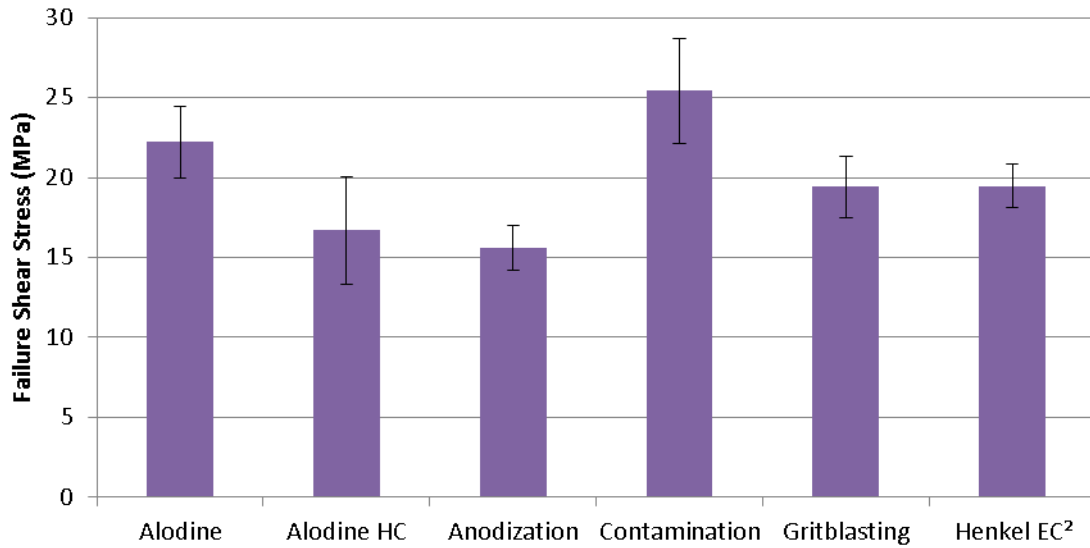


Figure 3-26: Summary of lap shear results (Adhesive: SA9850, Adherends: Aluminum, Day 0)

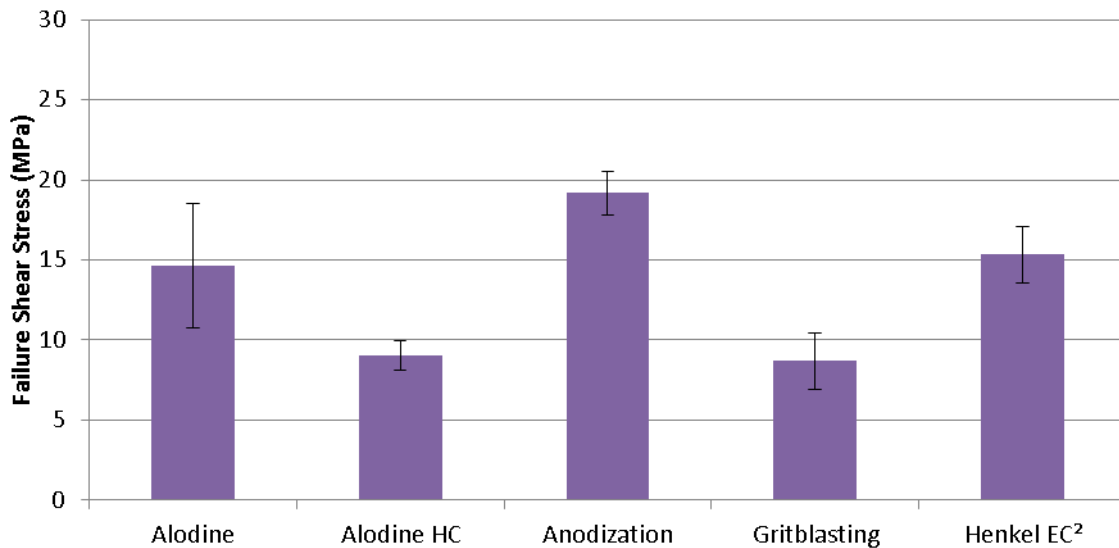


Figure 3-27: Summary of lap shear results (Adhesive: SA9850, Adherends: Magnesium, Day 0)

Lap shear strength numbers acquired from the samples that were bonded with SA9850 were generally higher than those bonded with DP460NS, with few exceptions (e.g gritblasted aluminum). The contaminated samples produced the highest joint strength values, for both aluminum and magnesium.

The samples that were prepared with the Alodine and Alodine HC pretreatments demonstrated reduced strength values between the preliminary results and the final test matrix. This raised concerns about the consistency of these pretreatment methods. An investigation study was done to address consistency

problems between batches of these pretreatments, by repeating the Alodine tests on aluminum 6061-T6 samples, bonded with DP460NS. The results confirmed the existence of significant variation between each batch of Alodine pretreatment that were unexplained by preparation methods alone (Figure 3-28).

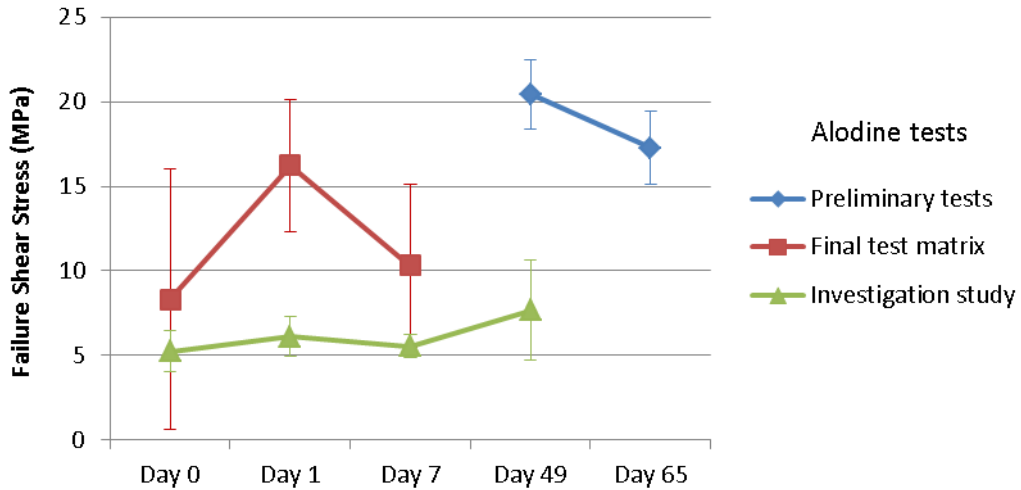


Figure 3-28: Comparison of results between different Alodine treatment batches. Adherend material used was aluminum 6061-T6, bonded with DP460NS

Bonds with contaminated surfaces demonstrated joint strengths that were relatively higher and more consistent than the other pretreatments. This result is counter intuitive as contaminating the adherend surface was done to demonstrate a non-ideal situation for bonding. To investigate this further, samples were created using the ‘open sandwich’ geometry (Figure 3-29).

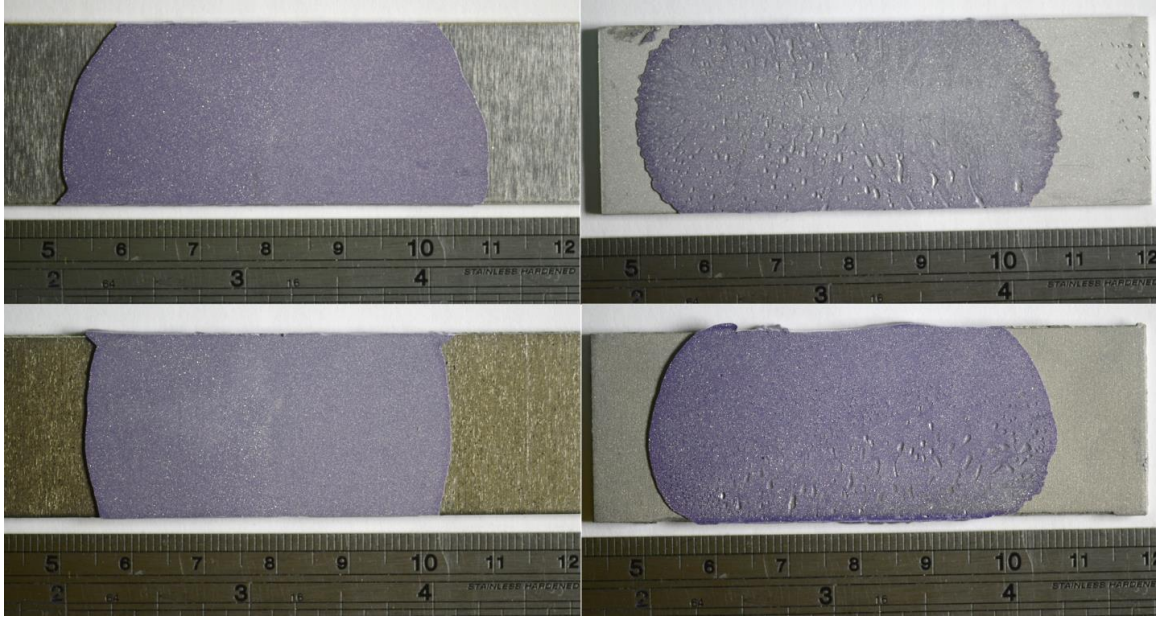


Figure 3-29: Open sandwich samples. (Contaminated aluminum [TL], gritblasted aluminum [TR], gritblasted magnesium [BR], contaminated magnesium [BL])

It can be seen from Figure 3-29 that the samples contaminated with Drylube E1 have visibly less porosity and more uniform coverage compared to the gritblasted samples. It was hypothesized that the lubricant increased the wettability of the adhesive; and subsequently reduced the porosity inside the adhesive joint.

Later in the test program, adherends with alternate pretreatment coatings including Bonderite EC² and Bonderite MgC were received for testing. Unlike the test samples prepared at UW, the Henkel conversion coatings (Bonderite EC² and Bonderite MgC) were provided as large sheets that were cut to size after coating. This situation was not ideal; as the edges of the samples had their coating chipped away during shearing and might introduce irregularity in the acquired data.

From the materials coated with Henkel conversion coatings (aluminum 5182 and magnesium ZEK100), three test samples were made for each combination of adherend and adhesive, totaling 12 samples. On the aluminum 5182 samples that were coated with Bonderite EC², the coating peeled off on all the samples. The strength numbers were lower compared to gritblasted results. The mode of failure was partially cohesive and partially interfacial. Tests conducted with gritblasted (DP460NS) and contaminated (SA9850) surfaces yield better results. It was concluded that the aluminum coating of Bonderite EC² was rather weak and prone to peeling off the base material. On the magnesium ZEK100 samples that were coated with Bonderite MgC, all of the failures were interfacial, signifying a low strength bond between the coating and the adhesive. Typically, the adhesive peeled off the magnesium surface, with a small

amount of cohesive failure area. The magnesium coating of Bonderite MgC stayed on the base material better than the Bonderite EC² coating, but produced poor bond to the adhesive layer.

DP460NS was found to be highly dependent on the surface pretreatment. It was discovered that the only acceptable surface preparation method for aluminum samples was gritblasting (Figure 3-24). No comparable surface preparation method was identified for magnesium samples in the experiments (Figure 3-25).

It was found that the SA9850 adhesive worked relatively well with both aluminum (Figure 3-26) and magnesium (Figure 3-27), and was relatively independent of the surface preparation methods. On both materials, the contaminated samples produced bonds with highest strength numbers. Contaminating the surface also produced lower variability in the data, but made manual application difficult.

3.5. EFFECT OF ENVIRONMENTAL EXPOSURE ON JOINT STRENGTH

This section covers the investigation into the effects of moisture caused by exposure to salt spray bath on single lap shear joints. The test samples were assembled at the University of Waterloo, and the exposure was carried out in a salt-spray chamber with accordance to ASTM standard B117 [144] at McMaster University in Hamilton, Ontario, Canada. The samples were sprayed with 5% salt concentration for durations as presented in Table 3-3. The exposure time was determined in discussions with Kish [145], based on experience of working with similar materials. Prior to and after exposure, the samples were prepared and cleaned following ASTM standard G1 [146].

Material and thickness	Adhesive	Surface prep	Length of Exposure
Aluminum 6061-T6 0.065" [1.59 mm]	DP460NS	Gritblasting	330 hours [13 d 18 h]
	SA9850	Contamination	
Magnesium AZ31b 0.079" [2.00 mm]	DP460NS	Gritblasting	24 hours
	SA9850	Contamination	

Table 3-3: Environmental exposure test matrix

‘Open sandwich’ samples were constructed and exposed to the salt spray for the duration as specified in Table 3-3. Three open sandwich samples were made for each combination as shown in Table 3-3. The detailed results can be found in Appendix G: Open sandwich samples. The adhesive layer experienced no observable defect from the exposure; however corrosion was evident on the exposed surfaces of the adherends.

The selected pretreatments for the single lap shear joints are presented in Table 3-3. Five samples were made of each combination. The results were shown in Figure 3-32 and Figure 3-33. Data acquired from prior experiments were also presented on the left side of each chart for comparison purposes.



Figure 3-30: Open sandwich sample. DP460NS, Magnesium AZ31b, Gritblasting. (Before exposure [T], after exposure of 24 hours [B])

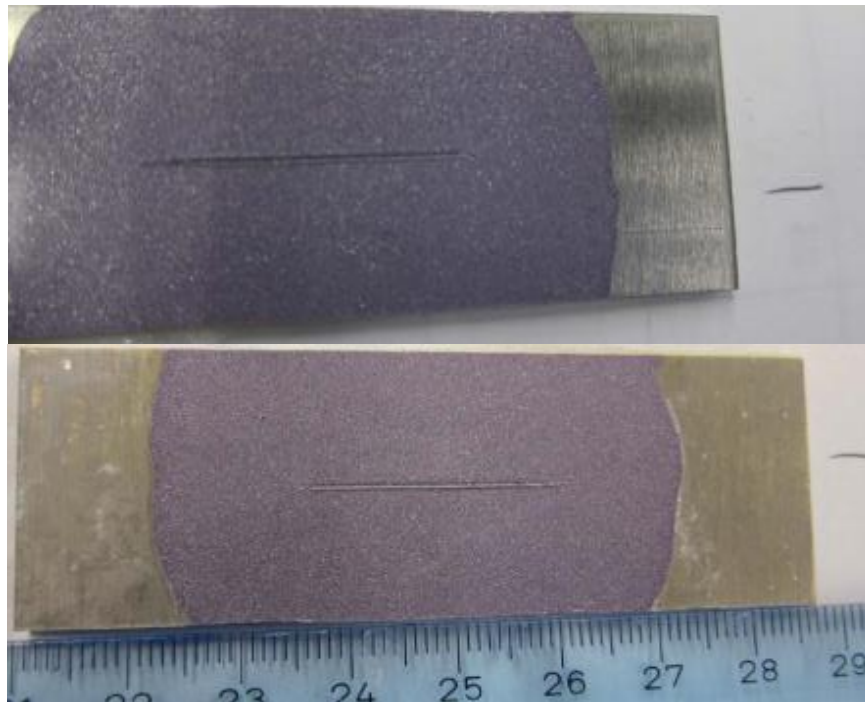


Figure 3-31: Open sandwich sample. SA9850, Aluminum 6061-T6, Contamination. (Before exposure [T], after exposure of 330 hours [B])

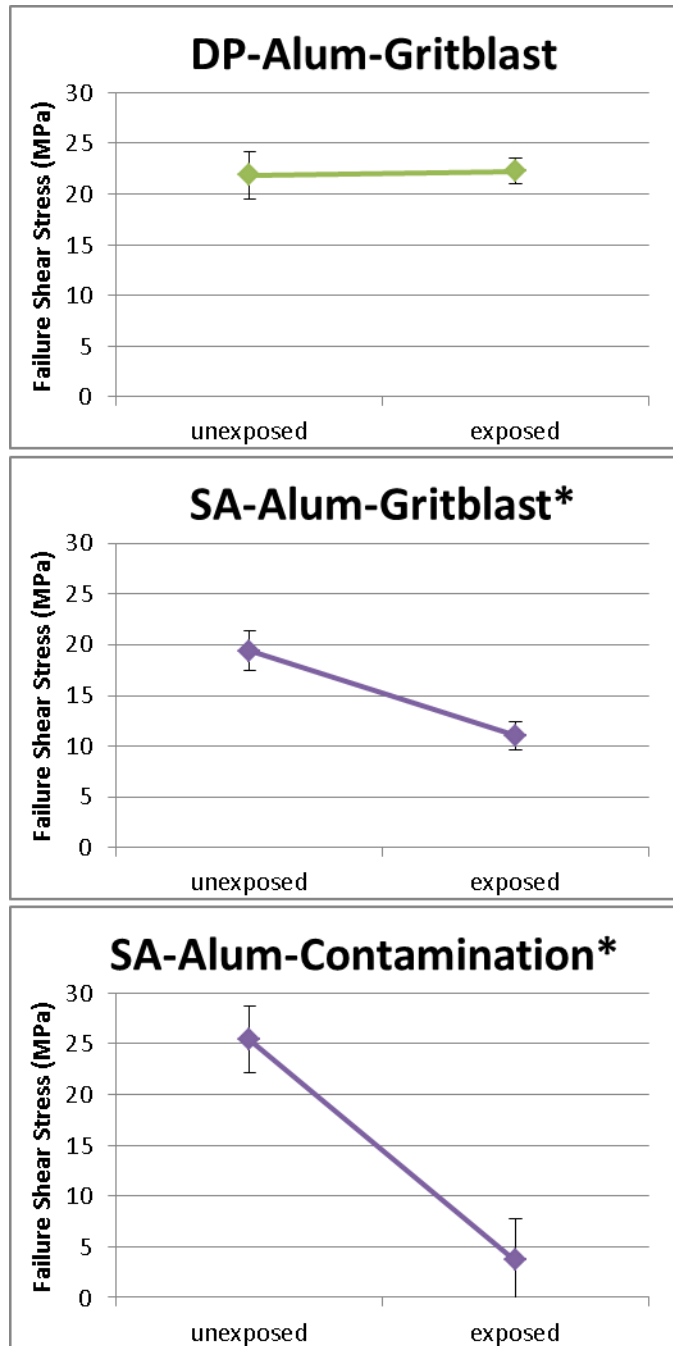


Figure 3-32: Aluminum 6061-T6 exposure test results. Statistically significant reduction of joint strength marked with an asterisk (*) next to its respective title.

The aluminum samples were exposed for 330 hours. Samples that were bonded with SA9850 showed statistically significant loss of strength. Two of the contaminated samples fractured during handling. It can be concluded that the SA9850 is hydrophilic, and increased moisture would decrease its strength. Samples constructed with DP460NS did not show a visible drop in joint strength.

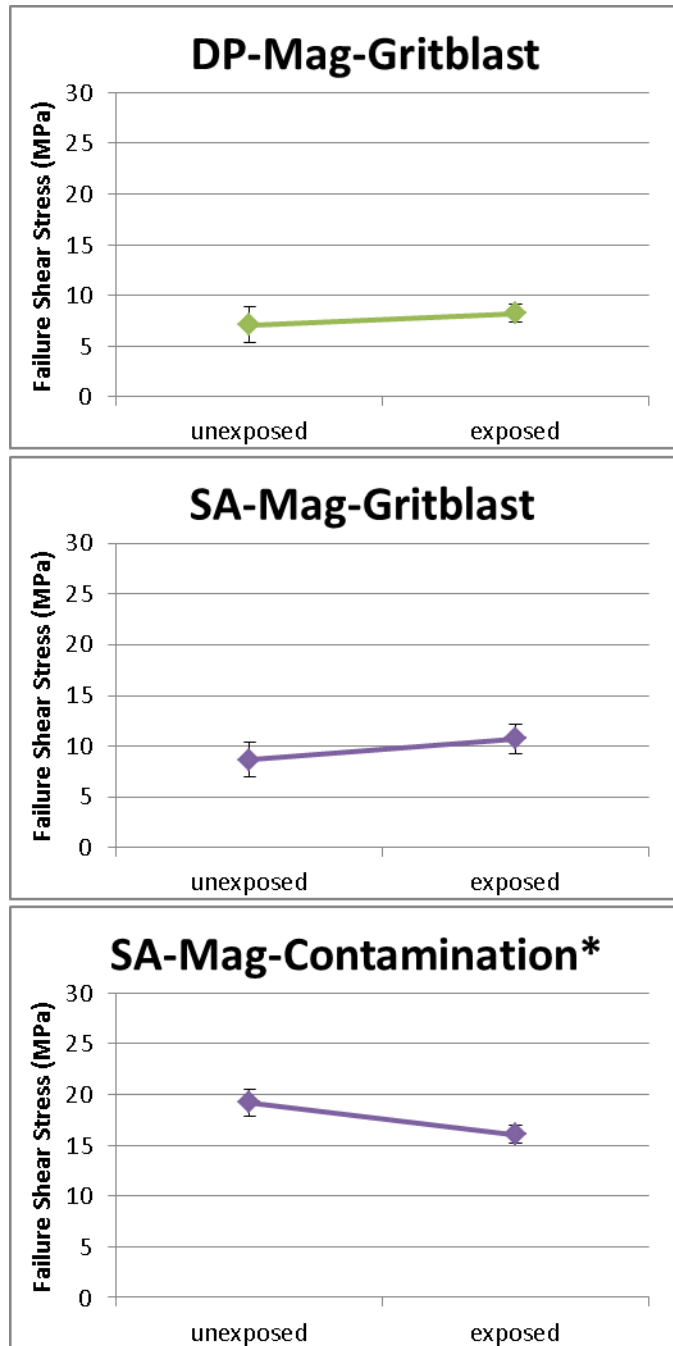


Figure 3-33: Magnesium AZ31b exposure test results. Statistically significant reduction of joint strength marked with an asterisk (*) next to its respective title.

The magnesium samples were exposed to the salt-spray bath for 24 hours. Similar to previous results, a noticeable drop in joint strength on samples assembled with SA9850 was detected, with contaminated samples reporting a more significant decrease compared to the gritblasted samples. Samples bonded with DP460NS did not show any statistically significant decrease in strength.

3.6. NUMERICAL SIMULATION

A commercial FEA software (LS-DYNA) was used to model the joint response and failure. The material model used in this study was developed by analyzing experiments conducted using gritblasted steel adherends. The results of numerical simulation were compared to the configurations which utilized gritblasted aluminum adherends.

Input decks for the numerical simulation for use with LS-DYNA can be found in Appendix D: LS-DYNA Cards.

3.6.1. GEOMETRY AND BOUNDARY CONDITIONS

The quasi-static loading conditions of the lap shear tests were replicated using LS-DYNA numerical code. The adhesive joint was modelled as a series of elements, with common nodes shared with the adherends. Cohesive elements were used to represent the adhesive bond between the adherends. The cohesive formulation requires one layer of elements across the thickness of the adhesive layer to represent the bond such that the elements were 0.178 mm x 0.5 mm x 0.5 mm for 0.5 mm adherend elements. To reduce computational time, symmetrical boundary conditions were applied along the length of the sample XY-plane.

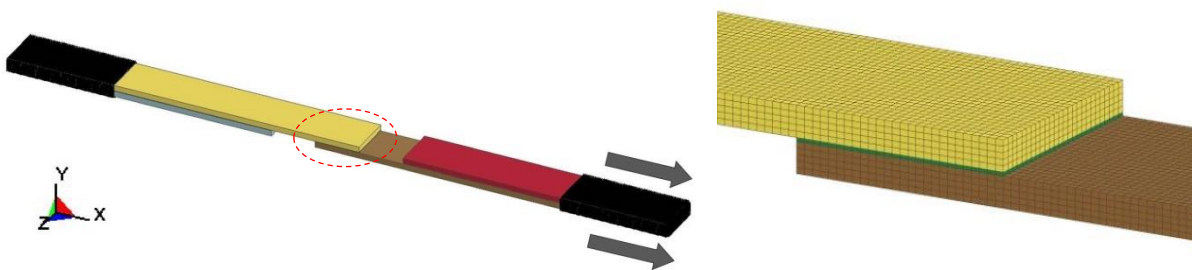


Figure 3-34: Lap shear mesh density (full view [L], zoomed in on the overlap joint [R])

To simulate the movement, a constant velocity was applied to the nodes on one end of the model, while the other end was restricted from moving. The nodes were selected to approximate the position of the test machine grips used during the experiments. Figure 3-34 shows these nodes as highlighted in black. To match the deformation rate of the experiments, the nodal velocity was set at 0.178 mm/s. An implicit formulation was utilized to minimize computational time for this quasi-static test.

3.6.2. MATERIAL MODEL

It was confirmed experimentally that some of the adherends underwent significant plastic deformation during loading, especially the combinations that exhibit high strength before failure. The material model

selected to represent the adherends was a conventional incremental plasticity material model. The material model does not an equation of state; it uses separate formulation to address elastic and plastic deformations [147]. The input properties for the aluminum adherends are presented in Figure 3-35.

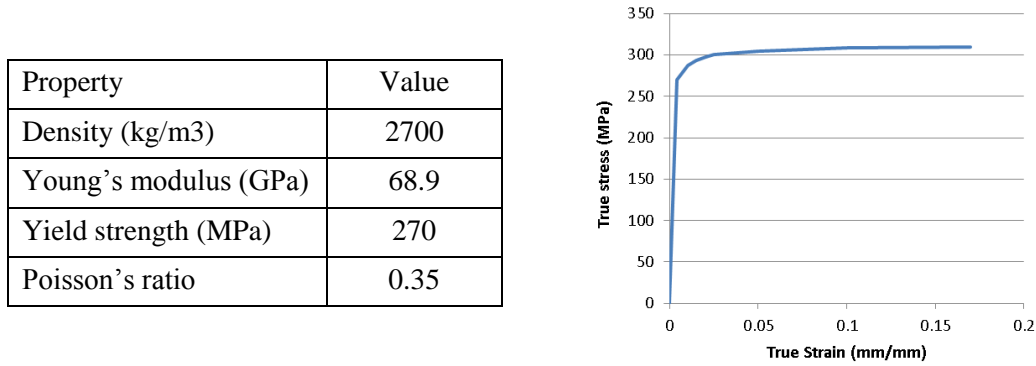


Figure 3-35: Mechanical properties of aluminum 6061-T6 adherends as imported into numerical simulation

Work by Trimiño and Cronin [49] provided a baseline material model for DP460NS, suitable for direct implementation into LS-DYNA cohesive material model. The input variables are presented in Figure 3-36 and Figure 3-37. These values were acquired from a series of tests [49], focusing on quantifying fracture behaviour of the material using double cantilever beam geometry and thick adherend lap shear. The relevant material input deck can be found in Appendix D: LS-DYNA Cards.

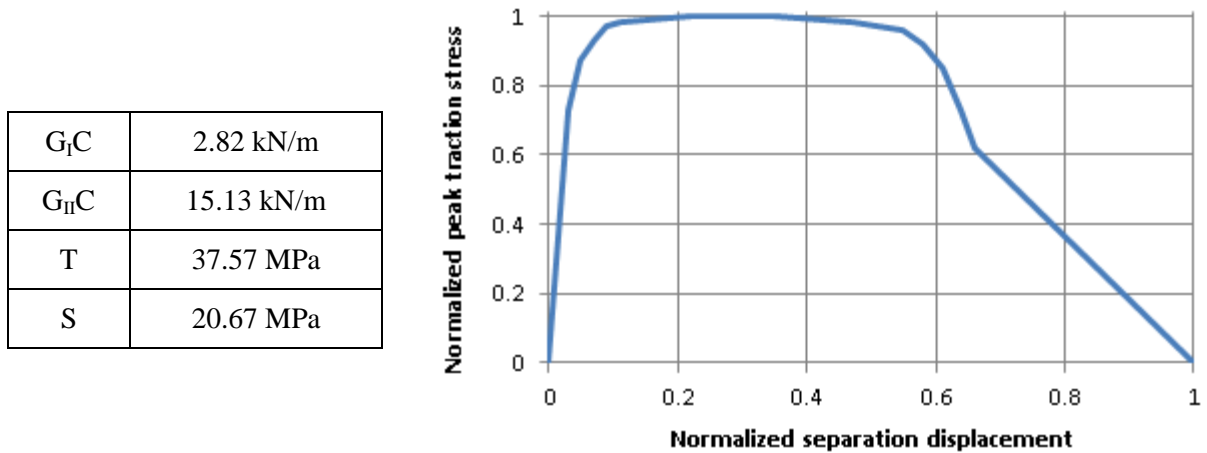


Figure 3-36 – DP460NS cohesive traction-separation properties

G_{IC}	2.97 kN/m
G_{IIC}	8.92 kN/m
T	28.19 MPa
S	24.9 MPa

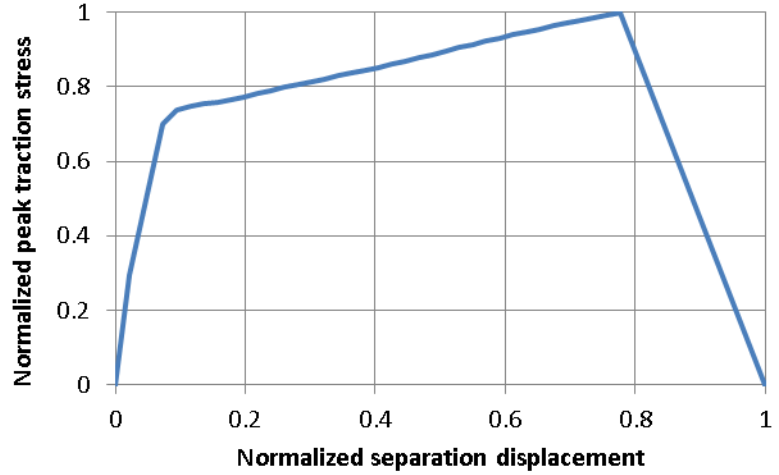


Figure 3-37 – SA9850 cohesive traction-separation properties

The shape of the traction-separation curves used in this study was trapezoidal [148], which is well suited for ductile materials as the large amount of plastic deformation can be represented with the plateau [149]. This shape was also observed experimentally in quasi-static thick adherend lap shear tests (Figure 2-3).

3.6.3. RESULTS

The numerical simulations were run up to the point of failure as determined by an abrupt drop in load for the displacement-controlled simulation. Stress was distributed non-linearly in the adhesive bond. Shear stresses develop at the joint edges (Figure 3-38) before spreading to the center of the adhesive (Figure 3-39). The failure of the adhesive joint occurred uniformly on all the elements, in contrast to experimental results where failure initiated at the edges of the joint. This behaviour persisted with higher mesh density and output plotting frequency. The stress distribution across the length of the adhesive joint at a crosshead displacement of 0.09 mm is compared with analytical results using equations developed by Goland and Reissner [61], and Hart-Smith [150] (Figure 3-40). Details of the analytical solution equations can be found in Appendix E: Lap Shear Test MathCAD Solution.

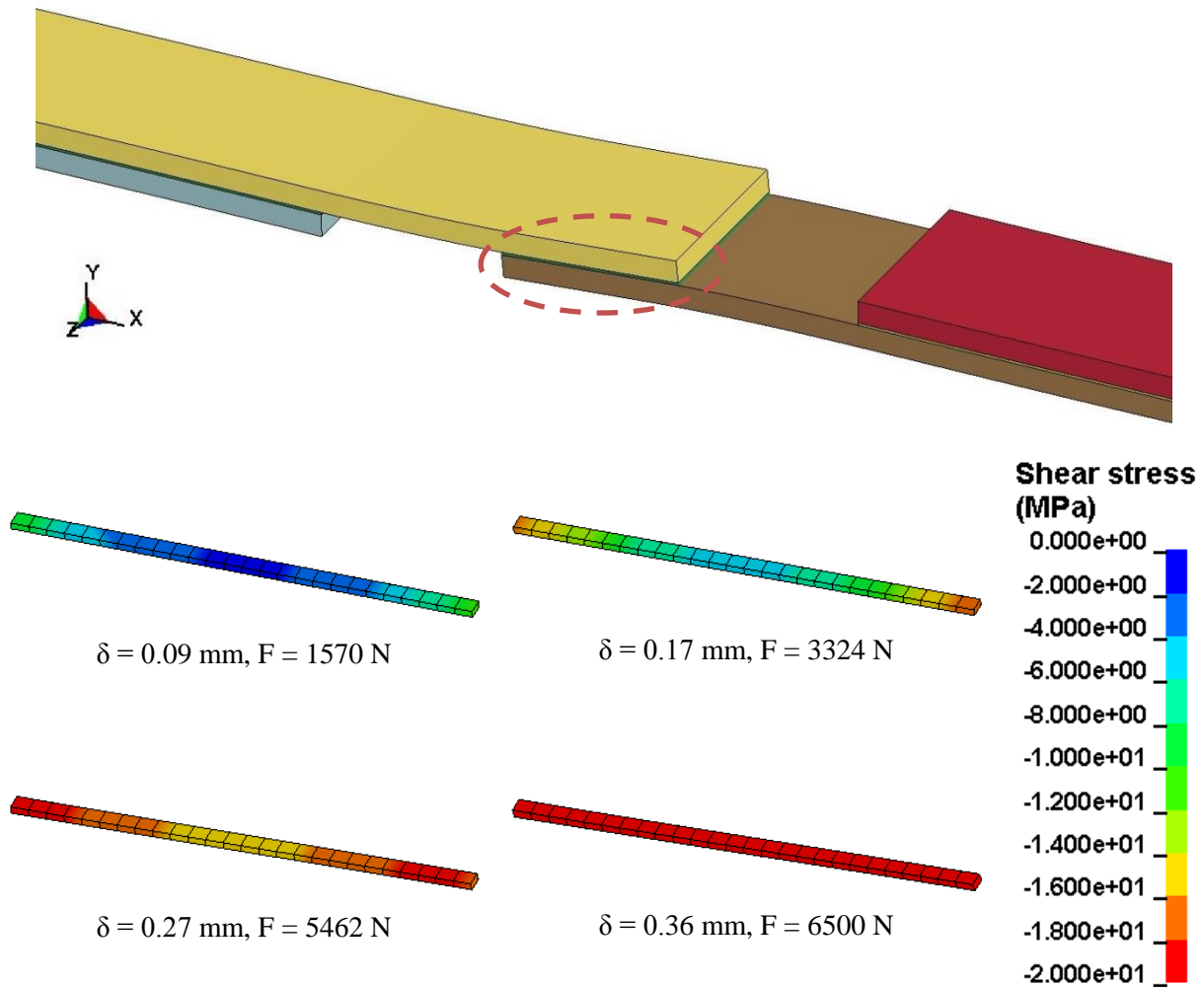


Figure 3-38: Stress distribution across the adhesive joint. Simulation depicted is DP460NS

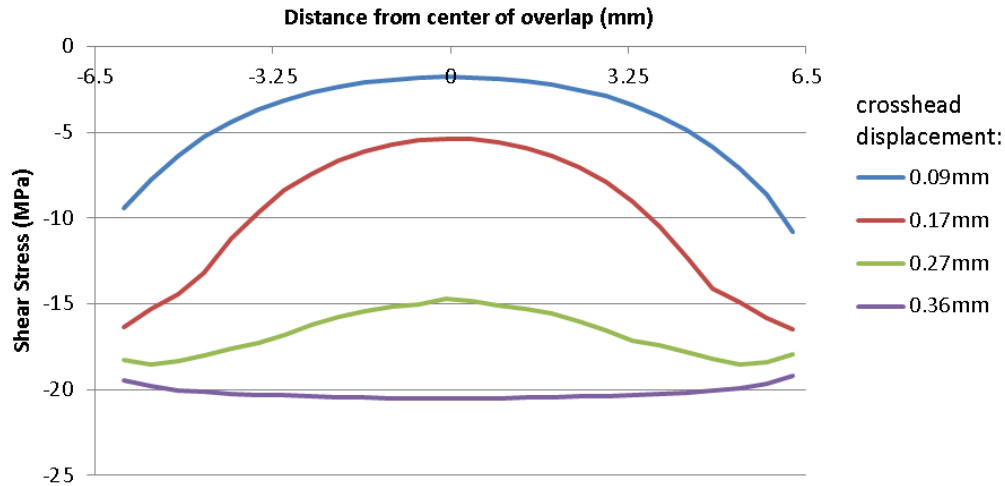


Figure 3-39: Shear stress distribution across the length of adhesive joint at various times

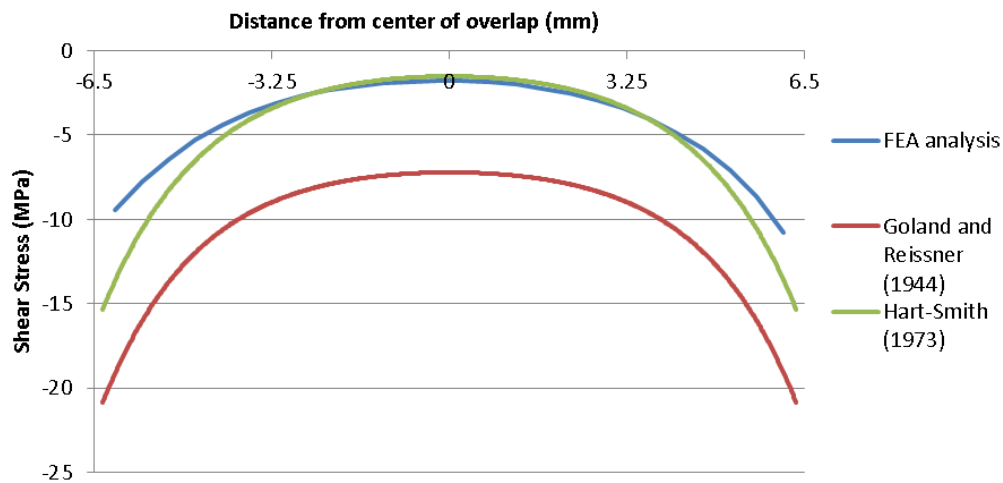


Figure 3-40: Shear stress distribution across the length of the adhesive joint, at outer edge of joint, in comparison with analytical results. Crosshead displacement is 0.09mm.

Solution proposed by Goland and Reissner [61] assumed infinitely thin adhesive layer, and considered its effect on bending moment factor to be negligible. Hart-Smith [150] improved on this by including adhesive layer thickness in the bending moment factor calculation. It is apparent in Figure 3-40 that the solution developed by Hart-Smith predicted the distribution of shear stress more closely compared to the one developed by Goland and Reissner. However, neither of the analytical solutions considered the effect of plasticity of the adhesive in their solutions. In a single lap shear configuration, adhesive joints experiences higher strains near the edges (Figure 3-41), which would result in lower shear stress compared to prediction by elastic formulations. Also, the element size of the adhesive joint in the

numerical simulation was not fine enough to capture large variations of stress near the joint edges. These two factors can explain the difference between the solutions acquired by FEA method and the one developed by Hart-Smith.

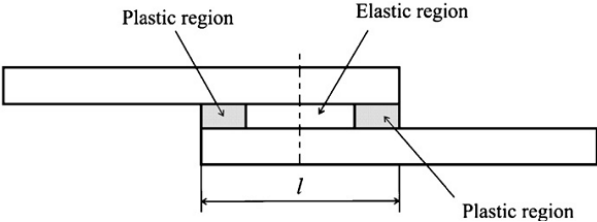


Figure 3-41: Regions of strain along a single lap shear adhesive joint (taken from Da Silva et al. [64])

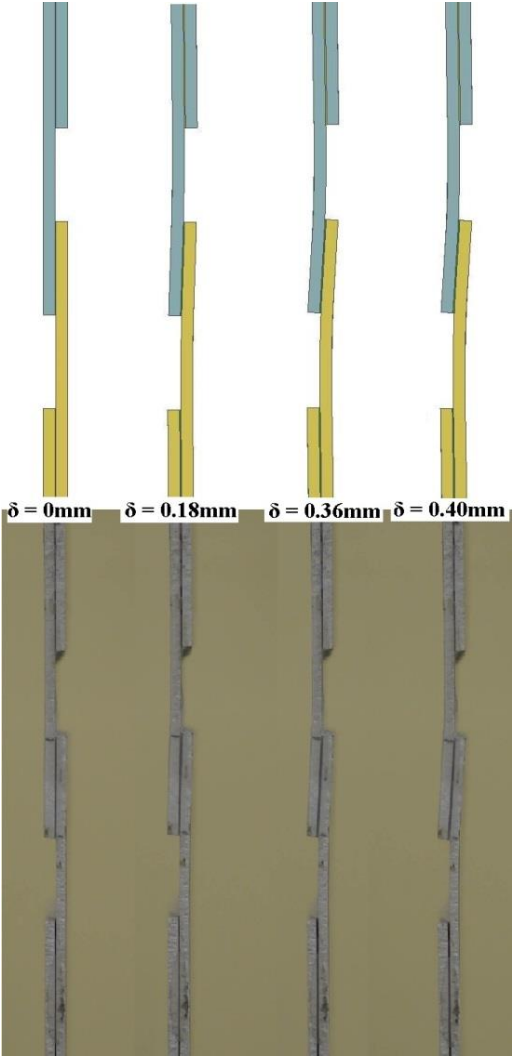


Figure 3-42: Test progression, experiment [T] versus simulation [B]. Simulation depicted is DP460NS with aluminum 6061-T6 adherends.

The amount of bending experienced by the adherends, while not directly measured, visually appears to be represented well in the simulation (Figure 3-42). For a proper comparison to be made, the displacement values recorded during the experiments were corrected for test apparatus compliance as discussed in chapter 3.3. Compliance corrected results are shown in Figure 3-43.

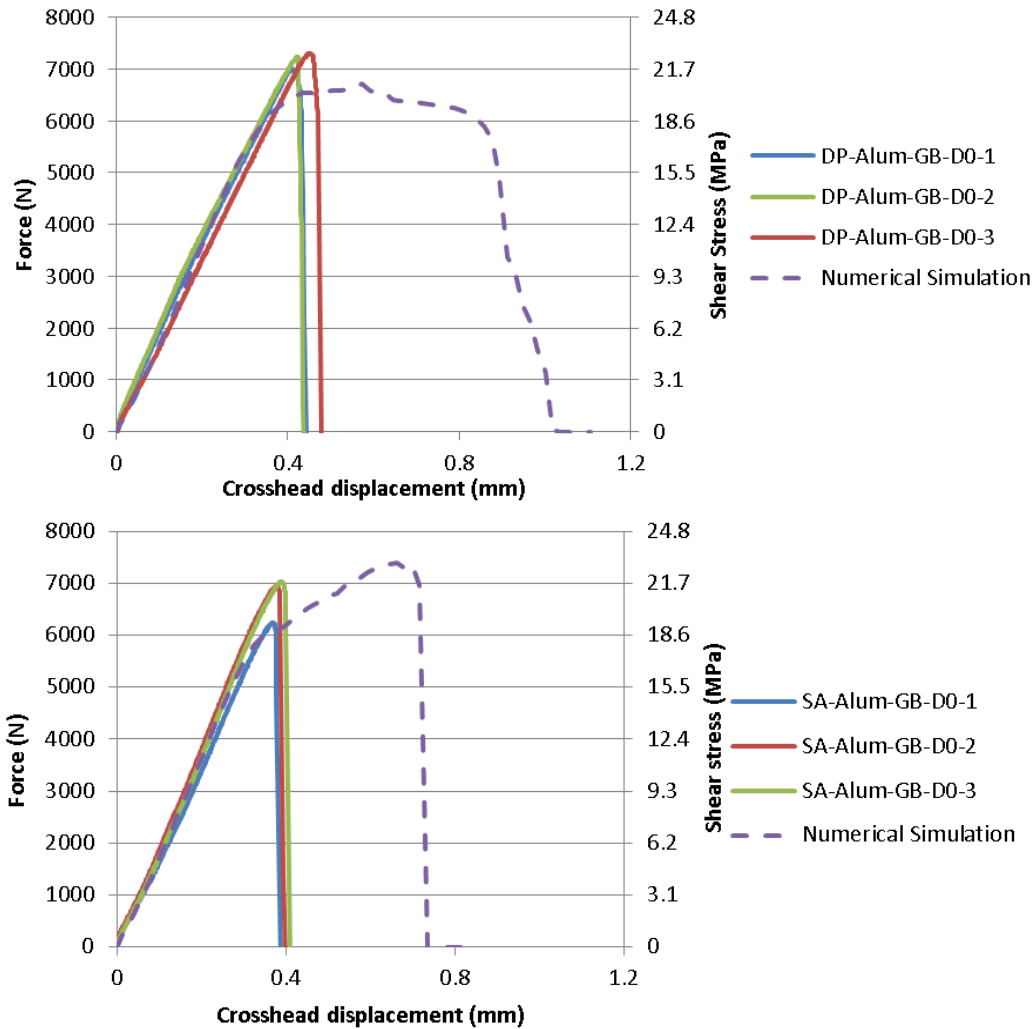


Figure 3-43: Force versus crosshead displacement, simulation versus experimental results (DP460NS [T], SA9850 [B])

Adhesive	Loading slope (N/mm)		
	experimental		numerical simulation
	max	min	
DP460NS	19144.1	16594.8	18106.2
SA9850	19110.1	17054.9	18216.5

Table 3-4: Loading slopes of lap shear tests

The loading force ramp-up predicted for both simulations are within the range acquired from experimental results (Table 3-4). However, the displacement to failure was over-predicted by a magnitude of approximately two (Figure 3-43). The most directly relevant variable regarding strain to failure in the material model is supplied in the form of critical energy release rate (G_{IC} and G_{IIC}). Figure 3-44 shows the results of SA9850 numerical simulation that were run with other G_{IIC} values while other variables were kept equal.

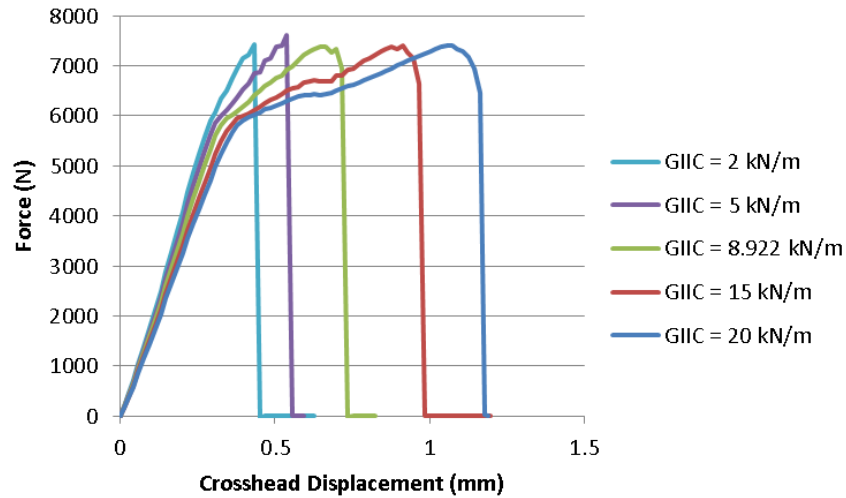


Figure 3-44: Results of SA9850 lap shear test numerical simulation with varying values of G_{IIC}

Within this thesis, the G_{IIC} values were acquired from thick adherend lap shear tests with bond thickness of 1mm, as described in chapter 3.6.2. There was a fundamental difference of thickness of adhesive bonds in these two tests, and as multiple studies have shown [151-155], this significantly affects the acquired values of G_{IC} and G_{IIC} .

Chai [152] conducted several tests to acquire G_{IIC} values of adhesive bonds using end-notched-flexure and napkin ring shear specimens. His study revealed that the various bond thicknesses affect the G_{IIC} values differently with brittle and ductile adhesives. It was found that for brittle adhesives, much of the variation in G_{IIC} values occur in the excessively thin range of bondline thickness (10 μm to 60 μm). For ductile adhesives, the variations exist in the range of thicknesses of common epoxy adhesive bond thicknesses (5 μm to > 600 μm) (Figure 3-45). These conclusions were supported by other researchers such as Daghyani et al. [154], using compact pure shear (CPS) specimens with ductile adhesives and Da Silva et al. [155], using edge notch fracture (ENF) specimens with ductile and brittle adhesives (Figure 3-46).

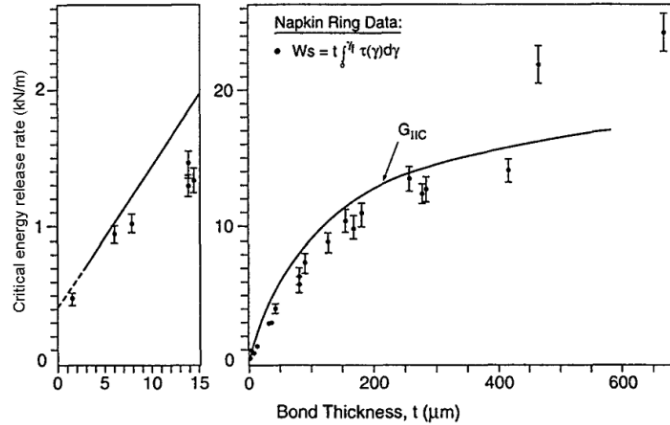


Figure 3-45: Variation of mode II energy release rate obtained by napkin ring tests with ductile adhesive (adapted from Chai [152])

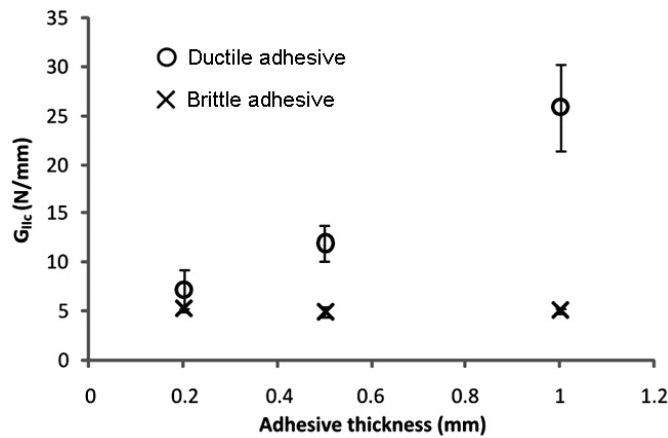


Figure 3-46: Variation of mode II energy release rate obtained by ENF tests (adapted from Da Silva et al. [155])

Both DP460NS and SA9850 are ductile adhesives. The aforementioned studies support the hypothesis that the G_{IIc} values for thinner bonds are significantly less compared to those measured with thicker bondlines. The overprediction of strain to failure shown in Figure 3-43 supports this finding.

3.6.4. DISCUSSION AND RECOMMENDATIONS

The use of single layer cohesive material model on a single lap shear test was successful; however a challenge was noted in the over-prediction of the strain to failure. The distribution of stress inside the adhesive joint was predicted by FEA methods to be highest at the edges of the overlap length, as was consistent with classical analysis of lap shear studies [63]. This draws the conclusion that lap shear failures initiate at the edges and propagate into the joint. This is an important feature to consider when

designing adhesive joints. The easiest method to take advantage of this knowledge is the inclusion of spew fillet on the edges of adhesive joint.

The predicted response for both adhesives was observed to be within the range of those observed at the experimental results. The failure strain was consistently over-predicted for both adhesives, and was attributed to the value of $G_{II}C$. One of the factors that significantly contribute to this discrepancy is the bondline thickness, as it has been shown by other studies to have a significant effect on the $G_{II}C$ value. It is recommended that shear strength data for the adhesives material parameters to be improved using data acquired from a test of which the bond thickness is equal to 0.178 mm.

CHAPTER 4

PIN AND COLLAR TEST

4.1. BACKGROUND

The pin and collar test was designed to introduce pure shear stress in an adhesive joint. The joint was created by assembling together a round pin and a hollow collar with a concentric ring of adhesive joining them together.

For most structural adhesives, the preferable mode of loading is shear and compression, as adhesive joints are typically weak in tension and peel [51]. It is also beneficial to design a joint where the distribution of stress and strain is as uniform as possible throughout the bond, minimizing the possibility of stress concentrations.

The shortcomings of the lap shear test as a measurement of adhesive shear response were discussed in the previous chapter. The bending effect that is present in lap shear tests can be minimized by increasing the adherend stiffness either by using materials with higher modulus of elasticity, making the pieces thicker, or by using the double lap shear configuration. Taking this into consideration, the pin and collar test is still superior to the lap shear test to acquire adhesive shear response as it minimizes the bending effect significantly.

The Short Beam Shear Test [156] is an ASTM standard test used to obtain the interlaminar shear strength of composite materials. A bulk sample of the material is loaded to failure in a three-point bending configuration (Figure 4-1). In elastic beam theory, the midplane of the beam would experience pure shear stress and fail when its shear strength is exceeded. This would allow one to acquire the shear strength of the adhesive in question.

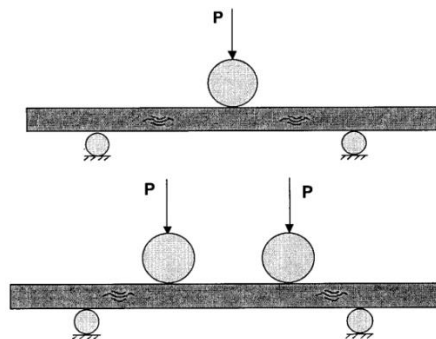


Figure 4-1: Short beam shear tests (3-point bending [T], 4-point bending [B]) (adapted from Abali et al. [157])

Due to the length of the beam, stress profile near its loading point and two supports are complex and sometimes cause midsurface buckling prior to the expected shear failure. Browning et al. [158] proposed to replace this test by using four-point bending which, in their experiments, produced interlaminar shear failure more consistently. ASTM standard D5379 [159] also uses a four point bending principle and proposed adding v-shaped notches, more commonly called the Iosipescu shear specimen, to improve the uniformity of shear stress distribution within its gage section.

A transformation to the Short Beam Shear Test from bulk material testing to an adhesive joint test was proposed by Moussiaux et al. [160]. It is based on bending of a beam specimen made by bonding together two metal plates with the adhesive (Figure 4-2). During three-point bending, the adhesive which is located in the center line of the specimen would be deformed with shear load and bending moment. With a sufficiently thin adhesive thickness, this bending moment can be considered negligible. The shear modulus of the adhesive can be deduced after an appropriate analysis of the amount of bending experienced by the specimen. A typical improvement of this geometry is the addition of a notch at one edge of the adhesive joint, to instigate crack propagation and to enable the characterization of the adhesive from a fracture mechanics standpoint.

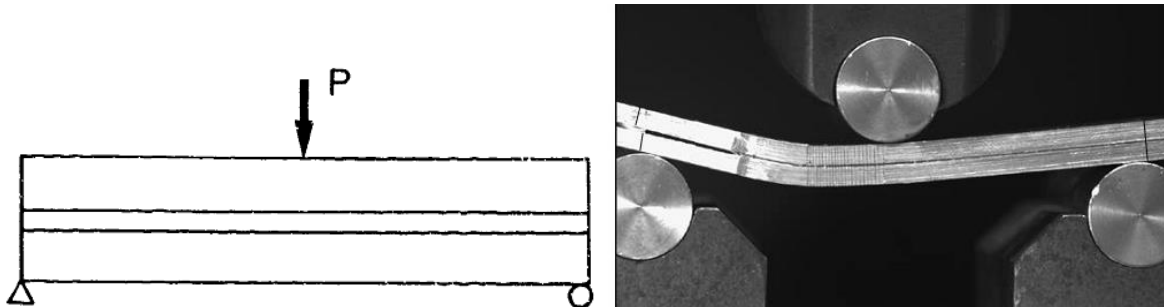


Figure 4-2: Single edge notched beam (schematics [L], actual [R]) (taken from Yang et al. [161])

The relative ease of manufacturing of this geometry makes it an attractive option for acquiring adhesive shear data. The adhesive bond is also visually exposed, which enables more detailed study into the mechanism of damage initiation and propagation, as was done by Chai [152]. However, it is challenging to adapt this test into higher deformation rates test apparatus such as SPHB, due to fixturing and strain wave transmission issues.

The napkin ring test (ASTM E229, withdrawn on 2003) is another test proposed to ensure a pure state of shear stress in the adhesive layer. It involves two tubes that are aligned, bonded together and loaded with a torsion torque until the adhesive fails. Specimen production is expensive and difficult, and the required equipment is intricate. Creating torque and measuring small angle of twist is a considerably bigger

challenge compared to creating compressive force and measuring linear deformation. However, some researchers have been successful in using this geometry for shear characterization studies using various bond thicknesses [162], materials [163] and deformation rates [164].

4.2. METHODS

The collars were cut from a cold-rolled round solid steel rod, 1 inch in diameter (Figure 4-3). The rod was machined to have an inner diameter of 13 mm by means of a reaming tool. In combination with the pin diameter of 12.7 mm, this resulted in adhesive bond thickness of 0.15 mm [150 μm].

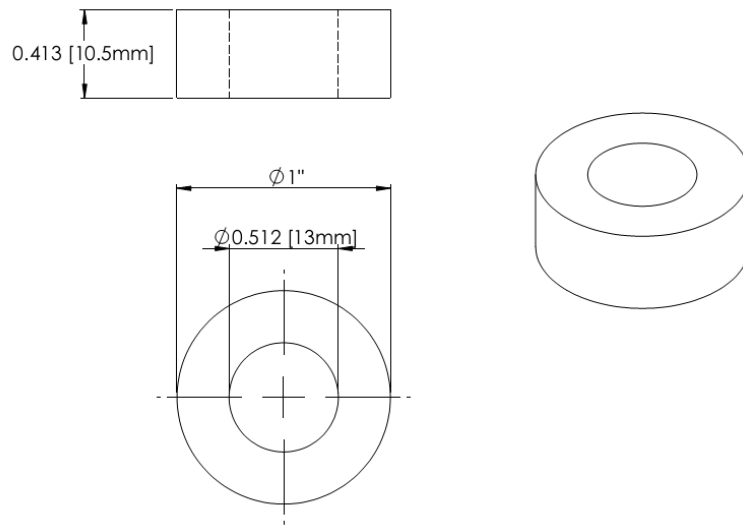


Figure 4-3: Dimensions of the collar substrate

The pins were manufactured from a cold-rolled round solid steel rod, half inch in diameter (Figure 4-4). The pieces were cut into 2 inch lengths each and deburred.

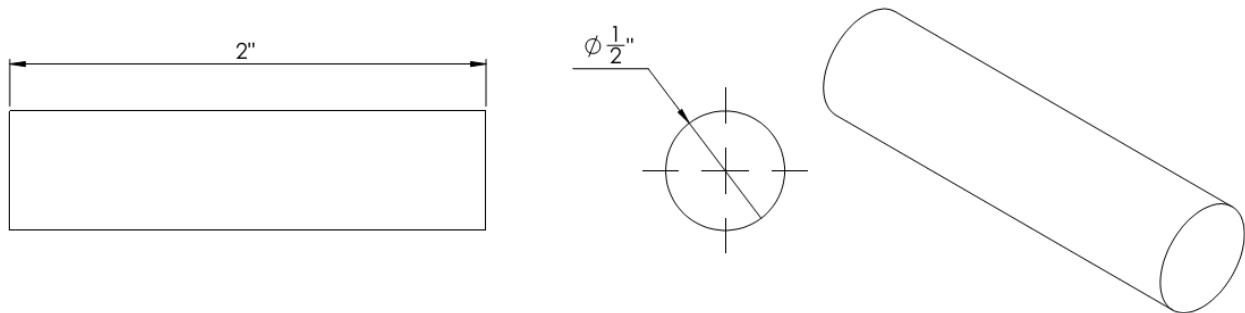


Figure 4-4: Dimensions of the pin substrate

The surfaces of the pin and the collar were gritblasted with commercial gritblasting equipment to an approximate roughness of 2 μm . The samples were cleaned with Methyl-Ethyl-Ketone immediately before the adhesive was applied. The same oven curing cycle developed for lap shear, as described in chapter 3.2 [142], was used for curing the pin and collar samples.

The pin and collar sections were placed in an aluminum fixture to maintain a consistent adhesive thickness around the pin, and then go through a curing process. The fixture was machined with tight tolerances ($\pm 0.001''$) to hold the pin and collar specimens in place during curing cycle. The excess adhesive was removed with a lathe to ensure consistency between all samples, Figure 4-5 shows the sample before and after this process. The machining process introduced a radius of 0.5 mm at the adhesive bonds, which made the effect of stress concentrations consistent. This process also causes a minor decrease of the diameter and length of the pin and collar sections.



Figure 4-5: Pin and collar sample specimen (before cleaning [L], after machining with lathe [R])

4.2.1. TEST MATRIX

The purpose of this study was to observe the adhesive response to different deformation rates in pure mode II. The parameters being observed in this study are listed as follows:

Adhesives	DP460NS
	SA9850
Nominal shear rates	0.1 /s [0.015 mm/s]
	1 /s [0.15 mm/s]
	10 /s [1.5 mm/s]
	100 /s [15 mm/s]

Table 4-1: Pin and collar test variables

The variables result in 8 different configurations to test. A minimum of three samples were created for each configuration.

4.2.2. EQUIPMENT

The same test frame used for the lap shear test was used for the pin and collar experiments. Although typically useful only for quasi-static tests, the relatively thin thickness (0.15 mm) of the adhesive layer translates to low crosshead velocity numbers at high shear rates. A load cell of $\pm 20,000$ lb capacity and actuator crosshead displacement measurement system was present for this experiment.

Long columns of solid steel were fastened into the top and bottom parts of the frame. A fixture was placed on the moving actuator piece to push the collar by its bottom plane, while the top plate stopped the pin from moving (Figure 4-6). The actuator required an average of one second of initial acceleration to ramp up to the constant desired velocity; therefore some distance was left between the specimens with the top platen to accommodate ramp-up acceleration.

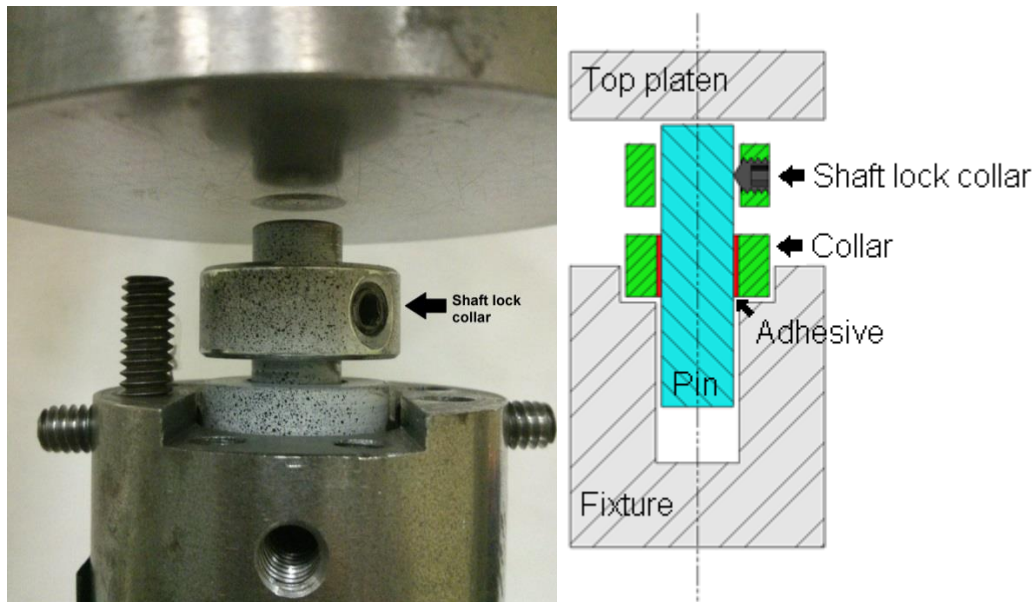


Figure 4-6: Pin and collar test rig [L], Schematic [R]

4.2.3. DISPLACEMENT MEASUREMENT

Measuring deformation of the adhesive was the main challenge of this type of test. Geometry of the pin and collar tests prevented direct observation of the bond. Previous attempts at providing displacement data with this test, such as those done by Yokoyama and Shimizu [73], was done by calculating the velocity of the test device actuators/impact bars instead of direct measurement. The results of their

research came with several characteristics that are atypical; such as excessively high shear strain to failure and excessively low shear modulus. Both of these support the idea that the traditional method of calculating displacements by actuator/impact bar velocity over-predicted the amount of actual deformation experienced by the adhesive.

The amount of displacement to be measured was on the order of the thickness of the adhesive bond of 0.15 mm. Four different displacement measurement devices were assessed to analyze the data:

1. Test frame hydraulic actuator travel distance (crosshead displacement)
2. Spring mounted LVDT (Linear Variable Differential Transformer) system, manufactured by Omega Engineering Inc.
3. Clip-on gage for fracture mechanics studies, manufactured by Epsilon Tech.
4. Video image analysis with *Tracker* [143].

Figure 4-7, Figure 4-8, and Figure 4-9 shows measurements from the actuator, the LVDT system, and the clip gauge during an idle period of one second. In an idle situation, the measurements were expected to be constant. Table 4-2 shows the accuracy comparison between the systems.

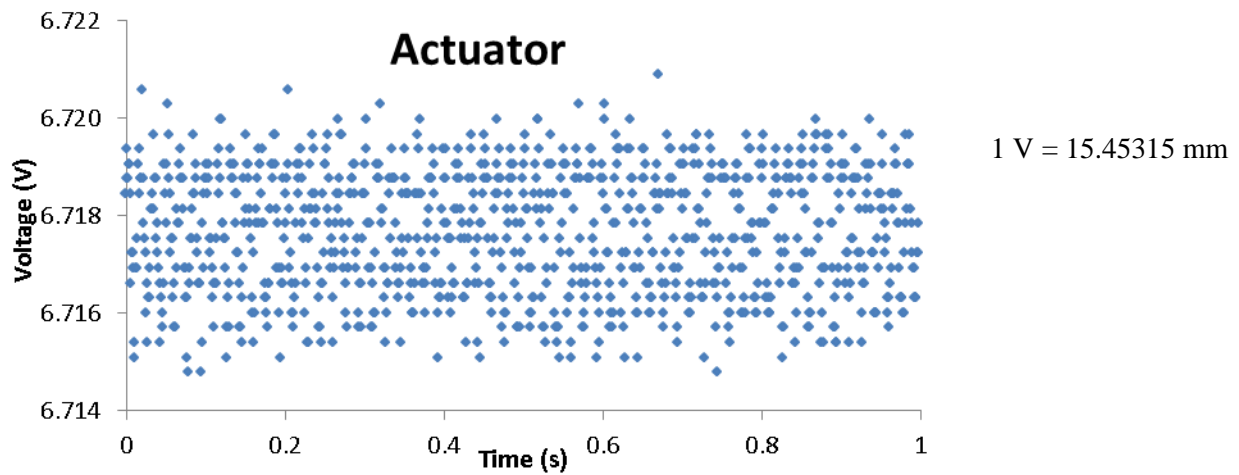


Figure 4-7: Actuator voltage reading during idle period of one second

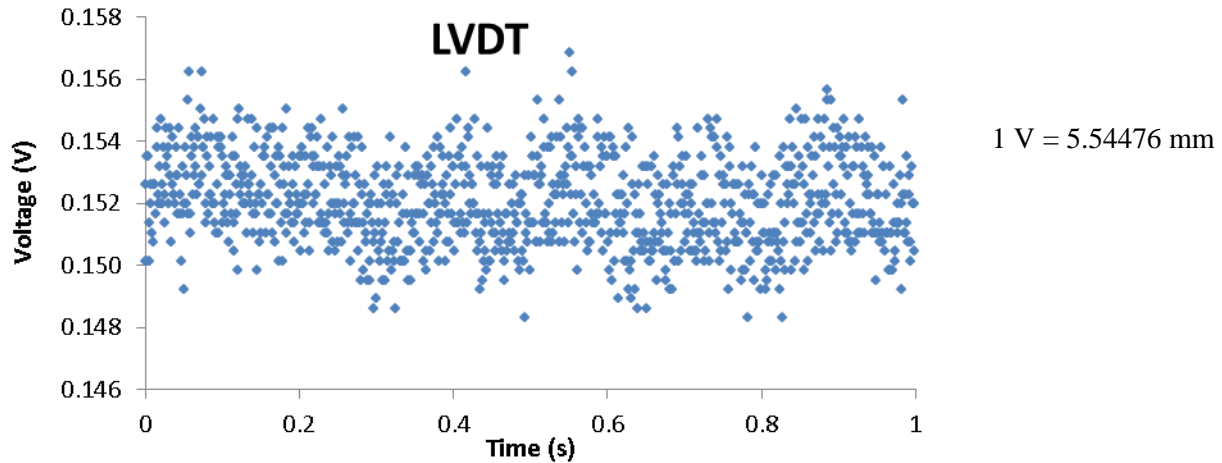


Figure 4-8: LVDT voltage reading during idle period of one second

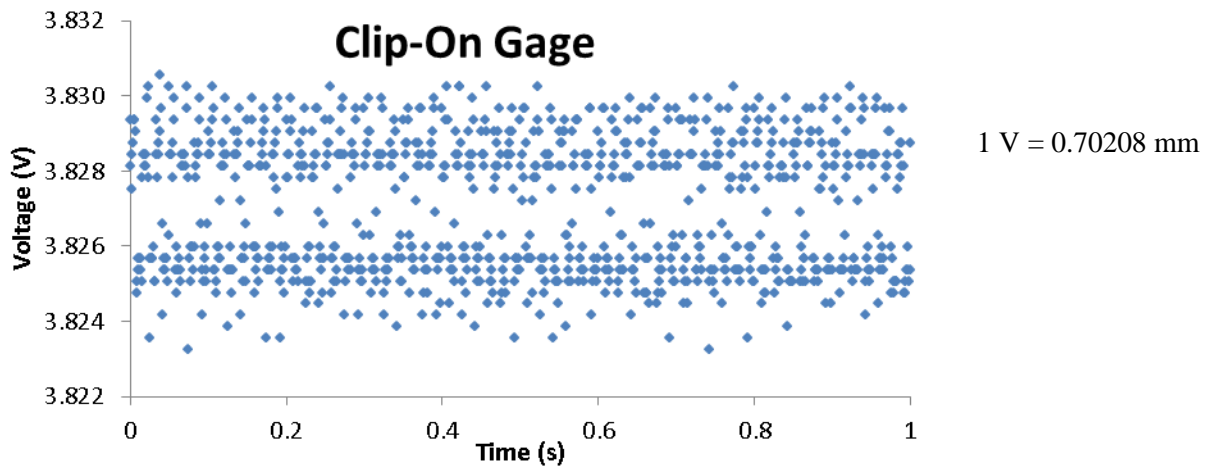


Figure 4-9: Clip-on gauge voltage reading during idle period of one second

The adhesive thickness was $150\ \mu\text{m}$. From data gathered using the thick adherend lap shear tests, it was estimated that the elastic region during shear loading would lie between 0 to $5\ \mu\text{m}$. The actuator, LVDT, and the clip gauge were considered incapable to capture the displacements to a reasonable accuracy. For this reason, the video image analysis approach was developed.

The software used for acquiring displacement data is *Tracker* [143], developed by Doug Brown, used under GNU general public license. The software works by identifying a template window in the first frame to be matched in subsequent frames by means of cross-correlation. The accuracy of the result is inherently dependent on the quality of the video image and the algorithm used by the software.

As a validation study, the software was compared with an established Digital Image Corellation (DIC) software *VIC-2D* [165]. A sample was moved under a constant velocity and was analyzed with both

methods. The results are shown in Figure 4-10. Linear fit were done for both set of curves, and the slopes were confirmed to be within 0.1% of each other. This confirms that *Tracker* worked equally as well as an established DIC software.

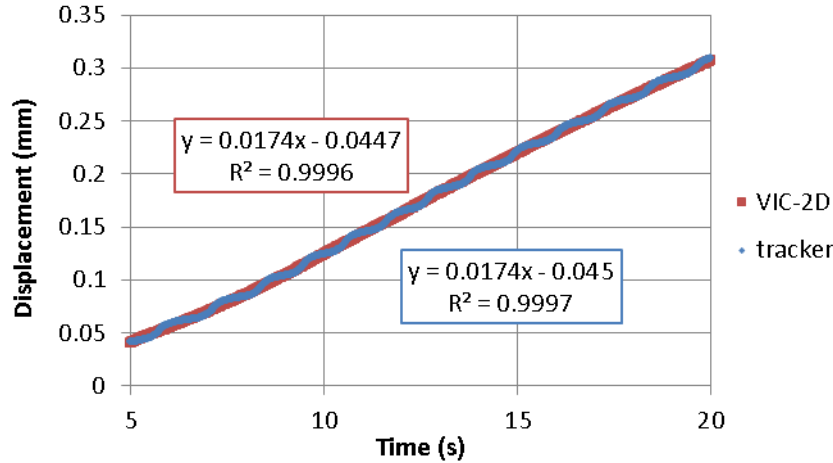


Figure 4-10: Comparison of results between *Tracker* and *VIC-2D*

There were several challenges in adapting the video image analysis approach to pin and collar tests. The surfaces of the pin and collar sample were curved and have different diameters, which made it difficult to acquire a focal length setting which worked for all surfaces. There was also a concern with parallax effect, which occurs when the objects being viewed are at different distances from the camera. To minimize these errors, a shaft lock collar of the same diameter as the collar (25.4 mm) was attached to the pin and the focus was aimed at the edge of the objects. The camera was also positioned in such a way so that the objects being tracked were all equidistant from the camera.

Steps were taken to improve the accuracy of the software, by means of painting distinctive speckled pattern on the pin and collar surfaces. This enabled the software to distinguish between patterns in a more consistent manner. Also, during tracking of video images, a relatively large template size was defined to reduce noise in tracked data.

The camera was setup with a tele-converter and a macro lens. It was positioned as close as possible to the specimens while maintaining acceptable focus level. This was done for the purpose of improving resolution of the video images, hence improving the precision of the tracked displacements. One example of such image is shown in Figure 4-11. The size of the image in the sample is 11.9 mm x 6.7 mm, corresponding with 1280 pixels x 720 pixels.

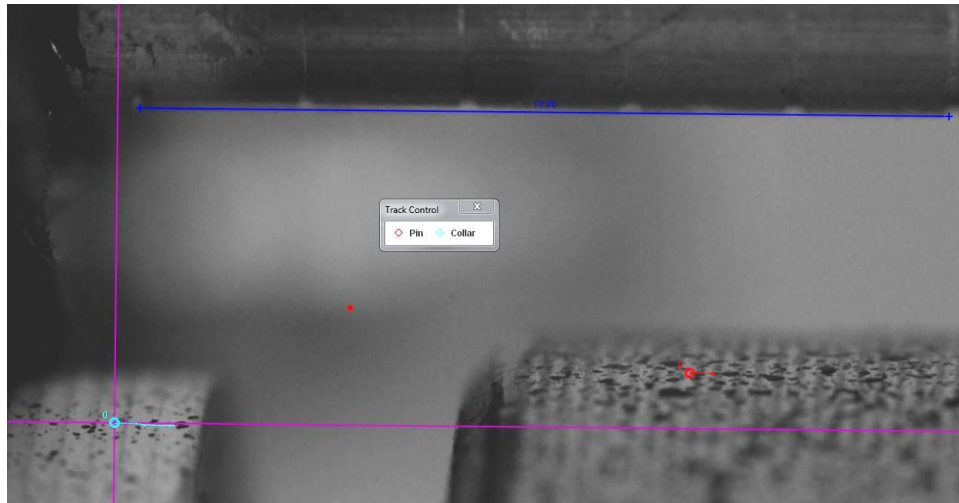


Figure 4-11: Sample of analyzed video image

To determine the accuracy of the software, a video of the pin and collar sample during idle condition was analyzed. The position of the pixel in x and y axes were tracked. The result is presented in Figure 4-12 and Table 4-2. The video image analysis method produced displacement data with lower standard deviation compared to the clip gauge displacement measurement system by 42.4%.

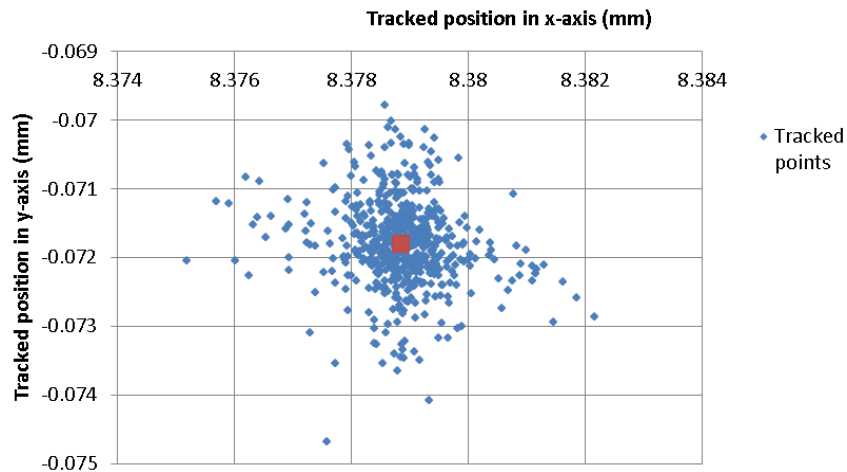


Figure 4-12: Position of tracked idle point in x and y coordinates

	Actuator	LVDT	Clip gauge	Video Image Analysis
Standard deviation (μm)	19.62	7.904	1.241	0.714
Resolution (μm)	4.71	1.69	0.214	< 0.1

Table 4-2: Accuracy comparison table between the actuator, LVDT and the clip gauge, and video image analysis

4.2.4. DEVELOPMENT OF AVERAGE CURVES

The intended purpose of the data obtained from pin and collar tests was to improve the finite element model of the adhesive by supplying it with more accurate shear stress-shear strain curves. Most material models developed for finite element packages construct a shear response curve based on supplied tensile curves. Polymers such as adhesives are anisotropic and would benefit from more accurate shear stress-strain information.

A minimum of three samples were made for each configuration of test, resulting in a minimum of three curves each. Statistically significant trends were found in the results, but each curve acquired has relatively different parameters. Curve averaging was done in an attempt to minimize the effects of variance in the data test, and to combine these multiple curves to one ideal curve to be used as input for numerical material model.

The force and displacement data were acquired by two different tools at different sampling rates. Force data was recorded by the load cell installed on the actuator at rates of 1000/s and 2000/s. The camera recorded video images which were used to acquire displacement data, the recording rates were 60/s (low speed), 250/s (medium speed) and 1000/s (high speed). The two set of data were synchronized by their timestamps. The actuator was setup in a way that the data recording started exactly when the actuator starts moving, this is set as $t=0$ s for the force data. An LED light was installed on the fixture and was setup to glow when the actuator moved. The frame of which the LED lit up is recognized as the $t=0$ s for the displacement data.

It was not possible to visually observe the failure of the adhesive joint, and the transmitted load did not get reduced to zero after failure initiation. This is caused by the pin continuing to be resisted by the frictional force created by the remaining adhesive layer. Attempts were made to pinpoint the fracture point of the samples by identifying the:

1. sharpest decline of recorded force, and
2. steepest incline of recorded crosshead velocity

These attempts were ultimately cancelled because the two parameters did not reliably exist in every graph. The curves acquired from samples bonded with SA9850 in particular generally did not feature any large/sudden changes in either force or velocity. To avoid arbitrariness, the failure point was determined to be the maximum force value recorded.

It was observed that the adhesives exhibited a response that was similar to the power-law strain hardening relationship, characterized with a smooth transition between elastic and plastic regions. The point of transition from elastic to plastic response was not visually obvious. The Ramberg-Osgood equation was

developed to describe a similar stress-strain relationship. The general form of Ramberg-Osgood equation is given in Equation 4.1, and the shear equivalent is shown in Equation 4.2.

$$\epsilon = \frac{\sigma}{E} + \alpha \frac{\sigma_0}{E} \left(\frac{\sigma}{\sigma_0} \right)^n$$

Equation 4.1: General form of Ramberg-Osgood equation

$$\gamma = \frac{\tau}{G} + \alpha \frac{\tau_0}{G} \left(\frac{\tau}{\tau_0} \right)^n$$

Equation 4.2: Shear equivalent form of Ramberg-Osgood equation

Where

γ = Shear strain (mm/mm)

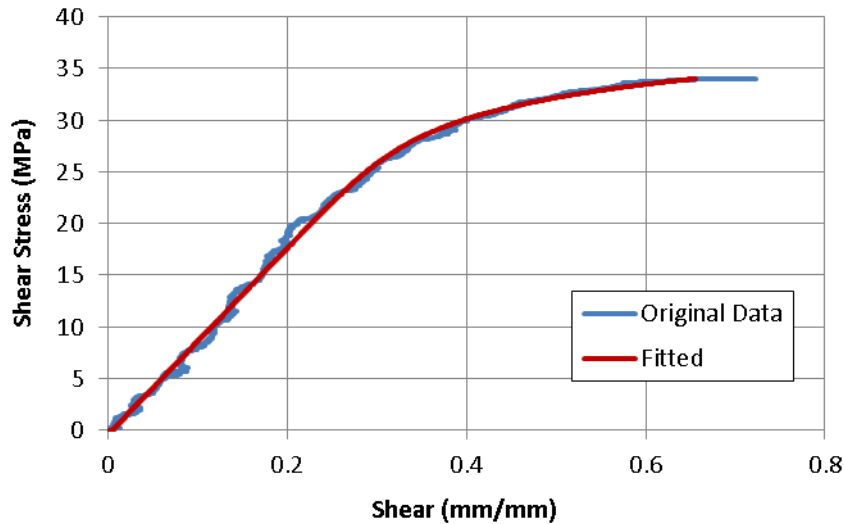
τ = Shear stress (MPa)

G = Shear modulus (MPa)

τ_0 = Yield shear stress (MPa)

α, n = Material strain hardening parameters

This equation was used to determine the shear variables for each curve. An example of this fit is shown in Figure 4-13. A code was written and compiled with *MATLAB* to process the data as provided by *Tracker*..



Adhesive: DP460NS
Rate: 0.1 /s

G	90.193 MPa
α	1.98×10^{-4}
τ_0	16.398 MPa
n	12.25
R^2	0.996

Figure 4-13: Comparison between original data and curve fit

The R^2 values were consistently above 0.96 for every curve, with most being above 0.99 (Table 4-4). This indicates an extremely good fit between the data and the equation selected.

For traditional steel materials, a 0.2% offset yield point is defined as the point where plastic deformation starts. This criterion did not work well for the acquired curves, since the shear strain values were larger than typical steel strain values by multiple magnitudes. To solve this problem, each of the curves was separated into elastic and plastic regions with the aid of coefficients acquired from the curve fit. The τ_0 parameter denotes the yield shear stress which signified the end of the elastic region. The G and τ_0 numbers were averaged to produce the elastic part of the average curve. The plastic region, which started and ended at different stress/strain values, were normalized at 20 discrete points (Figure 4-14) then averaged.

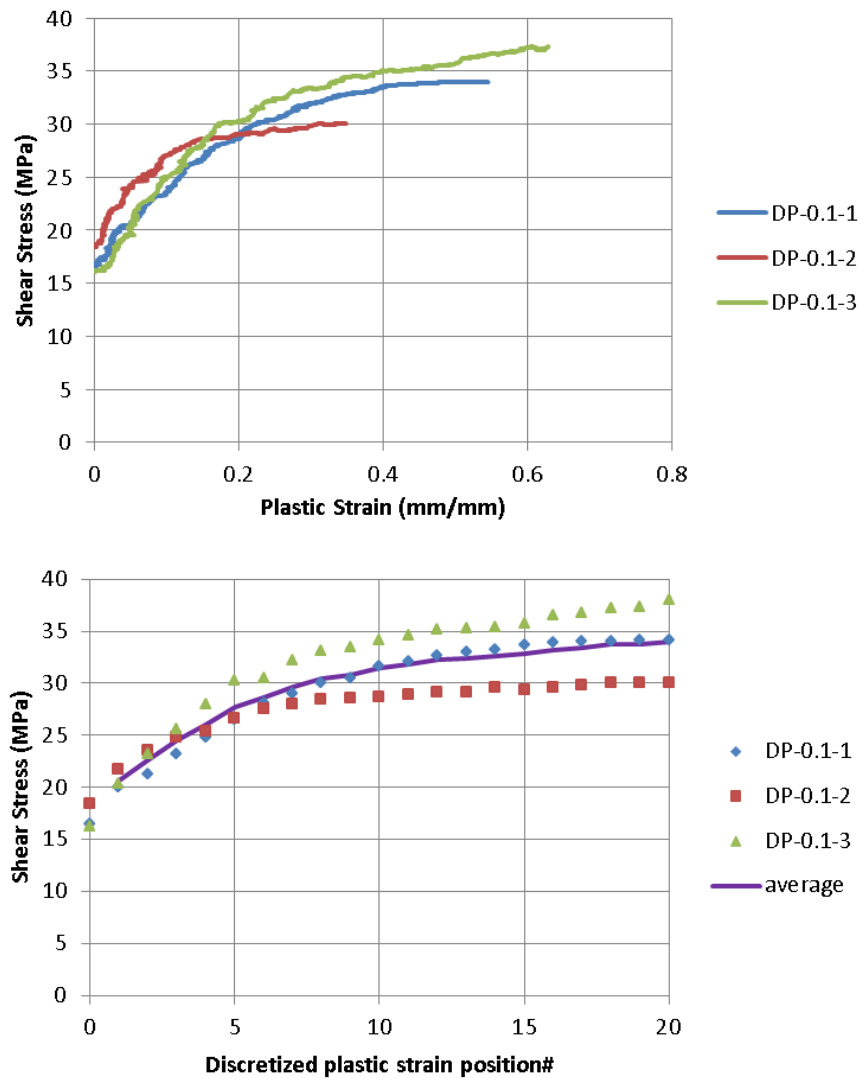


Figure 4-14: Plastic responses of DP460NS at 0.1/s (Original [T], Discretized [B])

Once the elastic and plastic responses of each of the curves were acquired, they were combined into one final curve. This curve represented idealized shear stress-shear strain curve for the adhesive at specific deformation rates.

4.2.5. SECTIONED SAMPLE ANALYSIS

The shear modulus values for that were calculated from bulk tension tests [49] is presented in Table 4-3. These values were calculated using Equation 4.3. Figure 4-15 shows the shear modulus value for DP460NS overlaid on shear stress – shear strain curves that were acquired by Tomblin et al. [166] in their research using lap shear specimens.

	Shear Modulus (MPa)
DP460NS	773.05
SA9850	851.06

Table 4-3: Calculated values of shear moduli of the adhesives

$$G = \frac{E}{2(1 + \nu)}$$

Equation 4.3: Shear modulus equation

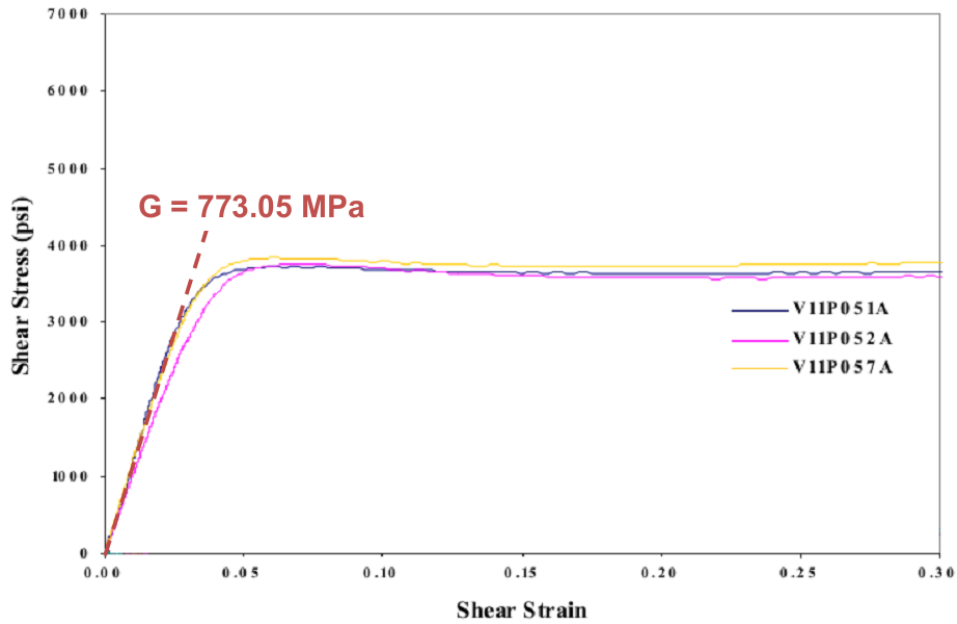


Figure 4-15: Shear stress – shear strain result of DP460NS with shear modulus line overlaid (adapted from Tomblin et al.[166])

Shear modulus values that were acquired from pin and collar curve fits are consistently lower than the values listed above by several magnitudes. To explain this discrepancy, an investigation was done onto a pin and collar sample. To be able to visualize the movements of the adherends directly on the bond line, the adhesive bond was exposed by sectioning the sample as shown in Figure 4-16. To eliminate imbalanced bending moments, the sectioning was done on both sides. The resulting geometry was closer in nature to a double lap shear arrangement (Figure 3-2) with non-constant thickness.

Random speckled pattern was sprayed onto the surface of the sample to improve accuracy of the video image analysis, and the experiment was run at nominal shear rate of 0.1 /s , which corresponded to a crosshead velocity of 0.015 mm/s [0.9 mm/min].

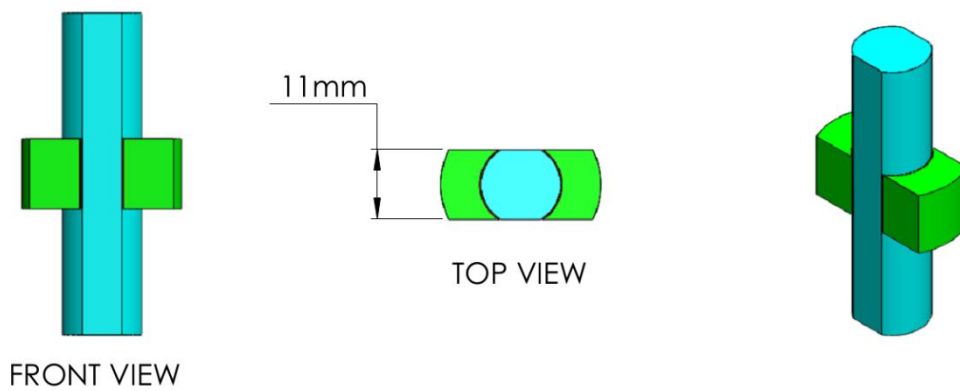


Figure 4-16: Sectioned sample (Schematic [T], Tested sample [B])

Multiple spots on the pin and the collar substrates were tracked with *tracker*. Details about this analysis are presented in chapter 4.3.1.

4.3. RESULTS

Twenty-five pin and collar samples were successfully tested at four different deformation rates. Curve fitting was applied to each individual shear stress-shear strain curve, the coefficients of which are summarized in Table 4-4. Also shown in the last column is the R^2 value of each of the curve fit. Each of these curves was plotted against its fit and can be found in Appendix C: Pin and Collar Data Charts.

Adhesive	Attempted rate	Sample#	G	α	τ_0	n	R^2
DP460NS	0.1 /s	1	90.19	1.98E-04	16.40	12.25	0.9961
		2	111.07	1.70E-05	18.40	23.06	0.9965
		3	87.24	2.42E-04	16.13	10.82	0.9973
	1 /s	1	126.25	2.94E-06	21.50	20.67	0.9950
		2	213.80	8.02E-06	20.38	18.34	0.9874
		3	139.02	5.46E-07	21.27	25.42	0.9984
	10 /s	1	162.64	5.52E-06	19.02	14.83	0.9969
		2	117.12	9.35E-05	17.16	11.21	0.9964
		3	159.90	6.64E-04	14.15	7.83	0.9715
		4	105.30	3.02E-05	18.73	12.72	0.9951
	100 /s	1	181.19	1.04E-09	30.14	43.33	0.9891
		2	184.51	1.91E-04	16.43	8.91	0.9974
3		247.53	4.47E-07	24.20	19.82	0.9977	
SA9850	0.1 /s	1	89.32	4.13E-03	11.21	6.95	0.9987
		2	121.86	8.28E-03	9.82	6.26	0.9849
		3	156.86	1.76E-02	8.29	5.25	0.9974
	1 /s	1	144.64	2.46E-03	12.40	8.70	0.9939
		2	199.39	3.48E-03	11.63	7.93	0.9973
		3	136.84	1.10E-02	8.81	5.36	0.9972
	10 /s	1	80.87	2.63E-06	19.13	28.00	0.9614
		2	122.62	2.11E-03	12.20	7.63	0.9983
		3	127.67	5.14E-04	14.77	12.47	0.9855
	100 /s	1	272.82	7.83E-04	14.19	10.77	0.9944
		2	100.84	3.12E-05	18.79	16.53	0.9959
		3	151.76	1.83E-04	16.54	11.93	0.9973

Table 4-4: Constants of the equation fit for all data

The type of failure experienced by the sample was mostly cohesive, as determined by visual inspections (Figure 4-17). However, spots of interfacial failure were observed on some samples, with increased frequency on samples that were tested at high deformation rates.

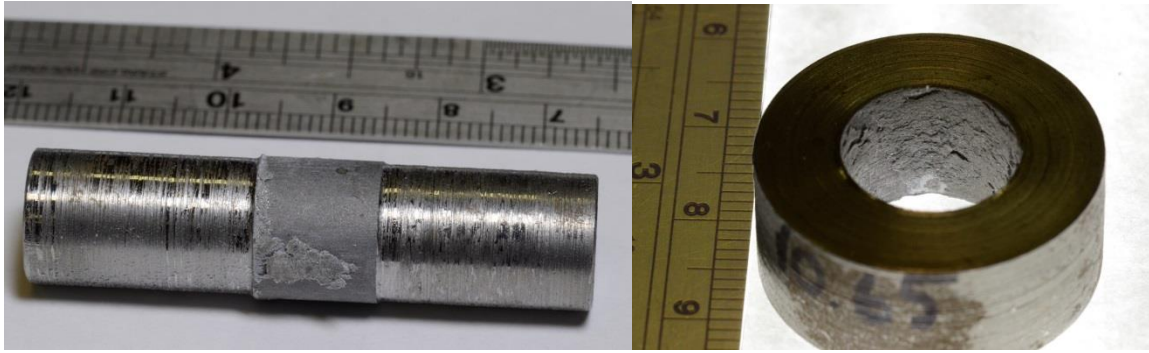


Figure 4-17: Figures of a failed specimen (pin [L], collar [R])

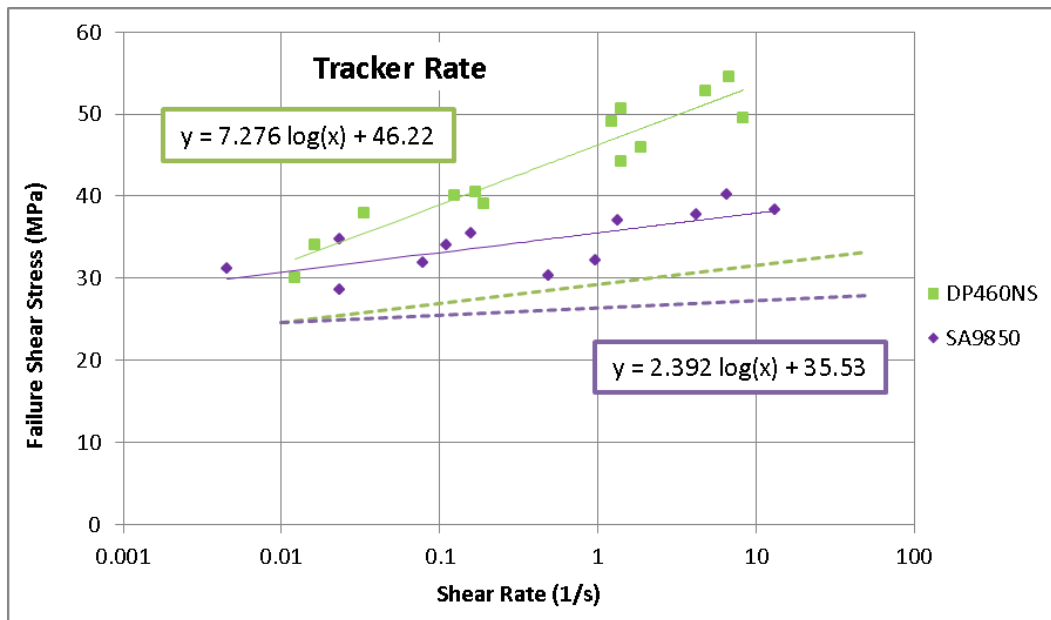


Figure 4-18: Shear rate dependency of DP460NS and SA9850 as obtained from pin and collar tests. Data acquired from thick adherend lap shear tests shown for comparison as dashed lines (green: DP460NS, purple: SA9850)

Strength of the adhesive bond increased with increasing deformation rate. DP460NS exhibited a higher dependency on deformation rate than the SA9850, as evidenced by the steeper line on Figure 4-18. This behaviour is also consistent with results acquired by thick adherend lap shear tests (Figure 2-4), to a lesser degree (Table 4-5). This can be explained by effects of bond thickness and geometric differences.

Adhesive	Shear strength increase per decade of shear rate	
	Pin and collar	Thick adherend lap shear
DP460NS	7.276 MPa	2.338 MPa
SA9850	2.392 MPa	0.880 MPa

Table 4-5: Increase of shear strength per decade of shear rate for DP460NS and SA9850

Every decade of increased shear rate increases the shear strength of the DP460NS by approximately 7.276 MPa, and SA9850 by approximately 2.392 MPa (Table 4-5). The shear rate values were acquired from the actual deformation rate measured with *tracker*, as opposed to the nominal values of shear rates based on crosshead velocity. The higher value of displacement rate measured from the actuator was attributed to compliance of test fixture, where the displacement of the actuator manifested into deformation of the various parts of the fixture itself, instead of into the pin and collar samples.

The final average curves are shown in Figure 4-19 and Figure 4-20. The min/max values of shear to failure are shown as error bars.

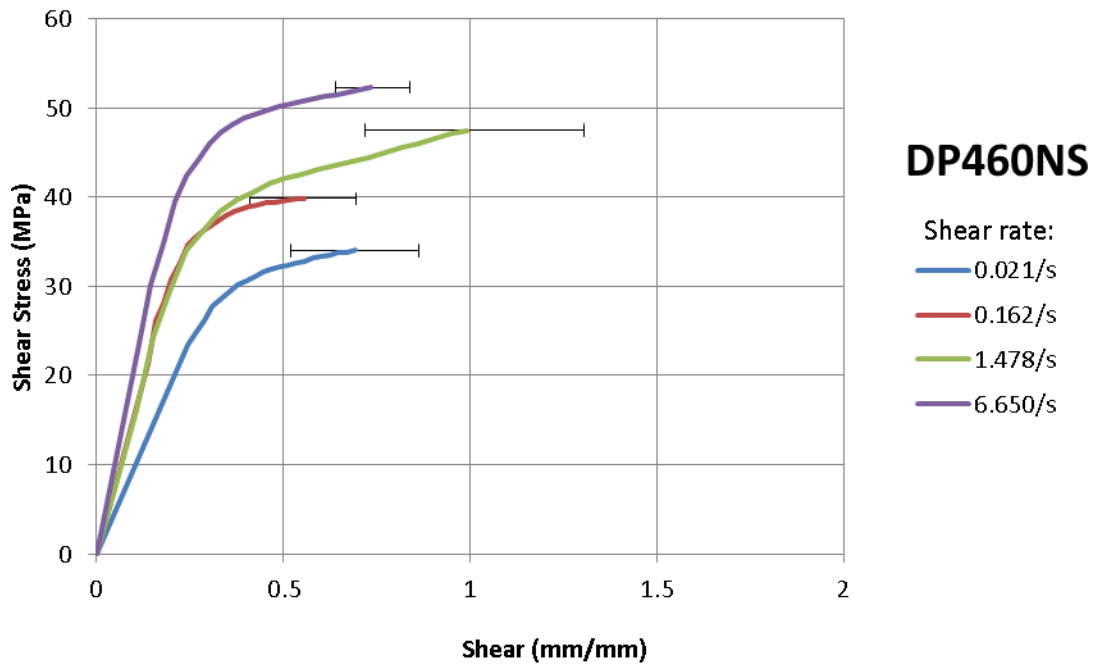


Figure 4-19: Average curves of DP460NS at various shear rates

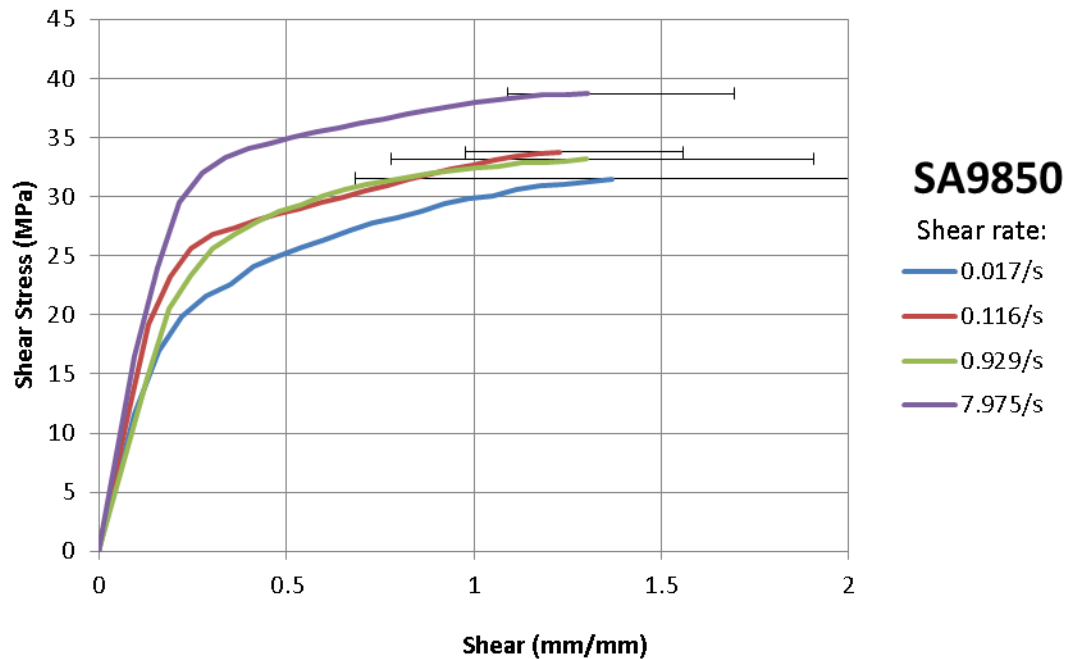


Figure 4-20: Average curves of SA9850 at various shear rates

The general trend in most polymers and other viscoelastic materials is that the shear strength and shear modulus of the adhesive joints increases with increasing deformation rate; while the amount of deformation to failure decreases [167].

The acquired data showed similar trend toward the shear strength of modulus with some notable exceptions primarily with those tested at nominal shear rates of 10 /s; while the deformation to failure did not follow a consistent pattern and was more sporadic in nature. Other than the camera capture rates, there were not any fundamental difference in technique and methodology involved among the samples tested.

Investigation of the variance of the acquired data revealed issues with the displacement measurement system. The variation of shear moduli and shear to failure for both adhesives at respective nominal shear rates are shown in Figure 4-21. The error bars on each chart represent 95% confidence interval.

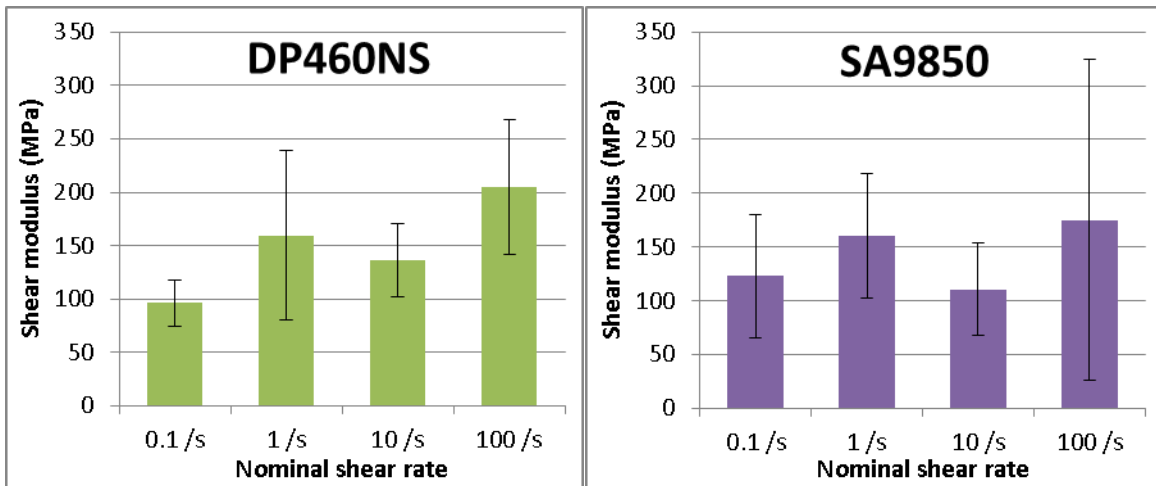


Figure 4-21: Variation of shear moduli at various nominal shear rates (DP460NS [L], SA9850 [R])

In addition to high variance, the shear moduli values acquired were much lower than the expected values as presented in Table 4-3. The values of shear strain to failure did not follow a consistent pattern and exhibited high amount of variance. Concerns were raised regarding the legitimacy of both the failure indicator method and the displacement measurement system. This issue is investigated into on chapter 4.3.1.

4.3.1. SECTIONED SAMPLE RESULTS

The resulting force versus crosshead displacement is shown in Figure 4-22. For the purpose of investigating elastic response, points were tracked before crosshead displacement of 0.174 mm. Force at crosshead displacement of 0.174 mm is equal to 2728 N, corresponding to shear stress of 9.75 MPa. Results from previous chapter justify the assumption that the material response was still within the elastic region before this point.

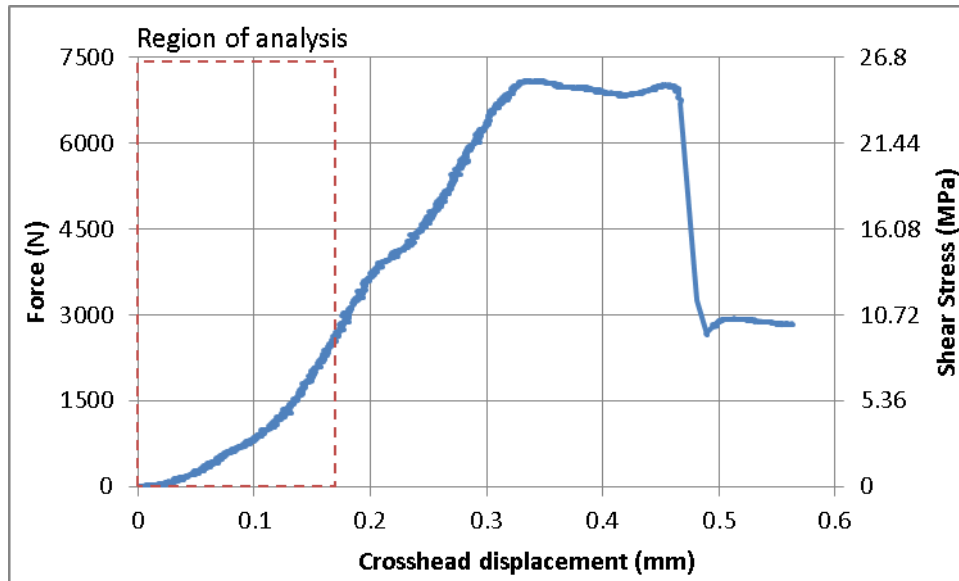


Figure 4-22: Plot of force versus crosshead displacement for the sectioned sample

The force versus crosshead displacement ramp up slope in the sectioned sample was characteristically lower than the ones used in previous section. A plateau of force was observed between crosshead displacement of 0.32 mm and 0.42 mm, which is uncharacteristic for DP460NS joints. Effect of machining and geometric differences between the regular pin and collar tests with the sectioned tests is likely to be too substantial for them to be compared to each other. For this reason, the sectioned sample results is only used to highlight the nuances of deformations occurring in the adhesive and adherends, instead of acquiring proper plot of shear stress versus shear strain.

Tracker was used to track multiple spots (three spots each) on the pin and the collar (Figure 4-23 and Figure 4-24) for the duration previously specified. The results are shown in Figure 4-25.



Figure 4-23: Section sample analysis window position

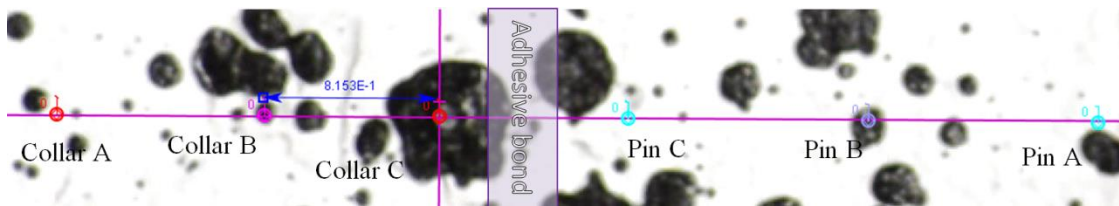


Figure 4-24: Sectioned sample analysis tracked points positions

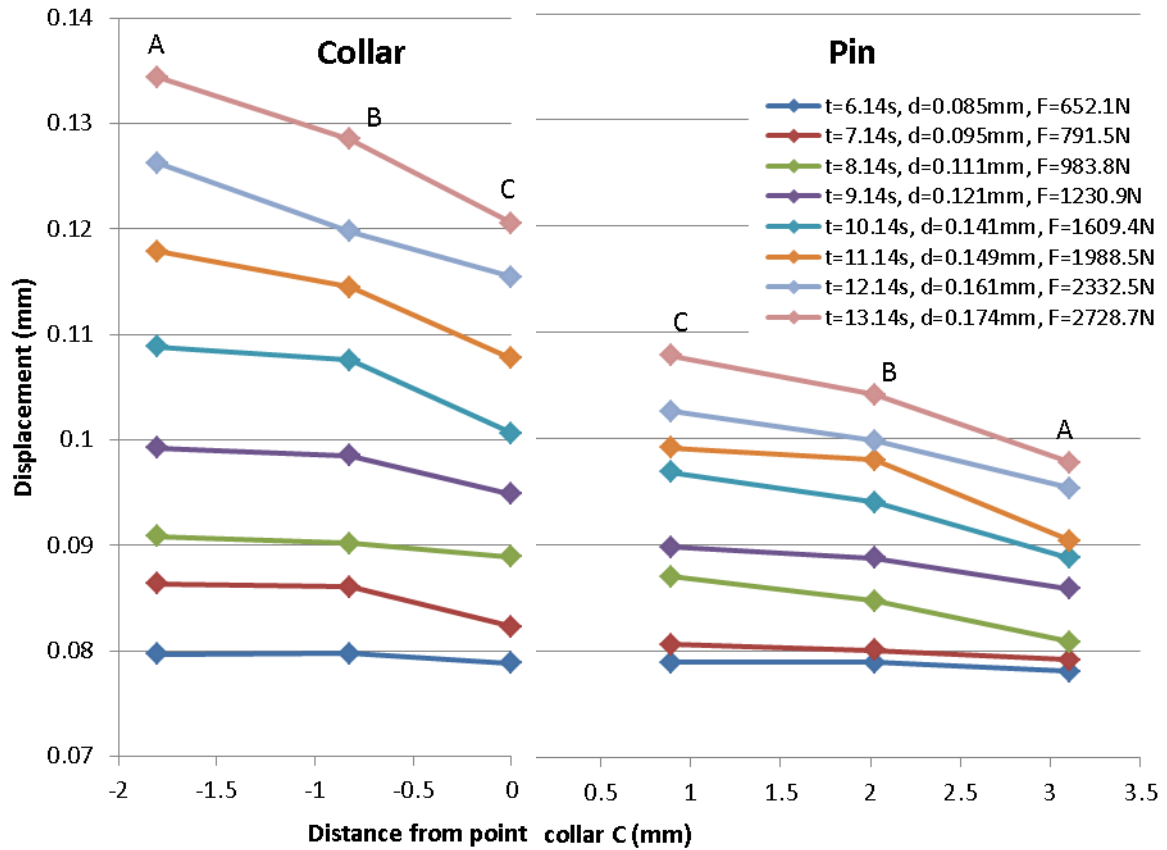


Figure 4-25: Tracked displacements of collar [L] and pin [R] points at various progressions

From this information, it was observed that the displacements inside the collar were maximized further away from the adhesive bond, and the deformation of the pin was maximized near the adhesive bond. This effect was greater in the collar than the pin, which suggests they received different amount of rotational displacements. This behaviour was also observed in the numerical simulation (Figure 4-26), but to a much lesser degree to the point of insignificance. The sectioned sample experienced displacements that were not explainable by deformations during loading alone. An explanation is that the sectioned sample experienced global rotation due to imperfect alignment between the fixture and the sample, and exaggerated local rotation on the collar adherend due to geometric differences between regular pin and collar sample and this sectioned sample. This exaggerated displacement on the surface of the collar would exaggerate the values of deformation of adhesive layer during elastic loading, resulting in lower shear moduli values.

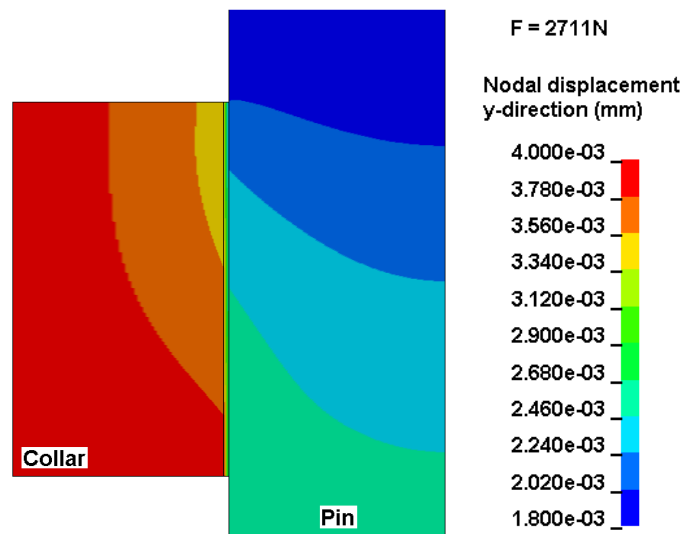


Figure 4-26: Predicted axial deformations of pin and collar adherends in y-direction during loading of 2711 N

Furthermore, imperfections on the surfaces of the sample and the fixtures typically necessitated an initial ‘settling’ period. During this period, the sample experienced small movements, both translation and rotation, while transmitted force equaled nonzero. For the case of this sectioned sample, it can be seen that force ramp up did not cause separation of the pin and the collar until approximately $t \approx 6.5$ s (Figure 4-27). Ideally, the movements experienced in this period by the pin and the collar would be very close to equal and can safely be considered negligible. However, deformations that were expected during elastic deformation of the adhesive bond ($< 4 \mu\text{m}$) was within the same magnitude with the movements that were expected during this settling period.

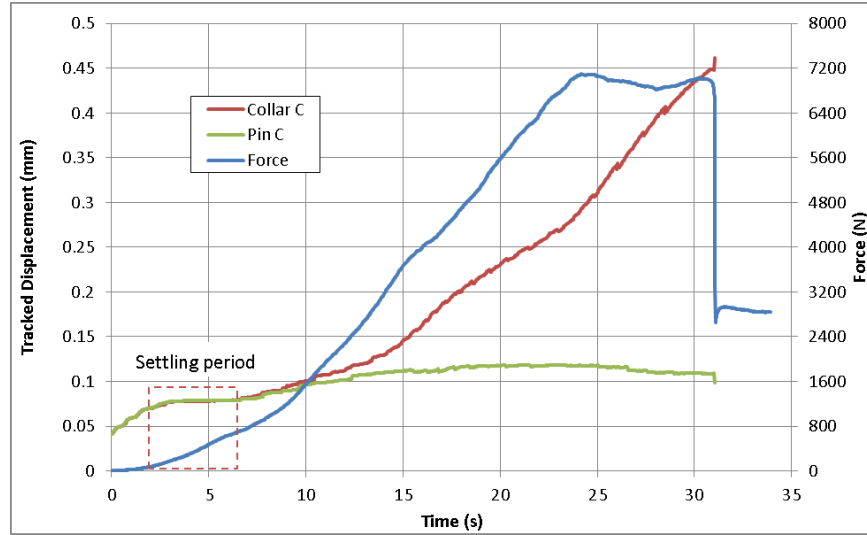


Figure 4-27: Plot of force and tracked adherend displacements against time

It also follows that the calculated value of shear modulus was highly sensitive to the choice of location of tracked points. Table 4-6 shows the calculated shear modulus value at $t=13.14$ s based on the points that were selected. The variations in the calculated shear moduli confirm the sensitivity of measurement with respect to the positions of the tracked points.

Shear modulus (MPa)			
	Collar A	Collar B	Collar C
Pin A	39.94	47.57	64.18
Pin B	48.36	60.01	89.12
Pin C	55.12	70.79	115.16

Table 4-6: Calculated shear modulus value using various tracked points

The experiment was able to effectively prove the importance of isolating the adhesive bond deformations from the adherend deformations. Direct consequence of this information is to develop a test where displacement measurement system can be done directly at the bond. The nature of pin and collar test geometry necessarily concealed the adhesive bond from sight, making this impossible.

4.4. DISCUSSION AND LIMITATIONS

The biggest challenge of this experiment was acquiring accurate displacement numbers. Calculating displacement numbers from the velocity of the actuator necessitates several assumptions: for the pin to stop moving as soon as force ramps up, and for the collar to move at exactly the same rate as the actuator. Both of these assumptions have been proven to be false in this research.

The optical method to measure displacements of pin and collar samples has been successful, but consideration was required when transforming the measured values into adhesive displacement. It was proven that deformation of the adherends and fixture can distort the information about the joint deformation significantly.

To accurately measure shear strain in the adhesive bond, the measurements will have to be made directly on the bondline on each of the substrates, isolated from adherend deformations. This is only possible with test geometries where the bond is visually apparent such as double-lap-shear or single edge notched flexural beam. Pin and collar geometry is not suitable for this effort. Also, the relatively thin bondline thickness translates to very small measurements, especially in the elastic region. This necessitates equipment with very high precision and accuracy.

While not an ideal test for measuring shear strains, the pin and collar test is useful for examining the strength of adhesive joints in a hypothetical pure shear scenario. It is also relatively easy to be adapted to higher strain rate testing using the Split Hopkinson Pressure Bar apparatus, and subsampling of geometry is straightforward. Shear rate dependency was also shown to be better characterised by pin and collar test compared to thick adherend lap shear.

4.5. NUMERICAL SIMULATION

Multiple researchers [69, 168, 169] studied stress variations in tubular joints and came up with analytical solutions. Martinez et al.[70] in particular adapted the work of Nemeş et al.[69] to a pin and collar joint over various collar thicknesses. They discovered that the stress distribution over the length of the pin and collar adhesive joint can be expressed by Equation 4.4.

$$\tau_{rz}^c(r, z) = \frac{-r_{ic}^2}{2r} \cdot \frac{d\sigma_{zz}^{(1)}}{dz}$$

$$\sigma_{zz}^{(1)} = -\frac{D}{2A} + M_1 \cdot e^{az} + M_2 \cdot e^{-az} + M_3 \cdot e^{bz} + M_4 \cdot e^{-bz}$$

Equation 4.4: Distribution of shear stress across the length of a pin and collar joint, as developed by Martinez et al.[70]

Details of each coefficient can be found on paper authored by Martinez et al.[70] and the solution of present work, solved with MathCAD, can be found in Appendix F: Pin and Collar MathCAD Solution.

For the present work, stress distribution inside the adhesive joint was studied using solid elements formulation.

4.5.1. GEOMETRY AND BOUNDARY CONDITIONS

The geometry of pin and collar test is entirely rotationally symmetrical. This means that the geometry of the numerical simulation model can be simplified into a 2D model which, if revolved around the Y axis, would be representative of the original 3D structure. Taking advantage of this feature would decrease computational cost by a significant amount, while losing none of the relevant information. In the case of the finite element code LS-DYNA LSTC, this feature was defined by creating shell elements centering on Y-axis, and applying axisymmetric element formulation for the defined parts. (Figure 4-28)

Five different mesh densities were used for this study, governed by the amount of elements through the thickness of the adhesive bond. Accuracy of the results of the five mesh sizes was compared to each other, and one was selected for further simulations.

The experiment was setup in a way such that the collar was pushed by the test fixture; this is represented by applying constant velocity to the bottom nodes of the collar. The pin was stopped from moving by the top platen, this was represented in the numerical simulation by restricting the nodes at the top of the pin from translation in the y-direction.

As per the experiment, four different values of velocity were applied to the bottom nodes of the collar, corresponding to the values presented on chapter 4.2.1.

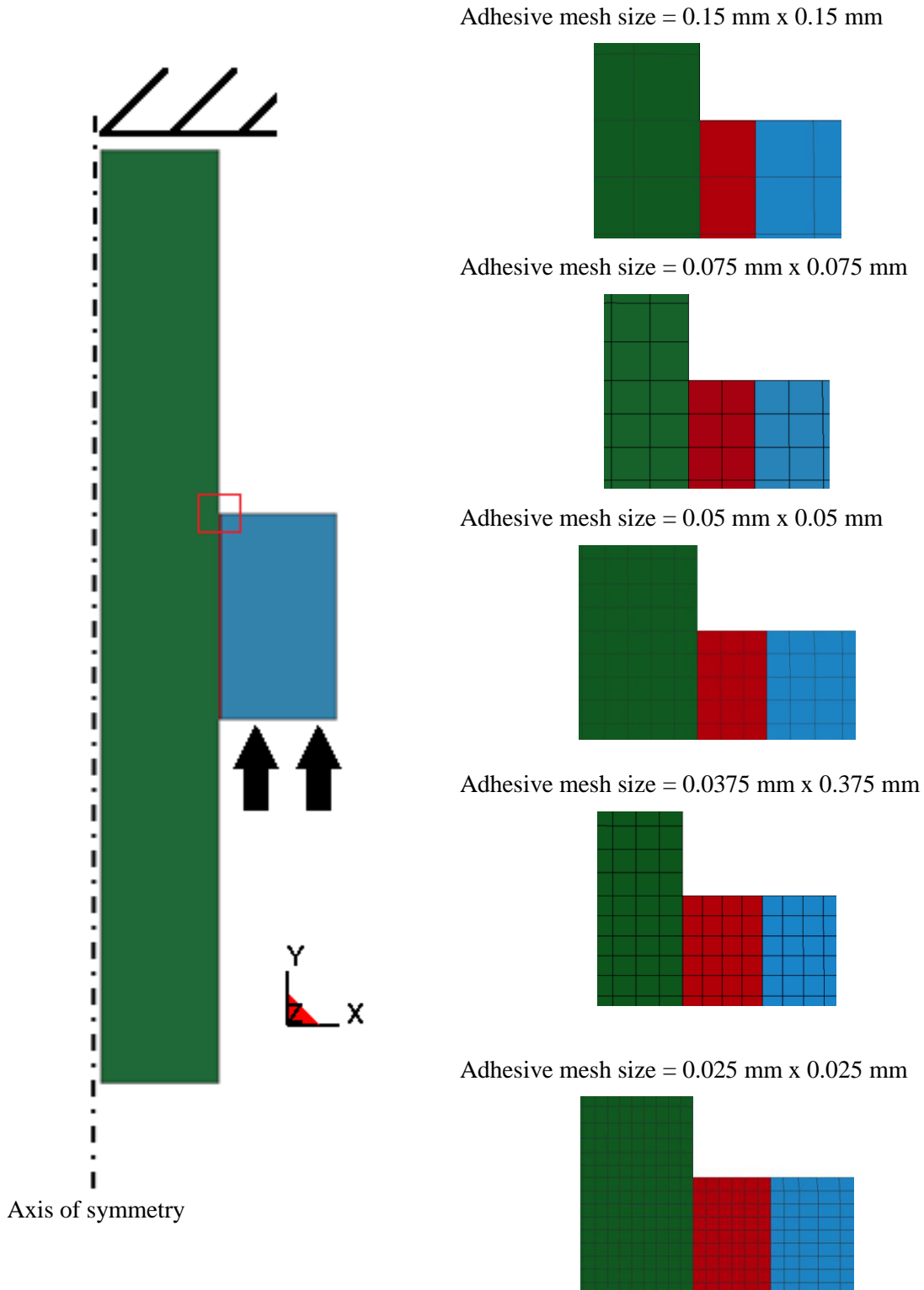


Figure 4-28: axisymmetric geometry elements (full [L]; five different densities, zoomed in view [R])

4.5.2. MATERIAL MODEL

The material model for the steel adherends were defined simply as elastic materials, as it was confirmed both analytically and through preliminary FEA that the amount of force exerted on the adherends did not cause the adherends to yield. Cold-rolled AISI 1018 steel material was used, the properties of which are presented in Table 4-7.

Property	Value
Density (kg/m ³)	7830
Young's modulus (GPa)	207
Poisson's ratio	0.35

Table 4-7: Properties of steel adherends used for pin and collar numerical simulation

The material model utilized to represent the adhesive layer was the SAMP-1 model (Semi Analytical Model for Polymer), developed by Kolling et al. [130] As mentioned in chapter 2.7.2, this material model has been confirmed to work reasonably well up to the yield point of the material during shear loading.

This particular material model requires an input of at least one tension curve, with any additional curves will be used to predict strain rate effects. Three tension curves (Figure 2-2) were supplied as input for this study, generated from a series of tests involving double cantilever beams [49]. A shear curve acquired from thick adherend lap shear test was also supplied as an input to improve the shear response prediction. Figure 4-29 shows the input curves for both tension and shear in plot format. LS-DYNA automatically removed any negative tangent curve prior to solving the simulation, to eliminate potential instability.

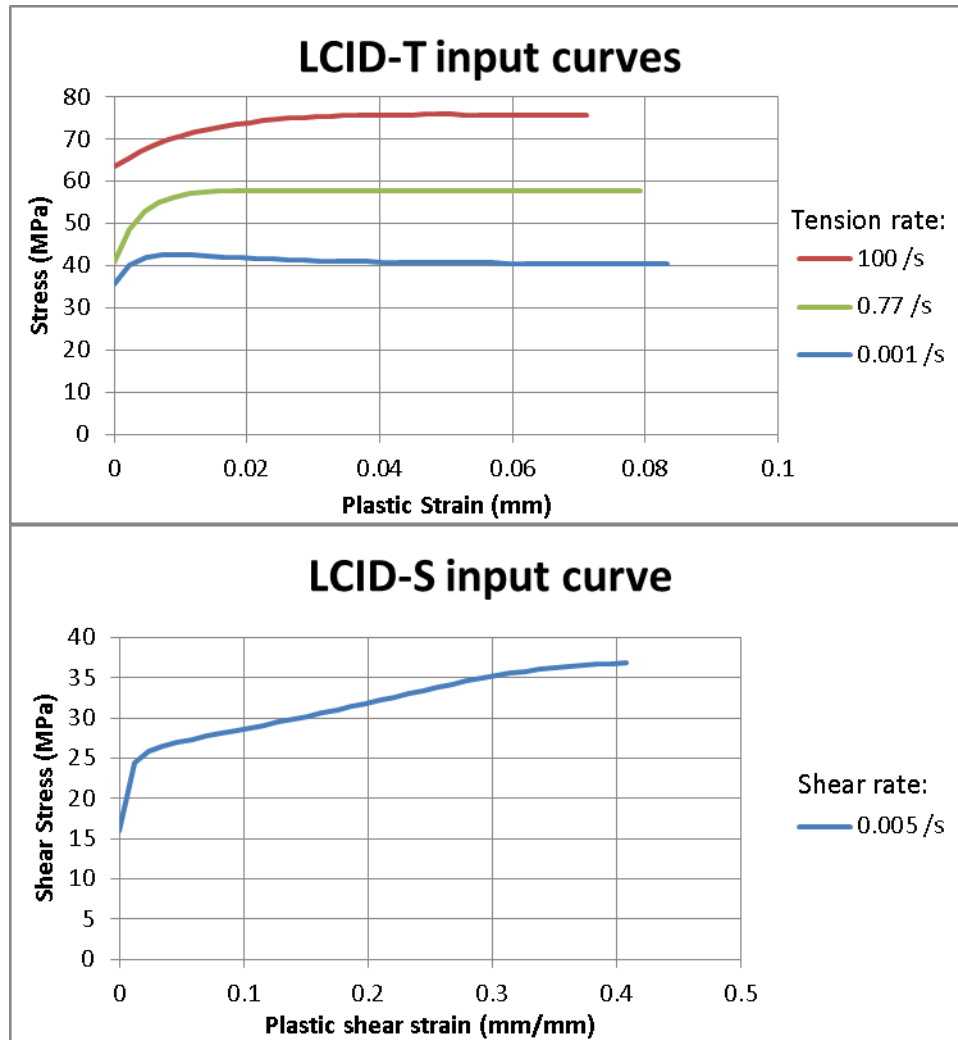


Figure 4-29: SAMP-1 input curves information (Tension [T], Shear [B])

The SAMP-1 material model has the capability of including a failure criterion based on effective plastic strain. This was utilized in this study by inputting the plastic strain to failure information acquired from the tension tests, in the three selected strain rates in Figure 4-29. The material input deck can be found in Appendix D: LS-DYNA Cards.

4.5.3. RESULTS

The differently-sized mesh elements were evaluated by comparing their shear stress profile versus time. Results from chapter 4.5.4 show that shear stress inside the bond is close to uniform at halfway across the length of the bond, and reached peak value at the edges. It follows that stress predictions on the edges of the adhesive bond are more sensitive to element size in comparison to the other elements in the adhesive bond. For this reason, the shear stresses at the top edge of the adhesive bond elements were selected for

mesh size convergence study. Stress profiles on this location on the five different mesh sizes are shown in Figure 4-30 (bottom). The simulations were run with the same parameters with respect to deformation rates, end time and computational cost (e.g. number of processors, memory allotment).

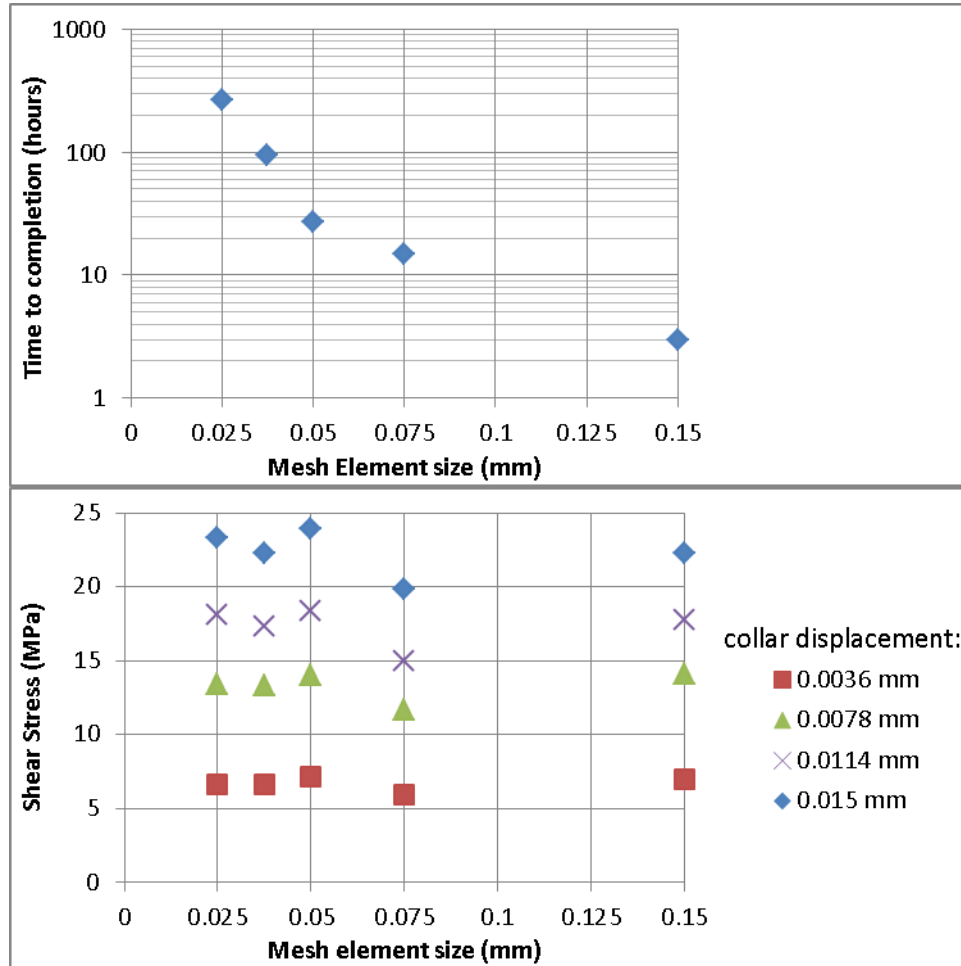


Figure 4-30: Shear stress on the top adhesive element across the bond at different mesh densities (Elapsed time to normal termination [T], shear stress at top adhesive bond element versus mesh element size [B])

It can be seen in Figure 4-30 that running the simulation with mesh element size of 0.05 mm resulted in shear stress numbers that were consistently within 10% of the values predicted by simulation ran with the densest mesh. With the accuracy it provided, the amount of time taken to finish the simulation is considered to be reasonable. Element size of 0.05 mm was therefore selected for future simulations.

The failure strains that were acquired from tension tests do not translate well into failure shear strains by shear loading. Adhesive bonds, especially on epoxies that are rubber toughened, deform by a much larger amount during shear than tension. SAMP-1 under-predicted the failure shear strain value by a large

magnitude. Figure 4-31 shows the deformation of adhesive bond just before failure, with maximum shear strain value of approximately 0.063 at the highlighted element.

The simulations were redone at different shear rates without failure strain criterion.

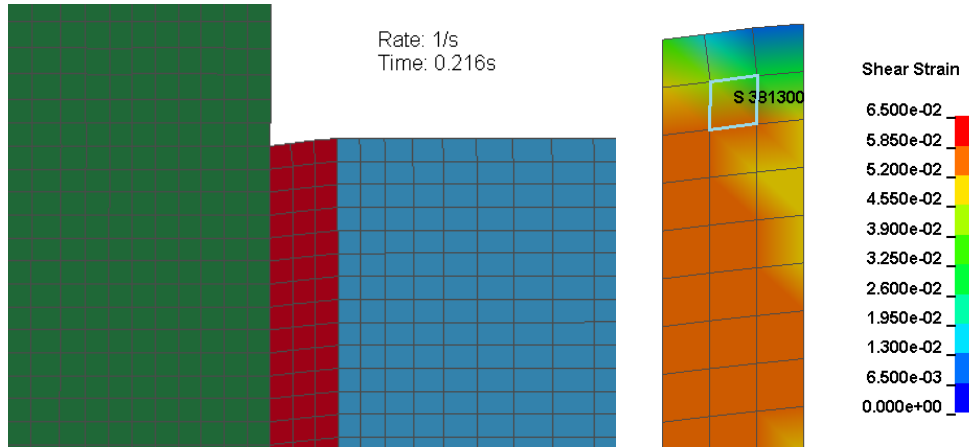


Figure 4-31: Adhesive bond shear strain prior to failure

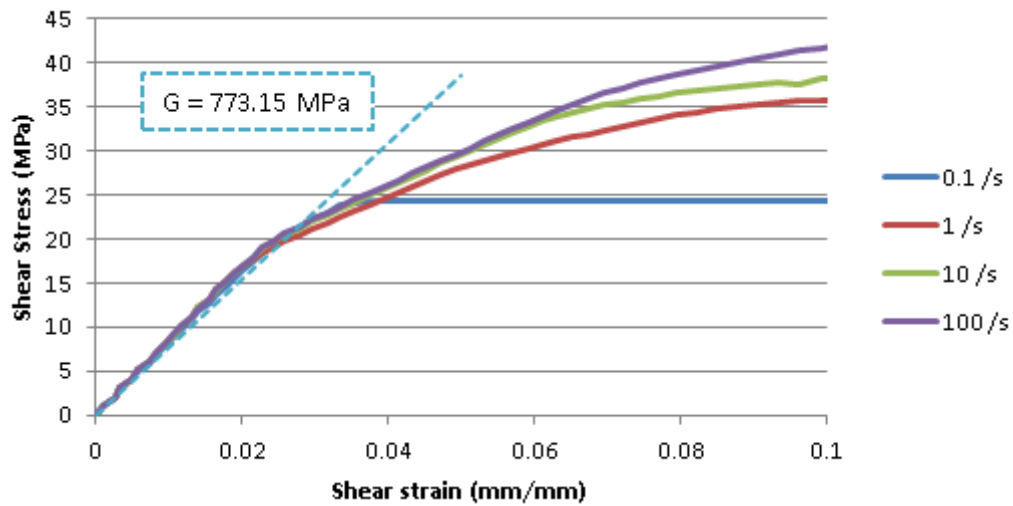


Figure 4-32: Shear stress versus shear strain FEA results at different nominal shear rates

Although the tension strength information supplied to the material model (Figure 4-29) linearly scaled with logarithmic strain rate, the acquired response from a shear simulation (Figure 4-32) did not follow the linear scale. The shear response at slowest deformation rate (0.1/s) was equal to the tension input of slowest tension curve supplied (0.001/s), multiplied by 0.577. This value is acquired from Von Mises equation based on pure shear conditions (Equation 4.6). But the shear responses at the other deformation rates did not follow the same behaviour.

$$\sigma_{VM} = \sqrt{\frac{1}{2}[(\sigma_{11} - \sigma_{22})^2 + (\sigma_{22} - \sigma_{33})^2 + (\sigma_{11} - \sigma_{33})^2 + 6(\sigma_{12}^2 + \sigma_{23}^2 + \sigma_{13}^2)]}$$

Equation 4.5: Von Mises yield criterion equation

$$\sigma_{VM} = \sqrt{3} |\sigma_{12}|$$

$$\sigma_{12} = \frac{1}{\sqrt{3}} \sigma_{VM} = 0.577 \sigma_{VM}$$

Equation 4.6: Von Mises yield criterion equation, simplified for pure shear condition

To show the distribution of shear stress along the length of the collar, four states were taken at different timestamps where the loading was still considered elastic (Table 4-8). These values were acquired by converting the values of compressive stress on an element which represented the top center part of the pin. The chosen element was sufficiently far from the adhesive bond to avoid stress concentration effects.

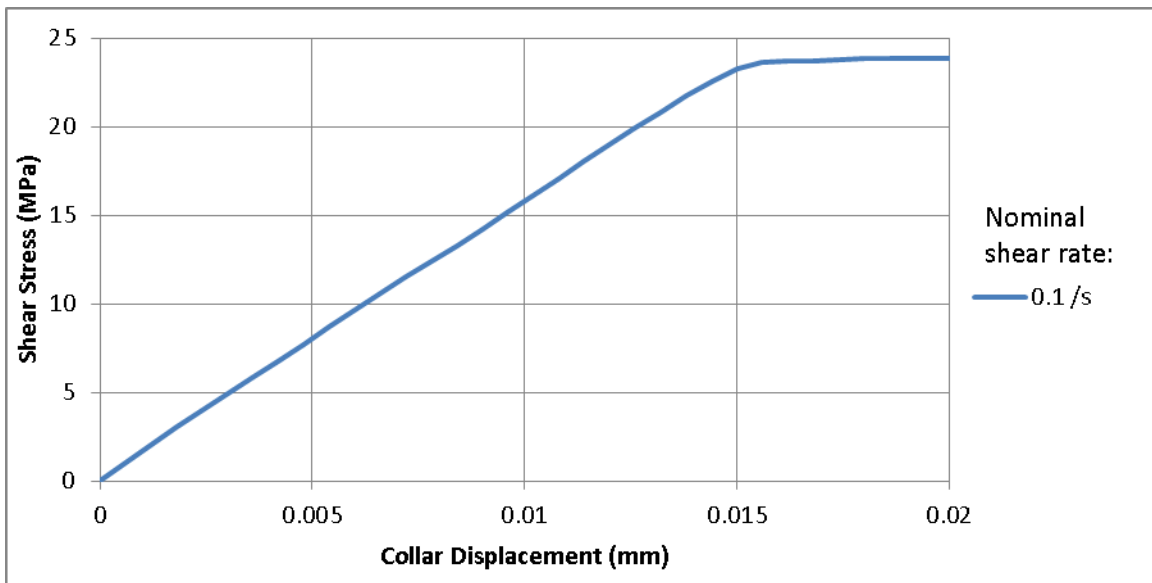


Figure 4-33: Shear stress versus collar displacement of pin and collar numerical simulation

The shear stress values at these different timestamps are given in Table 4-8.

Time	Collar displacement	Shear Stress
0.24 s	0.0036 mm	5.86 MPa
0.52 s	0.0078 mm	12.41 MPa
0.76 s	0.0114 mm	18.06 MPa
1.00 s	0.0150 mm	23.28 MPa

Table 4-8: Shear stress values at different timestamps from FEA

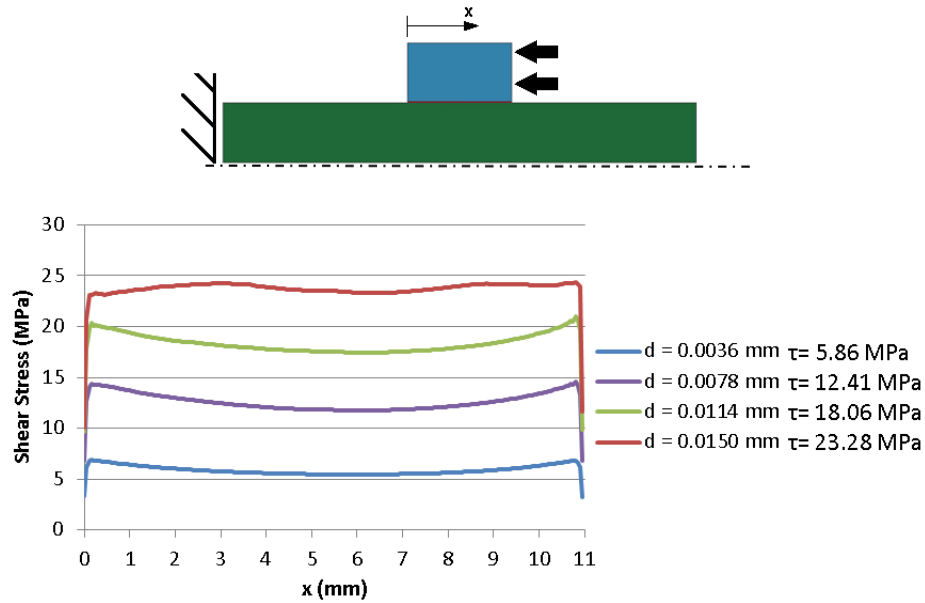


Figure 4-34: Stress distribution along the length of the adhesive joint at various collar displacement values

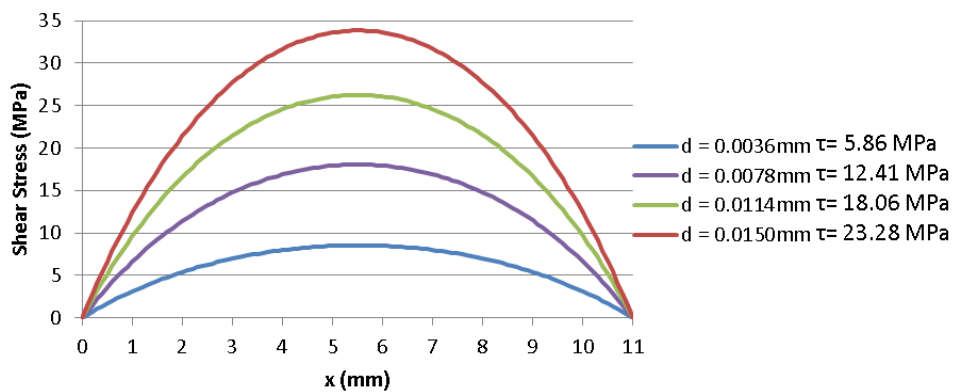


Figure 4-35: Stress distribution along the length of the adhesive joint, according to analytical method developed by Martinez et al.[70]

The distribution of shear stress across the length of the adhesive joint at various times is shown in Figure 4-34. No significant variation from the average shear stress value was found. However, a large difference was observed between the shear stress distributions predicted by FEA methods and analytical results developed by Martinez et al.[70], in both magnitude and general behaviour (Figure 4-34 and Figure 4-35).

4.5.4. DISCUSSIONS AND LIMITATIONS

In this particular modelling scenario, the mesh element size could be relatively coarse with little loss of accuracy. The adherends are sufficiently rigid to ensure nearly uniform shear strain throughout the length of the adhesive joint, minimizing shear strain variations.

Even though SAMP-1 material model was developed for polymers and has strain rate dependency factors, it does not currently include varying moduli of elasticity and rigidity at different rates of deformation. This can lead to inaccuracies since increasing modulus with increasing deformation rates is a trend that is observed in many polymers, adhesives included [167].

The failure criterion to be specified was acquired from uniaxial tension tests, and worked suitably for tensile conditions. Adhesives deform significantly more in shear than in tension, making this failure criterion unsuitable.

With three tension curves as the input, the scaling of shear strength at different rates is not linear as expected. More information for the intermediate rates might improve the accuracy of results.

With present FEA software it is relatively easy to obtain the stress distribution in a cylindrical joint. However, analytical calculations are still very useful as a design tool, because it gives answers immediately when different design parameters are tried. (e.g overlap dimensions, thickness, materials, etc) It would be useful for the solutions for pin and collar joint to be developed with better accuracy.

CHAPTER 5

SUMMARY AND RECOMMENDATIONS

The mechanical response of adhesive joints in shear was investigated using two toughened structural adhesives, three different adherend materials and several surface pretreatments. Efforts were concentrated on observing the effect of different pretreatments on the joint performance by means of single lap shear testing; and on acquiring more accurate shear information by means of pin and collar testing. Numerical simulations were undertaken to aid in the eventual implementation in full vehicle models to support integration of new materials, joining technologies and designs.

The lap shear test is widely used to evaluate joint performance due to the simple geometry of the sample, and is useful for comparing the effect of various parameters on bond strength. This test can be used to validate numerical implementations, although the mixed-mode loading and small deformations can present challenges.

Samples were created using two different adhesives (DP460NS and SA9850) and two adherend materials (aluminum and magnesium). Seven different pretreatment methods were investigated including Alodine conversion coating (all adherend and adhesives), Alodine with hexavalent chromate (all adherend and adhesives), anodization (aluminum only, all adhesives), gritblasting (all adherend and adhesives), contamination (all adherends, SA9850 only), Bonderite EC² (aluminum only, all adhesives), and Bonderite MgC (magnesium only, all adhesives).

The joint performance was found to depend on the adherend material, adhesive type, and surface pretreatment. In general terms, the DP460NS adhesive was found to be more dependent on surface pretreatment compared to the SA9850, assessed using a statistical comparison of the measured strengths and variability. The DP460NS provided good strength for a gritblasted surface pretreatment while the preferred pretreatment for the SA9850 was contamination of the surface using a forming lubricant (Drylube E1), this is true for both aluminum and magnesium adherends. However, tested pretreatments of magnesium did not result in joint strength numbers that were comparable to those of aluminum. Augmentation of the adhesive joint with secondary fasteners is recommended for magnesium adhesive joints.

Contaminating the adherends significantly increased the difficulty of manual application by decreasing the grip of the adhesive to the adherend surface. An approach to solve this would be to automate the dispensing application.

Three pretreatment methods (Alodine, Alodine HC, and anodization) were applied to the adherends by an external supplier, and variability between different lots of treated adherends was noted. Preliminary

results showed potential for these pretreatments to produce relatively high joint strength numbers, for example when bonding aluminum with DP460NS. However, these results were not reproducible, attributed to variability in the surface pretreatment. Further investigation is recommended to address this variability for Alodine conversion coatings and anodization to produce joints with strengths that are higher and more consistent.

Gritblasting was identified as a reliable technique for preparing aluminum for bonding with DP460NS, determined by the relatively high joint strength (average of 21.8 MPa) and low variability (standard deviation of 1.36 MPa) compared to other methods. Gritblasting was also identified to be the pretreatment which produced strongest (average of 7.1 MPa) and most consistent (standard deviation of 0.5 MPa) bonds with magnesium adherends among the other pretreatments tested.

Having a thin coating of contaminant in the form of metal forming lubricant on the adherends was proven to increase the strength and consistency of the bond with SA9850 adhesive. This is true for both aluminum (average of 25.4 MPa and standard deviation of 2.0 MPa) and magnesium (average of 19.2 MPa and standard deviation of 0.8 MPa).

The joint strength numbers from Bonderite EC² and Bonderite MgC conversion coatings (manufactured by Henkel, Germany) were not determined to be comparable to gritblasting and contamination. On aluminum samples that were prepared with Bonderite EC², the joint strength numbers are 9.9 MPa for DP460NS and 19.5 MPa for SA9850. For magnesium samples that were prepared with Bonderite MgC, the joint strength numbers are 5.8 MPa for DP460NS, and 15.3 MPa for SA9850. However, these conversion coatings were cut to size after the pretreatment was applied, which was not ideal for testing, as the cutting process might introduce chipping and peeling in the coatings. These materials were of different alloy to the other previously mentioned configurations, and the magnesium was of different thickness. In addition, the amount of time that passed between adherend treatment and bonding procedure was not controlled. These issues prevent direct comparison between the Henkel conversion coatings with the other pretreatments.

A statistically significant effect of time between coating and bonding was found only on samples pretreated with Alodine HC. However, in some cases the high variability of strength values and the low number of samples tested for some configurations resulted in wide confidence intervals. Future research should consider a larger number of test samples for specific pretreatments of interest.

Environmental exposure tests were conducted by means of exposing lap shear joints to a salt spray in an enclosed chamber (ASTM Standard B117). Lap shear joints prepared with DP460NS did not show any significant reduction in strength when exposed for 330 hours. The samples prepared with SA9850

demonstrated a reduction in strength following salt spray exposure for aluminum adherends exposed for 330 hours. This is demonstrated on samples assembled with gritblasted (19.4 MPa reduced to 11.0 MPa) and contaminated adherends (25.4 MPa reduced to 8.5 MPa). This effect was not assessed for magnesium adherends since they were significantly corroded after only 24 hours of exposure due to significant metal loss.

This study also investigated the applicability of numerical methods to predict the response and failure of a lap shear test sample using cohesive elements to represent the adhesive. The shape and loading behaviour were found to be comparable but accurate comparisons with experimental data could not be made as the model predicted exaggerated strain to failure. Multiple studies have concluded that the most directly relevant input variable regarding strain to failure ($G_{II}C$) possessed a strong correlation with bondline thickness, in the sense that lower $G_{II}C$ values are expected for thinner bonds. The $G_{II}C$ values were calculated from thick adherend lap shear tests where the bondline thickness was 1 mm, while this present study uses lap shear joints with bondline thickness of 0.178 mm. Lower value of $G_{II}C$ was therefore expected for this present study, which would result in lower predicted strain to failure.

Pin and collar direct shear tests were conducted on gritblasted steel adherends to investigate the response and failure of adhesive bonds in a pure shear condition over a range of deformation rates. The nominal target deformation rates was $10^{-1}/s$ to $10^2/s$; however, the actual deformation rates achieved were between $4 \times 10^{-3}/s$ and $14/s$. The geometry was beneficial to investigate aspects such as different adherends, bondline thickness, and deformation rate effects.

Accurate displacement information is important for acquiring complete shear characterization data. However, typical adhesive bond thickness ($\sim 0.15\text{mm}$) makes deformation measurement challenging due to deformation of the test sample. For the case of DP460NS joints, the elastic deformation was expected to be on the order of $4 \mu\text{m}$, and failure to occur within $15 \mu\text{m}$. It was concluded that the pin and collar test was not conducive to accurate deformation measurements, partly due to the nature of its geometry which conceals the adhesive bond from direct observation. Measurements can be taken close to the bondline, as was done in this research, but this data was still affected by the deformations of the adherends themselves. It is also problematic to identify the precise point of failure for these joints, as they cannot be determined visually and frictional forces inhibits a significant drop of transferred load at failure.

The video image analysis method produced displacement data that were more accurate in comparison with traditional methods of displacement measurement (e.g. crack opening displacement gauge). This study showed that accuracy of the optical method was highly dependent on the locations of the tracked points on the test sample. A numerical model of the pin and collar joint was developed using a solid element formulation, with a constitutive material model designed specifically for polymers including the

effect of strain rate on material strength. Another is the assumption of asymmetry in the material, which permits multiple force-displacement inputs on the varying modes of loading, as opposed to interpolating them strictly from tension information. Shear characterization studies can benefit more from using geometries where the adhesive bond is exposed, such as a double lap shear test or edge notch flexural tests. Exposed adhesive bonds would allow for direct measurement on the adhesive bond, isolated from adherend deformations, via the developed optical method. However, other methods such as those noted above are not conducive to high deformation rate testing, which is necessary for complete characterization of a material.

Although not ideal for displacement data acquisition, the pin and collar test is conducive for studying the effect of deformation rate to adhesive joint strength. It is easy to conduct on common test rigs, and is also straightforward to adapt to higher rate test apparatus, such as Split-Hopkinson Pressure Bar. The scatter in data acquired was relatively small, and the relationship between deformation rates and the failure strength is much more accurate compared to results acquired by the thick adherend lap shear tests. It was observed that DP460NS and SA9850 exhibited higher strength at higher deformation rates. The shear strength of DP460NS (increase of 7.3 MPa per decade of shear rate) was found to be more rate-dependent compared to SA9850 (increase of 2.4 MPa per decade of shear rate).

In this study, joint performance was measured using single lap shear joints to assess different adherend, surface pretreatment and adhesive combinations. The pin and collar tests provided insight into adhesive bond response during shear loading at various rates, including those associated with vehicle impact scenarios. In general terms, the numerical simulation studies conducted in this research were able to provide insight into the adherend and adhesive bond response during various loading conditions. Issues with specific cases were identified, and suggestions for future efforts include additional testing to provide accurate measures of properties such as fracture energy and failure strain. The information gathered from this study will ultimately aid the implementation of structural adhesives in multi-material lightweight vehicles.

APPENDIX A: TECHNICAL DATA SHEETS

Adhesive: DP460NS

3M

Scotch-Weld™

Epoxy Adhesives

DP460 Off-White • DP460 NS

Technical Data

Product Description	3M™ Scotch-Weld™ Epoxy Adhesives DP460 Off-White and DP460 NS are high performance, two-part epoxy adhesives offering outstanding shear and peel adhesion, and very high levels of durability.
----------------------------	--

Features	<ul style="list-style-type: none"> • High shear strength • High peel strength • Outstanding environmental performance • Easy mixing 	<ul style="list-style-type: none"> • Controlled flow • 60 minute worklife • Non sag (Scotch-Weld DP460 NS)
-----------------	---	---

Typical Uncured Physical Properties **Note: The following technical information and data should be considered representative or typical only and should not be used for specification purposes.**

Product		Scotch-Weld Epoxy Adhesive DP460 Off-White	Scotch-Weld Epoxy Adhesive DP460 NS
Viscosity (approx.) @ 73°F (23°C)	Base Accelerator	20,000-50,000 cps 8,000-14,000 cps	150,000-275,000 cps 8,000-14,000 cps
Base Resin	Base Accelerator	epoxy amine	epoxy amine
Color	Base Accelerator	white amber	white amber
Net Weight Lbs./Gallon	Base Accelerator	9.3-9.7 8.8-9.2	9.3-9.7 8.8-9.2
Mix Ratio (B:A)	Volume Weight	2:1 2:0.96	2:1 2:0.96
Worklife, 73°F (23°C)	20 g mixed 10 g mixed 5 g mixed	60 minutes 75 minutes 90 minutes	60 minutes 60 minutes 60 minutes

Scotch-Weld™
Epoxy Adhesives
 DP460 Off-White • DP460 NS

**Typical Cured
 Thermal Properties**

Note: The following technical information and data should be considered representative or typical only and should not be used for specification purposes.

Product	3M™ Scotch-Weld™ Epoxy Adhesive DP460 Off-White	3M™ Scotch-Weld™ Epoxy Adhesive DP460 NS
Physical Color	Opaque, off-white	Off-white
Shore D Hardness	75-80	78-84
Thermal Coefficient of Thermal Expansion (in./in.°F) Below Tg Above Tg	59 x 10 ⁻⁶ 159 x 10 ⁻⁶	74.44 x 10 ⁻⁶ 166 x 10 ⁻⁶
Thermal Conductivity (btu - ft./ft. ² - hr. - °F) @ 45°C	0.104	0.104
Electrical Dielectric Strength (ASTM D 149)	1100 volts/mil	727 volts/mil
Volume Resistivity (ASTM D 257)	2.4 x 10 ¹⁴ ohm-cm	3.25 x 10 ¹⁵ ohm-cm

**Typical Curing
 Characteristics**

Note: The following technical information and data should be considered representative or typical only and should not be used for specification purposes.

Rate of Strength Build-Up
Aluminum, Overlap Shear (7 mil Bondline) (ASTM D 1002-72)
Bonds Tested at 73°F (23°C)
Scotch-Weld Epoxy Adhesive DP460 Off-White

Time in Oven	Cure Temperature		
	73°F (23°C)	120°F ¹ (49°C)	140°F ¹ (60°C)
30 min.	—	<50	3000/60 ²
60	—	1300	4500/60 ²
90	—	4300/60 ²	—
2 hr.	—	4400/60 ²	4800
3	—	4800/60 ²	—
5	400	—	—
6	1000	—	—
7	3500	—	—
24	4000/60 ²	—	—

Scotch-Weld Epoxy Adhesive DP460 NS

Time in Oven	Cure Temperature		
	73°F (23°C)	120°F ¹ (49°C)	160°F ¹ (71°C)
15 min.	—	—	4860
30	—	10	5250
60	—	2800	5300
2 hr.	1	5050	5470
4	46	5400	5320
6	970	5570	5140
24	4500	—	5210

¹This represents the oven temperature to which the bonds were subjected for the prescribed time. The average bondline temperature during the cure time will be somewhat lower than the oven temperature.

²The value in the denominator is the expected minimum 73°F (23°C) T-peel strength (piw) measured after the indicated cure cycle.

NOTE: The data in this Technical Data Sheet were generated using the 3M™ EPX™ Applicator System equipped with an EPX static mixer, according to manufacturer's directions. Thorough hand-mixing will afford comparable results.

Scotch-Weld™
Epoxy Adhesives
DP460 Off-White • DP460 NS

Storage Store products at 60-80°F (15-27°C) or refrigerate for maximum shelf life.

Shelf Life These products have a shelf life of 15 months in original containers.

Precautionary Information Refer to Product Label and Material Safety Data Sheet for health and safety information before using this product. For additional health and safety information, call 1-800-364-3577 or (651) 737-6501.

For Additional Information To request additional product information or to arrange for sales assistance, call toll free 1-800-362-3550 or visit www.3M.com/adhesives. Address correspondence to: 3M Industrial Adhesives and Tapes Division, Building 21-1W-10, 900 Bush Avenue, St. Paul, MN 55144-1000. Our fax number is 651-778-4244. In Canada, phone: 1-800-364-3577. In Puerto Rico, phone: 1-787-750-3000. In Mexico, phone: 52-70-04-00.

Product Use All statements, technical information and recommendations contained in this document are based upon tests or experience that 3M believes are reliable. However, many factors beyond 3M's control can affect the use and performance of a 3M product in a particular application, including the conditions under which the product is used and the time and environmental conditions in which the product is expected to perform. Since these factors are uniquely within the user's knowledge and control, it is essential that the user evaluate the 3M product to determine whether it is fit for a particular purpose and suitable for the user's method of application.

Warranty and Limited Remedy Unless stated otherwise in 3M's product literature, packaging inserts or product packaging for individual products, 3M warrants that each 3M product meets the applicable specifications at the time 3M ships the product. Individual products may have additional or different warranties as stated on product literature, package inserts or product packages. 3M MAKES NO OTHER WARRANTIES, EXPRESS OR IMPLIED, INCLUDING, BUT NOT LIMITED TO, ANY IMPLIED WARRANTY OF MERCHANTABILITY OR FITNESS FOR A PARTICULAR PURPOSE OR ANY IMPLIED WARRANTY ARISING OUT OF A COURSE OF DEALING, CUSTOM OR USAGE OF TRADE. User is responsible for determining whether the 3M product is fit for a particular purpose and suitable for user's application. If the 3M product is defective within the warranty period, your exclusive remedy and 3M's and seller's sole obligation will be, at 3M's option, to replace the product or refund the purchase price.

Limitation of Liability Except where prohibited by law, 3M and seller will not be liable for any loss or damage arising from the 3M product, whether direct, indirect, special, incidental or consequential, regardless of the legal theory asserted, including warranty, contract, negligence or strict liability.



This Industrial Adhesives and Tapes Division product was manufactured under a 3M quality system registered to ISO 9001 standards.



Industrial Business
Industrial Adhesives and Tapes Division



Recycled Paper
40% pre-consumer
10% post-consumer



Impact Resistant Structural Adhesive SA9850

Preliminary Technical Data Sheet

November 2012

General Description	<p>3M™ Impact Resistant Structural Adhesive SA9850 is a one-part epoxy formulated for steel and aluminum body-in-white joint bonding applications involving high draw lubricant coated weights. It is toughened, designed for impact resistance and can be welded through. It is designed to cure in typical e-coat cycles (minimum bake is 10 minutes at 155 °C and maximum bake is 60 minutes at 190 °C).</p> <p>3M Impact Resistant Structural Adhesive SA9850 is an adhesive product designed to exceed the specifications of the world's automakers. It is available on a limited basis for evaluation in qualified applications. To discuss potential applications, please contact 3M Automotive Division Technical Service.</p>
Product Features	<ul style="list-style-type: none">• Compatible with significant coating weights of draw lubricants of several varieties, including dry lubricants• Excellent environmental durability (to heat, humidity, salt water, solvents)• Robust structural bonding performance; including untreated substrates• Excellent shear and impact peel performance over a wide service temperature range (-40°C to 80°C)• Non-sag adhesive with washout resistance• Compatible with automated application processing
Physical Properties	<p>The product is purple in color and remains purple throughout the bake cycle. It has a high viscosity at room temperature that decreases when heated. To aid in hand dispensing, we recommend heating up to 45°C.</p>
Storage and Handling	<p>When stored frozen, allow to thaw for up to 36 hours at room temperature in the unopened packaging. Do not open the container until the product has warmed to room temperature. The thaw time will vary based on container size. Once the container is opened, it is recommended the product be stored in a plastic bag with desiccant to minimize any humidity exposure when not in use.</p> <p>Dispensing Equipment: Cartridges can be dispensed manually; follow instructions included with the applicator. To aid in hand dispensing, we recommend heating up to 45°C.</p> <p>Clean-Up: Uncured adhesive can be removed by scraping with a putty knife or similar tool. For cured material, remove by cutting or sanding.</p>
Shelf Life	<p>1 month when stored at room temperature 23°C +/- 2°C in the unopened original packaging. 6 months when stored at -18°C or below in the unopened original packaging.</p>

Preliminary Technical Data Sheet

3M™ Impact Resistant Structural Adhesive SA9850

Page 2

Performance Properties The following table contains typical performance properties. Specific performance is dependent upon process conditions, metal type and thickness, and oil used.

Test	Test Condition	Underbake – 155°C for 20 min (MPa unless labeled)	Overbake – 190°C for 70 min (MPa unless labeled)
Lap Shear (ISO 4587)	RT	16.5	17
Lap Shear (ISO 4587)	80°C	12	13
Lap Shear (ISO 4587)	-40°C	19*	19*
Lap Shear after 10 days at 40°C , 100% RH	RT	15	16
T-Peel (ASTM D1876)	RT	200 N/25 mm	225 N/25 mm
Wedge impact peel (ISO 11343)	RT	28 N/mm	30 N/mm
Wedge impact peel (ISO 11343)	-40°C	20 N/mm	25 N/mm

*Metal failure

Notes:

1. All coupons were ACT HDG G70 70U Unpolished Steel. Oil used was Quaker FERROCOTE® 61A-US with a moderate coating weight.
2. All Lap Shear tests measured on 25.4 mm x 101.6 mm x .76 mm coupons using 12.7 mm over-lap bonds. Thickness of the bond line was 0.20 mm. Crosshead speed was 12.7 mm/min.
3. All T-peel tests measured on 25.4 mm x 203.2 mm x .76 mm coupons. Thickness of the bond line was 0.20 mm. Pull speed was 50 mm/minute.
4. All wedge impact test coupons were 20 x 90 mm, steel, with a bond flat of 20 x 30 mm, "symmetric wedge" configuration. Thickness of the bond line was 0.20 mm. An impact head drop rate of 2 m/s was used.

Test	Test Condition	160C for 20 min (MPa unless labeled)
Lap Shear (SAE J1523) - aluminum	RT	19
Lap Shear (ISO 4587) - aluminum	80°C	14
Lap Shear (ISO 4587) - aluminum	-30°C	19
Lap shear after 500 hour salt spray exposure (SAE J1523) – 24 hr test specimen recovery time – e-coated panels	RT	19
Lap shear after 500 hours in 98 +/- 2% RH, 25°C environment (CTUS)– e-coated panels	RT	17
T-Peel (ASTM D1876)	RT	250 N/25 mm
Wedge impact peel (ISO 11343)	RT	25 N/mm

Notes:

1. All coupons were 6111 aluminum. A moderate coating of dry lubricant, Dry Lube E1, was applied to the substrate.
2. All Lap Shear tests measured on 25.4 mm x 101.6 mm x .76 mm coupons using 12.7 mm over-lap bonds. Thickness of the bond line was 0.20 mm. Crosshead speed was 12.7 mm/min.
3. All T-peel tests measured on 25.4 mm x 203.2 mm x .76 mm coupons. Thickness of the bond line was 0.20 mm. Pull speed was 50 mm/minute.
4. All wedge impact test coupons were 20 x 90 mm, 6111 aluminum, with a bond flat of 20 x 30 mm, "symmetric wedge" configuration. Thickness of the bond line was 0.20 mm. An impact head drop rate of 2 m/s was used.

Preliminary Technical Data Sheet

3M™ Impact Resistant Structural Adhesive SA9850

Page 3

Contact Information	<p>The data presented in this preliminary data sheet are best estimates for the current product construction being scaled up. This product is still considered in scale up and changes in product construction or process conditions may occur that can cause subsequent changes in product characteristics or performance. User should not make any business plans in reliance upon the future availability or the current properties of this product.</p> <p>For more information, and help selecting a 3M product for an application, please contact your 3M technical service representative.</p>
----------------------------	---

FERROCOTE is a registered trademark of Quaker Chemical Corporation.
3M is a trademark of 3M Company.

Technical Information: The technical information, recommendations and other statements contained in this document are based upon tests or experience that 3M believes are reliable, but the accuracy or completeness of such information is not guaranteed. **Product Use:** Many factors beyond 3M's control and uniquely within user's knowledge and control can affect the use and performance of a 3M product in a particular application. Given the variety of factors that can affect the use and performance of a 3M product, user is solely responsible for evaluating the 3M product and determining whether it is fit for a particular purpose and suitable for user's method of application.

Warranty, Limited Remedy, and Disclaimer: Unless an additional warranty is specifically stated on the applicable 3M product packaging or product literature, 3M warrants that each 3M product meets the applicable 3M product specification at the time 3M ships the product. 3M MAKES NO OTHER WARRANTIES OR CONDITIONS, EXPRESS OR IMPLIED, INCLUDING, BUT NOT LIMITED TO, ANY IMPLIED WARRANTY OR CONDITION OF MERCHANTABILITY OR FITNESS FOR A PARTICULAR PURPOSE OR ANY IMPLIED WARRANTY OR CONDITION ARISING OUT OF A COURSE OF DEALING, CUSTOM OR USAGE OF TRADE. If the 3M product does not conform to this warranty, then the sole and exclusive remedy is, at 3M's option, replacement of the 3M product or refund of the purchase price.

Limitation of Liability: Except where prohibited by law, 3M will not be liable for any loss or damage arising from the 3M product, whether direct, indirect, special, incidental or consequential, regardless of the legal theory asserted, including warranty, contract, negligence or strict liability.

3M

Automotive Division
3M Center, Building 223-1S-02
St. Paul, MN 55144-1000
www.3M.com/autosolutions
1-800-328-1684

© 3M 2012
Printed in U.S.A.



ISO/TS 16949:2002
File No. A2109

Pretreatment: Alodine 1200



**Surface
Technologies**

Translation of the German Technical Process
Bulletin

Alodine® 1200
two component brush-on
process

Yellow chromating of aluminium

Fields of application:

Alodine® 1200 is a two package chemical used to produce a protective coating on aluminum which ranges in color from light iridescent golden to tan. The process is operated at room temperature. The coating produced minimizes corrosion and provides an improved bond for paint.

Alodine® 1200 is used in an immersion, spray and brush-on application. This Technical Product Bulletin is valid for a brush-on process.

Process components:

Alodine® 1200 is divided in two components:

Alodine® 1200 A - liquid, chromic acid containing component

Alodine® 1200 B - powder, fluoride containing accelerator

Nitric acid (62 %)

Coating bath make-up:

For the preparation of 10 l of the Alodine® 1200 coating solution add to 7 l water under stirring:

Alodine® 1200 A	0,27 kg
Alodine® 1200 B	0,17 kg

Remarks: The tank material containing Alodine® 1200 should be made out of rigid PVC (free of plasticisers) or austenic steel (type 1.4571).
Hooks and basket will have to be made out aluminum, rigid PVC (free of plasticisers) or austenic steel.
Spraying systems, pumps and heat exchangers have to be made out of stainless steel (type 1.4571).
Bathes of Alodine® 1200 as well as its rinsing bathes are not to be discharged into the public sewage system without prior detoxification and neutralization.

Caution: Alodine® 1200 A contains chromium trioxide!
Alodine® 1200 B contains fluorides.

Wear

- Eye goggles
- Rubber gloves
- Acid resistant wear
- Avoid contact with skin
- Provide air circulation

Equipment and chemicals for the analysis: pH-meter

The expiry date of the product is given on the packaging labels.

The expiry date of the product is given on the packaging labels.

This information is based on our current level of knowledge. It is given in good faith but it is not intended to guarantee any particular properties. The users must satisfy themselves that there are no circumstances requiring additional information or precautions or the verification of details given herein.

Henkel Oberflächentechnik GmbH
40191 Düsseldorf
Telefon +49 211 797 3000
Telefax +49 211 798 3636

Henkel Teroson GmbH
Postfach 10 56 20
69046 Heidelberg
Telefon +49 6221 704 0
Telefax +49 6221 704 698

Henkel Oberflächentechnik GmbH
Geschäftseinheit Wasserbehandlung
D-40191 Düsseldorf
Telefon +49 211 797 9190
Telefax +49 211 798 2262

Revision date: 19-04-2001

Pretreatment: Alodine 5200



Type of Bulletin: Technical Process Bulletin
Product Title: ALODINE® 5200 - Dry-in-place
Product View:
Description: Non-chrome conversion coating
Status: complete

Technical Process Bulletin

Technical Process Bulletin No. 236182
This Revision: 05/01/2006

ALODINE® 5200 - Dry-in-place
Non-chrome conversion coating

1. Introduction:

ALODINE 5200 treatment is a chromium free product and specifically formulated for treating non-ferrous alloys. Spray or immersion application may be used. The process provides an excellent base for bonding of adhesives and organic finishes.

2. Operating Summary:

<u>Chemical:</u>	<u>Bath Preparation per 100 gallons:</u>
ALODINE 5200	1.5 to 7.5 gallons
configuration and	(use concentration is surface metal dependant)
<u>Operation and Control (Rinsable):</u>	
Concentration*(points)	2.7 to 7.8
Time*(seconds)	5 to 30 seconds
pH*	2.0 - 3.5
Temperature*(° Fahrenheit)	70° to 100°F
* The actual control ranges used are application specific and will be established through application testing.	

3. The Process:

The complete process sequence normally consists of the following steps:

- A. Alkaline or Acid clean
- B. Water rinse

- C. Water rinse (optional)
- D. Deoxidizer (optional)
- E. Water rinse
- F. D.I. water rinse (desired)
- G. Alodine 5200 dry-in-place conversion coating

4. Materials:

ALODINE 5200
PARCOLENE® 95B Defoamer (only if required for spray)
Testing Reagents and Apparatus

5. Equipment

Process tank, housing, pumps and piping should be fabricated from 316L or 304L stainless steel or polypropylene. The 316L being preferred for maximum tank life. A secondary choice is 316 stainless steel fabricated with approved welding techniques or CPVC plastic.

Heat exchanger plates or other heating devices should be polished 316L stainless steel. All process circulation pump seals, valve seats, door seals, etc., which come into contact with the process solution and occasional acid equipment cleaners, should be EPDM, Viton™ or Teflon™.

Chemical feed pump parts and other elastomers which may come into contact with the concentrated replenishing chemical should be EPDM, Viton or Teflon.

Support equipment available from Henkel Surface Technologies for this process includes: chemical feed pumps, level controls, transfer pumps and bulk storage tanks.

Our sales representative should be consulted for information on Henkel Surface Technologies automatic process control equipment for this process and any additional questions. In addition, the "Henkel Surface Technologies Equipment Design Manual" may be consulted.

All equipment which will be in contact with ALODINE 5200 or processing solution should be thoroughly cleaned prior to use with the process. This includes such items as chemical metering pumps, solution tank, spray nozzles, spray zone shields and housings. Our representative will supply a recommended clean-out procedure which may be followed.

6. Surface Preparation:

Cleaning:

All metal to be treated with the processing solution must be free from grease, oil and other foreign matter before the treatment. Deoxidizing or metal activation may be needed. A complete line of cleaners is available and our representative will recommend the proper one for each installation.

Water Rinsing:

After cleaning, the metal must be thoroughly rinsed with water. The rinse should be overflowed continuously at a rate which will keep it clean and free from scum and contamination. D.I. or R.O. final rinsing is recommended before conversion coating.

7. Treating with the ALODINE 5200 Processing Solution:

Buildup:

Recommended buildup is 1.5 to 7.5 gallons of ALODINE 5200 per 100 gallons of processing solution volume. Higher concentrations may be required in roll applied applications.

Fill the tank about three-fourths full with D.I. water. Add the proper amount of ALODINE 5200 and then add sufficient water to bring the solution up to the working level. Mix thoroughly and heat to the operating temperature. PARCOLENE 95B Defoamer may be used in spray applications. If bath foams, add 0.1 ounce per 100 gallons of PARCOLENE 95B until foam subsides.

Operation:

Time: 5 to 30 seconds
Temperature: Ambient to 100°F

The solution concentration may be increased or reduced to meet specific line conditions. Our representative will assist in establishing the proper concentration.

Replenishment:

ALODINE 5200 Makeup will be used for replenishment, depending on the surface area of metal and type of work processed.

Dry-In-Place solutions and coatings by their very nature must remain free from contamination. As a result proper line design to minimize contamination must be used or the dry-in-place treatment must be frequently replaced.

8. Testing and Control:

Never pipet by mouth, use a pipet filler.

Concentration:

The concentration of the treatment solution is determined by a simple titration.

Since this is a reverse titration, the treatment bath is used to titrate the solution prepared below.

Pipet (or discharge from a buret) exactly 10 ml of Titrating Solution 15 into a 150 ml beaker, add 50 ml of water, then 5 ml of Reagent Solution 44. The endpoint for this titration is reached when the purple color completely disappears resulting in a clear or slightly brown solution.

The concentration may be determined from the following table:

<u>Titration</u> <u>(ml)</u>	<u>Concentration %</u> <u>by volume</u>
27	1.5
20.0	2.2
14.7	3.0
10.8	4.5
9.8	6.0
7.8	7.5

NOTE: The greater the concentration, the lower the number of mls (points) of titration.

pH Adjustment:

When ALODINE 5200 is used as a dry-in-place coating no pH adjustment is desirable. If the pH rises above 3.6 - 3.8 contamination is occurring and the bath should be discarded.

9. After Treatment:

Drying:

The treated metal surface must be dried as quickly as possible to ensure uniform deposition of the coating. The dry-off-unit should be sufficient to remove water, but must not physically disturb the deposited wet film.

Once applied, the treatment solution film must be properly disturbed before it has completely dried. Care must be taken to avoid physical contact with the metal before the film has dried.

10. Storage Requirements:

ALODINE 5200 should be protected from freezing. If the chemical is frozen, it will be irreversibly damaged and should not be used. ALODINE 5200 may precipitate if stored at temperatures below 40° or above 100° Fahrenheit. The product must be stored between 40° and 100° Fahrenheit. If exposed to temperatures outside that range for short periods, the product should be immediately returned to the proper temperature and stirred.

11. Waste Disposal Information:

Applicable regulations covering disposal and discharge of chemicals should be consulted and followed.

Disposal information for ALODINE 5200 is given on the Material Safety Data Sheet.

The processing bath is at pH 3 to 4 and contains fluorides. Waste treatment and neutralization may be required prior to discharge.

12. Precautionary Information:

When handling the chemical product used in this process, the first aid and handling recommendations on the Material Safety Data Sheet for the product should be read, understood, and followed.

The processing solution is acidic and may be irritating to skin and may cause burns to eyes. Avoid contact with skin and eyes. In case of contact follow the recommendations for contact given on the Material Safety Data Sheet for ALODINE 5200.

Testing Reagents and Apparatus
 (Order only those items which are not already on hand)

<u>Code</u>	<u>Quantity</u>	<u>Item</u>
592462	2*	Beaker, 150-ml
	1	Buret Assembly, 25-ml Automatic
595344	2*	Pipet, 10-ml Volumetric
595345	1	Pipet Filler
592499	1	Pitcher, Graduated, Plastic
593842	2.5 L	Reagent Solution 44 (5% H ₂ SO ₄)
592428	1.0 L	Titrating Solution 15 (0.042N KMnO ₄)

* Includes one more than actually required, to allow for possible breakage.

-* * * * *

®Registered trademark of Henkel Corporation.

Henkel Technologies
 32100 Stephenson Highway
 Madison Heights, MI 48071
 Telephone: 248-583-9300
 Fax: 248-583-2976

"The information presented herein is our interpretation of certain test results and field experience to date. This information is not to be taken as warranty or representation for which we assume legal responsibility, nor as permission or recommendation to practice any patented invention without a license. It is offered solely for your consideration, investigation and verification." © Henkel Corporation.

Henkel Technologies
 32100 Stephenson Highway
 Madison Heights, MI 48071
 Telephone: 248-583-9300
 Fax: 248-583-2976

"The information presented herein is our interpretation of certain test results and field experience to date. This information is not to be taken as warranty or representation for which we assume legal responsibility, nor as permission or recommendation to practice any patented invention without a license. It is offered solely for your consideration, investigation and verification." © Henkel Corporation.

Stand vom: gedruckt am: 09/18/2006

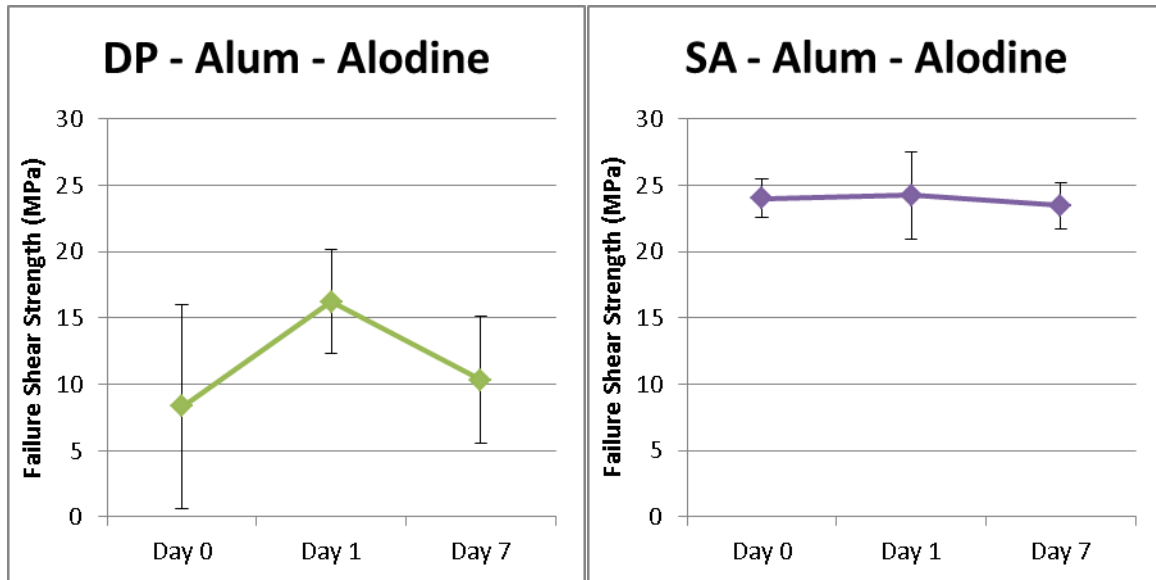
 Verborgene Felder: 3Parker Amchem

Form Revised 04 June 2001

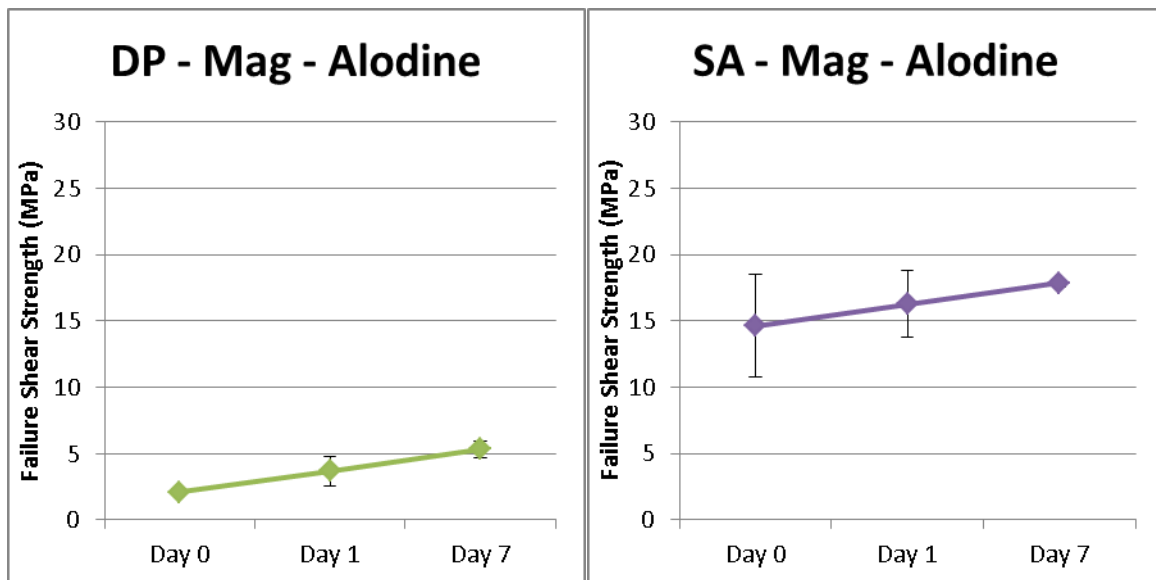
APPENDIX B: LAP SHEAR DATA CHARTS

Pretreatment: Alodine (Test matrix)

Aluminum 6061-T6

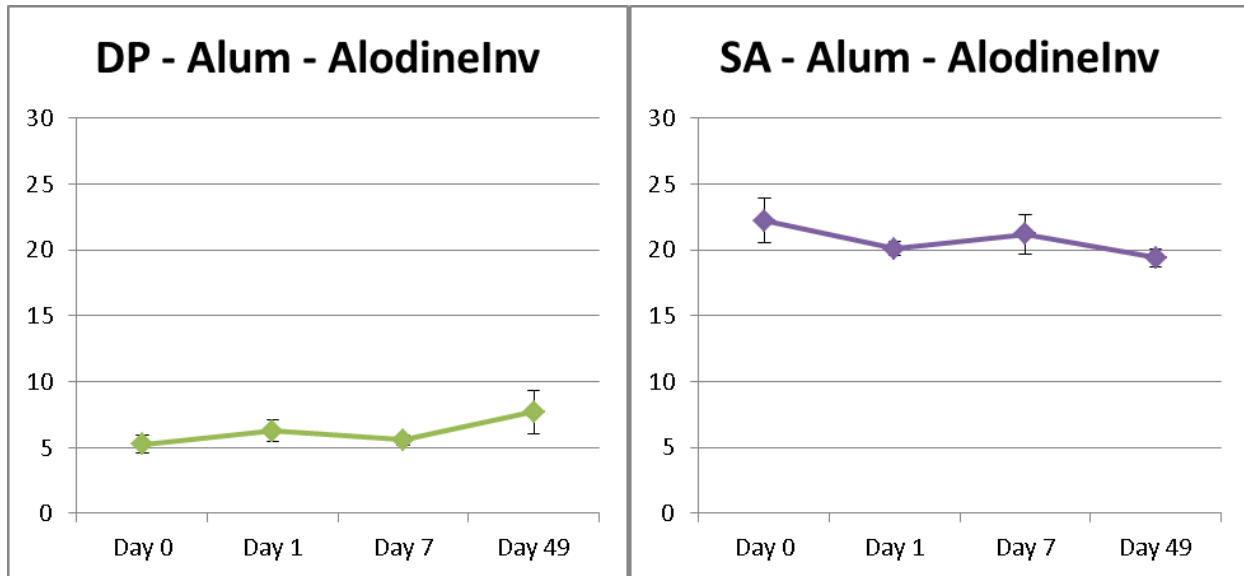


Magnesium AZ31b



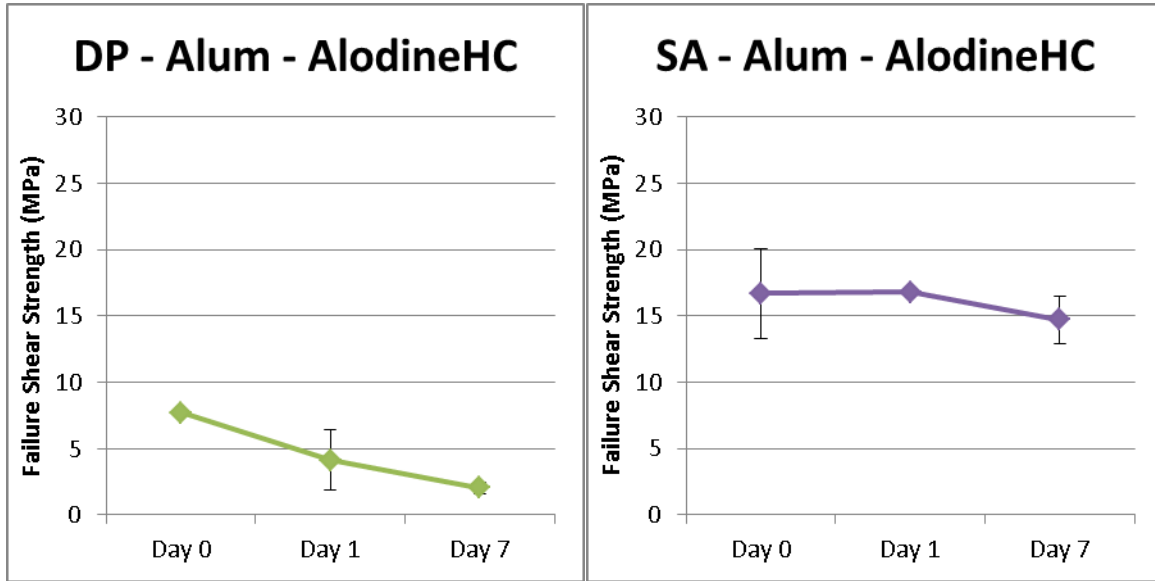
Pretreatment: Alodine (Investigation)

Aluminum 6061-T6

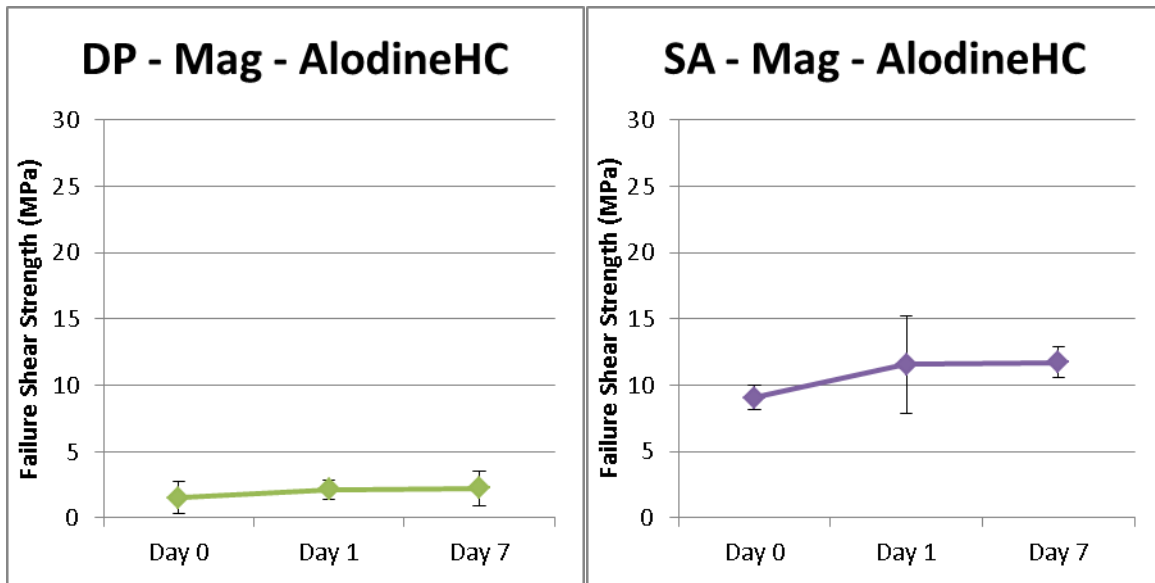


Pretreatment: Alodine HC

Aluminum 6061-T6

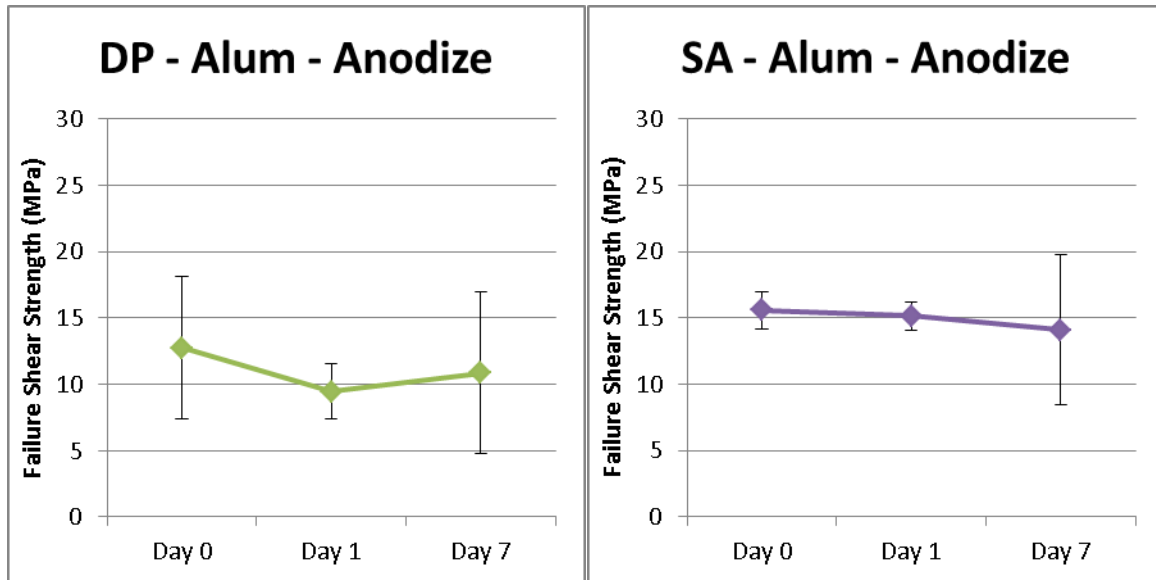


Magnesium AZ31b



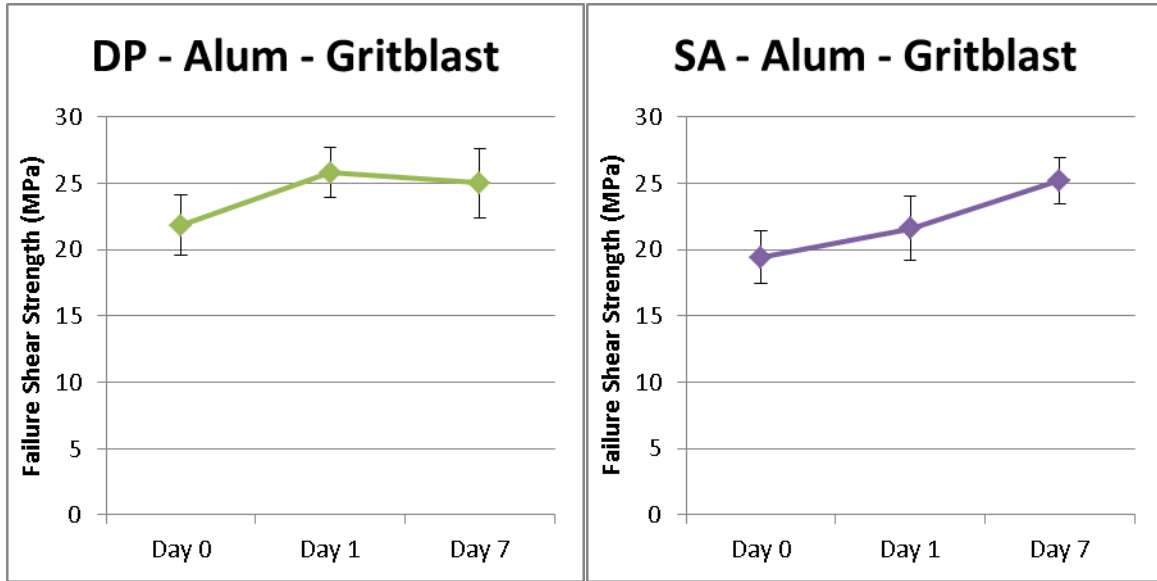
Pretreatment: Anodization

Aluminum 6061-T6

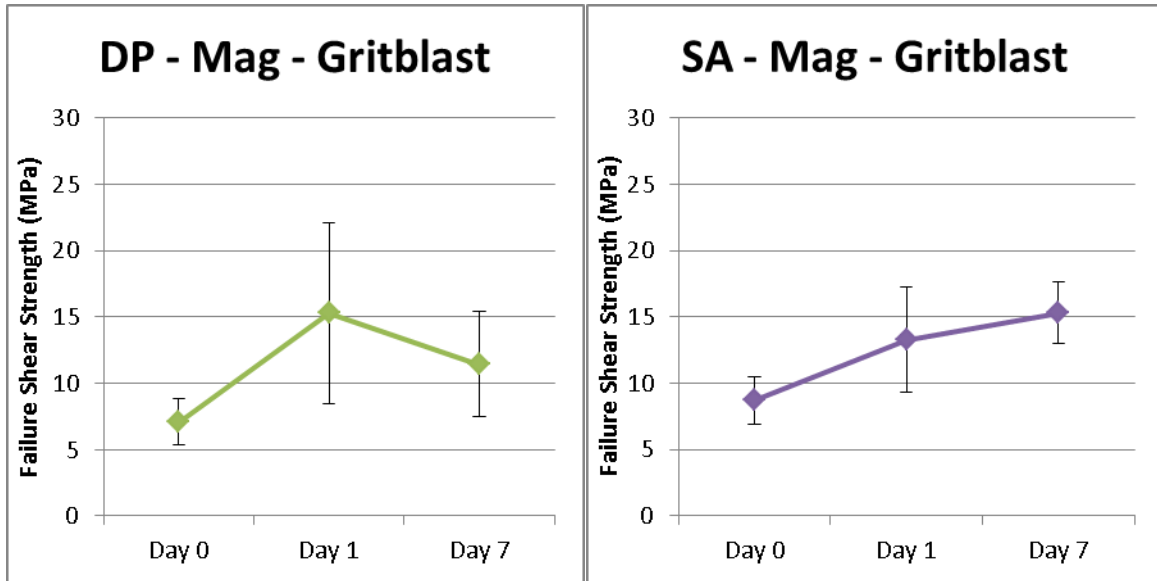


Pretreatment: Gritblasting

Aluminum 6061-T6

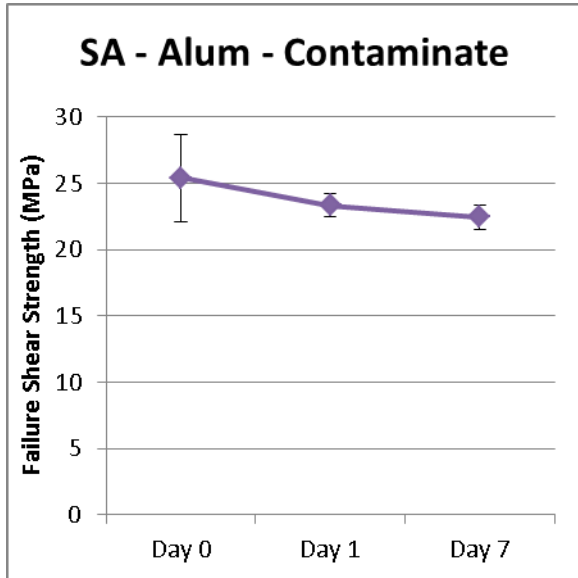


Magnesium AZ31b

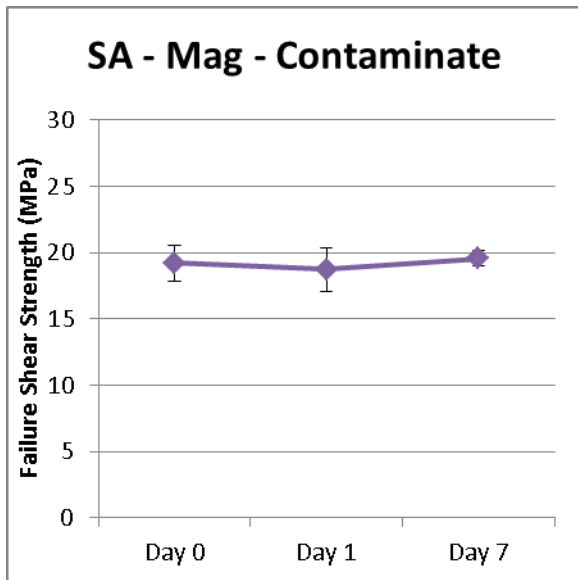


Pretreatment: Contamination

Aluminum 6061-T6

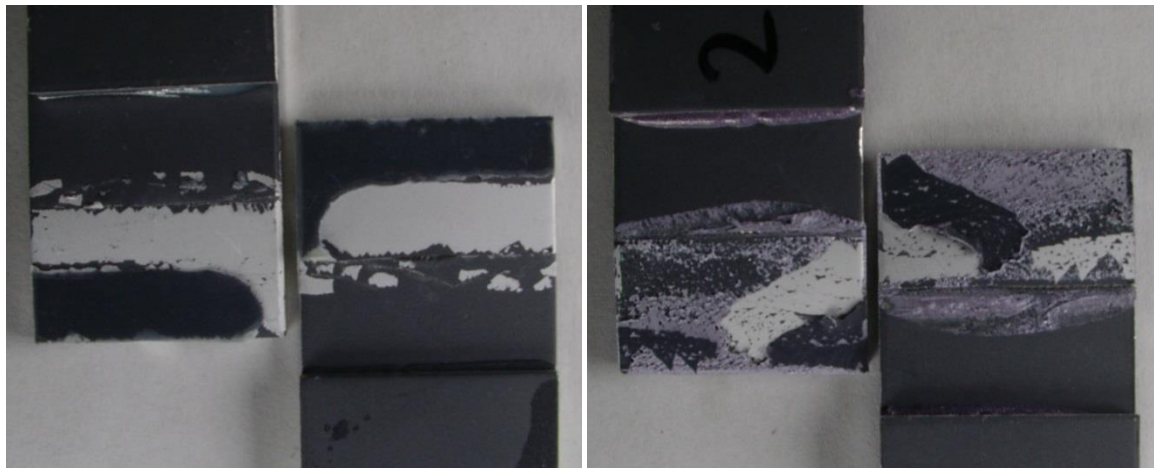
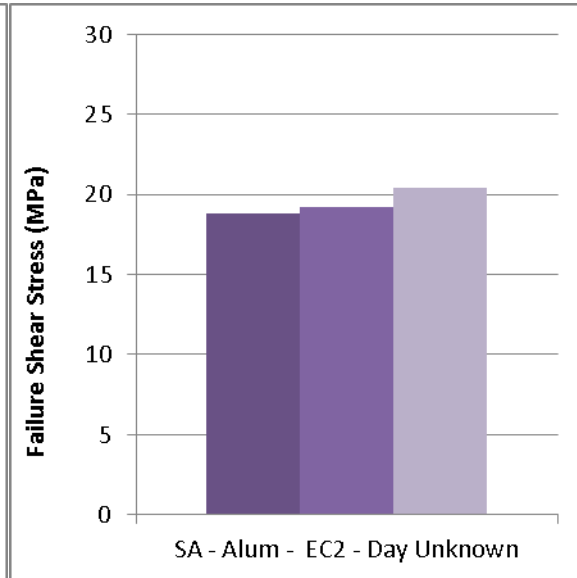
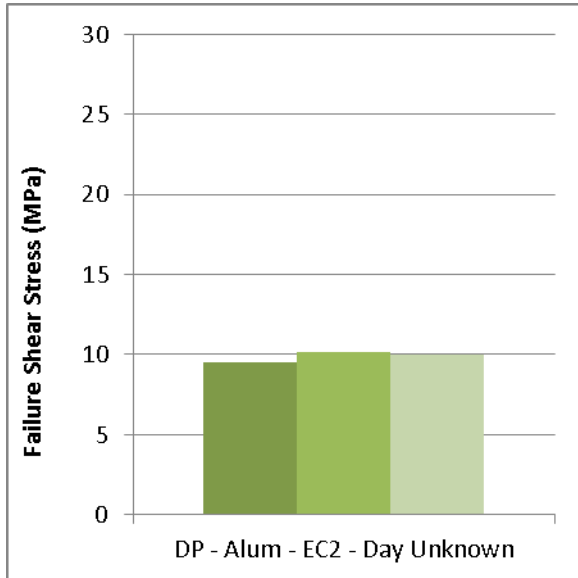


Magnesium AZ31b



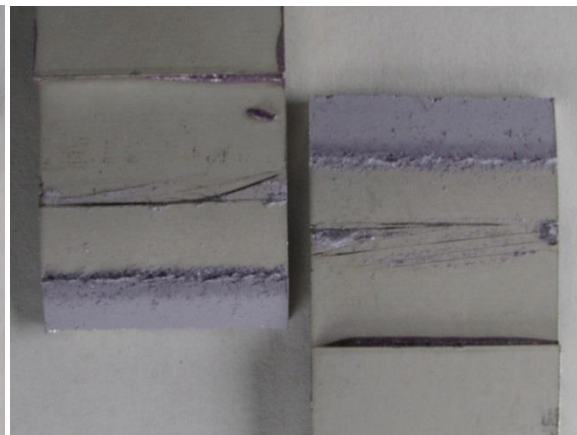
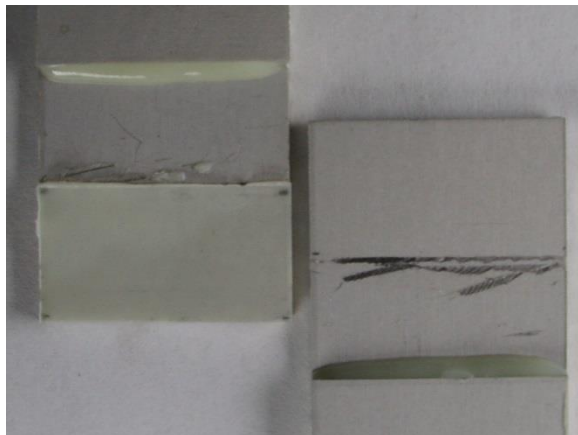
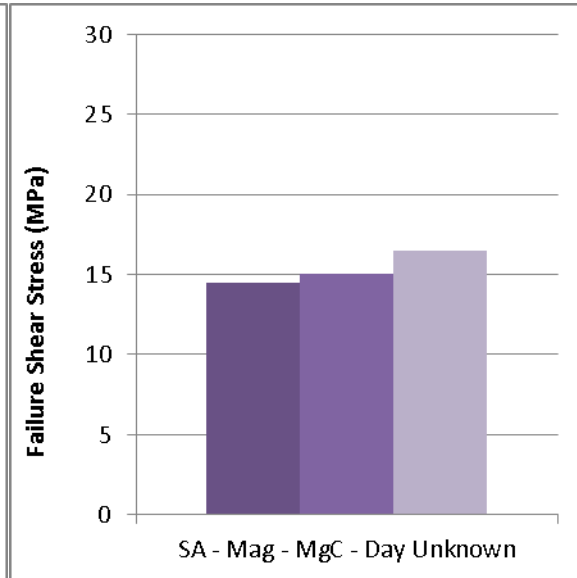
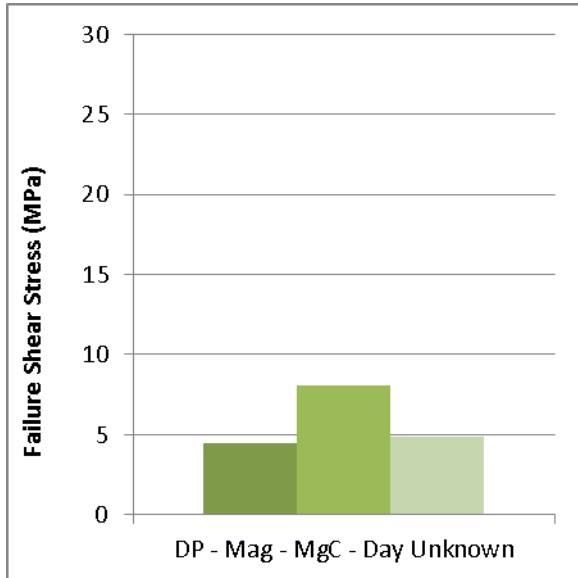
Pretreatment: Henkel Bonderite EC²

Aluminum 5182



Pretreatment: Henkel Bonderite MgC

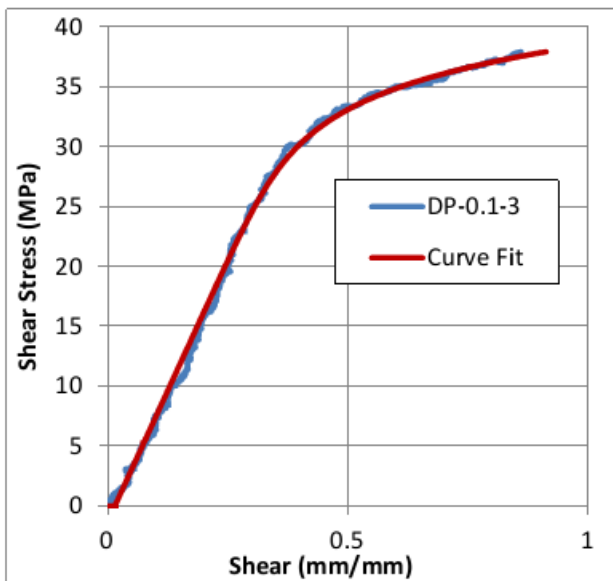
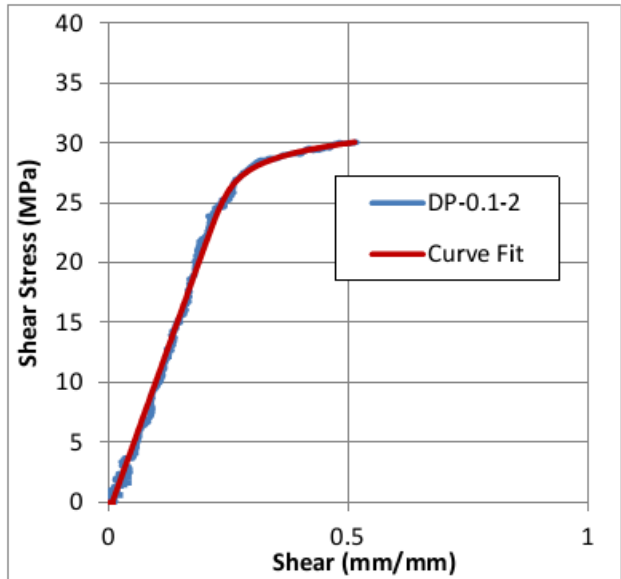
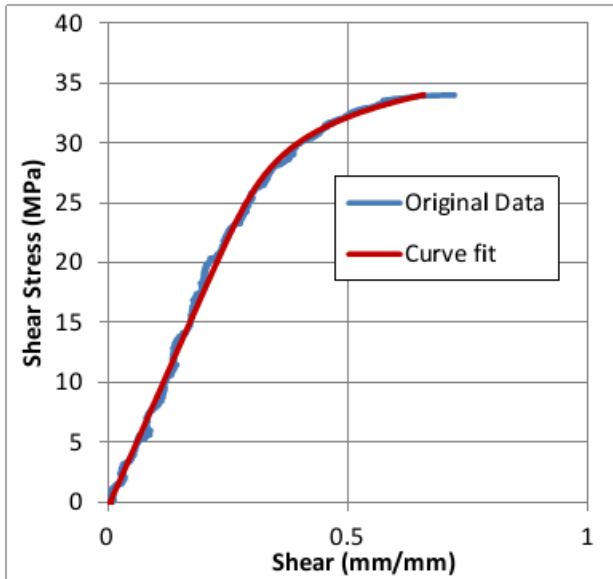
Magnesium ZEK100



APPENDIX C: PIN AND COLLAR DATA CHARTS

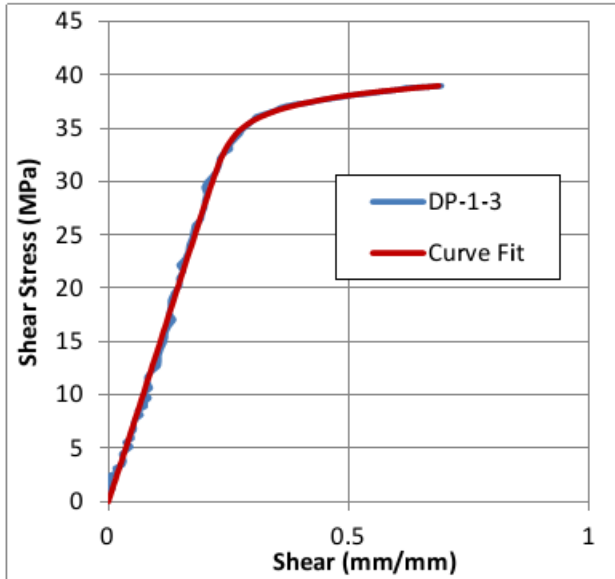
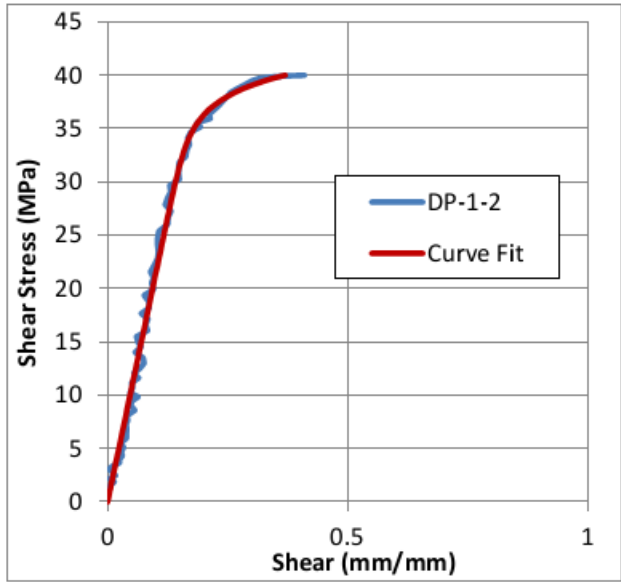
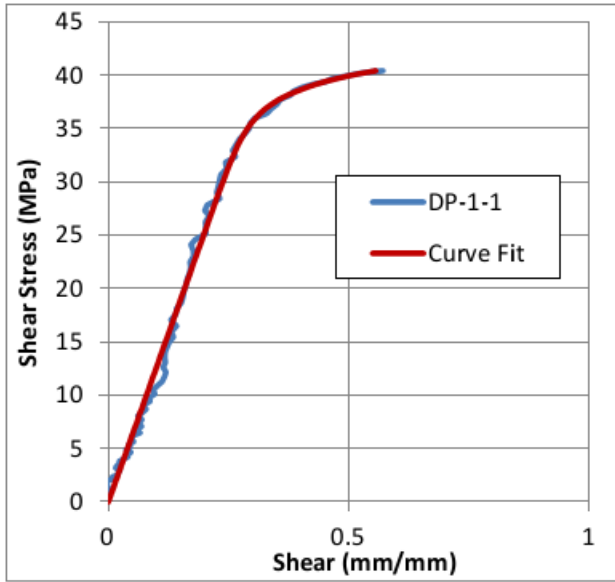
Adhesive: DP460NS

Rate: 0.1/s



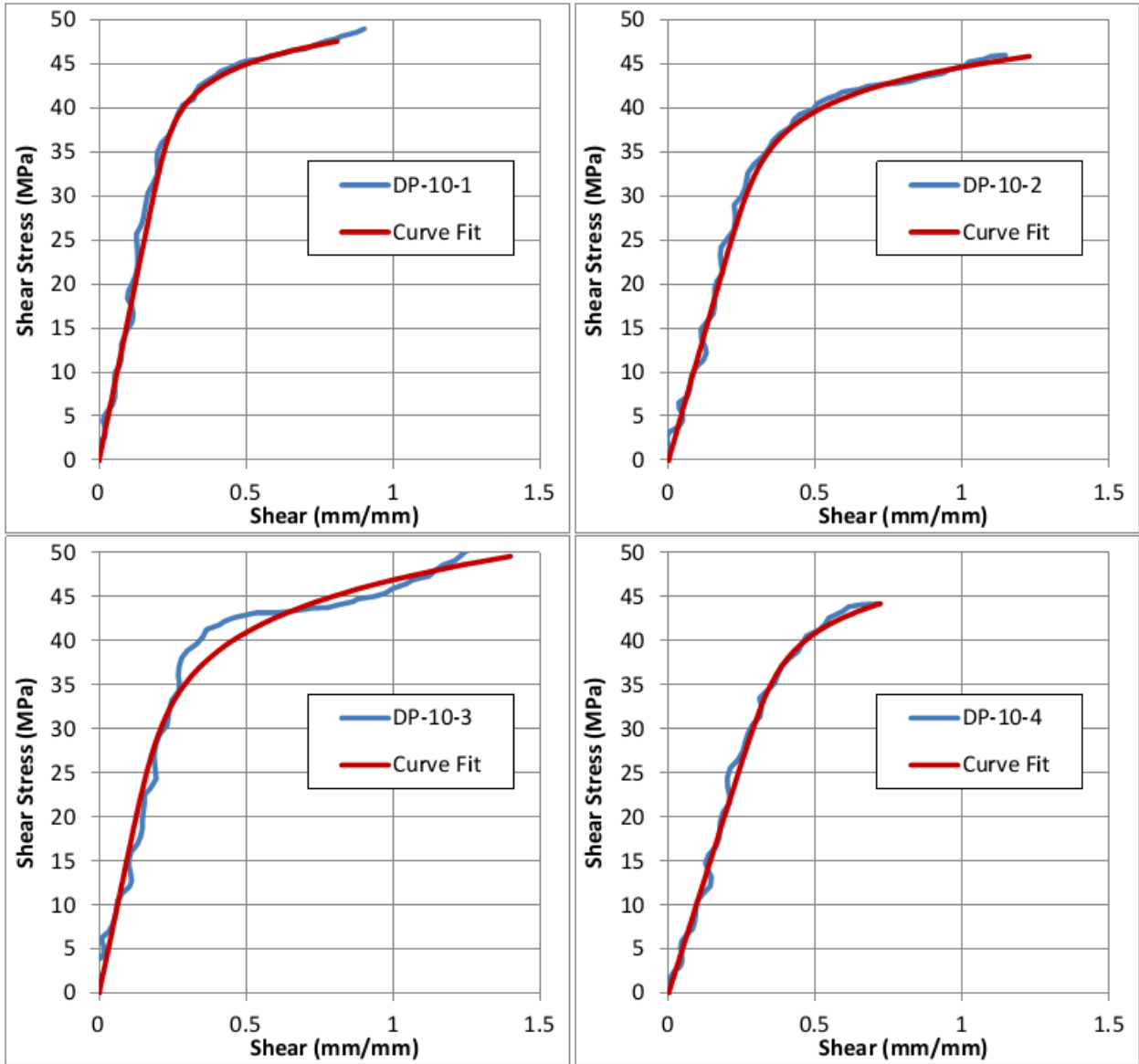
Adhesive: DP460NS

Rate: 1/s



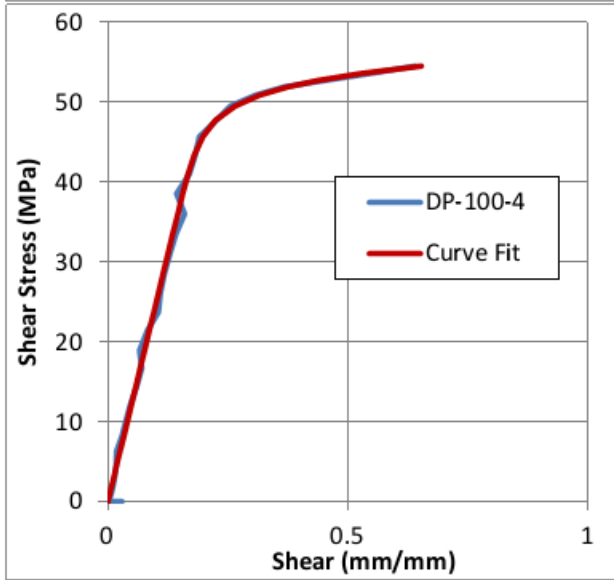
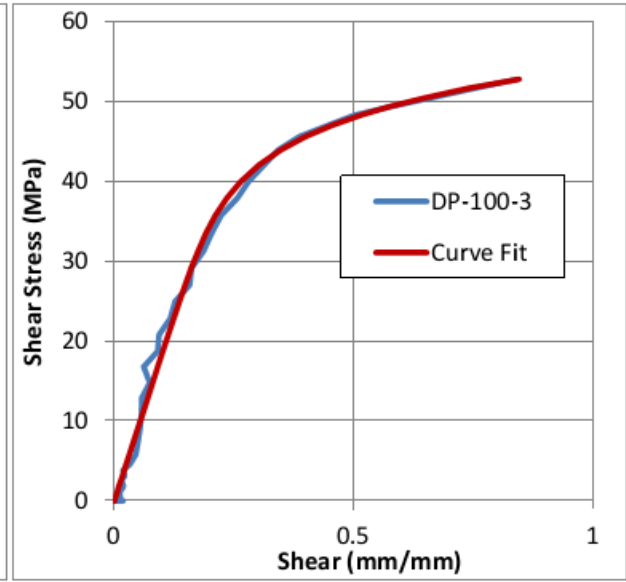
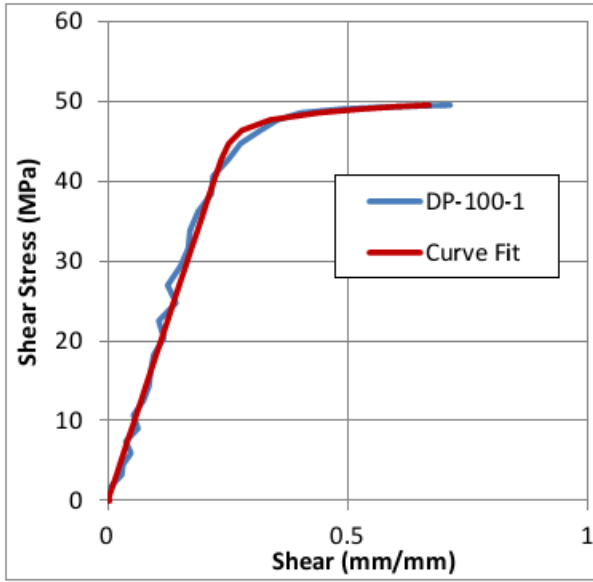
Adhesive: DP460NS

Rate: 10/s



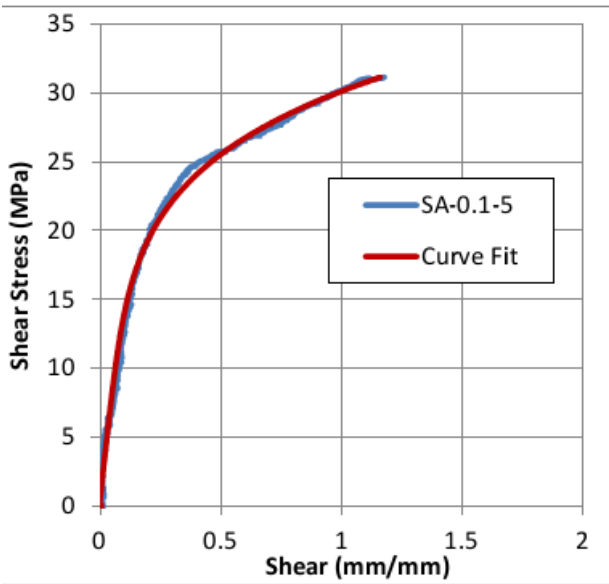
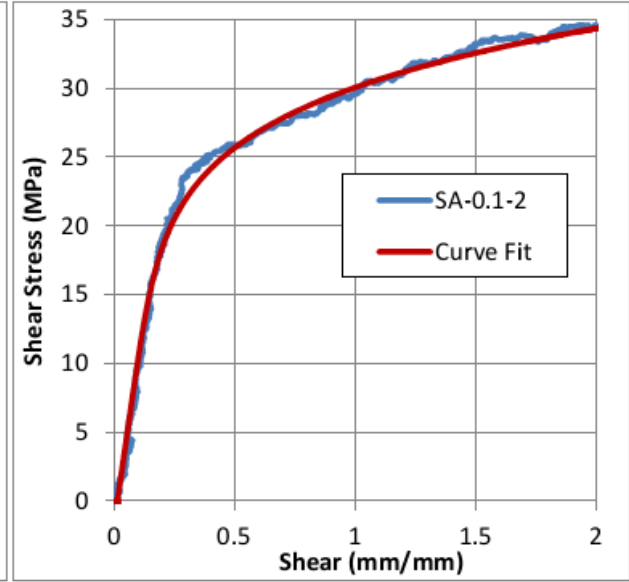
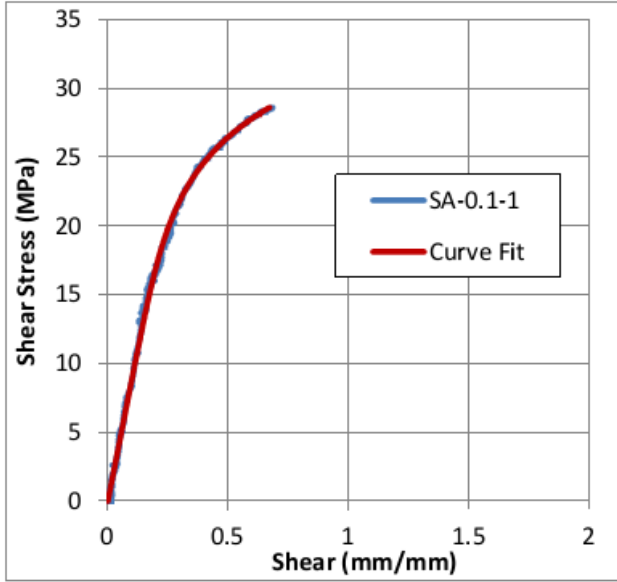
Adhesive: DP460NS

Rate: 100/s



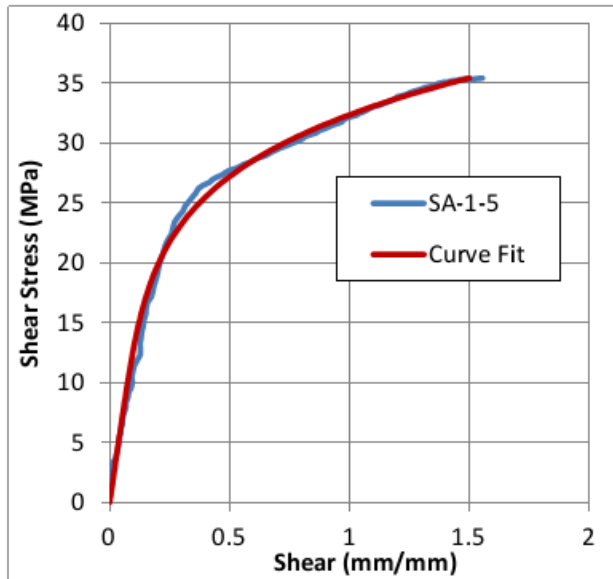
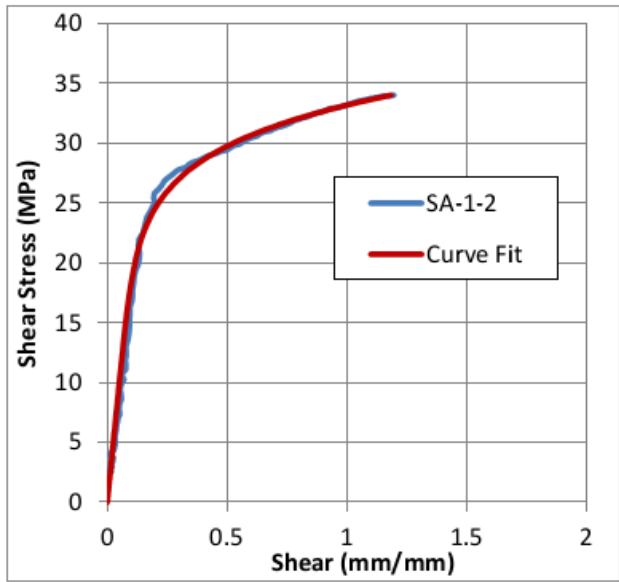
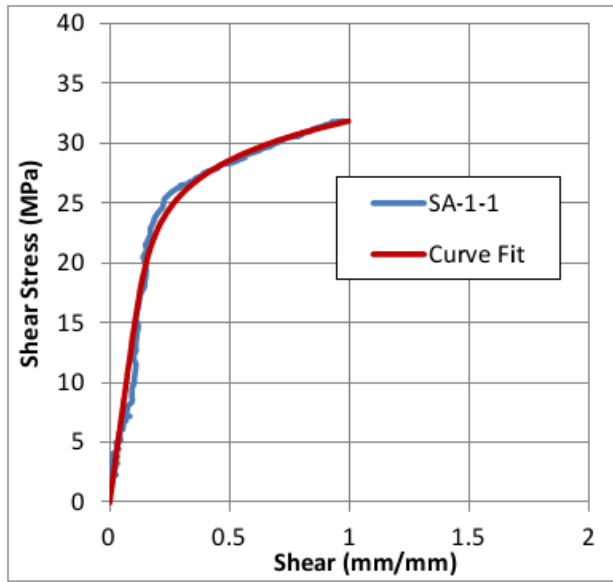
Adhesive: SA9850

Rate: 0.1/s



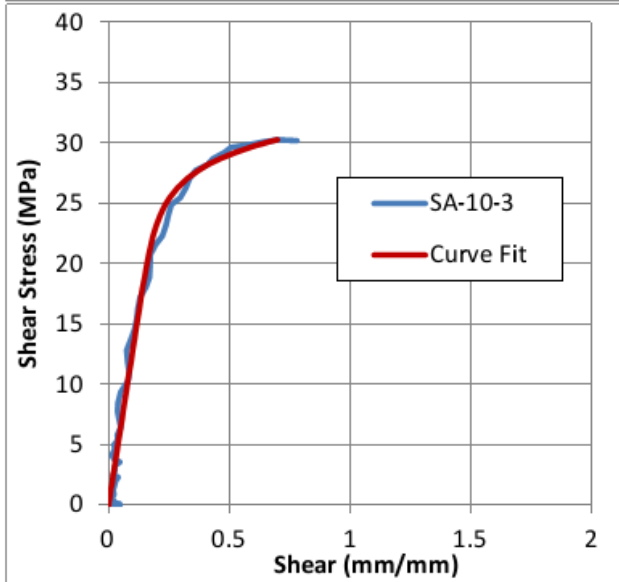
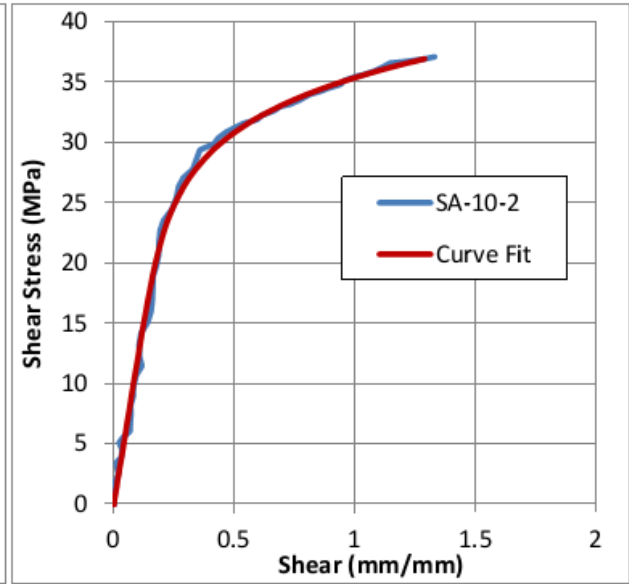
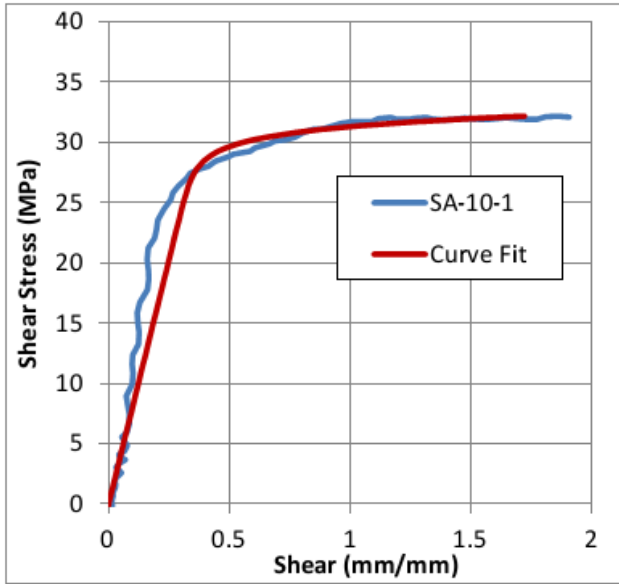
Adhesive: SA9850

Rate: 1/s



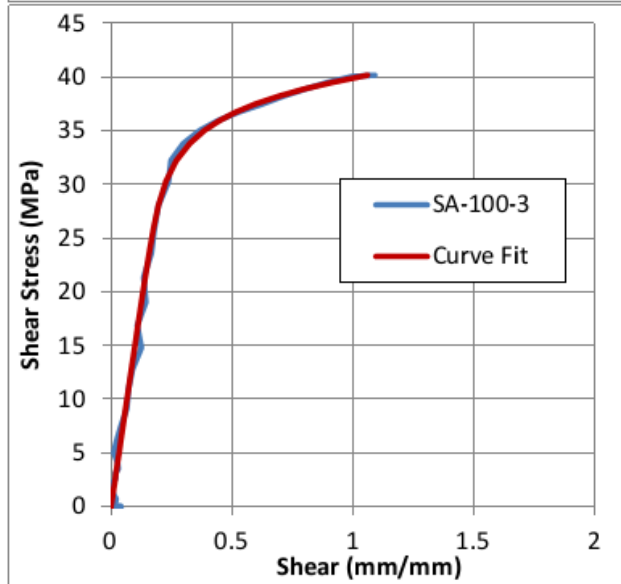
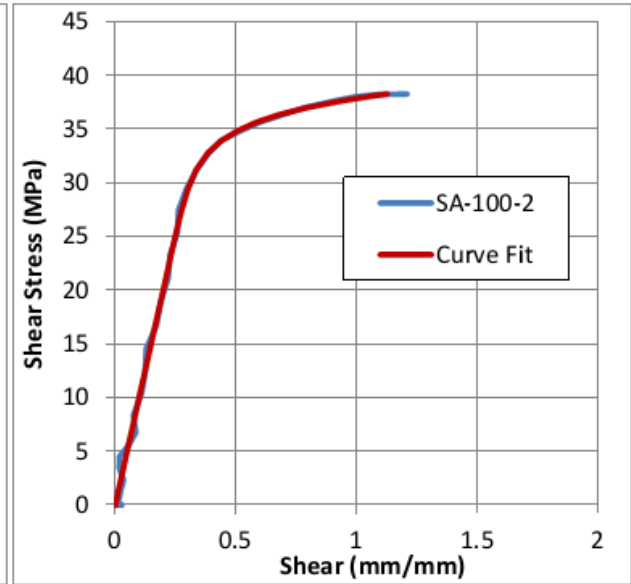
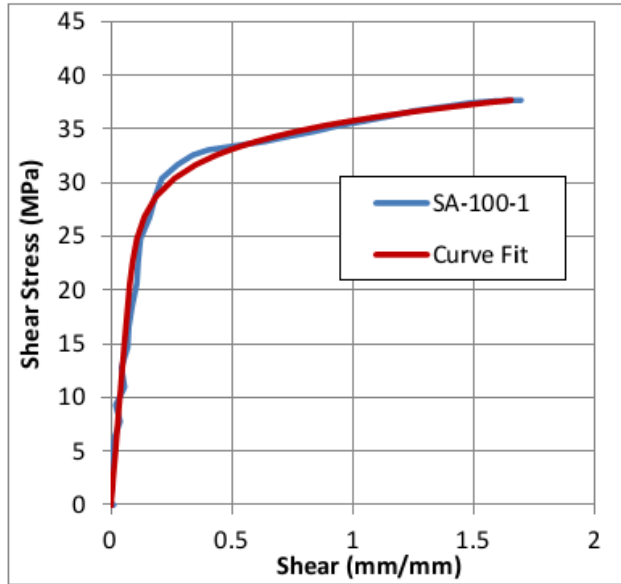
Adhesive: SA9850

Rate: 10/s



Adhesive: SA9850

Rate: 100/s



APPENDIX D: LS-DYNA CARDS

DP460NS cohesive material card

```
*MAT_COHESIVE_GENERAL
$
$
$
$ MATERIAL PROPERTIES DP-460NS USING EXPERIMENTAL DATA; SEE THESIS DOCUMENT ANALYSIS AND PERFORMANCE OF
ADHESIVELY
$ BONDED CRUSH TUBES, BY LUIS F. TRIMINO, UNIVERSITY OF WATERLOO.
$
$ THE VALUES OF T, GIC, GIIC AND TSLC WERE DETERMINED FROM EXPERIMENTAL TESTING
$ USING THE PROCEDURE DESCRIBED IN THE THESIS DOCUMENT
$
$ DAMAGE MODEL (TES) = 0, USES POWER LAW FOR DAMAGE, SEE LS-DYNA MANUAL
$ ALTHOUGH THE LS-DYNA MANUAL LABELS THE ENTRIES IN THE CARDS AS GIC AND GIIC, IT SHOULD BE NOTED THAT
$ THESE VALUES CORRESPONDS TO ENERGY RELEASE RATES. THEY ARE USED INTERCHANGANGEABLY IN THE MANUAL, SEE
MAT_186 VOLUME II
$ LS-DYNA MANUAL
$ NORMAL ENERGY RELEASE RATE ERATEN (LABEL AS GIC IN CARDS)=(KIC)^2 / YOUNG MODULUS = (2.38^2)/2 KIC VALUE
FROM 3M TESTING DATA
$
$ Sy= 37.57 MPA (T)
$ SHEAR STRESS (S) DEFINED FROM LOWEST MEASSURED SHEAR VALUE IN LAP SHEAR TEST AT 0.005 1/S SAMPLE S-14DP
TESTING
$ OCTOBER THE 13 2011 BY J. WEMP
$ A CURVE TO DESCRIBE TRACTION-FORCE MUST BE PROVIDED (TSLC), USED SHEAR LAP TEST STRAIN versus. STRESS CURVE
FROM SAMPLE S-14DP
$ AND NORMALIZED, SELECTED 16 SIGNIFICANT POINTS
$ TO DEFINE ERATES VALUE (LABEL AS GIIC IN CARD) USE  $d=G/(T \times Atsc)$  SEE LS-DYNA MANUAL
$
$MID, RO, ROFLG, INTFAIL, TES, TSLC, GIC, GIIC
31, 1.250E-9, 0, 1, 0, 1000, 2.82061, 3.133205
$UNITS FOR GIC ENTRY ARE MPa x mm WHICH IS CONSISTENT WITH ENERGY RELEASE RATE
$
$XMU, T, S, STFSF
1, 37.57, 20.67, 0
$
$
*DEFINE_CURVE
$ LCID, SIDR, SFA corrected scale of displacement
1000, .22
$
0.00,0.00
0.03,0.73
0.05,0.87
0.07,0.93
0.09,0.97
0.11,0.98
0.22,1.00
0.35,1.00
0.47,0.98
0.55,0.96
0.58,0.92
0.61,0.85
0.64,0.73
0.66,0.62
1.00,0.00
$
```

SA9850 cohesive material card

```
*MAT_COHESIVE_GENERAL
$
$ GIC & GIIC FIT TO TENSILE & LAP SHEAR
$ T FROM TENSILE TEST, S FROM SHEAR TEST
$
$ID, RO, ROFLG, INTFAIL TES, TSLC, GIC, GIIC
$2, 1.20e-9, 0, 1, 0, 1000, 7.68, 5.3
$UPDATE 04/11/2014
$2, 1.20e-9, 0, 1, 0, 1000, 2.974, 1.487
$ UPDATE NOV-26-104
31, 1.20e-9, 0, 1, 0, 1001, 2.974, 8.922
$UNITS FOR GIC ENTRY ARE MPa x mm WHICH IS CONSISTENT WITH ENERGY RELEASE RATE
$
$XMU, T, S, STFSF
$1, 30.55, 20.84, 0
$ UPDATE 04/11/2014
1, 28.19, 24.9, 0
*DEFINE_CURVE
1000
0, 0
0.05, 0.8
0.1, 0.95
0.125, 0.965
0.15, 0.975
0.2, 0.98
0.5, 1
0.65, 0.96
0.75, 0.9
0.8, 0.65
1, 0
$
*DEFINE_CURVE
1001
0.000, 0.000
0.022, 0.296
0.072, 0.699
0.095, 0.739
0.116, 0.749
0.136, 0.754
0.157, 0.759
0.177, 0.765
0.198, 0.773
0.219, 0.781
0.239, 0.789
0.260, 0.798
0.281, 0.806
0.301, 0.814
0.322, 0.821
0.343, 0.829
0.363, 0.836
0.384, 0.844
0.404, 0.852
0.425, 0.860
0.446, 0.868
0.467, 0.877
0.487, 0.886
0.508, 0.895
0.529, 0.905
0.550, 0.914
0.570, 0.923
0.591, 0.931
0.612, 0.940
```

0.632, 0.948
0.653, 0.956
0.674, 0.963
0.694, 0.971
0.715, 0.978
0.735, 0.986
0.756, 0.993
0.777, 1.000
1.000, 0.000
\$

DP460NS SAMP-1 material card

```
*MAT_SAMP-1
$MID, RO, BULK, GMOD, EMOD, NUE
 31, 1.2E-9, 4.04E3, 0.770E3, 2.180E3, 0.41
$LCID-T, LCID-C, LCID-S, LCID-B, NUPE, LCID-P
1, , 10,
$LCID-D, DC, DEPRPT, LCID-TRI, LCID-LC
,,
$MITER, MIPS, IVM, IQUAD, ICONV, ASAF

$ UNIAXIAL TENSILE CURVES
*DEFINE_TABLE_2D
$ CHANGED DEFINITION OF KEYWORD, FROM *DEFINE_TABLE TO *DEFINE_TABLE_2D
$ ID
1
$CARD 2
0.001, 2
0.77, 3
100, 4
$ TENSILE CURVES
$ CURVE FOR 0.001 1/S STRAIN RATE, from file DP-460NS-001-Uniaxial-Plastic
$ THIS CURVE IS NOT MONOTONIC, SO IT CAN HAVE PROBLEMS WITH THE NUMERICAL CONVERGENCE
*DEFINE_CURVE
2
$ PLASTIC STRAIN versus. TRUE SRESS [MPa]
0,35.63
0.00238118,40.06
0.00476236,41.95
0.00714354,42.62
0.00952472,42.72
0.0119059,42.59
0.01428708,42.36
0.01666826,42.13
0.01904944,41.91
0.02143062,41.71
0.0238118,41.55
0.02619298,41.41
0.02857416,41.29
0.03095534,41.19
0.03333652,41.10
0.0357177,41.03
0.03809888,40.96
0.04048006,40.91
0.04286124,40.85
0.04524242,40.81
0.0476236,40.77
0.05000478,40.73
0.05238596,40.70
0.05476714,40.67
0.05714832,40.64
0.0595295,40.61
0.06191068,40.59
0.06429186,40.57
0.06667304,40.55
0.06905422,40.53
0.0714354,40.52
0.07381658,40.50
0.07619776,40.49
0.07857894,40.48
0.08096012,40.47
0.0833413,40.46
$
$ CURVE FOR 0.77 1/S STRAIN RATE from file DP-460NS-077-Uniaxial-Plastic
*DEFINE_CURVE
```

3

\$ PLASTIC STRAIN versus. TRUE STRESS [MPa]

0.000000,40.62
0.002263,48.53
0.004526,52.82
0.006788,55.15
0.009051,56.41
0.011314,57.09
0.013577,57.47
0.015840,57.67
0.018102,57.78
0.020365,57.84
0.022628,57.87
0.024891,57.89
0.027153,57.90
0.029416,57.90
0.031679,57.90
0.033942,57.91
0.036205,57.91
0.038467,57.91
0.040730,57.91
0.042993,57.91
0.045256,57.91
0.047519,57.91
0.049781,57.91
0.052044,57.91
0.054307,57.91
0.056570,57.91
0.058833,57.91
0.061095,57.91
0.063358,57.91
0.065621,57.91
0.067884,57.91
0.070146,57.91
0.072409,57.91
0.074672,57.91
0.076935,57.91
0.079198,57.91

\$

\$ CURVE FOR 100 1/S STRAIN RATE from file DP-460NS-100-Uniaxial-Plastic

*DEFINE_CURVE

4

\$ PLASTIC STRAIN versus. TRUE STRESS [MPa]

0.000000,63.58
0.002033,65.54
0.004067,67.20
0.006100,68.63
0.008134,69.83
0.010167,70.86
0.012201,71.73
0.014234,72.47
0.016268,73.09
0.018301,73.62
0.020335,74.06
0.022368,74.43
0.024402,74.74
0.026435,74.99
0.028468,75.20
0.030502,75.37
0.032535,75.51
0.034569,75.62
0.036602,75.71
0.038636,75.78
0.040669,75.83
0.042703,75.86
0.044736,75.88

APPENDIX E: LAP SHEAR TEST MATHCAD SOLUTION

Solution developed by Goland and Reissner:

Given

$$b := 25.4 \text{ mm}$$

$$L := 12.7 \text{ mm}$$

$$E_a := 218 \text{ GPa}$$

$$LS := \frac{-L}{2}$$

$$LL := \frac{L}{2}$$

$$E := 67.9 \text{ GPa}$$

$$c := 0.5L$$

$$\nu := 0.3$$

$$t_a := 0.1778 \text{ mm}$$

$$\nu_a := 0.4$$

$$t := 1.5875 \text{ mm}$$

$$P := 785 \text{ N}$$

$$\text{Phat} := \frac{P}{b}$$

$$G_a := \frac{E_a}{2(1 + \nu_a)} = 7.73 \times 10^8 \text{ Pa}$$

$$x := LS, LS + 10^{-2} \text{ mm}, LL$$

$$\beta := \sqrt{8 \cdot \frac{G_a \cdot t}{E \cdot t_a}}$$

$$u_2 := \sqrt{\frac{3(1 - \nu^2)}{2} \cdot \frac{1}{t} \cdot \sqrt{\frac{\text{Phat}}{t \cdot E}}}$$

$$k := \frac{\cosh(u_2 \cdot c)}{\cosh(u_2 \cdot c) + 2 \cdot \sqrt{2} \cdot \sinh(u_2 \cdot c)}$$

$$\gamma := \sqrt[4]{6 \cdot \frac{Ea}{E} \cdot \frac{t}{ta}}$$

$$\lambda := \gamma \cdot \frac{c}{t}$$

$$R_1 := \cosh(\lambda) \cdot \sin(\lambda) + \sinh(\lambda) \cdot \cos(\lambda)$$

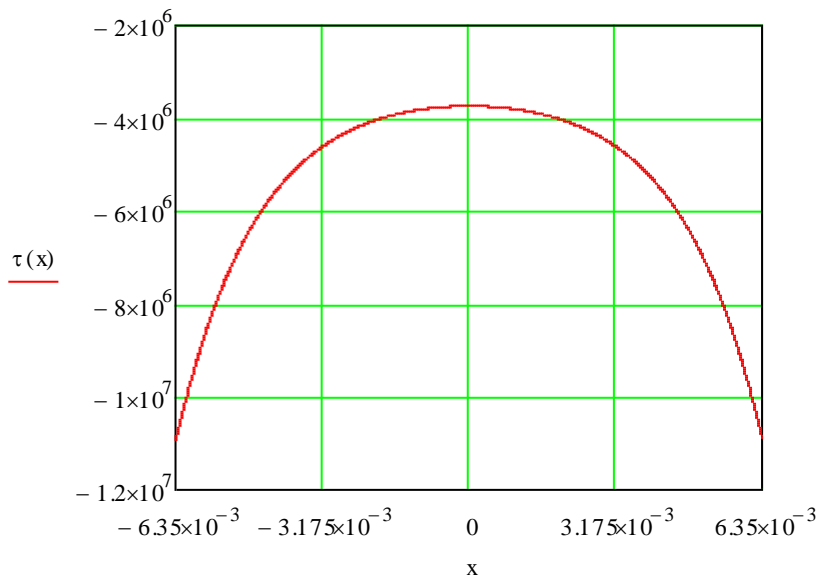
$$R_2 := \cosh(\lambda) \cdot \sin(\lambda) + \sinh(\lambda) \cdot \cos(\lambda)$$

$$\Delta := 0.5(\sin(2 \cdot \lambda) + \sinh(2 \cdot \lambda))$$

$$kmark := \frac{k \cdot c}{t} \cdot \sqrt{3 \cdot (1 - v^2)} \cdot \frac{Phat}{t \cdot E}$$

$$\sigma(x) := \frac{1}{\Delta} \cdot \frac{Phat \cdot t}{c^2} \cdot \left[\left(R_2 \lambda^2 \cdot \frac{k}{2} + \lambda \cdot kmark \cosh(\lambda) \cdot \cos(\lambda) \right) \cdot \cosh\left(\frac{\lambda \cdot x}{c}\right) \cdot \cos\left(\frac{\lambda \cdot x}{c}\right) \dots \right. \\ \left. + \left(R_1 \lambda^2 \cdot \frac{k}{2} + \lambda \cdot kmark \sinh(\lambda) \cdot \sin(\lambda) \right) \cdot \sinh\left(\frac{\lambda \cdot x}{c}\right) \cdot \sin\left(\frac{\lambda \cdot x}{c}\right) \right]$$

$$\tau(x) := \frac{-1}{8} \cdot \frac{Phat}{c} \cdot \left[\frac{\beta \cdot c}{t} \cdot (1 + 3 \cdot k) \cdot \frac{\cosh\left[\left(\frac{\beta \cdot c}{t}\right) \cdot \left(\frac{x}{c}\right)\right]}{\sinh\left(\frac{\beta \cdot c}{t}\right)} + 3 \cdot (1 + k) \right]$$



Solution developed by Hart-Smith.

Given

$$b := 25.4 \text{ mm}$$

$$L := 12.7 \text{ mm}$$

$$E_a := 218 \text{ GPa}$$

$$L_S := \frac{-L}{2}$$

$$L_L := \frac{L}{2}$$

$$E := 67.9 \text{ GPa}$$

$$c := 0.5L$$

$$\nu := 0.3$$

$$t_a := 0.1778 \text{ mm}$$

$$\nu_a := 0.4$$

$$t := 1.5875 \text{ mm}$$

$$P := 785 \text{ N}$$

$$\text{Phat} := \frac{P}{b}$$

$$G_a := \frac{E_a}{2(1 + \nu_a)} = 7.73 \times 10^8 \text{ Pa}$$

$$x := L_S, L_S + 10^{-2} \text{ mm}, L_L$$

$$\lambda_{\text{mark}} := \sqrt{\frac{1 + 3(1 - \nu^2)}{4} \cdot \frac{2 \cdot G_a}{t_a \cdot E \cdot t}}$$

$$D := \frac{E \cdot t^3}{12(1 - \nu^2)}$$

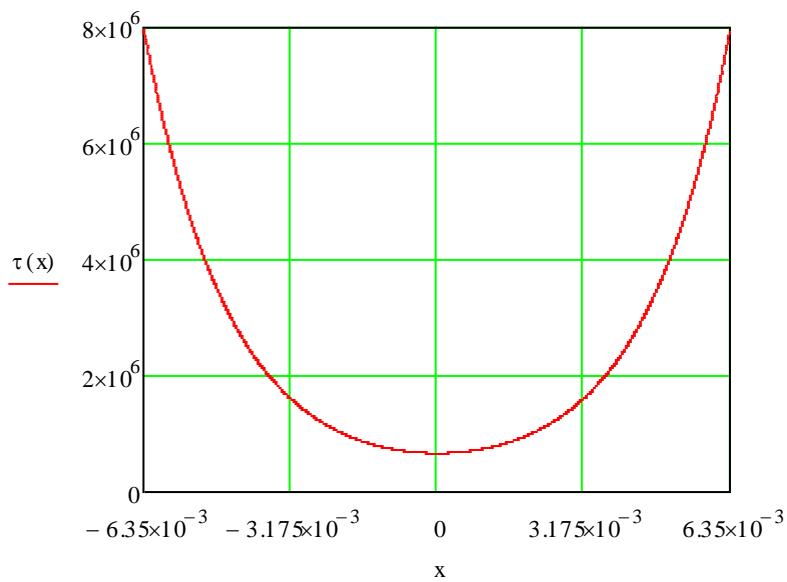
$$\zeta := \sqrt{\frac{\text{Phat}}{D}}$$

$$M := \text{Phat} \cdot \left(\frac{t + t_a}{2} \right) \cdot \frac{1}{1 + \zeta \cdot c + \left(\frac{\zeta^2 \cdot c^2}{6} \right)}$$

$$A2 := \frac{Ga}{t_a \cdot E \cdot t} \left[\text{Phat} + \frac{6 \cdot (1 - \nu^2) \cdot M}{t} \right] \cdot \frac{1}{2 \cdot \lambda_{\text{mark}} \cdot \sinh(2 \cdot \lambda_{\text{mark}} \cdot c)}$$

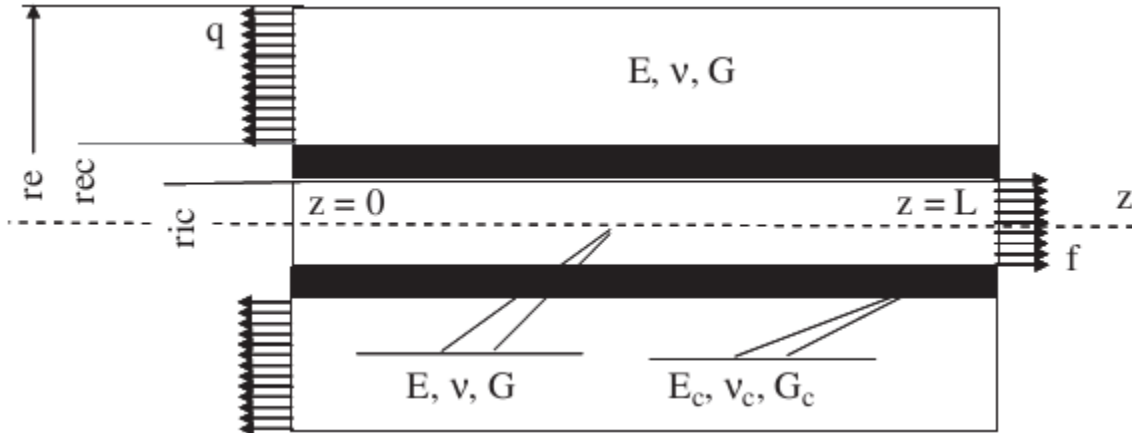
$$C2 := \frac{1}{2 \cdot c} \cdot \left(\text{Phat} - 2 \cdot \frac{A2}{2 \cdot \lambda_{\text{mark}}} \cdot \sinh(2 \cdot \lambda_{\text{mark}} \cdot c) \right)$$

$$\tau(x) := A2 \cdot \cosh(2 \cdot \lambda_{\text{mark}} \cdot x) + C2$$



APPENDIX F: PIN AND COLLAR MATHCAD SOLUTION

Given



$$r_{ic} := 6.35 \cdot 10^{-3}$$

$$r_{ec} := 6.5 \cdot 10^{-3}$$

$$r_e := 12.7 \cdot 10^{-3}$$

$$t = 0.24s, F = 2573.3 \text{ N}$$

$$t = 0.52s, F = 5446.3 \text{ N}$$

$$t = 0.76s, F = 7925.2 \text{ N}$$

$$t = 1.00s, F = 10217.7 \text{ N}$$

$$L := 10.5 \cdot 10^{-3}$$

$$\text{Force} := 2573.3$$

$$A_{\text{collar}} := \pi \cdot (r_e^2 - r_{ec}^2) = 3.74 \times 10^{-4}$$

$$A_{\text{pin}} := \pi \cdot (r_{ic}^2) = 1.267 \times 10^{-4}$$

$$q := \frac{\text{Force}}{\pi \cdot (r_e^2 - r_{ec}^2)} = 6.881 \times 10^6$$

$$f := \frac{\text{Force}}{\pi \cdot (r_{ic}^2)} = 2.031 \times 10^7$$

$$E_{\text{steel}} := 210 \cdot 10^9$$

$$E_{\text{c}} := 254 \cdot 10^6$$

$$\nu_{\text{steel}} := 0.3$$

$$\nu_{\text{c}} := 0.4$$

$$G_{\text{steel}} := \frac{E_{\text{steel}}}{2(1 + \nu_{\text{steel}})} = 7.778 \times 10^{10}$$

$$G_{\text{c}} := \frac{E_{\text{c}}}{2(1 + \nu_{\text{c}})} = 9.007 \times 10^7$$

$$\sigma_{zz}(z) := q - \frac{r_{\text{ic}}^2}{r_{\text{e}}^2 - r_{\text{ec}}^2} \cdot \mathbf{Y}(z)$$

$$\tau_{rz}^{(1)}(r, z) = \frac{(-r^2)}{2 \cdot r} \cdot \frac{d\sigma_{zz}^{(1)}}{dz}$$

$$\sigma_{\theta\theta}^{(1)}(r, z) = \frac{(-r^2)}{2} \cdot \frac{d^2\sigma_{zz}^{(1)}}{dz^2}$$

$$\tau_{rz}(r, z) := \frac{-r^2}{2r} \cdot \left(\frac{d}{dz} \mathbf{Y}(z) \right)$$

$$\sigma_{\theta\theta}(r, z) := \frac{-r^2}{2} \cdot \left(\frac{d^2}{dz^2} \mathbf{Y}(z) \right)$$

$$\tau_{rz}^{(C)}(r, z) = \frac{(-r_{\text{ic}}^2)}{2 \cdot r} \cdot \frac{d\sigma_{zz}^{(1)}}{dz}$$

$$\sigma_{\theta\theta}^{(C)}(r, z) = \frac{(-r_{\text{ic}}^2)}{2} \cdot \frac{d^2\sigma_{zz}^{(1)}}{dz^2}$$

$$\tau_{rz}(r, z) := \frac{-r_{\text{ic}}^2}{2r} \cdot \left(\frac{d}{dz} \mathbf{Y}(z) \right)$$

$$\sigma_{\theta\theta}(r, z) := \frac{-r_{\text{ic}}^2}{2} \cdot \left(\frac{d^2}{dz^2} \mathbf{Y}(z) \right)$$

$$\tau_{yz}^{(2)}(r, z) = \frac{(r_e^2 - r^2) \cdot (r_{ic}^2)}{2 \cdot r \cdot (r_{ec}^2 - r_e^2)} \cdot \frac{d\sigma_{zz}^{(1)}}{dz}$$

$$\sigma_{\theta\theta}^{(C)}(r, z) = \frac{(r_e^2 - r^2) \cdot (r_{ic}^2)}{2 \cdot (r_{ec}^2 - r_e^2)} \cdot \frac{d^2\sigma_{zz}^{(1)}}{dz^2}$$

$$\tau_{rz}(r, z) := \frac{(r_e^2 - r^2)r_{ic}^2}{2r(r_{ec}^2 - r_e^2)} \cdot \left(\frac{d}{dz} Y(z) \right)$$

$$\sigma_{\theta\theta}(r, z) := \frac{(r_e^2 - r^2)r_{ic}^2}{2(r_{ec}^2 - r_e^2)} \cdot \left(\frac{d^2}{dz^2} Y(z) \right)$$

$$\zeta_{pin}(z) := \int_0^{r_{ic}} \left(\frac{\sigma_{\theta\theta}(r, z)^2}{E_{steel}} + \frac{Y(z)^2}{E_{steel}} - \frac{2 \cdot v_{steel} \cdot Y(z) \cdot \sigma_{\theta\theta}(r, z)}{E_{steel}} + \frac{\tau_{rz}(r, z)^2}{G_{steel}} \right) r dr$$

$$A1 := \frac{r_{ic}^2 \cdot Y(z)^2}{2 \cdot E_{steel}}$$

$$C1 := \frac{r_{ic}^4 \cdot \left(\frac{d}{dz} Y(z) \right)^2}{16 G_{steel}}$$

$$B1 := \frac{r_{ic}^4 \cdot v_{steel} \cdot Y(z) \cdot \frac{d^2}{dz^2} Y(z)}{4 \cdot E_{steel}}$$

$$H1 := \frac{r_{ic}^6 \cdot \left(\frac{d^2}{dz^2} Y(z) \right)^2}{24 E_{steel}}$$

$$\zeta_{c1}(z) := \int_{r_{ic}}^{r_{ec}} \left(\frac{1}{E_c} \right) \left(\sigma_{\theta\theta}(r, z)^2 \right) r dr \rightarrow 1.5422883720703125e-24 \left(\frac{d^2}{dz^2} Y(z) \right)^2$$

$$\int_{r_{ic}}^{r_{ec}} \frac{r_{ic}^4 \cdot (2 \cdot v_c + 2)}{4 \cdot E_c \cdot r} dr \cdot \left(\frac{d}{dz} Y(z) \right)^2 \rightarrow \left(\frac{d}{dz} Y(z) \right)^2 \cdot \int_{0.00635}^{0.0065} \frac{4.512843796875e-18}{r} dr$$

$$\zeta_c2(z) := \int_{r_{ic}}^{r_{ec}} \left(\frac{1}{E_c} \right) \left[2 \cdot (1 + \nu_c) \cdot \tau_{rz}(r, z)^2 \right] r dr \rightarrow \int_{0.00635}^{0.0065} \frac{4.512843796875e-18 \left(\frac{d}{dz} Y(z) \right)^2}{r} dr$$

$$C2 := \frac{r_{ic}^4 \cdot \left(\frac{d}{dz} Y(z) \right)^2 \cdot (\ln(r_{ec}) - \ln(r_{ic})) \cdot (\nu_c + 1)}{2 \cdot E_c}$$

$$H2 := \frac{r_{ic}^4 \cdot \left(\frac{d^2}{dz^2} Y(z) \right)^2 \cdot (r_{ec}^2 - r_{ic}^2)}{8 \cdot E_c}$$

$$\zeta_P(z) := \pi \cdot \int_0^L \zeta_{pin}(z) dz + \pi \cdot \int_0^L \zeta_c(z) dz + \pi \cdot \int_0^L \zeta_{col}(z) dz$$

$$\zeta_{co1}(z) := \int_{r_{ec}}^{r_e} \left(\frac{\sigma_{2\theta\theta}(r, z)^2}{E_{steel}} \right) r dr \rightarrow 3.8402304147619047618e-26 \left(\frac{d^2}{dz^2} Y(z) \right)^2$$

$$H3 := \frac{r_{ic}^4 \cdot \left(\frac{d^2}{dz^2} Y(z) \right)^2 \cdot (r_e^2 - r_{ec}^2)}{24 E_{steel}}$$

$$\left[q \cdot (r_{ec}^2 - r_e^2) + Y(z) \cdot r_{ic}^2 \right]^2$$

$$\zeta_{co2}(z) := \int_{r_{ec}}^{r_e} \left(\frac{\sigma_{2zz}(z)^2}{E_{steel}} \right) r dr$$

$$K := \frac{(q^2 \cdot r_e^4 - 2 \cdot q^2 \cdot r_e^2 \cdot r_{ec}^2 + q^2 \cdot r_{ec}^4)}{[2 \cdot E_{steel} \cdot (r_e^2 - r_{ec}^2)]} \text{ simplify } \rightarrow 0.0134195788359236658$$

$$D := \frac{(-2 \cdot q \cdot r_e^2 \cdot r_{ic}^2 \cdot Y(z) + 2 \cdot q \cdot r_{ec}^2 \cdot r_{ic}^2 \cdot Y(z))}{[2 \cdot E_{steel} \cdot (r_e^2 - r_{ec}^2)]} \rightarrow \text{simplify } \rightarrow -1.3212219645010321633e-9 \cdot Y(z)$$

$$\zeta_{co3}(z) := \int_{r_{ec}}^{r_e} \left(\frac{-2 \cdot v_{steel} \cdot \sigma_{zz}(z) \cdot \sigma_{\theta\theta}(r, z)}{E_{steel}} \right) r dr$$

$$A2 := \frac{(r_{ic}^4 \cdot Y(z)^2)}{[2 \cdot E_{steel} \cdot (r_e^2 - r_{ec}^2)]}$$

$$F := \frac{-r_{ic}^2 \cdot v_{steel} \cdot \frac{d^2}{dz^2} Y(z) \cdot (q \cdot r_{ec}^2 - q \cdot r_e^2)}{4 \cdot E_{steel}} \text{ simplify } \rightarrow 1.3761847982242751012e-14 \frac{d^2}{dz^2} Y(z)$$

$$\zeta_{co4}(z) := \int_{r_{ec}}^{r_e} \frac{\tau_{rz}(r, z)^2}{G_{steel}} \cdot r dr$$

$$B2 := \frac{r_{ic}^2 \cdot v_{steel} \cdot \frac{d^2}{dz^2} Y(z) \cdot (Y(z) \cdot r_{ic}^2)}{4 \cdot E_{steel}} \text{ simplify } \rightarrow -6.7746000260416666667e-22 Y(z) \cdot \frac{d^2}{dz^2} Y(z)$$

$$C3 := \frac{r_{ic}^4 \cdot \left(\frac{d}{dz} Y(z) \right)^2 \cdot \left(r_e^4 \cdot \ln(r_{ec}) - r_e^4 \cdot \ln(r_e) + \frac{3 \cdot r_e^4}{4} + \frac{r_{ec}^4}{4} - r_e^2 \cdot r_{ec}^2 \right)}{4 \cdot G_{steel} \cdot r_e^4 - 8 \cdot G_{steel} \cdot r_e^2 \cdot r_{ec}^2 + 4 \cdot G_{steel} \cdot r_{ec}^4}$$

$$A := \frac{A1}{Y(z)^2} + \frac{A2}{Y(z)^2} \rightarrow 1.2852611379628296211e$$

$$B := \frac{B1}{\left(Y(z) \cdot \frac{d^2}{dz^2} Y(z) \right)} + \frac{B2}{\left(Y(z) \cdot \frac{d^2}{dz^2} Y(z) \right)} \rightarrow 0.$$

$$C := \frac{C1}{\left(\frac{d}{dz} Y(z) \right)^2} + \frac{C2}{\left(\frac{d}{dz} Y(z) \right)^2} + \frac{C3}{\left(\frac{d}{dz} Y(z) \right)^2} \rightarrow 1.0509037280350952877e$$

$$D := \frac{D}{Y(z)} \rightarrow -1.3212219645010321633$$

$$\underline{\underline{H}} := \frac{H1}{\left(\frac{d^2}{dz^2}Y(z)\right)^2} + \frac{H2}{\left(\frac{d^2}{dz^2}Y(z)\right)^2} + \frac{H3}{\left(\frac{d^2}{dz^2}Y(z)\right)^2} \rightarrow 1.5936987147679346478e$$

$$K \rightarrow 0.0134195788359236658$$

$$\underline{\underline{F}} := \frac{F}{\frac{d^2}{dz^2}Y(z)} \rightarrow 1.3761847982242751012e$$

$$a := \frac{\sqrt{2\sqrt{(B-C)^2 - 4\cdot A\cdot H - B + C}}}{2\cdot\sqrt{H}} = 254.351$$

$$b := \frac{\sqrt{\sqrt{(B-C)^2 - 4\cdot A\cdot H + B - C} \cdot \sqrt{\frac{-2}{H}}}}{2} = -35.307$$

$$Y(z) := \frac{-D}{2A} + M1\cdot e^{a\cdot z} + M2\cdot e^{-a\cdot z} + M3\cdot e^{b\cdot z} + M4\cdot e^{-b\cdot z}$$

$$\text{MATRIX1} := \begin{pmatrix} 1 & 1 & 1 & 1 \\ e^{a\cdot L} & e^{-a\cdot L} & e^{b\cdot L} & e^{-b\cdot L} \\ a & -a & b & -b \\ a\cdot e^{a\cdot L} & -a\cdot e^{-a\cdot L} & b\cdot e^{b\cdot L} & -b\cdot e^{-b\cdot L} \end{pmatrix}$$

$$\text{MATRIX2} := \begin{pmatrix} \frac{D}{2\cdot A} \\ f + \frac{D}{2A} \\ 0 \\ 0 \end{pmatrix}$$

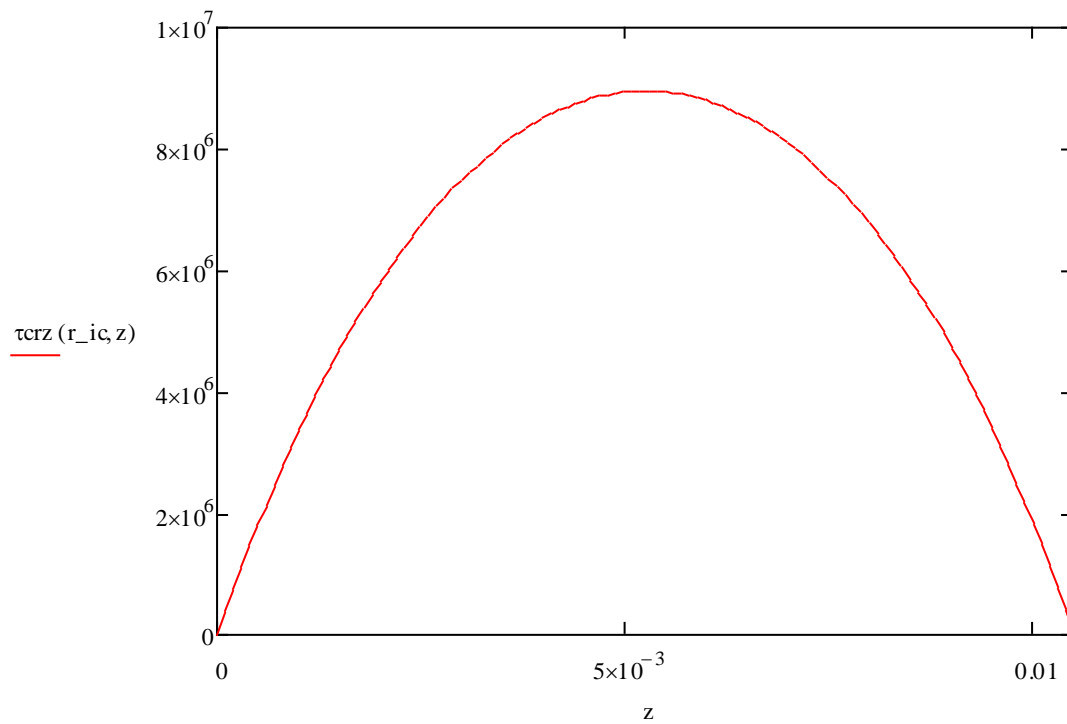
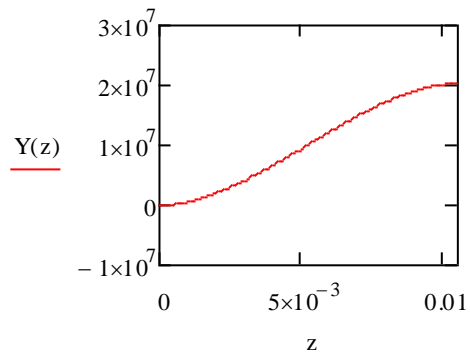
$$\begin{pmatrix} M1 \\ M2 \\ M3 \\ M4 \end{pmatrix} := \text{MATRIX1}^{-1} \cdot \text{MATRIX2} = \begin{pmatrix} -1.472 \times 10^6 \\ 2.098 \times 10^7 \\ -9.321 \times 10^7 \\ 6.855 \times 10^7 \end{pmatrix}$$

$$z := 0, 10^{-4} \dots L$$

$$Y(z) := \frac{-D}{2A} + M1 \cdot e^{a \cdot z} + M2 \cdot e^{-a \cdot z} + M3 \cdot e^{b \cdot z} + M4 \cdot e^{-b \cdot z}$$

$$\tau_{crz}(r, z) := \frac{(-r_{ic})^2}{2r} \cdot \left(\frac{d}{dz} Y(z) \right)$$

$$\alpha_{\theta\theta}(r, z) := \frac{-r_{ic}^2}{2} \cdot \left(\frac{d^2}{dz^2} Y(z) \right)$$



$$\frac{1}{L} \cdot \left(\int_0^L -\tau_{crz}(r_{ic}, z) dz \right) = -6.143 \times 10^6$$

zans := 0.00:

$$\text{maxim}(z) := -\tau_{\text{crz}}(r_{\text{ic}}, z)$$

$$z_{\text{star}} := \text{Maximize}(\text{maxim}, z_{\text{ans}}) = -5 \times 10^{-9}$$

$$-\tau_{\text{crz}}(r_{\text{ic}}, z_{\text{ans}}) = -8.937 \times 10^6$$

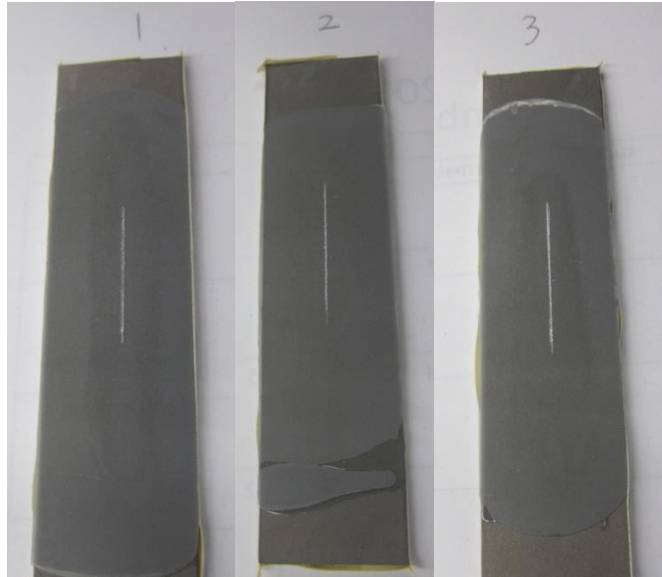
APPENDIX G: OPEN SANDWICH SAMPLES

Adhesive: DP460NS

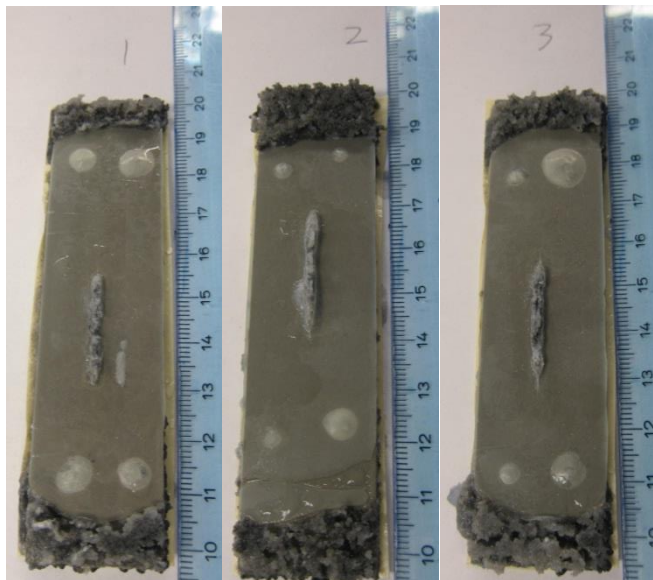
Adherend: Magnesium AZ31b

Preparation: Gritblasting

Before exposure:

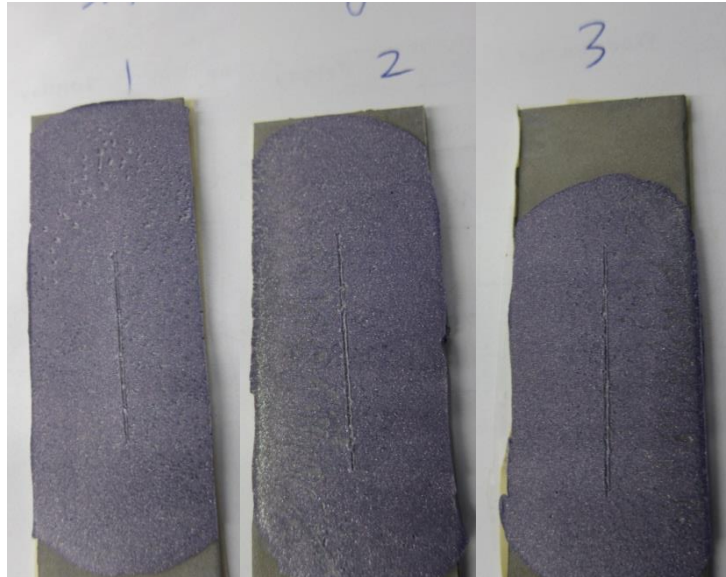


After exposure of 24 hours:

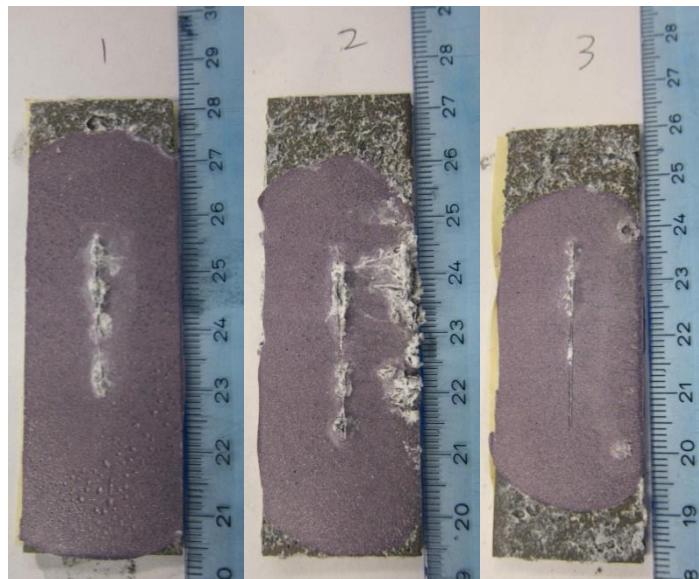


Adhesive: SA9850
Adherend: Magnesium AZ31b
Preparation: Gritblasting

Before exposure:

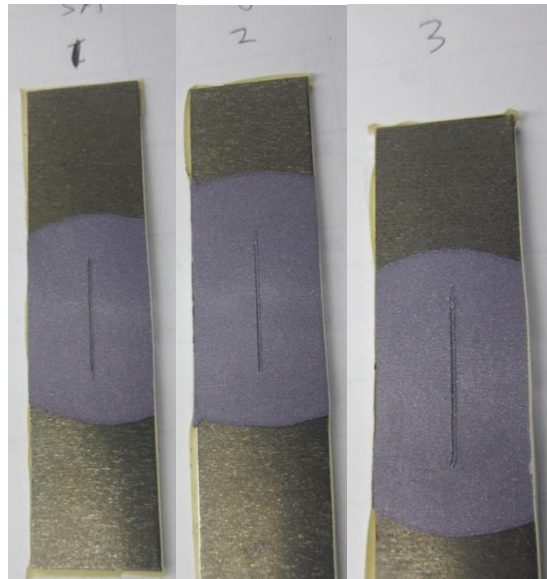


After exposure of 24 hours:

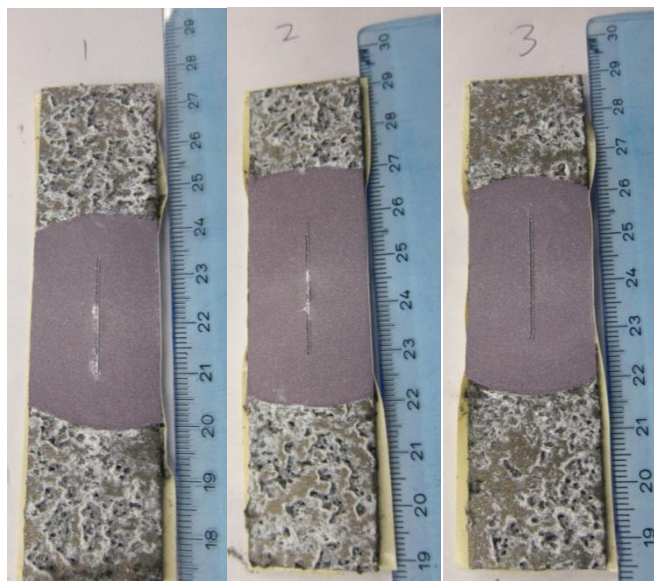


Adhesive: SA9850
Adherend: Magnesium AZ31b
Preparation: Contaminated / Drylube E1

Before exposure:

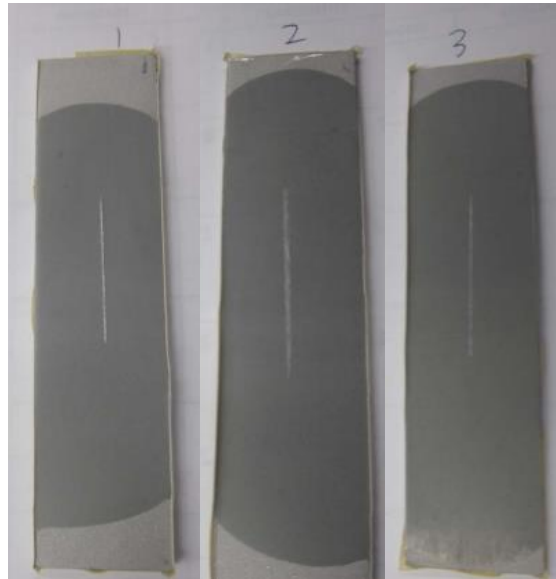


After exposure of 24 hours:

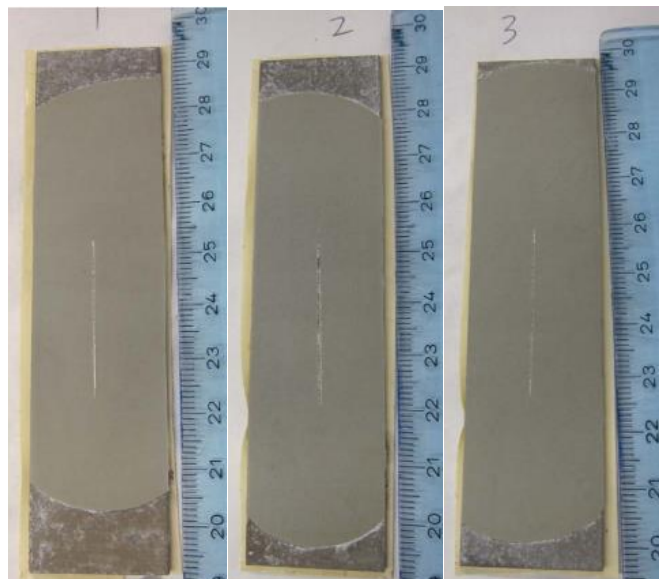


Adhesive: DP460NS
Adherend: Aluminum 6061-T6
Preparation: Gritblasting

Before exposure:

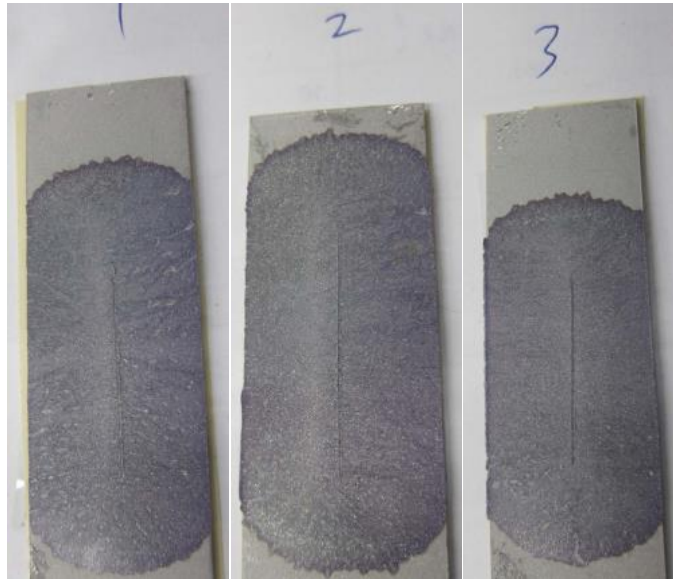


After exposure of 330 hours:

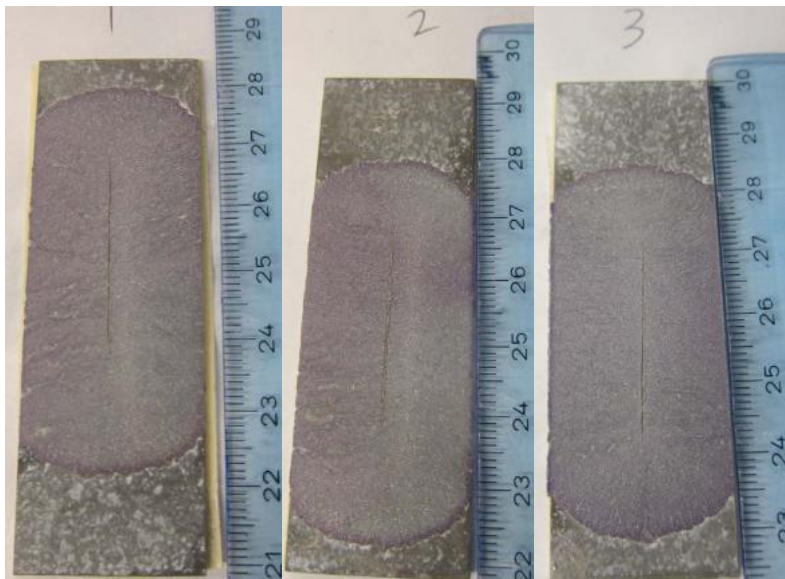


Adhesive: SA9850
Adherend: Aluminum 6061-T6
Preparation: Gritblasting

Before exposure:

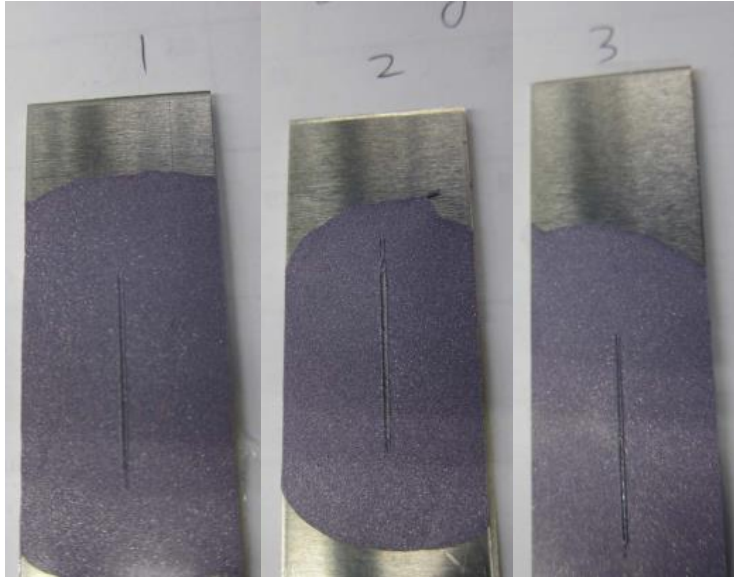


After exposure of 330 hours:

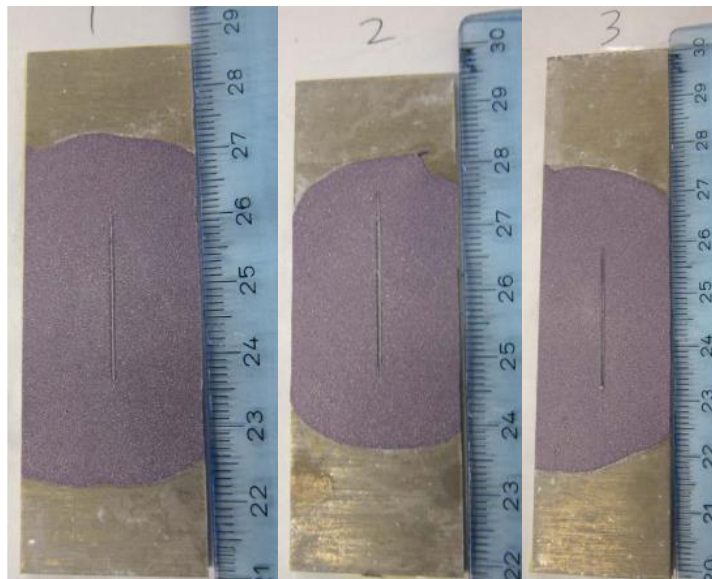


Adhesive: SA9850
Adherend: Aluminum 6061-T6
Preparation: Contamination / Drylube E1

Before exposure:



After exposure of 330 hours:



APPENDIX H: SAMP-1 MATERIAL MODEL INFORMATION

The four stress-strain information curves that can be supplied to SAMP-1 material model are:

- LCID-T: Tensile yield stress versus plastic strain curves.
- LCID-C: Compression yield stress versus plastic strain curve, this input is optional.
- LCID-S: Shear yield stress versus plastic strain curve, this input is optional.
- LCID-B: Biaxial yield tensile stress versus plastic strain curve, this input is optional.

If only LCID-T is specified, then the yield surface created will be identical to the Von Mises yield surface. (Figure 0-1)

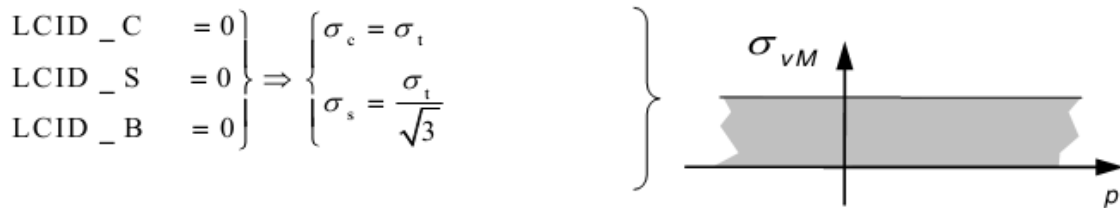


Figure 0-1: Yield surface utilized when only tension curves are defined (taken from LS-DYNA manual [133])

With two curves specified, the Drucker-Prager cone will be created (Figure 0-2). With three curves specified, a custom quadratic yield surface will be defined (Figure 0-3). With all four curves specified, SAMP-1 would interpolate the material stress response using least squares method.

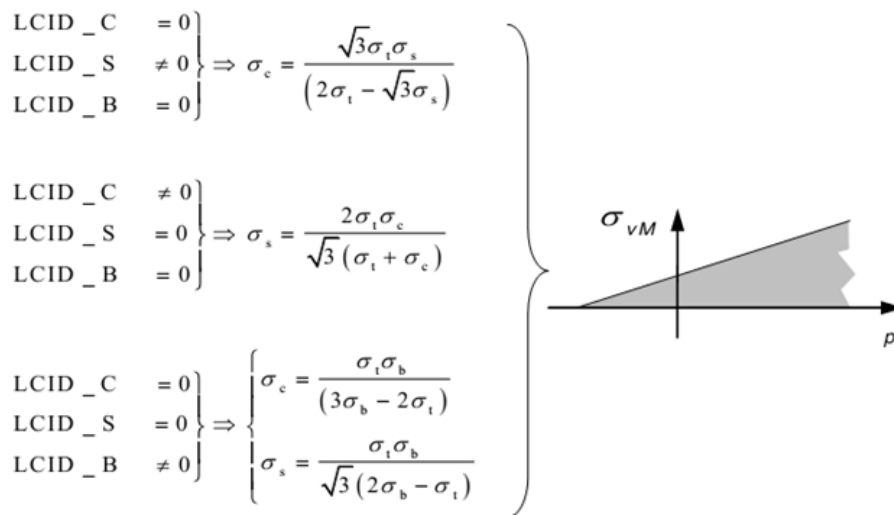


Figure 0-2: Yield surface with two curves defined (taken from LS-DYNA manual [133])

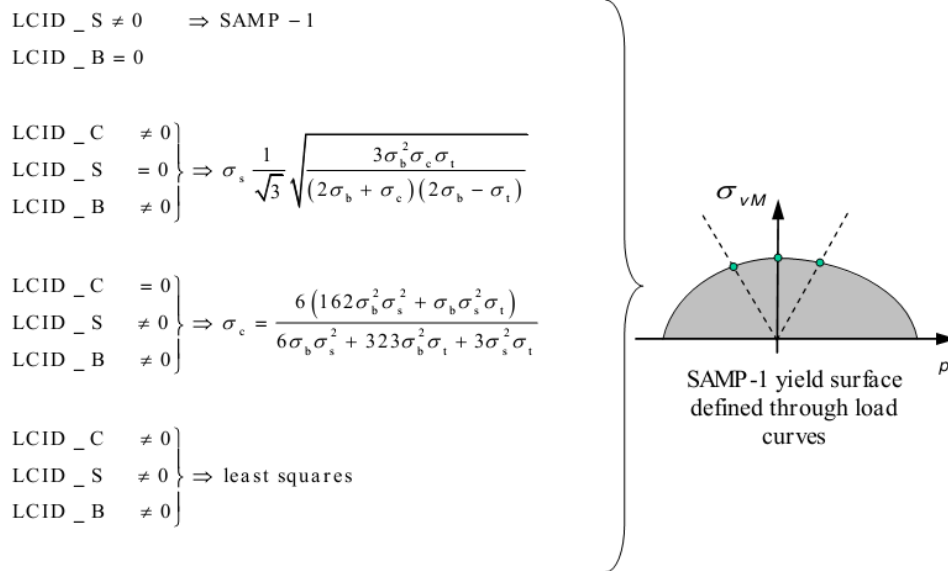


Figure 0-3: Yield surface with three curves defined (taken from LS-DYNA manual [133])

Rate effects are implemented in SAMP-1 by supplying LCID-T with several tension curves at different testing rates. It is also assumed that the rate effect in compression and shear is similar to the rate effect in tensile loading:

$$\sigma_s = \sigma_{s0} \frac{\sigma_t}{\sigma_{t0}}$$

$$\sigma_c = \sigma_{c0} \frac{\sigma_t}{\sigma_{t0}}$$

Equation 0.1: Yield stress interpolations

Where

σ_s = Yield shear strength

σ_{s0} = Yield shear strength defined at the slowest rate by input curve

σ_t = Yield tension strength

σ_{t0} = Yield tension strength defined at the slowest rate by input curve

σ_c = Yield compression strength

σ_{c0} = Yield compression strength defined at the slowest rate by input curve

Whether this assumption holds true for the particular set of adhesives tested will be investigated.

Damage of material is implemented in SAMP-1 material model in the form of variable d , a damage parameter which is a function of plastic strain. A load curve is provided relating d as a function of plastic strain during uniaxial tension. Fracture happens as soon as the value of d gets up to the critical damage value, which is specified in the input material card as D_c .

BIBLIOGRAPHY

- [1] Ghassemieh E. (2011) Materials in automotive application, state of the art and prospects. INTECH Open Access Publisher
- [2] Harrington W. (1997) Fuel economy and motor vehicle emissions. *J. Environ. Econ. Manage.*, 33: 240-252
- [3] Thorpe SG. (1997) Fuel economy standards, new vehicle sales, and average fuel efficiency. *Journal of Regulatory Economics*, 11: 311-326
- [4] National Highway Traffic Safety Administration. (2012) Corporate Average Fuel Economy for MY 2017 - MY 2025 Passenger Cars and Light Trucks. U.S. Department of Transportation
- [5] Yamane K, Furuhashi S. (1998) A study on the effect of the total weight of fuel and fuel tank on the driving performances of cars. *Int J Hydrogen Energy*, 23: 825-831
- [6] Jambor A, Beyer M. (1997) New cars — new materials. *Mater Des*, 18: 203-209
- [7] Miller WS, Zhuang L, Bottema J, Wittebrood AJ, De Smet P, Haszler A, Vieregge A. (2000) Recent development in aluminium alloys for the automotive industry. *Materials Science and Engineering: A*, 280: 37-49
- [8] Cole GS, Sherman AM. (1995) Light weight materials for automotive applications. *Mater Charact*, 35: 3-9
- [9] 2014 Ford F-150 Specifications. <http://www.ford.com/trucks/f150/2014/specifications/view-all/>
- [10] 2015 Ford F-150 Specifications. <http://www.ford.com/trucks/f150/specifications/view-all/>
- [11] Blawert C, Hort N, Kainer K. (2004) Automotive applications of magnesium and its alloys. *Trans. Indian Inst. Met*, 57: 397-408
- [12] Davies G. (2003) Magnesium. *Materials for Automotive Bodies*, 91: 1327
- [13] Friedrich H, Schumann S. (2001) Research for a “new age of magnesium” in the automotive industry. *J. Mater. Process. Technol.*, 117: 276-281
- [14] Hirsch J, Al-Samman T. (2013) Superior light metals by texture engineering: Optimized aluminum and magnesium alloys for automotive applications. *Acta Materialia*, 61: 818-843
- [15] Eliezer D, Aghion E, Froes FH. (1998) Magnesium Science, Technology and Applications. *Advanced Performance Materials*, 5: 201-212
- [16] Thomas WM, Nicholas ED. (1997) Friction stir welding for the transportation industries. *Mater Des*, 18: 269-273

- [17] Goede M, Stehlin M, eds. (2009) SuperLIGHT-Car project - An integrated research approach for lightweight car body innovations. Wolfsburg, Germany
- [18] Cotter J, Hockney M. (1974) Metal joining with adhesives. *International Metallurgical Reviews*, 19: 103-115
- [19] Barnes T, Pashby I. (2000) Joining techniques for aluminium spaceframes used in automobiles: Part II—adhesive bonding and mechanical fasteners. *J.Mater.Process.Technol.*, 99: 72-79
- [20] Critchlow GW, Yendall KA, Bahrani D, Quinn A, Andrews F. (2006) Strategies for the replacement of chromic acid anodising for the structural bonding of aluminium alloys. *Int J Adhes Adhes*, 26: 419-453
- [21] Bikerman JJ. (2013) *The science of adhesive joints*. Elsevier
- [22] Adams RD. (2005) *Adhesive bonding: science, technology and applications*. Elsevier
- [23] Oldfield JW. (1988) Electrochemical theory of galvanic corrosion. *Galvanic Corrosion*: 5-22
- [24] Digby R, Packham D. (1995) Pretreatment of aluminium: topography, surface chemistry and adhesive bond durability. *Int J Adhes Adhes*, 15: 61-71
- [25] Audi Collision Frame Technology Guide (2011): 39
- [26] Du Bois P, Chou CC, Fileta BB, Khalil TB, King AI, Mahmood HF, Mertz HJ, Wismans J, Prasad P, Belwafa JE. (2004) Vehicle crashworthiness and occupant protection
- [27] Federal Motor Vehicle Safety Standard. (2005) No. 208. Occupant Crash Protection, CFR, 49
- [28] Bauer CL, Lessmann GG. (1976) Metal-joining methods. *Annual Review of Materials Science*, 6: 361-387
- [29] Pilkey WD, Pilkey DF. (2008) *Peterson's stress concentration factors*. John Wiley & Sons
- [30] Junker GH. (1969) *New Criteria for Self-Loosening of Fasteners Under Vibration*
- [31] Handbook A. (1993) Volume 6: *Welding, Brazing and Soldering*. ASM International: 2603
- [32] Sun Z, Karppi R. (1996) The application of electron beam welding for the joining of dissimilar metals: an overview. *J.Mater.Process.Technol.*, 59: 257-267
- [33] Cotovsky S. (1965) *Method of friction welding dissimilar metals*
- [34] European Commission, ed. (2000) *Directive 2000/53/EC on end-of-life vehicles*
- [35] Haydon DW. (2002) ElectRelease - Electrically disbonding epoxy adhesive. *Assem.Autom.*, 22: 326-329

- [36] Ishikawa H, Seto K, Shimotuma S, Kishi N, Sato C. (2005) Bond strength and debonding behavior of elastomer and emulsion-type dismantlable adhesives used for building materials. *Int J Adhes Adhes*, 25: 193-199
- [37] Verna E, Cannavaro I, Brunella V, Koricho EG, Belingardi G, Roncato D, Martorana B, Lambertini V, Alina Neamtu V, Ciobanu R. (2013) Adhesive joining technologies activated by electro-magnetic external trims. *Int J Adhes Adhes*, 46: 21-25
- [38] Nishiyama Y, Uto N, Sato C, Sakurai H. (2003) Dismantlement behavior and strength of dismantlable adhesive including thermally expansive particles. *Int J Adhes Adhes*, 23: 377-382
- [39] Kim D, Chung I, Kim G. (2012) Dismantlement studies of dismantlable polyurethane adhesive by controlling thermal property. *J.Adhes.Sci.Technol.*, 26: 2571-2589
- [40] Khalil AA, Kagho AN. (1991) Non-destructive testing of adhesively bonded joints using vibrational analysis. *Int J Adhes Adhes*, 11: 121-127
- [41] Schliekelmann RJ. (1972) Non-destructive testing of adhesive bonded metal-to-metal joints 2. *Non-Destructive Testing*, 5: 144-153
- [42] Kubaschewski O. (2013) *Iron—Binary phase diagrams*. Springer Science & Business Media
- [43] Lapique F, Redford K. (2002) Curing effects on viscosity and mechanical properties of a commercial epoxy resin adhesive. *Int J Adhes Adhes*, 22: 337-346
- [44] Nicholson C. (1991) *History of Adhesives*. Educational Services Committee. Glen Ellyn, IL
- [45] Kinloch AJ, Shaw SJ, Tod DA, Hunston DL. (1983) Deformation and fracture behaviour of a rubber-toughened epoxy: 1. Microstructure and fracture studies. *Polymer*, 24: 1341-1354
- [46] Kinloch AJ, Shaw SJ, Hunston DL. (1983) Deformation and fracture behaviour of a rubber-toughened epoxy: 2. Failure criteria. *Polymer*, 24: 1355-1363
- [47] 3M, ed. (2009) Material Safety Data Sheet. Scotch-Weld™ Epoxy Adhesives DP460 Off-White - DP460NS
- [48] 3M, ed. (2012) Preliminary Technical Data Sheet. Impact Resistant Structural Adhesive SA9850
- [49] Trimino LF, Cronin DS, eds. (2013) *Adhesively Joined Crush Tube Structures Subjected to Impact Loading*. Lombard, IL
- [50] Thom C, Cronin DS. (2011) *Structural Adhesives: Thick Adherend Lap Shear*. Unpublished raw data
- [51] Adderley CS. (1988) Adhesive Bonding. *Mater Des*, 9: 287-293
- [52] Gali S, Dolev G, Ishai O. (1981) An effective stress/strain concept in the mechanical characterization of structural adhesive bonding. *Int J Adhes Adhes*, 1: 135-140

- [53] Cui H, Koussios S, Li Y, Beukers A. (2014) Constitutive law of adhesive layer measured with mixed mode bending test. *Eng.Fract.Mech.*, 127: 235-251
- [54] Kahraman R, Sunar M, Yilbas B. (2008) Influence of adhesive thickness and filler content on the mechanical performance of aluminum single-lap joints bonded with aluminum powder filled epoxy adhesive. *J.Mater.Process.Technol.*, 205: 183-189
- [55] Arenas JM, Narbón JJ, Alía C. (2010) Optimum adhesive thickness in structural adhesives joints using statistical techniques based on Weibull distribution. *Int J Adhes Adhes*, 30: 160-165
- [56] Teutenberg D, Hahn O. (2013) Predicting production influences on adhesively bonded joints subjected to cyclic load. *Weld.World*, 57: 203-213
- [57] Adams RD, Peppiatt NA. (1974) Stress Analysis of Adhesive-Bonded Lap Joints. *J Strain Anal*, 9: 185-196
- [58] Davies P, Sohier L, Cognard J-, Bourmaud A, Choqueuse D, Rinnert E, Créac'hcadec R. (2009) Influence of adhesive bond line thickness on joint strength. *Int J Adhes Adhes*, 29: 724-736
- [59] ASTM D3165. (2014) Standard Test Method for Strength Properties of Adhesives in Shear by Tension Loading of Single-Lap-Joint Laminated Assemblies
- [60] Volkersen O. (1938) Die Nietkraftverteilung in zugbeanspruchten Nietverbindungen mit konstanten Laschenquerschnitten. *Luftfahrtforschung*, 15: 41-47
- [61] Goland M, Reissner E. (1944) The Stresses in Cemented Joints. *Journal of Applied Mechanics*, 11: 17-27
- [62] Hart-Smith LJ. (1973) Adhesive-bonded single-lap joints. Langley Research Center Hampton, VA
- [63] da Silva LFM, das Neves PJC, Adams RD, Spelt JK. (2009) Analytical models of adhesively bonded joints—Part I: Literature survey. *Int J Adhes Adhes*, 29: 319-330
- [64] da Silva LFM, das Neves PJC, Adams RD, Wang A, Spelt JK. (2009) Analytical models of adhesively bonded joints—Part II: Comparative study. *Int J Adhes Adhes*, 29: 331-341
- [65] Kafkalidis MS, Thouless MD. (2002) The effects of geometry and material properties on the fracture of single lap-shear joints. *Int.J.Solids Structures*, 39: 4367-4383
- [66] Knox EM, Cowling MJ. (2000) Durability aspects of adhesively bonded thick adherend lap shear joints. *Int J Adhes Adhes*, 20: 323-331
- [67] ASTM D5656. (2004) Standard Test Method for Thick-Adherend Metal Lap-Shear Joints for Determination of the Stress-Strain Behavior of Adhesives in Shear by Tension Loading
- [68] ASTM D4562. (2007) Shear Strength of Adhesives Using Pin-and-Collar Specimen
- [69] Nemeş O, Lachaud F, Mojtabi A. (2006) Contribution to the study of cylindrical adhesive joining. *Int J Adhes Adhes*, 26: 474-480

- [70] Martínez MA, Velasco F, Abenojar J, Pantoja M, Del Real JC. (2008) Analytical solution to calculate the stress distribution in pin-and-collar samples bonded with anaerobic adhesives (following ISO 10123 standard). *Int J Adhes Adhes*, 28: 405-410
- [71] Thomsen OT. (1992) Elasto-static and elasto-plastic stress analysis of adhesive bonded tubular lap joints. *Composite Structures*, 21: 249-259
- [72] Cognard JY, Devaux H, Sohier L. (2010) Numerical analysis and optimisation of cylindrical adhesive joints under tensile loads. *Int J Adhes Adhes*, 30: 706-719
- [73] Yokoyama T, Shimizu H. (1998) Evaluation of Impact Shear Strength of Adhesive Joints with the Split Hopkinson Bar. *JSME International Journal Series A*, 41: 503-509
- [74] Dolev G, Ishai O. (1981) Mechanical characterization of adhesive layer in-situ and as bulk material. *The Journal of Adhesion*, 12: 283-294
- [75] ASTM D638. (2008) Standard test method for tensile properties of plastics. PA (USA)
- [76] Cole GS. (2007) Summary of “Magnesium vision 2020: A North American automotive strategic vision for magnesium”. *Essential Readings in Magnesium Technology*: 35-40
- [77] Seyfried P, Taiss EJM, Calijorne AC, Li F, Song Q. (2015) Light weighting opportunities and material choice for commercial vehicle frame structures from a design point of view. *Advances in Manufacturing*, 3: 19-26
- [78] Billur M, Altan T. (2012) Challenges in forming advanced high strength steels. *Proceedings of New Developments in Sheet Metal Forming*: 285-304
- [79] Totten GE. (2006) *Steel heat treatment: metallurgy and technologies*. crc Press
- [80] Kuziak R, Kawalla R, Waengler S. (2008) Advanced high strength steels for automotive industry. *Archives of Civil and Mechanical Engineering*, 8: 103-117
- [81] Li Y, Lin Z, Jiang A, Chen G. (2003) Use of high strength steel sheet for lightweight and crashworthy car body. *Mater Des*, 24: 177-182
- [82] Hirsch J. (2014) Recent development in aluminium for automotive applications. *Transactions of Nonferrous Metals Society of China*, 24: 1995-2002
- [83] Leyens C, Peters M. (2003) *Aerospace and Space Materials*. In: *Materials Science and Engineering Vol. III*. Wiley Online Library
- [84] Muraoka Y, Miyaoka H. (1993) Development of an all-aluminum automotive body. *J.Mater.Process.Technol.*, 38: 655-674
- [85] Schretzenmayr H. (1999) Technical report: the aluminium body of the Audi A8. *Int.J.Veh.Des.*, 21: 303-312

- [86] Major J, Makinde A, Lee P, Chamberlain B, Scappaticci T, Richman D. (1994) The lincoln mark VIII cast aluminum suspension control arm (parallel development). SAE transactions, 103: 635-646
- [87] Agarwala VK, Fort Jr. T. (1976) Nature of the stable oxide layer formed on an aluminum surface by work function measurements. Surf Sci, 54: 60-70
- [88] Oh H, Jang K, Chi C. (1999) Impedance Characteristics of Oxide Layers on Aluminium. Bull.Korean Chem.Soc, 20: 1341
- [89] Fridlyander I, Sister V, Grushko O, Berstenev V, Sheveleva L, Ivanova L. (2002) Aluminum alloys: Promising materials in the automotive industry. Metal science and heat treatment, 44: 365-370
- [90] Online Materials Information Resource. <http://www.matweb.com/>
- [91] Kulekci M. (2008) Magnesium and its alloys applications in automotive industry. The International Journal of Advanced Manufacturing Technology, 39: 851-865
- [92] Mordike B, Ebert T. (2001) Magnesium: properties—applications—potential. Materials Science and Engineering: A, 302: 37-45
- [93] Molodov KD, Al-Samman T, Molodov DA, Gottstein G. (2014) Mechanisms of exceptional ductility of magnesium single crystal during deformation at room temperature: Multiple twinning and dynamic recrystallization. Acta Materialia, 76: 314-330
- [94] Kurukuri S, Worswick M, Bardelcik A, Mishra R, Carter J. (2014) Constitutive Behavior of Commercial Grade ZEK100 Magnesium Alloy Sheet over a Wide Range of Strain Rates. Metallurgical and Materials Transactions A, 45: 3321-3337
- [95] Kurukuri S, Tari DG, Worswick MJ, Mishra RK, Carter JT Dynamic characterization of AZ31B and ZEK100 magnesium alloy sheets
- [96] Cabrera N, Mott N. (1949) Theory of the oxidation of metals. Reports on progress in physics, 12: 163
- [97] Gray JE, Luan B. (2002) Protective coatings on magnesium and its alloys — a critical review. J.Alloys Compounds, 336: 88-113
- [98] Miles MP, Fullwood D, Adams BL, Khosravani A, Scott J, Mishra RK. (2011) Room Temperature Ductility and Microstructure of Magnesium AZ31B Sheet. Journal of Materials Engineering and Performance, 20: 1357-1363
- [99] Boba M, ed. (2014) Warm Forming Behaviour of ZEK100 and AZ31B Magnesium Alloy Sheet
- [100] Davis JR. (2001) Surface engineering for corrosion and wear resistance. ASM international
- [101] Harris AF, Beevers A. (1999) The effects of grit-blasting on surface properties for adhesion. Int J Adhes Adhes, 19: 445-452

- [102] Brewis DM, Critchlow GW, Curtis CA. (1999) Cryoblasting as a pretreatment to enhance adhesion to aluminium alloys: an initial study. *Int J Adhes Adhes*, 19: 253-256
- [103] Rudawska A. (2014) Selected aspects of the effect of mechanical treatment on surface roughness and adhesive joint strength of steel sheets. *Int J Adhes Adhes*, 50: 235-243
- [104] The home of surface measurement. <http://www.rubert.co.uk/faqs/roughness-parameters/>
- [105] Hunter M, Fowle P. (1956) Natural and thermally formed oxide films on aluminum. *J.Electrochem.Soc.*, 103: 482-485
- [106] Descamps P, Iker J, Wolf AT. (1996) Effects of anodized aluminium surface parameters on the long-term adhesion of silicone structural glazing sealants. *Constr.Build.Mater.*, 10: 527-538
- [107] Wood GC, O'Sullivan JP. (1970) The anodizing of aluminium in sulphate solutions. *Electrochim.Acta*, 15: 1865-1876
- [108] Diggle JW, Downie TC, Goulding CW. (1969) Anodic oxide films on aluminum. *Chem.Rev.*, 69: 365-405
- [109] Kollek H. (1985) Some aspects of chemistry in adhesion on anodized aluminium. *Int J Adhes Adhes*, 5: 75-80
- [110] Brockmann W, Hennemann O-, Kollek H. (1982) Surface properties and adhesion in bonding aluminium alloys by adhesives. *Int J Adhes Adhes*, 2: 33-40
- [111] ArÅ«nas Jagminas. (2012) How and Why Alumina Matrix Architecture Influence the Shape and Composition of Nanowires Grown by AC Deposition?. In:
- [112] Gao G, Ricketts M. (2002). Evaluation of protective coatings on magnesium for phosphate process compatibility and galvanic corrosion prevention
- [113] Pellerin C, Booker SM. (2000) Reflections on hexavalent chromium: health hazards of an industrial heavyweight. *Environ.Health Perspect.*, 108: A402-7
- [114] Schuman TP. (2005) Chapter 17 - Protective coatings for aluminum alloys. In: Kutz M, ed. *Handbook of Environmental Degradation of Materials*. Norwich, NY. William Andrew Publishing: 345-366
- [115] Gledhill RA, Kinloch AJ. (1974) Environmental Failure of Structural Adhesive Joints. *The Journal of Adhesion*, 6: 315-330
- [116] Ahmad Z, Ansell MP, Smedley D. (2010) Effect of nano- and micro-particle additions on moisture absorption in thixotropic room temperature cure epoxy-based adhesives for bonded-in timber connections. *Int J Adhes Adhes*, 30: 448-455
- [117] Brewis DM, Comyn J, Tegg JL. (1980) The durability of some epoxide adhesive-bonded joints on exposure to moist warm air. *Int J Adhes Adhes*, 1: 35-39

- [118] Bowditch MR. (1996) The durability of adhesive joints in the presence of water. *Int J Adhes Adhes*, 16: 73-79
- [119] Da Silva LF, Campilho RD. (2012) *Advances in numerical modelling of adhesive joints*. Springer
- [120] Zhao X, Adams R, Da Silva L. (2011) Single lap joints with rounded adherend corners: stress and strain analysis. *J.Adhes.Sci.Technol.*, 25: 819-836
- [121] Roylance D. (2001) *Introduction to fracture mechanics*. Massachusetts Institute of
- [122] Barenblatt GI. (1962) The mathematical theory of equilibrium cracks in brittle fracture. *Adv.Appl.Mech.*, 7: 55-129
- [123] De Moura MFSF, Gonçalves JPM, Chousal JAG, Campilho RDSG. (2008) Cohesive and continuum mixed-mode damage models applied to the simulation of the mechanical behaviour of bonded joints. *Int J Adhes Adhes*, 28: 419-426
- [124] Christensen ET, Sjølund JH, Glud JA, eds. (2013) *Formulation of Cohesive Finite Element for Analysing Strength of Wrinkles in Glass-Epoxy Laminates*
- [125] Bala S. (2007) *Tie-break contacts in LS-DYNA*. Livermore Software
- [126] Xiao X, Foss PH, Schroeder JA. (2004) Stiffness prediction of the double lap shear joint. Part 2: Finite element modeling. *Int J Adhes Adhes*, 24: 239-246
- [127] Lubowiecka I, Rodríguez M, Rodríguez E, Martínez D. (2012) Experimentation, material modelling and simulation of bonded joints with a flexible adhesive. *Int J Adhes Adhes*, 37: 56-64
- [128] Duncan B, Dean G. (2003) Measurements and models for design with modern adhesives. *Int J Adhes Adhes*, 23: 141-149
- [129] Ali A, Hosseini M, Sahari BB. (2010) A Review of Constitutive Models for Rubber-Like Materials. *American Journal of Engineering and Applied Sciences* 3, 1: 232-239
- [130] Kolling S, Haufe A, Feucht M, Du Bois PA, eds. (2006) *A Constitutive Formulation for Polymers Subjected to High Strain Rates*. Detroit
- [131] Anderson TL, Anderson T. (2005) *Fracture mechanics: fundamentals and applications*. CRC press
- [132] Yang QD, Thouless MD. (2001) Mixed-mode fracture analyses of plastically-deforming adhesive joints. *Int.J.Fract.*, 110: 175-187
- [133] Livermore software technology corporation (LSTC), ed. (2012) *LS-DYNA Keyword User's Manual Volume II: Material Models*, version 971 R6.1.0
- [134] ASTM D1002. (2010) *Standard Test Method for Apparent Shear Strength of Single-Lap-Joint Adhesively Bonded Metal Specimens by Tension Loading (Metal-to-Metal)*

- [135] ASTM D3528. (2008) Standard Test Method for Strength Properties of Double Lap Shear Adhesive Joints by Tension Loading
- [136] DeVries KL, Borgmeier PR. (2003) Testing of Adhesives, Chapter 11. In: Handbook of Adhesive Technology, 2nd Edition. NY. Marcell Dekker Publ. Co.: 223
- [137] Broughton WR, Crocker LE, Urquhart JM . (2001) Strength of adhesive joints: a parametric study. National Physical Laboratory. Teddington, Middlesex
- [138] da Silva LFM, Carbas RJC, Critchlow GW, Figueiredo MAV, Brown K. (2009) Effect of material, geometry, surface treatment and environment on the shear strength of single lap joints. Int J Adhes Adhes, 29: 621-632
- [139] Frostig Y, Thomsen OT, Mortensen F. (1999) Analysis of adhesive-bonded joints, square-end, and spew-fillet-high-order theory approach. J.Eng.Mech., 125: 1298-1307
- [140] Adams RD, Comyn J, Wake WC. (1997) Structural adhesive joints in engineering. Springer Science & Business Media
- [141] 3M, ed. (2015) DP460NS Technical Data Sheet
- [142] Thom C, ed. (2011) Experimental Work Documentation V2
- [143] Tracker v4.05. D. Brown. Licensed under GNU General Public License.
<http://www.cabrillo.edu/~dbrown/tracker/>
- [144] ASTM B117. (2011) Standard Practice for Operating Salt Spray (Fog) Apparatus
- [145] Personal communication with J. Kish. McMaster University, Hamilton, Ontario, Canada. (2014)
- [146] ASTM G1-03. (2003) Standard practice for preparing, cleaning, and evaluating corrosion test specimens
- [147] Hallquist JO. (2006) LS-DYNA theory manual. Livermore software Technology corporation, 3
- [148] Tvergaard V, Hutchinson JW. (1993) The Influence of Plasticity On Mixed Mode Interface Toughness. Journal of the Mechanics and Physics of Solids, 41: 1119-1135
- [149] da Silva, Lucas Filipe Martins. (2011) Handbook of adhesion technology: with 97 tables. In: . Springer Science & Business Media: 655
- [150] Hart-Smith LJ. (1973) Adhesive-Bonded Double-Lap Joints. National Aeronautics and Space Administration. Long Beach, California
- [151] Chai H. (1986) Bond thickness effect in adhesive joints and its significance for mode I interlaminar fracture of composites. ASTM STP, 893: 209-231
- [152] Chai H. (1993) Observation of deformation and damage at the tip of cracks in adhesive bonds loaded in shear and assessment of a criterion for fracture. Int.J.Fract., 60: 311-326

- [153] Mall S, Ramamurthy G. (1989) Effect of bond thickness on fracture and fatigue strength of adhesively bonded composite joints. *Int J Adhes Adhes*, 9: 33-37
- [154] Daghyani H, Ye L, Mai Y. (1996) Evaluation of mode-II fracture energy of adhesive joints with different bond thickness. *The Journal of Adhesion*, 56: 171-186
- [155] da Silva LF, De Magalhaes F, Chaves F, De Moura M. (2010) Mode II fracture toughness of a brittle and a ductile adhesive as a function of the adhesive thickness. *The Journal of Adhesion*, 86: 891-905
- [156] ASTM D2344, ed. (1995) Standard Test Method for Apparent Interlaminar Shear Strength of Parallel Fiber Composites by Short-Beam Method
- [157] Abali F, Pora A, Shivakumar K. (2003) Modified short beam shear test for measurement of interlaminar shear strength of composites. *J.Composite Mater.*, 37: 453-464
- [158] Browning CE, Abrams FL, Whitney JM. (1983) A Four-Point Shear Test for Graphite/Epoxy Composites. In: *Composite Materials: Quality Assurance and Processing, ASTM STP 797*. American Society for Testing and Materials: 54
- [159] ASTM D5379. (1993) Standard test method for shear properties of composite materials by the V-notched beam method. Philadelphia: American Society for Testing and Materials
- [160] Moussiaux E, ed. (1987) Bending of a bonded beam as a test method for adhesive properties
- [161] Yang Q, Thouless M, Ward S. (2001) Elastic-plastic mode-II fracture of adhesive joints. *Int.J.Solids Structures*, 38: 3251-3262
- [162] Chai H. (1993) Deformation and failure of adhesive bonds under shear loading. *J.Mater.Sci.*, 28: 4944-4956
- [163] Wang M, Kornfield JA. (2012) Measuring shear strength of soft-tissue adhesives. *Journal of Biomedical Materials Research Part B: Applied Biomaterials*, 100: 618-623
- [164] Raykhere SL, Kumar P, Singh R, Parameswaran V. (2010) Dynamic shear strength of adhesive joints made of metallic and composite adherents. *Mater Des*, 31: 2102-2109
- [165] VID-2D v2009. Anonymous Corellated Solutions <http://www.correlatedsolutions.com/vic-2d/>
- [166] Tomblin J, Seneviratne W, Escobar P, Yoon-Khian Y. (2002). Shear stress-strain data for structural adhesives
- [167] Raman SN, Ngo T, Lu J, Mendis P. (2013) Experimental investigation on the tensile behavior of polyurea at high strain rates. *Mater Des*, 50: 124-129
- [168] Lubkin J, Reissner E. (1955) Stress distributions and design data for adhesive lap joints between circular tubes. American Society of Mechanical Engineers

[169] Shi YP, Cheng S. (1993) Analysis of adhesive-bonded cylindrical lap joints subjected to axial load. J.Eng.Mech., 119: 584-602